2022

Synthesis And Reactivity Of Flexible Dicopper Bis(pyridyldiimine) Macrocyclic Complexes

Sam Brooks
University of Pennsylvania

Synthesis And Reactivity Of Flexible Dicopper Bis(pyridyldiimine) Macrocyclic Complexes

Abstract

Methanol is a viable fuel source and a common feedstock in the chemical industry. Currently, much of the methanol produced by industry is derived from natural gas (methane). Yet, the one-step selective oxidation of methane to methanol remains challenging due to the potential formation of overoxidation products (CO_2, H_2O, etc.). Within the past 20 years, the reactive Cu2(II,II)-μ-O site within Cu(II)-ZSM-5 has been shown capable of the selective oxidation of methane to methanol through a hydrogen atom transfer (HAT)/radical rebound mechanism. The proximity of the metals and geometric constraints may allow for the copper centers to work in concert when facilitating HAT. To probe how metal-metal distance and coordination geometry influence C–H bond oxidation, it is highly desirable to study the properties and reactivity profile of discrete multinuclear model complexes. Here, we report a new protocol for the synthesis of homobimetallic copper(II) complexes using various derivatives of a macrocycle containing two pyridyldiimine units. A series of Cu2-(μ-X)n bis(4-tert-butylpyridyldiimine) macrocyclic complexes (n = 1, 2; X = Cl, Br, N_3, NO_2, OTMS, OH) were synthesized and crystallographically characterized. The development of new macrocyclic ligands was also undertaken to provide a modular synthesis of bis(pyridyldiimine) ligand scaffolds, in which the steric and electronic profiles can be easily tuned. Using the newly established synthetic protocols and macrocyclic ligands, two Cu2(II,II)-μ-OH complexes were prepared and analyzed by cyclic voltammetry and low-temperature 1H NMR spectroscopy. The macrocyclic complexes differed in the aliphatic linkers between the pyridyldiimine units (ethylene vs. propylene linker). New Cu2(II,II)-μ-O complexes were accessed through deprotonation of the hydroxide starting materials. The μ-oxo complexes were found competent for hydrogen atom transfer reactions, showing reactivity towards weak C-H and N-H bonds. From these studies, the size of the macrocycle was found to influence the reactivity of the μ-oxo complexes. The HAT reactions afforded Cu2(I,II)-μ-OH complexes, and O-H BDFEs of 74.3 ± 1.4 (propylene-linked complex) and 79.0 ± 1.5 kcal/mol (ethylene-linked complex) were estimated using Bordwell's thermodynamic square scheme approach.

Degree Type

Dissertation

Degree Name

Doctor of Philosophy (PhD)

Graduate Group

Chemistry

First Advisor

Neil C. Tomson

Subject Categories

Inorganic Chemistry

SYNTHESIS AND REACTIVITY OF FLEXIBLE DICOPPER *BIS*(PYRIDYLDIIMINE) MACROCYCLIC COMPLEXES

Sam H. Brooks

A DISSERTATION

in

Chemistry

Presented to the Faculties of the University of Pennsylvania

in

Partial Fulfillment of the Requirements for the

Degree of Doctor of Philosophy

2022

Supervisor of Dissertation

_____

Neil C. Tomson

Assistant Professor of Chemistry

Graduate Group Chairperson

_____

Daniel J. Mindiola

Brush Family Professor of Chemistry

Dissertation Committee

Daniel J. Mindiola	Brush Family Professor of Chemistry
Karen I. Goldberg	Vagelos Professor of Energy Research
Donald H. Berry	Professor of Chemistry

ABSTRACT

SYNTHESIS AND REACTIVITY OF FLEXIBLE DICOPPER *BIS*(PYRIDYLDIIMINE) MACROCYCLIC COMPLEXES

Sam H. Brooks

Neil C. Tomson

Methanol is a viable fuel source and a common feedstock in the chemical industry. Currently, much of the methanol produced by industry is derived from natural gas (methane). Yet, the one-step selective oxidation of methane to methanol remains challenging due to the potential formation of overoxidation products (CO_2, H_2O, *etc*.). Within the past 20 years, the reactive Cu_2(II,II)-μ-O site within Cu(II)-ZSM-5 has been shown capable of the selective oxidation of methane to methanol through a hydrogen atom transfer (HAT)/radical rebound mechanism. The proximity of the metals and geometric constraints may allow for the copper centers to work in concert when facilitating HAT. To probe how metal-metal distance and coordination geometry influence C–H bond oxidation, it is highly desirable to study the properties and reactivity profile of discrete multinuclear model complexes. Here, we report a new protocol for the synthesis of homobimetallic copper(II) complexes using various derivatives of a macrocycle containing two pyridyldiimine units. A series of Cu_2-(μ-X)$_n$ *bis*(4-*tert*-butylpyridyldiimine) macrocyclic complexes (n = 1, 2; X = Cl, Br, N_3, NO_2, OTMS, OH) were synthesized and crystallographically characterized. The development of new macrocyclic ligands was also undertaken to provide a modular synthesis of *bis*(pyridyldiimine) ligand scaffolds, in which the steric and electronic profiles can be easily tuned. Using the newly established synthetic protocols and macrocyclic ligands, two Cu_2(II,II)-μ-OH complexes were prepared and analyzed by cyclic voltammetry and low-temperature ^{1}H NMR spectroscopy. The

macrocyclic complexes differed in the aliphatic linkers between the pyridyldiimine units (ethylene vs. propylene linker). New Cu_2(II,II)-μ-O complexes were accessed through deprotonation of the hydroxide starting materials. The μ-oxo complexes were found competent for hydrogen atom transfer reactions, showing reactivity towards weak C-H and N-H bonds. From these studies, the size of the macrocycle was found to influence the reactivity of the μ-oxo complexes. The HAT reactions afforded Cu_2(I,II)-μ-OH complexes, and O-H BDFEs of 74.3 ± 1.4 (propylene-linked complex) and 79.0 ± 1.5 kcal/mol (ethylene-linked complex) were estimated using Bordwell's thermodynamic square scheme approach.

TABLE OF CONTENTS

LIST OF TABLES

LIST OF FIGURES

LIST OF SCHEMES

CHAPTER 1 : INTRODUCTION

1.1 Dissertation Statement

This dissertation focuses on the design and synthesis of Cu_2(II,II) clusters bound by *bis*(pyridyldiimine) macrocycles for the application of selective hydrocarbon oxidation. In particular, Cu_2(II,II)-μ-oxo macrocyclic complexes are targeted to assess the geometric/electronic factors that govern C-H bond oxidation.

1.2 Industrial Methanol Production

The growing energy demand by the world population necessitates a constant source of fuel. In recent years, natural gas has risen as one of the prominent players and is projected to surpass the use of petroleum fuel resources.[1] The gaseous hydrocarbon methane (CH_4) is the primary component of natural gas and has a greater energy density compared with other hydrocarbons. The molecule provides a high value of mass heat (*ca*. 56 kJ/g), thus making natural gas an efficient fuel source.[2] Yet, methane is a potent greenhouse gas and poses a global concern if natural gas cannot be transported safely and efficiently once extracted from the Earth's crust.[3] If transportation needs cannot be met, natural gas may be burned (*i.e.* flared) to produce carbon dioxide, a less but still harmful greenhouse gas. A proposed solution to transportation challenges involves the conversion of methane to an easily transportable, safer liquid alternative. Methanol, CH_3OH, the partially oxidized form of methane, is liquid at room temperature and offers a practical answer to the obstacles faced in natural gas transportation.

Methanol, the simplest alcohol, is a common C_1 building block in the chemical industry with high potential as an alternative fuel source.[4] With a low boiling point of 64.7 °C, methanol offers a safer advantage to transporting natural gas from both economic and

environmental standpoints. The synthesis of methanol from methane, however, is nontrivial. Industry performs this transformation over two steps in which methane is first steam-reformed into synthesis gas (syngas, a mixture of carbon monoxide and dihydrogen).[5] The process is performed over a Ni/Al_2O_3 catalyst at temperatures ranging from 900-1000 °C and pressures ranging from 15-30 bar (note: all C-H bonds in methane are broken during this step). Syngas is then converted to methanol over a $Cu/ZnO/Al_2O_3$ catalyst using temperatures of 240-260 °C and pressures of 50-100 bar. While the overall two-step synthesis achieves high conversion and selectivity for methanol, the energetic requirements make this transformation infeasible at methane flaring sites that do not house industrial plants.

Identifying new systems that mediate the one-step, selective oxidation of methane to methanol may address the natural gas transportation dilemma. Importantly, implementing a mild oxidation route that requires less energy and is atom economical has its own challenges. Selectively oxidizing methane to methanol proves difficult due to the high C–H bond strength of methane (105 kcal/mol).[3] Moreover, methanol is prone to overoxidation. An ideal pathway would include a catalyst capable of facilitating both selective C–H bond activation and functionalization, in which an oxygen atom from the oxidant is incorporated directly into methanol. The oxidant dioxygen is used in the industrial production of many base chemicals. Dioxygen is abundant, environmentally benign, and offers a green alternative to syngas in the production of methanol. Examples of the oxidation of methane to methanol using dioxygen are scarce. The search continues for a worthy, competent catalyst for the difficult C–H bond oxidation reaction.

1.3 Selective Methane Hydroxylation by Cu-ZSM-5

Addressing alternative, milder means of oxidizing methane to methanol proves challenging from selectivity, conversion and scale-up concerns. Within the last 20 years, copper-exchanged zeolite materials have made a direct impact on the oxidation of methane by allowing lower-temperature routes to be accessed.[6] Zeolites are porous materials composed of an aluminosilicate framework, which varies depending on the zeolite topology. Transition metals, such as copper, are readily exchanged within these frameworks and display varying degrees of reactivity toward small molecule activation and functionalization. Regarding methane oxidation, numerous reviews cover the role of copper-impregnated zeolites in mediating the oxidative transformation.[7-9] While this dissertation does not cover the exhaustive list of zeolites used, the first example, Cu-ZSM-5 (ZSM-5 = Zeolite Socony Mobil-5), is highlighted due to the well-defined nature of the active site and thorough mechanistic studies on the oxidation of methane to methanol.

1.3.1 ZSM-5 Topology Defined

Zeolite pore sizes and shapes constitute the topology of the framework. The zeolite ZSM-5 adopts a three-dimensional framework. The framework contains two interconnected channels consisting of 10-membered aluminosilicate rings (Figure 1.1, A).[10,11] (Ring sizes are dependent on the number of aluminum and silicon vertices; each aluminum and silicon are bridged by oxygen atoms.) The remainder of the ZSM-5 lattice consists of 5- and 6-membered rings (Figure 1.1, B). Pore size dictates/constrains the sizes of molecules that can move throughout the lattice. Within ZSM-5, CH_4 and O_2 are of suitable size to pass through the 10-membered ring channels but are unable to pass through the smaller-sized pores (Figure 1.1, C).[12] Additionally, crystallographic analysis by Mentzen and coworkers revealed that once copper is introduced to the ZSM-5 lattice,

a dinuclear site is found within the 10-membered ring.[13] Thus, with a dicopper site present and accessible to small molecules, the larger pore is understood to house the active site that is responsible for selective methane hydroxylation using dioxygen as the oxidant.

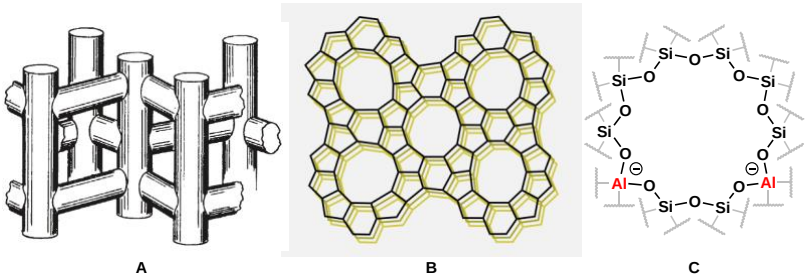

Figure 1.1 ZSM-5 framework: A) Three-dimensional interconnected channels in ZSM-5 (Adapted with permission from ref. 11**.** Copyright 1978 Spring Nature); B) Representation of channels along face [010]; C) "Naked" 10-membered aluminosilicate ring.

1.3.2 Cu-ZSM-5 Promoted Activation of O_2

Selective methane oxidation by Cu-ZSM-5 is achieved in a two-step process: activation of O_2 followed by C–H bond functionalization (*vide infra*). Groothaert and coworkers previously described the treatment of Cu(II)-ZSM-5 at 450 °C with O_2.[14] The oxygenated zeolite was found to be competent for the stoichiometric conversion of CH_4 to CH_3OH at 175 °C (Scheme 1.1). Examining the active oxidant by fiber-optic UV-vis spectroscopy led to the assignment of an intense ligand-to-metal charge transfer (LMCT) band at 22,700 cm^{-1}, suggesting the formation of a Cu_2(III,III)-*bis*(μ-oxo) core. Later analysis by Solomon and coworkers using resonance Raman spectroscopy excluded the presence of a *bis*(μ-oxo) core based on the observed Cu–O bond vibrational stretching frequencies (rR vibrations – 456 cm^{-1} and 870 cm^{-1}).[12] Instead, a bent Cu_2(II,II)-μ-oxo core better described the active site in the ZSM-5 lattice.

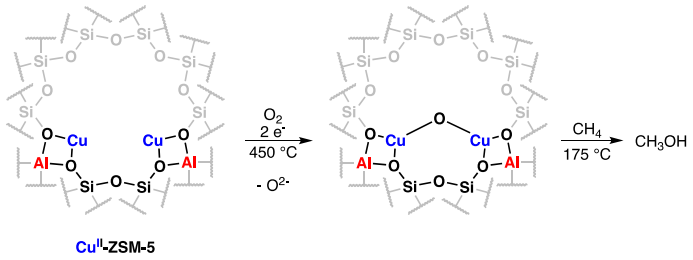

Scheme 1.1 Selective methane hydroxylation by Cu(II)-ZSM-5 using O_2 as the oxidant.

Initial structural analysis of the Cu_2(II,II)-μ-oxo core suggested a close Cu–Cu distance of ~2.9 Å using EXAFS spectroscopy.[15] However, the distance was brought into question as the copper ions composing the μ-oxo active sites (~5% of the total Cu content in ZSM-5) were indistinguishable from the spectator Cu ions in the EXAFS spectrum. A Cu-O-Cu angle of 140° was identified using normal coordinate analysis calculations. DFT (Density Functional Theory) calculations were able to reproduce the Cu_2(II,II)-μ-oxo core within a 10-membered aluminosilicate ring.[12] The optimized structure displayed a Cu-O-Cu angle of 139° and a Cu–Cu distance of 3.29 Å, indicating a close distance of the copper ions is required to stabilize the bridging oxo ligand.

The currently accepted mechanism of O_2 activation by the dinuclear copper core was elucidated by Solomon and coworkers (Scheme 1.2).[16] Exposure of Cu(I)-ZSM-5 to O_2 at room temperature led to the generation of Cu_2(II,II)-μ(η^2:η^2)-peroxide intermediate with a distinct LMCT band at 29,000 cm^{-1}. Resonance Raman spectroscopy confirmed the bridging peroxide unit with characteristic rR vibrations at 269 cm^{-1} and 736 cm^{-1}. Upon heating the zeolite, the peroxide intermediate converted to the bent μ-oxo, as evidenced by UV-vis spectroscopy. Using $^{18}O_2$ in tandem with temperature-programmed desorption experiments, Solomon found that the second oxygen atom of the peroxide intermediate is lost to the zeolite lattice upon oxo formation. The electrons required for the reduction of the peroxide intermediate are thought to originate from spectator Cu(I) ions within the lattice.

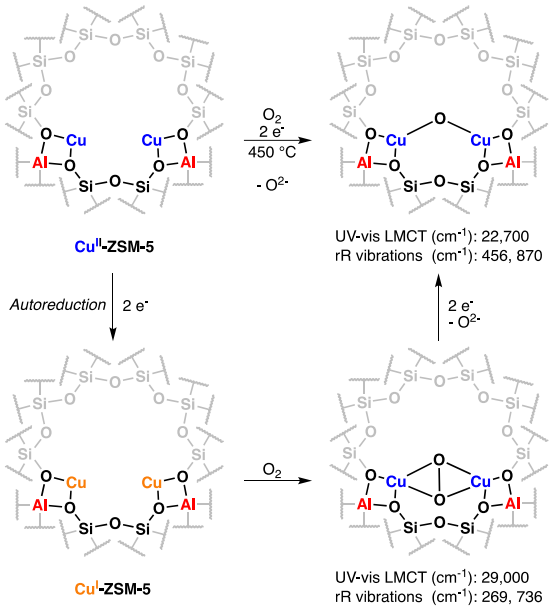

Scheme 1.2 Proposed mechanism of Cu_2(II,II)-μ-oxo core formation in ZSM-5.

1.3.3 Selective Methane Oxidation within Cu-ZSM-5

Methane hydroxylation by the bent μ-oxo core in Cu(II)-ZSM-5 affords methanol with 98% selectivity but low yield (8.2 μmol CH_3OH per gram of ZSM-5). Solomon reported a kinetic isotope effect of 3.1 (at 175 °C), indicating C–H bond cleavage plays a role in the rate-determining step of oxidation. DFT calculations supported a hydrogen atom abstraction/radical-rebound mechanism (Scheme 1.3), driven by the formation of a strong O–H bond (BDE calc. = 90 kcal/mol). In the transition state, the Cu_2O unit was found to have significant oxyl-character at the bridging oxygen, which may facilitate hydrogen atom abstraction through a radical-based mechanism.

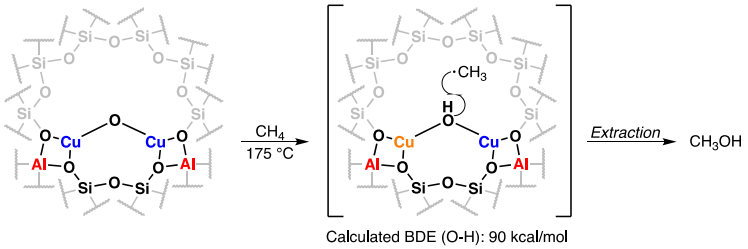

Scheme 1.3 Hydrogen atom abstraction by a Cu_2(II,II)-μ-oxo in ZSM-5.

Following Solomon's experimental/computational mechanistic analysis, Wu and coworkers evaluated the mechanistic hypothesis using a combination of EPR and solid-state NMR spectroscopy.[17] To support a radical-rebound mechanism, the spin-trapping agent DMPO (DMPO = 5,5-dimethyl-1-pyrroline-N-oxide) was employed in the reaction mixture. Both DMPO/·CH_3 and DMPO/·OH adducts were observed by EPR spectroscopy, supporting the radical-like mechanism for selective methane hydroxylation. Solid-state NMR spectroscopy techniques were then used to discern the fate of the methanol product. The spectral data indicated that methanol remained adsorbed on the zeolite surface in the form of surface methoxy species. Upon extraction, free methanol was obtained.

1.3.4 Perspective on Advantages and Drawbacks of ZSM-5 in Methane Oxidation

The role of Cu(II)-ZSM-5 in selective methane oxidation to methanol offers a promising alternative to the conventional industrial pathway. The zeolite-based transformation is achieved at milder temperatures and achieves high selectivity. Importantly, dioxygen is used as the oxidant, which is a less expensive and more atom-economical alternative to the steam reformation process. Moreover, a successful catalytic application of the zeolite has been demonstrated using a mixture of CH_4, O_2 and water, albeit with lower productivity than the stoichiometric pathway.[18]

Despite these advantages, the zeolite system needs further refinement before translation to industry, due to issues with conversion and scale-up. Low yields of methanol continue to make the scale-up process cost-prohibitive. The most productive pathways are achieved through a stepwise batch process, in which the zeolite is continuously temperature-cycled, thus decreasing the industrial value of the system. While Cu(II)-ZSM-5 mediates the stoichiometric/catalytic conversion of methane to methanol using dioxygen,

new avenues of efficient catalysis are crucial to addressing the concerns of natural gas transportation and flaring.

1.4 Synthetic Cu_2(II,II)-μ-Oxo Complexes

The successful demonstration of methane C–H bond functionalization by Cu(II)-ZSM-5 offers evidence for the highly reactive nature of a Cu_2(II,II)-μ-oxo core. Designing Cu_2(II,II) complexes capable of housing such a core may lead to the discovery of new systems capable of hydrocarbon oxidation and influence future homogeneous/heterogeneous catalyst designs. However, limited information remains available on the synthesis and reactivity of Cu_2(II,II)-μ-oxo complexes.[19] Of the established systems, few show reactivity towards hydrocarbon substrates, leaving the area in need of further advancement. Selected examples of molecular Cu_2(II,II)-μ-oxo complexes are presented in sections 1.41 and 1.4.2 to highlight common synthetic techniques and similarities/differences in reactivity.

1.4.1 Cu_2(II,II)-μ-Oxo Complexes Supported by Mononucleating Ligands

Karlin and coworkers reported the synthesis of a Cu_2(II,II)-μ-oxo complex bearing the $PhCH_2$(PY2) ligand (PY2 = *bis*(2-pyridylethyl)amine) (Scheme 1.4).[20] Upon treating the yellow mononuclear Cu(I) precursor with O_2 at 0 °C, a new green species was observed. Dioxygen uptake experiments supported a Cu(I):O_2 ratio of 4:1, indicative of a four-electron reduction of dioxygen. The same green species was obtained by treating 2.0 equiv. of the Cu(I) precursor with PhIO (iodosobenzene). From these experiments, along with analytical characterization data, the product was identified as the bridging oxo complex. Additional support for the bridging oxo was revealed through reactivity studies. Treatment with excess PPh_3 led to the stoichiometric formation of PPh_3O, the product of O atom transfer. The oxo complex was also prone to reversible hydrolysis. The Cu_2(II,II)-

di(μ-OH) complex was isolated from solutions treated with water, while the oxo complex was isolated from heating the hydroxide complex under vacuum.

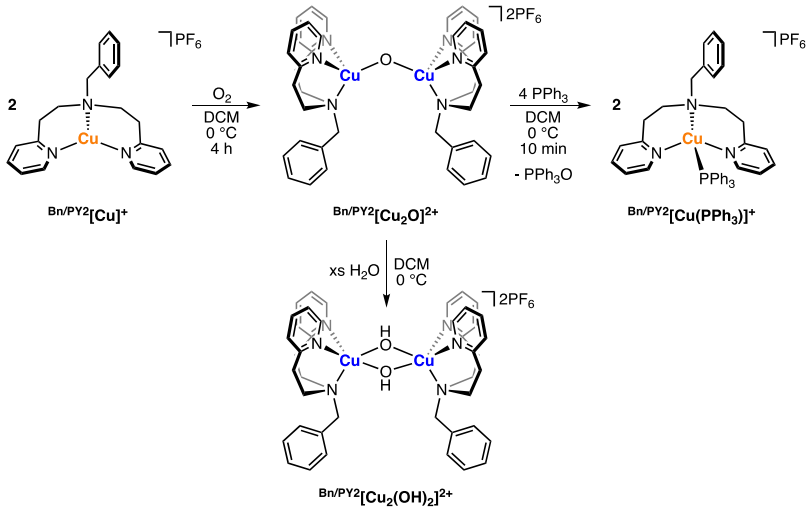

Scheme 1.4 Synthesis and reactivity of Karlin's Cu_2(II,II)-μ-oxo $PhCH_2$(PY2) complex.

Further extension of Karlin's work to other R(PY2) derivatives (R = CH_3, Ph) showed similarities to the original $PhCH_2$(PY2) system in terms of synthesis and reactivity.[21] A new route to an oxo complex was revealed with the Me(PY2) scaffold by oxidizing the Cu(I) precursor with a stoichiometric quantity of NO, affording N_2O as a byproduct.[22] All ligand scaffolds supported a dinuclear core, and the complexes were all sensitive to water. Low-temperature oxygenation studies (-80 °C) allowed elucidation of the mechanism of μ-oxo formation (Scheme 1.5). Similar to the Cu-ZSM-5 zeolite activation of O_2, a Cu_2(II,II)-$\mu(\eta^2{:}\eta^2)$-peroxide was first generated upon oxygenation. Upon warming the sample, the bridging peroxide complex decomposes to the observed μ-oxo intermediate. Additionally, no reactivity towards hydrocarbon substrates was reported for the Cu_2(II,II)-μ-oxo R(PY2) complexes.

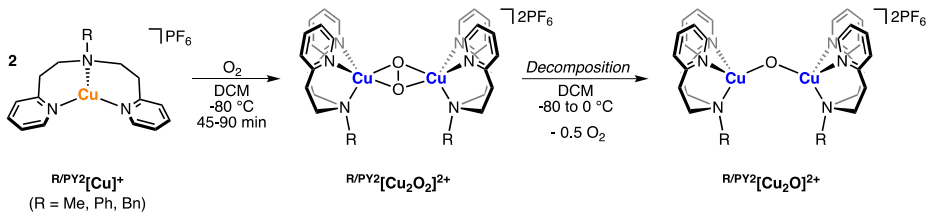

R/PY2[Cu]+ (R = Me, Ph, Bn) R/PY2[Cu2O2]2+ R/PY2[Cu2O]2+

Scheme 1.5 Generation of $^{R/PY2}[Cu_2O]^{2+}$ via a $\mu(\eta^2{:}\eta^2)$-peroxide intermediate.

Analogous to the R(PY2) ligand system, the Tp^{Me} (Tp^{Me} = hydrotris(3,5-dimethyl-1-pyrazolyl)borate) ligand was found to stabilize a Cu_2(II,II)-μ-oxo core at low temperatures.[23-25] Kitajima and coworkers accessed an μ-oxo complex by treating the precursor $Tp^{Me}CuPPh_3$ with excess PhIO. $Tp^{Me}{}_2Cu_2(\mu\text{-}O)$ displayed nucleophilic reactivity towards water, CO_2, and H_2O_2 (Scheme 1.6). Akin to the R(PY2) system, $Tp^{Me}{}_2Cu_2(\mu\text{-}O)$ reversibly hydrolyzed in the presence of water to generate the $Tp^{Me}Cu_2(\mu\text{-}OH)_2$ complex. Exposing the oxo to an atmosphere of CO_2 led to the clean formation of the μ-carbonato complex, $Tp^{Me}{}_2Cu_2(\mu\text{-}CO_3)$. The addition of H_2O_2 afforded the peroxide complex $Tp^{Me}{}_2Cu_2(\mu\text{-}O_2)$, in which the O_2 adopts a $\eta^2{:}\eta^2$ bridging mode. The peroxide complex decomposed upon warming to regenerate the oxo complex, similar to the observation made by Karlin and coworkers.

In contrast to the nucleophilic reactivity described above for $Tp^{Me}{}_2Cu_2O$, treating this complex with an excess of PPh_3 gave PPh_3O along with stoichiometric amounts of $Tp^{Me}CuPPh_3$. This electrophilic reactivity was strictly observed for PPh_3, as $Tp^{Me}{}_2Cu_2O$ was unreactive towards other oxygen atom acceptors such as dimethylsulfide and cyclohexene. However, oxidation of such substrates was achieved under UV irradiation, in which dimethylsulfoxide and 2-cyclohexen-1-ol were observed, albeit in low yield. While limited hydrocarbon oxidation was observed, the role of $Tp^{Me}{}_2Cu_2O$ in these reactions has not been determined.

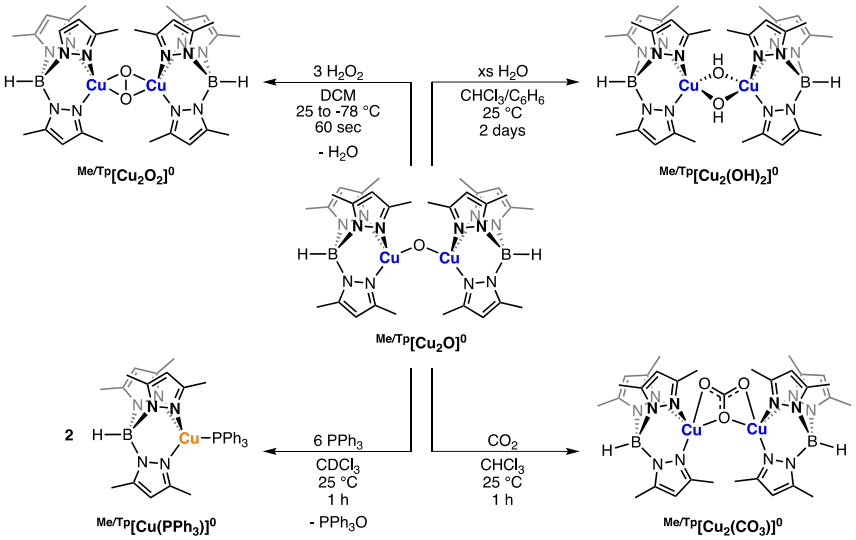

Scheme 1.6 Reactivity of Kitajima's Tp^{Me}-bound Cu_2(II,II)-μ-oxo complex.

Recently, a unique approach to the generation of a Cu_2(II,II)-μ-oxo complex was reported using the TMPA ligand (TMPA = *tris*(2-pyridylmethyl)amine) by Kieber-Emmons and coworkers.[26] Deprotonation of $[(TMPA)_2Cu_2OH][OTf]_3$ (^{TMPA}**[Cu$_2$OH]$^{3+}$**) with the strong Verkade base, 2,8,9-triisobutyl-2,5,8,9-tetraaza-1-phosphabicyclo[3.3.3]undecane (Verkade^{iBu}), afforded $[(TMPA_2Cu_2O][OTf]_2$ (^{TMPA}**[Cu$_2$O]$^{2+}$**) at -30 °C in MeCN (Figure 1.2). Reversible protonation was also demonstrated upon the addition of 2,6-lutidinium triflate to ^{TMPA}**[Cu$_2$O]$^{2+}$**. The μ-oxo complex was found to be thermally sensitive and decomposed by warming or sitting in solution for prolonged periods ($t_{1/2}$ = 3.5 hours at -30 °C). Reactivity with weak E-H (E = O, C) bonds was observed at -30 °C, in which TEMPOH and 1,4-cyclohexadiene (1,4-CHD) underwent hydrogen atom transfer reactions with ^{TMPA}**[Cu$_2$O]$^{2+}$** to form the mixed-valent μ-hydroxide species $[(TMPA_2Cu_2OH][OTf]_2$ (^{TMPA}**[Cu$_2$OH]$^{2+}$**). Additional details on the thermodynamics of hydrogen atom transfer by ^{TMPA}**[Cu$_2$O]$^{2+}$** are presented in Chapter 4.

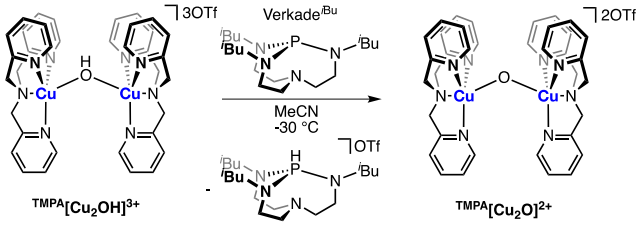

Figure 1.2 Synthesis of Kieber-Emmons' ^{TMPA}**[Cu$_2$O]$^{2+}$** complex.

1.4.2 Cu$_2$(II,II)-μ-Oxo Complexes Supported by Dinucleating Ligands

Unlike their mononucleating counterparts, dinucleating ligands allow for the two copper centers to be pre-oriented towards another. Réglier and coworkers took advantage of this type of ligand design when attempting to design a Cu$_2$(II,II)-μ-peroxide mimic of tyrosinase. The BPImPy (BPImPy = 1,1'-biphenyl-2,2'-dimethylidene-N,N'-(2-(2-pyridyl)-ethylamine)) scaffold was successfully metalated with Cu(I).[27] The biphenyl spacer was implemented to allow for enough distance between the metal centers for a peroxide ligand to bind. However, oxygenation of BPImPyCu$_2$ led to the formation of BPImPyCu$_2$O, as evidenced by oxygen uptake experiments (Figure 1.3). The room temperature-stable μ-oxo complex was found to exhibit electrophilic reactivity towards PPh$_3$, producing PPh$_3$O stoichiometrically.

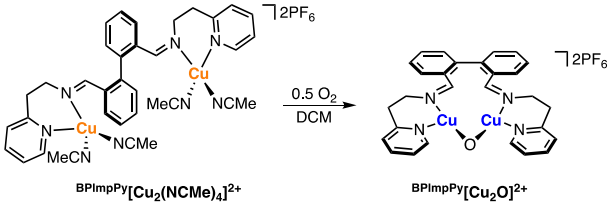

Figure 1.3 Oxygenation of Réglier's Cu$_2$(I,I) BPImPy complex.

Limberg and coworkers designed the dinucleating FurNeu (FurNeu = 4,6-(*bis*((N',N'-dimethylaminoethyl)(2-pyridylmethyl)amine))dibenzofuran) ligand to allow for adequate spacing between two metal centers.[28] Upon the addition of either O$_2$ or PhIO, FurNeuCu$_2$ reacted to form FurNeuCu$_2$O (see Scheme 1.7 for structure) at room temperature. Compared to previous examples of Cu$_2$(II,II)-μ-oxo complexes, FurNeuCu$_2$O

appeared fairly inert. A significant decrease in nucleophilicity/basicity was observed; the complex was unreactive towards water, CO_2, and CS_2. The complex reacted with a stronger acid, acetic acid, but the identity of the product remains unknown. Furthermore, minor quantities of PPh_3O were obtained when the complex was treated with an excess of PPh_3, demonstrating a decrease in electrophilic reactivity compared to previous examples of Cu_2(II,II)-μ-oxo complexes.

The FurNeuCu_2O system did not show HAT reactivity towards external substrates, such as 9,10-dihydroanthracene (DHA). However, prolonged periods in MeCN afforded ligand C–H bond-oxidized products. A unique mode of oxidative reactivity was observed through the reaction of FurNeuCu_2O with 2,4-di-*tert*-butylphenol (Scheme 1.7). Not only was the *ortho*-coupled TBBP product (TBBP = 3,3',5,5'-tetra-*tert*-butyl-2,2'-biphenol) formed, but further oxidation occurred to generate TBOBF (TBOBF = 2,4,7,9-tetra-*tert*-butyloxepino[2,3-b]-benzofuran), an isomer of the diquinone species TBDQ (TBDQ = 3,3',5,5'-tetra-*tert*-butyl-2,2'-diphenoquinone). FurNeuCu_2O was found to be a competent catalyst for this latter oxidation reaction under an atmosphere of O_2.

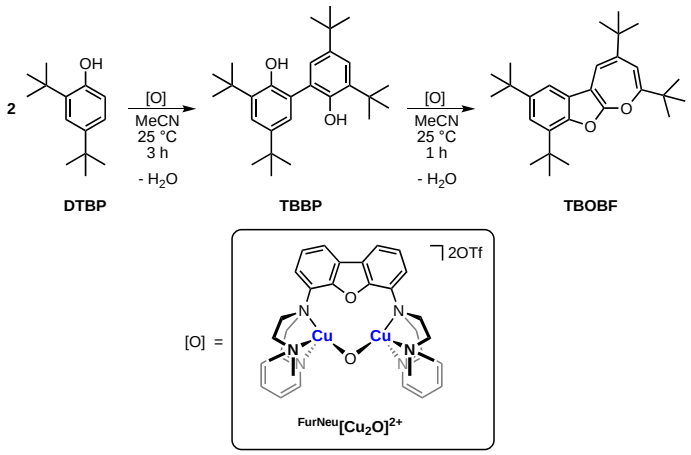

Scheme 1.7 Oxidative coupling of DTBP using Limberg's FurNeu system.

Although the FurNeu system provided access to a novel oxidation of 2,4-di-*tert*-butylphenol, the μ-oxo core oxygen atom was not incorporated into the oxidized

hydrocarbon product, which differs from the reactivity observed for Cu(II)-ZSM-5. This oxygenase-like reactivity remained elusive in molecular systems until 2021. Rübhausen, Tuczek and coworkers synthesized a series of low-temperature stable Cu_2O complexes using the bdpdz (bdpdz = 3,6-*bis*(di(pyridin-2-yl)methyl)pyridazine) and bdptz (bdptz = 1,4-*bis*(di(pyridin-2-yl)methyl)phthalazine) ligand frameworks.[29] From either Cu_2(I,I) complex ($bdptzCu_2(MeCN)_2$ or $bdptzCu_2(MeCN)_2$), the respective oxo complex was generated at -25 °C using O_2, PhIO or N_2O (Figure 1.4). Intriguingly, oxygenation at -90 °C afforded a new copper-oxygen species with spectroscopic characterization supporting the presence of a tetracopper(II,II,II,II)-μ_4-peroxide complex. Upon warming, the μ_4-peroxide intermediate decomposed to the μ-oxo complex.

Both $bdpdzCu_2O$ and $bdptzCu_2O$ displayed markedly higher reactivity towards external hydrocarbon substrates than previous Cu_2(II,II)-μ-oxo complexes. The oxidations of xanthene, DHA, fluorene, triphenylmethane and diphenylmethane, were carried out under catalytic conditions using O_2 as the oxidant. As an example, the oxidized products of DHA were the HAT product anthracene (A) and the four-electron oxidized product 9,10-anthraquinone (AQ) (Figure 1.4). Isotopically-enriched ($^{18}O_2$) samples confirmed that the oxygen atoms incorporated into the quinone product originated from O_2. Although turnover numbers were low for catalysis (TON = 1-5), Cu_2(II,II)-μ-oxo complexes were shown to catalyze C-H bond oxidation with the incorporation of oxygen atoms into the two- or four-electron oxidized products.

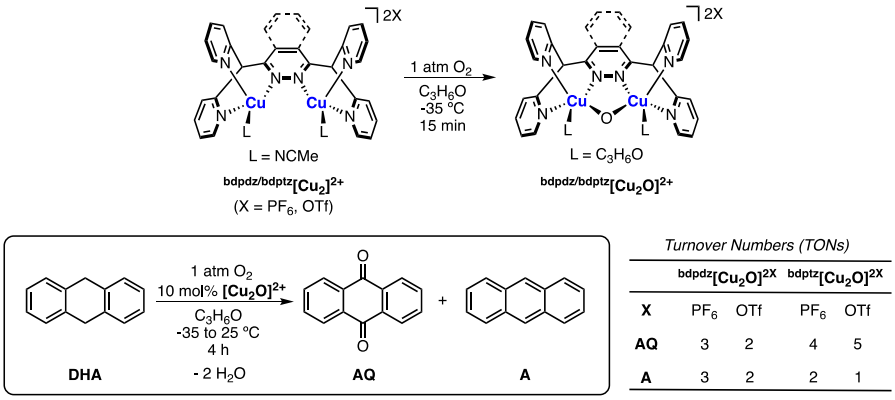

Turnover Numbers (TONs)

	bdpdz[Cu2O]2X		bdptz[Cu2O]2X	
X	PF_6	OTf	PF_6	OTf
AQ	3	2	4	5
A	3	2	2	1

Figure 1.4 Catalytic oxygenation of DHA by Cu_2(II,II)-μ-oxo complexes.

1.4.3 Outlook on Synthetic Cu_2(II,II)-μ-Oxo Complexes

Since the discovery of the Cu(II)-ZSM-5 active site's role in selective methane to methanol oxidation, Cu_2(II,II)-μ-oxo complexes are beginning to shift towards the forefront of synthetic copper-oxygen chemistry. Dinucleating ligands have shown promise in stabilizing the bridging oxo moiety but examples of intermolecular hydrocarbon oxidation reactions are limited. New ligand systems capable of binding two copper centers bridged by a single oxygen atom are desirable for the advancement of hydrocarbon oxidation catalysts. Moreover, developing ligand systems with tunable sites for steric/electronic modification may induce new reactivity at Cu_2(II,II)-μ-oxo cores. Thus, the focus of this dissertation aims to address these areas in need of advancement and further inform on the role of dicopper-based systems in oxidation reactions.

1.5 Dissertation Overview

In the following chapters, this dissertation highlights work towards the development of Cu_2(II,II) *bis*(pyridyldiimine) macrocyclic complexes for the oxidation of organic substrates. Specifically, hydrogen atom transfer pathways are targeted through the generation of reactive Cu_2(II,II)-μ-oxo complexes. Synthesis and characterization of a series of Cu_2(II,II)-μ-$X_{(n)}$ (X = Cl, Br, N_3, OTMS, OH, n = 1,2) are first discussed in Chapter

2. A simple protocol is presented for using the *bis*(4-*tert*-butylpyridyldiimine) macrocyclic ligand in the stabilization of Cu_2(II,II) complexes. Chapter 3 outlines progress towards a modular *bis*(pyridyldiimine) ligand synthesis. A new synthetic route to substituted 4-phenyl-2,6-dibenzoylpyridines is reported that allows for facile substitution at both the pyridyl and imino moieties of the PDI unit. Moreover, new macrocyclic ligands with phenyl substitution are synthesized. Chapter 4 then details the synthesis of various-sized Cu_2(II,II)-μ-hydroxide macrocyclic complexes using the synthetic techniques in Chapter 2 and the new ligand framework in Chapter 3. Deprotonation of each hydroxide complex is achieved and subsequent hydrogen atom transfer reactivity is assessed. The efforts outlined in this dissertation offer a new perspective on dinucleating ligands used to support reactive dicopper-based fragments in oxidation pathways.

CHAPTER 2 **:** ANION SUBSTITUTION AT AN “OPEN-CORE” DICOPPER(II,II) *BIS*(4-*TERT*-BUTYLPYRIDYLDIIMINE) MACROCYCLE

2.1 Introduction

As detailed in Chapter 1, the first step in the selective oxidation of methane to methanol by Cu(II)-ZSM-5 is the activation of dioxygen. At the active site, two geometrically constrained copper(II) ions are involved in the binding of O_2 and subsequent formation of a reactive Cu_2(II,II)-μ-oxo active site (calc. Cu-Cu distance of 3.3 Å). Constrained geometry sites for small molecule activation and functionalization are also a defining feature in many multinuclear copper-containing proteins found in Nature. Enzymes that selectively oxidize methane (particulate methane monooxygenase), phenols (tyrosinase) and quinones (tyrosinase and catechol oxidase), or the dioxygen-carrying protein hemocyanin, rely on multiple geometrically constrained copper sites at fixed distances for substrate binding/activation.[30]

To further inform our understanding of the modes of reactivity demonstrated by multinuclear copper sites in Nature, the design of synthetic homogeneous model copper complexes offers a way forward. Copper-copper distances have been observed over a range of 2.2 – 4.9 Å in numerous proteins and are known to change upon binding of substrate.[30] Modulating the distance between copper centers in molecular systems may influence how a small molecule interacts at a multicopper active site and subsequent reactivity therein. Accomplishing such a feat requires the use of suitable multinucleating ligands that allow for tunable copper-copper distances with additional coordination sites available for small molecule binding. The influence of copper-copper distance on reactivity will be explored further in Chapter 4.

Recent examples of ligands capable of housing multiple copper centers and binding molecules of various size have been in the areas of anion-recognition/sensing,[31-33] dioxygen activation,[28,29] organic azide reduction,[34] aryl group transfer and alkyne activation.[35,36] From these studies, an important feature of ligand design is the preorientation of the copper centers at defined distances for cooperative substrate binding/activation and subsequent functionalization. Drew and Nelson (see section 2.1.2) originally targeted this aspect in the 1980s when designing and synthesizing macrocyclic *bis*(pyridyldiimine) ligands.[37-40] The two pyridyldiimine (PDI) units linked by aliphatic spacers were suitable for binding two copper(II) centers at specific distances and oriented the metals towards one another in the macrocyclic cavity (Figure 2.1). The Cu–Cu distance was influenced by the length of the linkers used in connecting the two PDI units. Preliminary analysis also indicated that the macrocyclic ligands were flexible and allowed for ligand conformational changes to support changes in Cu–Cu distances upon external ligand binding.

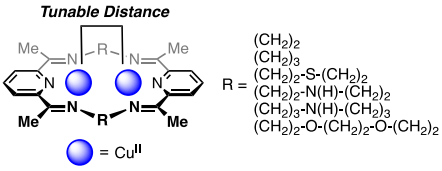

Figure 2.1 *Bis*(pyridyldiimine) macrocyclic ligands developed by Drew and Nelson.

The *bis*(pyridyldiimine) macrocyclic ligands offer a platform to study multinuclear copper chemistry. Yet, synthetic and structural information on these systems is limited. Herein, new synthetic routes to Cu_2(II,II) *bis*(pyridyldiimine) macrocyclic complexes are explored with versatile ligand substitution being achieved. Selected examples of both mononuclear and dinuclear copper PDI complexes are first introduced to demonstrate the synthetic methods used thus far in designing copper-based PDI complexes.

2.1.1 Mononuclear Copper PDI Complexes

The tridentate PDI ligand has been used over the last 50 years in stabilizing numerous monocopper complexes with a range of ligand substitutions. Approaching 100 reported crystal structures, the CSD (Cambridge Crystallographic Data Centre) database displays a large breadth of copper PDI complexes, spanning PDI derivatives with imino substitutions including aromatic, heteroatom and tethered alkyl groups.[41] Other variations include copper bound by two PDI units to afford octahedral complexes. Wieghardt and coworkers have analyzed a host of these complexes, determining key structural features of monocopper-PDI complexes.[42] Typically, PDI binds to copper(II); only three copper(I) examples have been reported (*vide infra*). Copper PDI complexes have been observed as four-, five-, and six-coordinate species depending on the number of ancillary ligands in addition to the PDI unit. An overview of selected monocopper PDI complexes with different ligand substitutions is provided below.

The most common ligand bound to copper(II) in PDI-based complexes is the chloride ligand.[43-46] Copper(II) chloride dihydrate offers a simple starting material for the synthesis of corresponding PDI complexes. Depending on the synthetic route, the copper(II) center can bind up to two chloride ligands. When two chlorides are bound to the copper(II) center, in all cases, the metal geometries are observed as distorted trigonal bipyramidal or distorted square pyramidal in the solid-state. Many copper(II) dichloride PDI complexes have been reported to date with various substitutions made at the imino nitrogen (Figure 2.2)

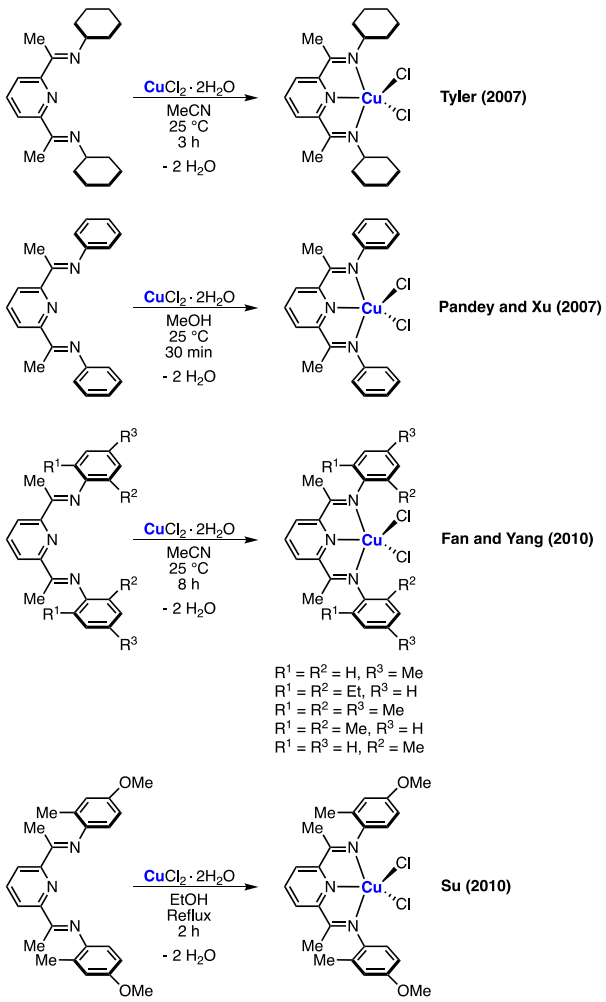

Figure 2.2 Synthesis of five-coordinate copper(II) chloride PDI complexes.

A notable example of a structurally characterized copper(II) monochloride PDI complex was reported by Conan and coworkers (Figure 2.3).[47] Treatment of a dipp-substituted (dipp = diisopropyl) PDI (^{dipp}PDI) unit with $[Cu(MeCN)_4][PF_6]$ afforded a Cu(I) complex which was susceptible to oxidation by $CHCl_3$. Based on the solid-state structure, the resulting monochloride complex appears to be the four-coordinate square planar copper(II) PDI complex $[^{dipp}PDICuCl][PF_6]$. However, the hexafluorophosphate anion displays a weak axial Cu–F interaction of 2.485 Å, and the complex may thus be regarded as five-coordinate. This same approach afforded the first copper(II) bromide PDI complex when using $CHBr_3$ ($[^{dipp}PDICuBr][Br_3]$). A Br_3 anion was found weakly coordinated instead

of the PF_6 anion. Later, Gorelsky, Richeson and coworkers showed synthetic access to a five-coordinate copper(II) dibromide complex using a bulky 2,6-di-*tert*-butylphenyl-substituted PDI ligand ($^{t\text{Bu}}$PDI) and $CuBr_2$ ([$^{t\text{Bu}}$PDI$CuBr_2$]).[48]

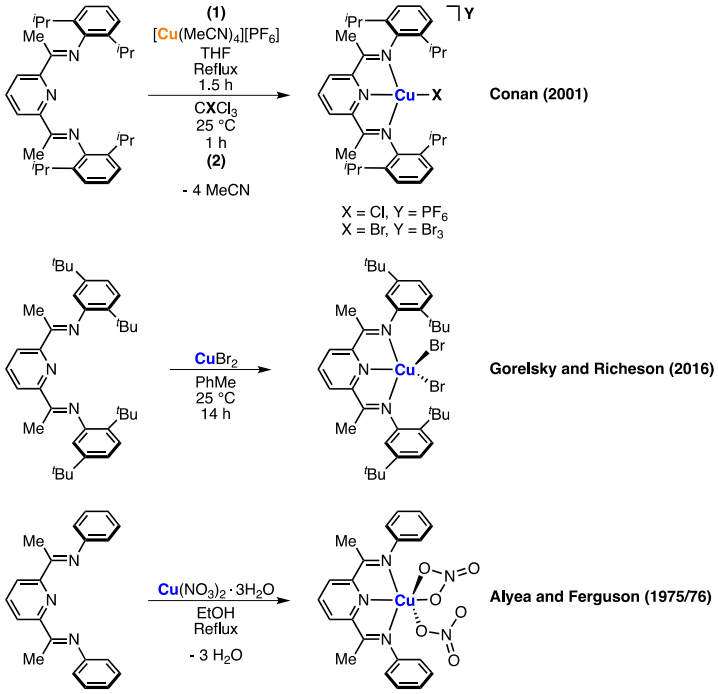

Figure 2.3 Other substitution patterns of copper(II) PDI complexes.

In addition to chloride and bromide ligands, the nitrate ligand was implemented in the synthesis of a copper(II) *bis*(nitrate) complex. Alyea, Ferguson and coworkers demonstrated that upon the addition of $Cu(NO_3)_2$ to N,N'-(2,6-pyridinediyldiethylidyne)*bis*(benzenamine) (^{Ph}PDI), the copper(II) dinitrate PDI complex [^{Ph}PDI$Cu(NO_3)_2$] formed.[49,50] Crystallographic analysis was later performed by Ferguson. The two nitrate ligands were found to have different coordination modes. One nitrate was found to bind in a κ^1 fashion and the other in a κ^2 fashion. Thus, the complex is a unique example of a six-coordinate copper(II) PDI complex.

The three examples of PDI ligands bound to Cu(I) were reported by Gilbertson and coworkers (Scheme 2.1).[51] Using the synthetic methodology developed by Conan,

Gilbertson successfully characterized the solid-state structure of [^{dipp}PDICu(NCMe)][PF_6]. The crystal structure displayed a four-coordinate copper(I) center in a distorted square planar geometry. The copper(I) oxidation state was supported by reaction with CO to afford the carbonyl-bound complex [^{dipp}PDICu(CO)][PF_6] in a similar geometry. The stabilization of copper(I) in a distorted square planar geometry was proposed to result from the steric protection of the PDI ligand with the bulky dipp groups. Reducing the steric protection to phenyl groups afforded the five-coordinate monocopper(I) *bis*(PDI) complex [^{Ph}PDI$_2$Cu][PF_6].

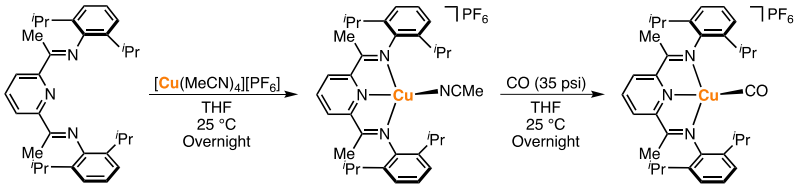

Scheme 2.1 Gilbertson's synthesis of square-planar copper(I) PDI complexes.

2.1.2 Dinuclear Copper PDI Complexes

Unlike the mononuclear counterparts, few Cu_2(II,II) PDI complexes are structurally characterized. To our knowledge, no reports of dicopper(I,I) or dicopper(I,II) PDI complexes exist. Intriguingly, no Cu_2(II,II) chloride, bromide or nitrate PDI complexes are reported. Many of the Cu_2(II,II) examples incorporate the use of a *bis*(pyridyldiimine) macrocyclic ligands, with selected examples introduced below.

A useful feature of *bis*(pyridyldiimine) macrocyclic ligands is that the spacing between the two PDI units is tunable. Drew, Nelson and coworkers originally demonstrated this by using different aliphatic linkers to isolate Cu_2(II,II) macrocyclic complexes of different sizes. For example, a 3,6-dioxaoctylene spacer was incorporated between the PDI subunits. Upon treating the Cu_2(II,II) macrocyclic complex [^{Oct}PDI$_2$Cu$_2$][ClO_4]$_4$·3H_2O (^{oct}PDI$_2$ = two PDI subunits linked by two 3,6-dioxaoctylene

spacers) with NaN_3, the bridging azide complex [^{Oct}PDI$_2$Cu$_2$(N_3)$_3$][ClO_4] was isolated.[38] The azide bridges in a 1,3-mode due to the large cavity of the macrocycle and long Cu–Cu distance of 6.02 Å. Additionally, an azide ligand was terminally bound to each copper(II). Later studies showed that different anions (Figure 2.4) – imidazolate (**A**, [^{Oct}PDI$_2$Cu$_2$(im)][ClO_4]$_3$) and hydroxide (**B**, [^{Oct}PDI$_2$Cu$_2$OH][ClO_4]$_3$·H_2O) – could bridge the two copper(II) centers.[37] The Cu–Cu distance with the imidazolate bridge falls in a similar range as the azide complex, 5.99 Å. However, to accommodate the smaller bridging-hydroxide anion, the macrocycle contorts (the aliphatic linkers display flexibility) and the Cu–Cu distance shortens to 3.57 Å.

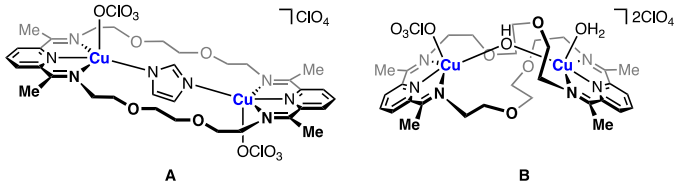

Figure 2.4 Comparison of Cu_2(II,II) *bis*(pyridyldiimine) macrocycles with 3,6-dioxaoctylene spacers, and imidazolate and hydroxide bridging ligands.

Drew and Nelson also incorporated smaller aliphatic spacers between the PDI units with the use of ethylenediamine and 1,3-diaminopropane. Molecular models predicted that the smaller of the two macrocycles was not suitable for housing a Cu_2(II,II) core with a bridging ligand. However, the Cu_2(II,II)-μ-OH complex [^{Et}PDI$_2$Cu$_2$OH][ClO_4]$_3$·H_2O (^{Et}PDI$_2$ = two PDI subunits linked by two ethylene spacers) was successfully isolated through reaction of [^{Et}PDI$_2$Ba][ClO_4]$_2$ with Cu(ClO_4)$_2$·6H_2O (Figure 2.5).[40] The formation of [^{Et}PDI$_2$Cu$_2$OH][ClO_4]$_3$·H_2O was thought to arise from the flexibility of the ethylene linkers. Although no crystal structure was reported, the macrocycle most likely folds to allow each copper(II) center to adopt a square pyramidal geometry with a bridging hydroxide ligand occupying an equatorial position of each copper(II) center. The

presence for a dinuclear core was further supported by elemental analysis and solution-state magnetic susceptibility measurements.

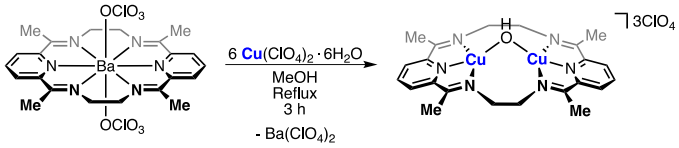

Figure 2.5 Synthesis of $[^{Et}PDI_2Cu_2OH][ClO_4]_3$ in MeOH.

Using the larger spacer, 1,3-diaminopropane, Drew and Nelson reported the crystal structure of a related Cu_2(II,II)-μ-OH complex $[^{Pr}PDI_2Cu_2OH][ClO_4]_3 \cdot 2H_2O$ ($^{Pr}PDI_2$ = two PDI subunits linked by two propylene spacers) (Scheme 2.6).[39] At first, infrared spectroscopy suggested that treatment of $[^{Pr}PDI_2Ba][ClO_4]_2$ with $Cu(ClO_4)_2 \cdot 6H_2O$ afforded the bridging methoxide complex $[^{Pr}PDI_2Cu_2(OMe)][ClO_4]_3 \cdot 2H_2O$. When $[^{Pr}PDI_2Cu_2(OMe)][ClO_4]_3 \cdot 2H_2O$ was recrystallized from acetonitrile, $[^{Pr}PDI_2Cu_2OH][ClO_4]_3 \cdot 2H_2O$ was isolated (the likely source of the hydroxide anion was water in the organic solvent). The crystal structure shows the macrocycle folds to accommodate the Cu_2(II,II) core. A shorter Cu–Cu distance of 3.145(4) Å was reported. The bridging hydroxide was found occupying an equatorial position of each copper(II) center and a Cu-O-Cu angle of 110.3(7)° was observed. Additionally, a weakly bridging aqua ligand occupied the axial positions of each copper center at a distance of 2.519(12) Å. Further substitution was carried out using NaN_3 in an anion metathesis reaction with $[^{Pr}PDI_2Cu_2(OMe)][ClO_4]_3 \cdot 2H_2O$ to afford $[^{Pr}PDI_2Cu_2(N_3)][ClO_4]_3$, as evidenced by the azide stretching frequency at 2070 cm^{-1}. However, no crystal structure was reported for the azide complex.

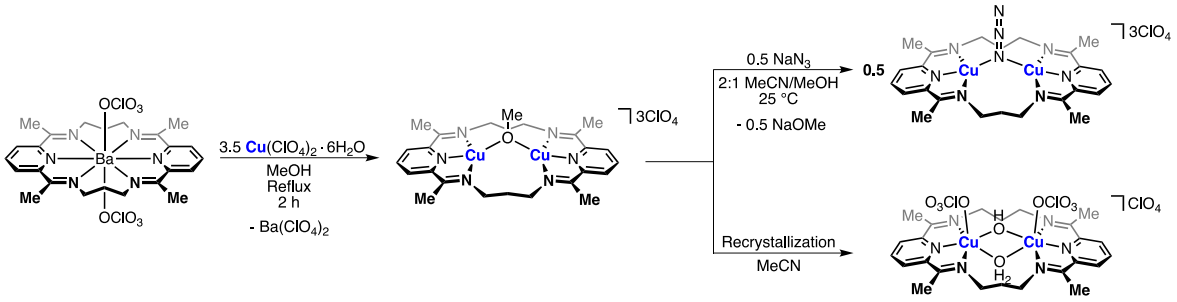

Scheme 2.2 Synthetic elaboration of Cu_2(II,II) *bis*(pyridyldiimine) macrocycles.

2.2 Synthesis of an "Open-Core" Cu_2(II,II) Macrocycle

The limited reactivity and structural data on Cu_2(II,II) *bis*(pyridyldiimine) macrocycles prompted further investigation into the synthesis of new macrocyclic complexes. Previous work in our lab has shown that synthetic elaborations of dinuclear first-row transition metal *bis*(pyridyldiimine) macrocyclic complexes were aided by the installation of *tert*-butyl groups at the 4-position of the PDI units.[52-59] The *tert*-butyl groups allow for an enhancement in solubility in less polar organic solvents (THF, DCM, and MeCN) compared to the original macrocycles reported by Drew and Nelson. We thus sought to synthesize a new series of Cu_2(II,II) *bis*(pyridyldiimine) macrocycles for structural/solution-state characterization.

2.2.1 Isolation of $^{n/Me}[Cu_2Cl_2]^{2+}$ (n = 2,3) Complexes

The synthesis of a Cu_2(II,II) *bis*(4-*tert*-butylpyridyldiimine) macrocyclic complex was first carried out using the strontium-templated macrocycle $[^{3/Me}PDI_2Sr][OTf]_2$ ($^{3/Me}$**[Sr]**$^{2+}$, where 3 refers to the aliphatic chain length and Me refers to methyl group on the imino moiety). Treatment of a yellow methanolic solution of $^{3/Me}$**[Sr]**$^{2+}$ with 2.0 equiv. of $CuCl_2 \cdot 2H_2O$ afforded the paramagnetic, dark green dinuclear macrocycle-bound complex $[^{3/Me}PDI_2Cu_2Cl_2][OTf]_2$ ($^{3/Me}$**[Cu$_2$Cl$_2$]**$^{2+}$) in good yield (Scheme 2.3). Crystallographic analysis revealed that the copper(II) centers are related by an inversion center (Figure

2.6). The metal sites adopt a distorted octahedral geometry, with a meridional PDI subunit and a bridging chloride occupying the equatorial positions, and a triflate anion and a bridging chloride occupying the axial positions (selected bond metrics are presented in Table 2.1). No six-coordinate mononuclear copper(II) chloride PDI complexes have been reported in the literature. However, the Cu–N bond lengths are in good agreement with the related four-coordinate [^{dipp}PDICuCl][PF_6] reported by Conan. The equatorial Cu–Cl bond length of 2.18602(11) Å agrees well with Conan's observed Cu–Cl bond length of 2.1450(5) Å. The axial Cu–O (2.710 Å) and Cu–Cl (2.873 Å) distances are elongated, owing to a strong Jahn-Teller distortion at the d^9 Cu(II) ion. Due to this distortion, the Cu_2Cl_2 diamond core exhibits a very acute Cu-Cl-Cu angle (75.05°).

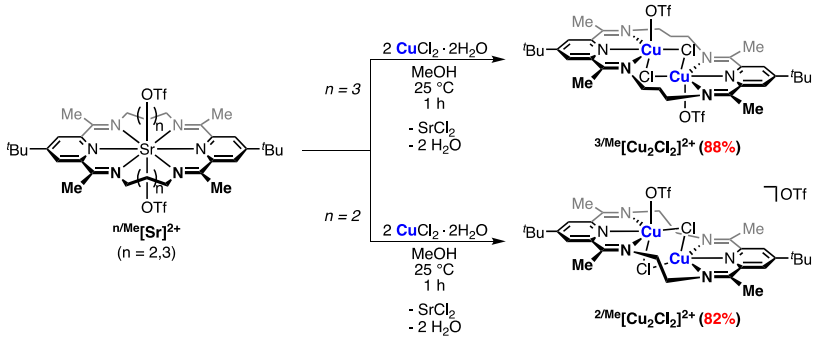

Scheme 2.3 Synthesis of $^{n/Me}$**[Cu_2Cl_2]$^{2+}$** complexes in MeOH.

An additional parameter that can be gleaned from the crystal structure of $^{3/Me}$**[Cu_2Cl_2]$^{2+}$** is the oxidation state of the (redox-active) PDI ligand.[42] Wieghardt and coworkers previously reported the Δ parameter as a means of identifying how much electron density resides in the PDI π* manifold. Our lab recently adapted the Δ parameter in describing the *bis*(4-*tert*-butylpyridyldiimine) macrocyclic ligand oxidation state, which includes the average of each Δ parameter for each PDI subunit.[56] Using this analysis on the crystal structure of $^{3/Me}$**[Cu_2Cl_2]$^{2+}$**, the average Δ parameter of 0.187 Å supports the assignment of a neutral physical oxidation state on the $^{3/Me}$$PDI_2$ ligand. A neutral ligand for

copper PDI complexes is not uncommon, as both mononuclear $Cu^{II}(PDI^0)$ and $Cu^{I}(PDI^0)$ examples are well established in the literature.[42]

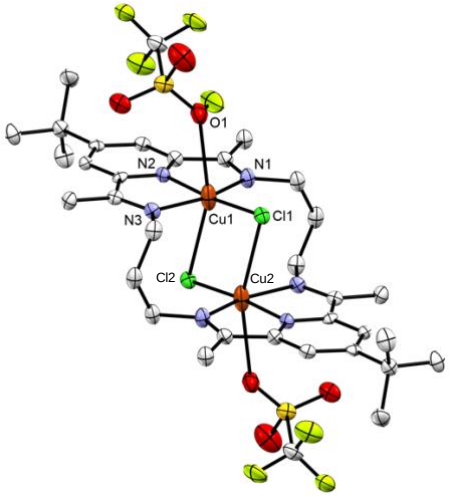

Figure 2.6 Crystal structure of $^{3/Me}[Cu_2Cl_2]^{2+}$ (thermal ellipsoids set at 50% probability; hydrogen atoms and triflate disorder omitted for clarity).

Table 2.1 Selected bond metrics of copper(II) chloride PDI complexes.

	$^{3/Me}[Cu_2Cl_2]^{2+}$*a*	$^{2/Me}[Cu_2Cl_2]^{2+}$*b*	$[^{dipp}PDICuCl][PF_6]$
Cu(1) – N(1) / Å	2.056(4)	2.057	2.070(2)
Cu(1) – N(2) / Å	1.902(3)	1.903	1.922(2)
Cu(1) – N(3) / Å	2.047(3)	2.044	2.062 (2)
Cu(1) – Cl(1) / Å	2.1860(11)	2.2056	2.1450(5)
Cu(1) – Cl(2) / Å	2.873(1)	3.021	-
Cu(1) – O(1) / Å	2.710(1)	2.4015	-
Cu(1) – Cu(2) / Å	3.129(1)	2.9922	-
Cu(2) – N(4) / Å	-	2.041	-
Cu(2) – N(5) / Å	-	1.898	-
Cu(2) – N(6) / Å	-	2.042	-
Cu(2) – Cl(1) / Å	-	2.7273	-
Cu(2) – Cl(2) / Å	-	2.2043	-
∠Cu(1)-Cl(1)-Cu(2) / °	75.05(4)	73.83	-
∠Cu(1)-Cl(2)-Cu(2) / °	-	67.80	-
Δ / Å	0.187	0.182	0.178

a – Macrocycle is symmetric; bond metrics are the same for Cu(2)
b – Average values; two macrocycles are present in the asymmetric unit

The IR spectrum of $^{3/Me}$**[Cu$_2$Cl$_2$]$^{2+}$** contained a characteristic imine stretching frequency at 1601 cm^{-1}. UV-vis-NIR spectroscopic analysis revealed an absorption profile representative of *bis*(pyridyldiimine) macrocyclic complexes in an unfolded ligand conformation.[55] Distinct absorption bands at 237 nm (7.71 x 10^4 M^{-1} cm^{-1}) and 676 nm (242 M^{-1} cm^{-1}) result from a π→π* transition and a d→d transition, respectively.

The successful synthesis and characterization of $^{3/Me}$**[Cu$_2$Cl$_2$]$^{2+}$** prompted further investigation into the effect of macrocycle size in the preparation of Cu$_2$(II,II) macrocyclic complexes. Upon addition of 2.0 equiv. CuCl$_2$·2H$_2$O to the smaller macrocycle $^{2/Me}$**[Sr]$^{2+}$**, an immediate color change from yellow to dark blue-green was observed. The macrocycle [$^{2/Me}$PDI$_2$Cu$_2$Cl$_2$][OTf]$_2$ ($^{2/Me}$**[Cu$_2$Cl$_2$]$^{2+}$**) was isolated in good yield (Scheme 2.3). The solid-state structure of $^{2/Me}$**[Cu$_2$Cl$_2$]$^{2+}$** depicts a similar ligand conformation to $^{3/Me}$**[Cu$_2$Cl$_2$]$^{2+}$** (Figure 2.7). Two chloride ligands bridge between the copper centers; however, variations in the Cu$_2$Cl$_2$ core are evident when compared to $^{3/Me}$**[Cu$_2$Cl$_2$]$^{2+}$**. Unlike the larger macrocycle, each copper center adopts a different coordination geometry. One copper is found in a distorted octahedral geometry, capped by a triflate anion and a bridging chloride (analogous to $^{3/Me}$**[Cu$_2$Cl$_2$]$^{2+}$**). The second copper adopts a square pyramidal geometry (avg. τ_5 = 0.04),[60] with the second triflate anion residing in the outer coordination sphere. The difference in the coordination geometries about the copper centers is reflected in the distortion of the Cu$_2$Cl$_2$ core, which now appears asymmetric [∠Cu(1)-Cl-Cu(2) = 73.83(4)° and (∠Cu(2)-Cl-Cu(1) = 67.80(4)°]. Aside from the noted differences in the Cu$_2$Cl$_2$ core, the bond metrics remain comparable to $^{3/Me}$**[Cu$_2$Cl$_2$]$^{2+}$** and [^{dipp}PDICuCl][PF$_6$] (Table 2.1).

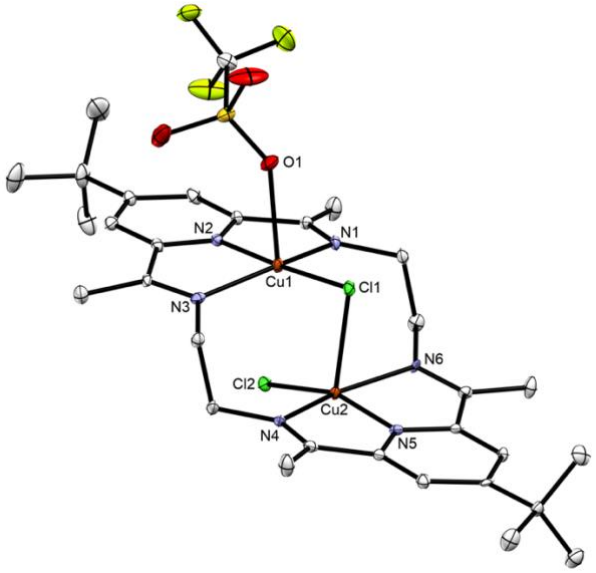

Figure 2.7 Crystal structure of $^{2/Me}[Cu_2Cl_2]^{2+}$ (thermal ellipsoids set at 50% probability; hydrogen atoms, solvent molecules and outersphere anions omitted for clarity; one macrocycle of the asymmetric unit shown).

2.2.2 Chloride Abstraction from $^{3/Me}[Cu_2Cl_2]^{2+}$

With $^{3/Me}[Cu_2Cl_2]^{2+}$ isolated, anion metathesis was targeted to introduce new ligands at the copper(II) centers, but because of the strong bridging-chloride interactions, little to no reactivity was observed. Chloride abstraction routes were thus employed to enhance the reactivity of the pocket towards anion metathesis. Attempts at chloride abstraction with traditional reagents (KOTf, Ag_nX [n = 1,2; X = BF_4, SO_4, OTf, $BAr^F{}_4$ ($BAr^F{}_4$ = tetrakis(3,5-*bis*(trifluoromethyl)phenyl)borate)]) were met with either intractable mixtures or no reaction. Chloride abstraction was achieved with the addition of an excess of TMS-OTf (TMS = trimethylsilyl) to $^{3/Me}[Cu_2Cl_2]^{2+}$ in MeCN. The formation of a new macrocyclic product was apparent by a sharp color change from dark green to dark blue. Concentration of the reaction mixture afforded the blue acetonitrile-coordinated macrocycle complex $[^{3/Me}PDI_2Cu_2(NCMe)_2][OTf]_4$ ($^{3/Me}[Cu_2(NCMe)_2]^{4+}$) (Scheme 2.4). Unlike $^{3/Me}[Cu_2Cl_2]^{2+}$,

$^{3/Me}$**[Cu$_2$(NCMe)$_2$]$^{4+}$** remained insoluble in common organic solvents (THF, DCM, MeCN), which prohibited further solution-state characterization.

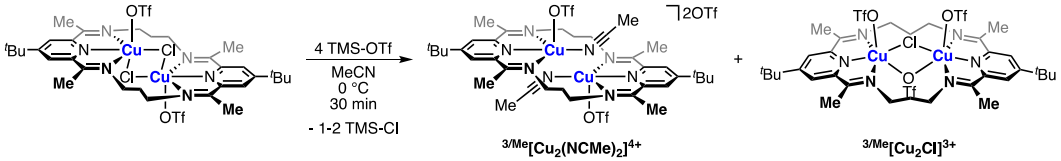

Scheme 2.4 Abstraction of bridging chlorides from $^{3/Me}$**[Cu$_2$Cl$_2$]$^{2+}$** using TMS-OTf in MeCN.

Owing to its partial solubility in MeCN, single crystals of $^{3/Me}$**[Cu$_2$(NCMe)$_2$]$^{4+}$** were grown from the slow diffusion of Et_2O into a concentrated MeCN solution. The solid-state structure was found to resemble that of $^{3/Me}$**[Cu$_2$Cl$_2$]$^{2+}$**, with the two chloride ligands replaced by MeCN ligands (Figure 2.8). The macrocyclic ligand adopts an unfolded ligand conformation, and the two Cu(II) centers are related by a center of symmetry with a spacing of 3.3479(7) Å. Both Cu(II) centers adopt a distorted square pyramidal geometry (τ_5 = 0.36 for each Cu(II) center) with an evident Jahn-Teller distortion causing a long Cu–O (2.275(2) Å) bond length. The axial Cu-*N*CMe bond lengths (3.160(3) Å) fall outside the sum of the van der Waals radii of copper and nitrogen (2.95 Å). Thus, five-coordinate copper(II) is a better description of the metal centers in this crystal structure. The equatorial Cu-*N*CMe distance of 1.973(3) Å is significantly shorter than the reported distance of 2.271(13) in McKee and coworkers' related Cu_2(II,II) alkoxy PDI macrocycle.[61] However, the MeCN ligand occupies a distorted axial position of a square pyramidal Cu(II) center in McKee's example, rather than the equatorial position as observed in $^{3/Me}$**[Cu$_2$(NCMe)$_2$]$^{4+}$**. Gilbertson's distorted square planar copper(I) acetonitrile PDI complex displays a short Cu-*N*CMe distance of 1.907(7) Å, which better agrees with $^{3/Me}$**[Cu$_2$(NCMe)$_2$]$^{4+}$**.[51]

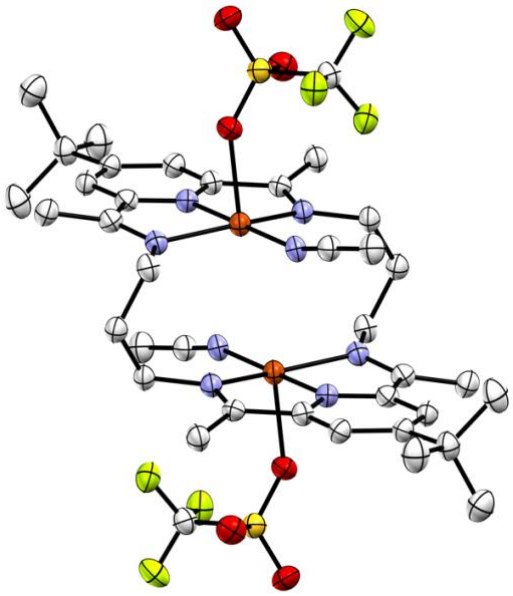

Figure 2.8 Crystal structure of $^{3/Me}$**[Cu$_2$(NCMe)$_2$]$^{4+}$** (thermal ellipsoids set at 50% probability; hydrogen atoms, solvent molecules and outersphere anions omitted for clarity).

Surprisingly, the IR spectrum of $^{3/Me}$**[Cu$_2$(NCMe)$_2$]$^{4+}$** includes three distinct nitrile stretching frequencies in the expected region for acetonitrile (2307 cm^{-1}, 2278 cm^{-1}, 2255 cm^{-1}). The presence of multiple signals may indicate more than one acetonitrile molecule binds to each copper(II) center. Although satisfactory elemental analysis data was collected, alternative routes of crystallization were assessed to address the discrepancy in the IR spectral data. The product was found to be partially soluble in *o*-difluorobenzene. Crystallization from this solvent afforded single crystals that were identified as the monochloride product [$^{3/Me}$PDI$_2$Cu$_2$Cl][OTf]$_3$ (**$^{3/Me}$[Cu$_2$Cl]$^{3+}$**), indicative of incomplete chloride abstraction. Prolonged reaction times in the presence of excess TMS-OTf were not able to improve the purity of **$^{3/Me}$[Cu$_2$(NCMe)$_2$]$^{4+}$**. Although not the desired product, the crystal structure of **$^{3/Me}$[Cu$_2$Cl]$^{3+}$** offered insight into how the ligand is able to change in conformation to accommodate one bridging ligand upon loss of a bridging chloride from **$^{3/Me}$[Cu$_2$Cl$_2$]$^{2+}$**.

The solid-state structure of $^{3/Me}[Cu_2Cl]^{3+}$ introduces an arched ligand conformation around the dinuclear Cu_2Cl core (Figure 2.9). Both copper(II) centers adopt distorted octahedral geometries, with two triflate anions occupying the axial positions *cis* to the μ-Cl. Jahn-Teller distortions are evident by the elongated Cu–O axial bond lengths (avg. 2.5042 Å). A single chloride bridges the two copper(II) centers with a Cu-Cl-Cu angle of 108.50(3)° (an increase of 33° compared to $^{3/Me}[Cu_2Cl_2]^{2+}$). The bridging chloride ligand sits above the Cu–Cu plane, and the Cu–Cl bond distances elongate to 2.2906(7) and 2.2739(7) Å. These longer bond distances are still in the expected range for copper(II) chloride PDI complexes, agreeing well with related five-coordinate complexes. To accommodate the increases in the Cu-Cl-Cu angle and the Cu–Cl distances upon loss of a bridging chloride from $^{3/Me}[Cu_2Cl_2]^{2+}$, the macrocycle conformation changes and the Cu–Cu distance increases from 3.129(1) Å to 3.7045(7) Å.

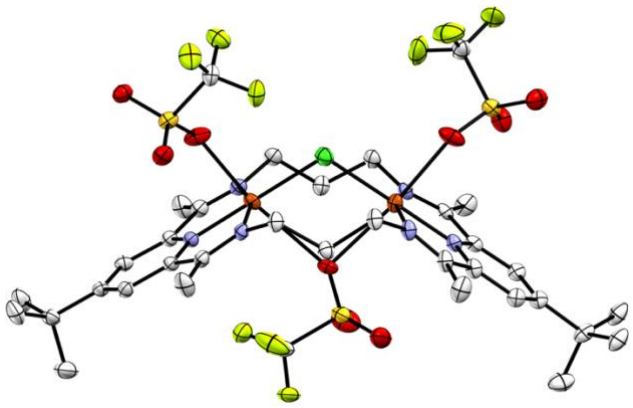

Figure 2.9 Crystal structure of $^{3/Me}[Cu_2Cl]^{3+}$ (thermal ellipsoids set at 50% probability; hydrogen atoms and triflate disorder omitted for clarity).

2.2.3 A Synthetic Route to an "Open-Core" Cu_2(II,II) Macrocycle

Due to incomplete chloride abstraction from $^{3/Me}[Cu_2Cl_2]^{2+}$ we sought a new approach to the synthesis of an "open-core" macrocycle. We proposed that strong bridging interactions in $^{3/Me}[Cu_2Cl_2]^{2+}$ may limit the reactivity towards TMS-OTf. To address this

concern, a single bridging halide may improve the outcome of the halide abstraction reaction. Moreover, swapping the chloride ligand for a fluoride ligand would allow for the generation of TMS-F, a stronger thermodynamic driving force due to the strong silicon-fluorine bond formation.

The synthetic changes were carried out in a one-pot fashion (Scheme 2.5). A mixture of $^{3/Me}$**[Sr]**$^{2+}$ and 2.0 equiv. $Cu(OTf)_2$ was stirred in DCM and treated with $[NBu_4][Ph_3SiF_2]$ to produce a new paramagnetic, blue macrocyclic product. The monofluoride product $[^{3/Me}PDI_2Cu_2F][OTf]_3$ (**$^{3/Me}$[Cu$_2$F]$^{3+}$**) was identified using single crystal X-ray crystallography as the first structurally-characterized example of a copper(II)-fluoride PDI complex (Figure 2.10). Unlike the monochloride product **$^{3/Me}$[Cu$_2$Cl]$^{3+}$**, the dinuclear Cu_2F core is accommodated by an unfolded conformation of the macrocyclic ligand. The crystal structure also displays a linear arrangement of atoms within the macrocyclic pocket leading to a Cu-F-Cu angle of 180.00°. In order for the fluoride ligand to fit in this linear arrangement, the Cu–Cu distance increases to 3.7240(4) Å, a similar distance to **$^{3/Me}$[Cu$_2$Cl]$^{3+}$**. Each Cu(II) center is capped by a triflate anion (Cu–O distance of 2.2707(19) Å) and adopts a square pyramidal geometry (τ_5 = 0.03 for each Cu(II) center). A large thermal ellipsoid is present on the μ-F, indicating that the bridging fluoride unit is oscillating back and forth in the macrocyclic pocket. The short Cu–F bond length (1.8620(3) Å) agrees with the related four-coordinate pyridyldiamide copper(II)-fluoride complex reported by Zhang and coworkers (1.828(2) Å).[62, 63]

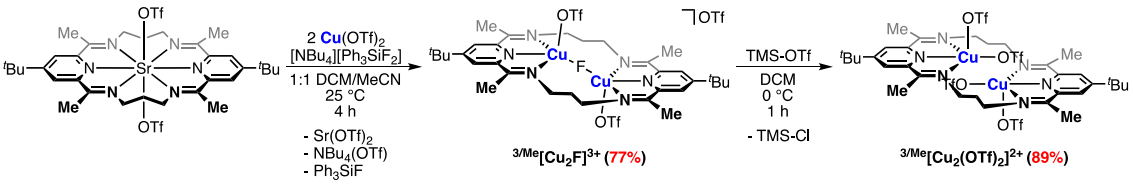

Scheme 2.5 Abstraction of bridging fluoride from **$^{3/Me}$[Cu$_2$F]$^{3+}$** using TMS-OTf in DCM.

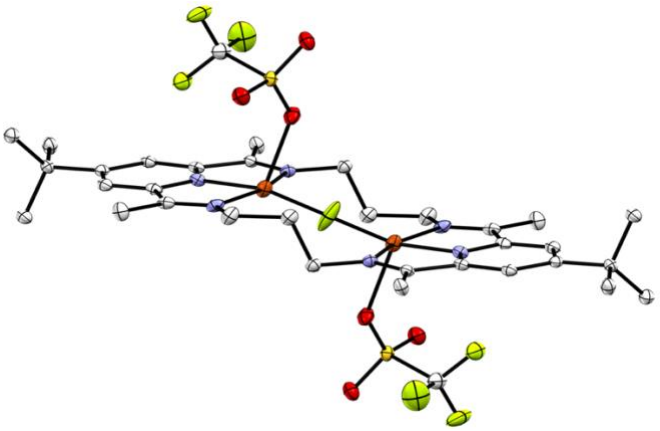

Figure 2.10 Crystal structure of $^{3/Me}$**[Cu$_2$F]$^{3+}$** (thermal ellipsoids set at 50% probability; hydrogen atoms, triflate disorder and outersphere anions omitted for clarity).

Removal of the fluoride ligand using TMS-OTf was carried out in DCM at -78 °C. The dark blue slurry became light blue upon the slow addition of TMS-OTf. Combustion analysis supported the formation of the Cu_2(II,II) tetratriflate macrocyclic complex [$^{3/Me}$PDI$_2$Cu$_2$][OTf]$_4$ (**$^{3/Me}$[Cu$_2$(OTf)$_2$]$^{2+}$**). The product, like **^{3}[Cu$_2$(NCMe)$_2$]$^{4+}$,** was insoluble in common organic solvents. Due to the increased insolubility, single crystals of the product remained elusive. However, based on the structural data obtained for **$^{3/Me}$[Cu$_2$Cl$_2$]$^{2+}$** and **$^{3/Me}$[Cu$_2$(NCMe)$_2$]$^{4+}$**, an unfolded ligand conformation is a reasonable assignment of the product's overall geometry, with two triflate anions now occupying the equatorial positions of each copper(II) center rather than acetonitrile ligands.

2.3 Anion Substitution Reactions with $^{3/Me}$[Cu$_2$(OTf)$_2$]$^{2+}$

2.3.1 Anion Substitution with Halides and Pseudohalides

To assess anion binding within the macrocyclic pocket of **$^{3/Me}$[Cu$_2$(OTf)$_2$]$^{2+}$**, the material was first treated with 2.0 equiv. of NBu_4Cl to generate the previously isolated **$^{3/Me}$[Cu$_2$Cl$_2$]$^{2+}$** (Scheme 2.6, Top). As the reaction proceeded in MeCN, the insoluble blue **$^{3/Me}$[Cu$_2$(OTf)$_2$]$^{2+}$** was consumed. A sharp color change to dark green signified the

conversion to the desired product. Qualitatively, the solubility profile and color of the resulting product matched that of the independently synthesized $^{3/Me}$**[Cu$_2$Cl$_2$]$^{2+}$**. Moreover, both IR and UV-vis-NIR spectroscopic measurements confirmed the identity of the product as $^{3/Me}$**[Cu$_2$Cl$_2$]$^{2+}$**. Facile anion substitution demonstrated the enhanced reactivity of $^{3/Me}$**[Cu$_2$(OTf)$_2$]$^{2+}$** compared to the more inert $^{3/Me}$**[Cu$_2$Cl$_2$]$^{2+}$**.

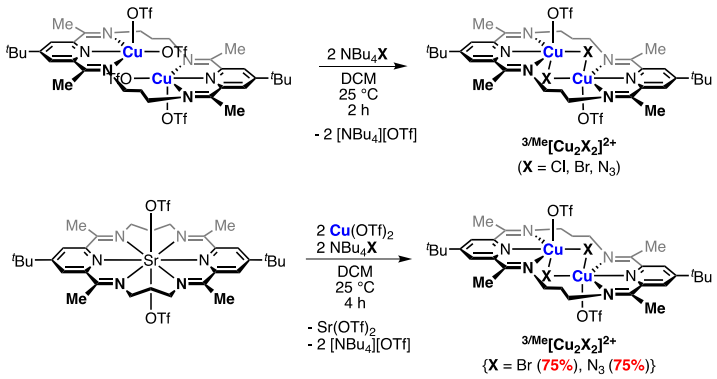

Scheme 2.6 Top) Anion metathesis with $^{3/Me}$**[Cu$_2$(OTf)$_2$]$^{2+}$** and Bottom) One-pot anion metathesis with $^{3/Me}$**[Sr]$^{2+}$**.

Introducing a new bridging group was achieved by treating $^{3/Me}$**[Cu$_2$(OTf)$_2$]$^{2+}$** with 2.0 equiv. NBu_4Br (Scheme 2.6, Top). Upon the addition of NBu_4Br to a blue MeCN slurry of $^{3/Me}$**[Cu$_2$(OTf)$_2$]$^{2+}$**, a reaction was signified by a color change to green. After two hours of stirring, the solution appeared homogeneous. The product was obtained as a bright green powder. Attempts at crystallization of the macrocyclic complex afforded powders. The identity of product was confirmed through combustion analysis as the Cu_2-di(μ-Br) complex [$^{3/Me}$$PDI_2Cu_2Br_2$][OTf]$_2$ ($^{3/Me}$**[Cu$_2$Br$_2$]$^{2+}$**). The infrared spectrum displayed an imine stretching frequency at 1600 cm^{-1}. Further confirmation of the dinuclear product was confirmed through UV-vis-NIR spectroscopy. Absorption bands were identified at 238 nm ($\pi \rightarrow \pi$ transition) and 680 nm (d$\rightarrow$d transition), which agree well $^{3/Me}$**[Cu$_2$Cl$_2$]**$^{2+}$.

Similarly, the treatment of $^{3/Me}$**[Cu$_2$(OTf)$_2$]$^{2+}$** with 2.0 equiv. NBu_4N_3 cleanly afforded the paramagnetic, dark green complex [$^{3/Me}$$PDI_2Cu_2(N_3)_2$][OTf]$_2$ ($^{3/Me}$**[Cu$_2$(N$_3$)$_2$]$^{2+}$**).

Crystallization of the product allowed for structural elucidation (Figure 2.11). Two azide ligands now bridge the two copper(II) centers, while the macrocyclic ligand remains in the unfolded ligand conformation. Each Cu(II) center adopts a distorted octahedral geometry. The elongated Cu–N (2.5353(1) Å) and Cu–O (2.4361(9) Å) axial bond lengths are consistent with Cu-d^9 Jahn-Teller distortions. A symmetric $Cu_2(\mu\text{-}N_3)_2$ core is noted in the crystal structure, with a Cu–Cu distance of 3.1362(6) Å and symmetry-related Cu-N-Cu angles of 88.02(4)°. Although the Cu–Cu distance is similar to that in the analogous $^{3/Me}[Cu_2Cl_2]^{2+}$ complex, the bridging angle observed for $^{3/Me}[Cu_2(N_3)_2]^{2+}$ is larger, owing to the shorter equatorial Cu–N bond lengths of 1.936(1) Å. Further support for the di(μ-azide) core was noted in the compound's IR spectrum. An asymmetric azide stretching frequency was observed at 2062 cm^{-1}. Similar stretching frequencies have been observed in analogous Schiff base complexes.[64-67]

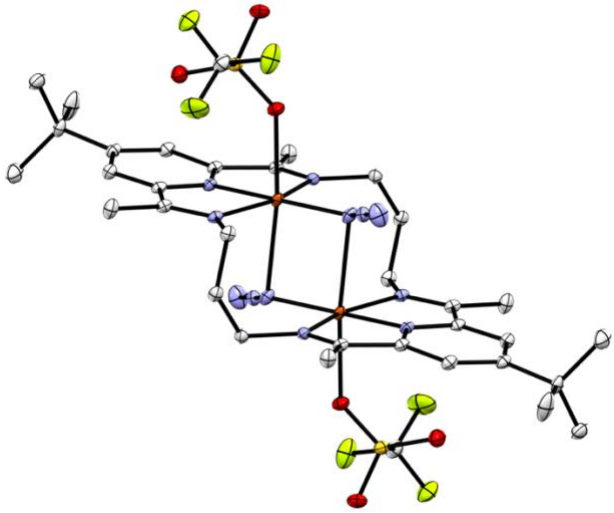

Figure 2.11 Crystal structure of $^{3/Me}[Cu_2(N_3)_2]^{2+}$ (thermal ellipsoids set at 50% probability; hydrogen atoms omitted for clarity).

Considering the ease of anion substitution displayed by $^{3/Me}[Cu_2(OTf)_2]^{2+}$, we pursued a simplified one-pot protocol in which $^{3/Me}[Cu_2(OTf)_2]^{2+}$ would be formed *in situ* and then treated with an external anion source (Scheme 2.6, Bottom) to reduce the

number of steps to achieve anion metathesis. We were surprised to find that stirring $^{3/Me}$**[Sr]**$^{2+}$ and 2.0 equiv. $Cu(OTf)_2$ in DCM afforded no reaction. However, found upon addition of 2.0 equiv. of NBu_4X (X = N_3, Br) to the mixture, an anion metathesis reaction was initiated to yield the $^{3/Me}$**[Cu$_2$(μ-X)$_2$]**$^{2+}$ products. These results indicate that anion metathesis is facile in this system and that the formation of $^{3/Me}$**[Cu$_2$(OTf)$_2$]**$^{2+}$ is not necessary prior to the generation of the $^{3/Me}$**[Cu$_2$(μ-X)$_2$]**$^{2+}$ products. While this one-pot route afforded comparable yields to the stepwise procedure, the extended workup and separation of multiple salt byproducts proved more challenging. Anion metathesis studies with $^{3/Me}$**[Cu$_2$(OTf)$_2$]**$^{2+}$ were continued to avoid such difficulties.

2.3.2 Anion Substitution with Nitrite and Trimethylsilanolate Anions

We next pursued the inclusion of the nitrite anion, which is known to be capable of adopting a range of coordination modes at Cu(II) ions. To first probe if $^{3/Me}$**[Cu$_2$(OTf)$_2$]**$^{2+}$ was capable of binding nitrite, a similar protocol was followed as that described above, in which $NaNO_2$ was used in the anion metathesis reaction (Figure 2.12). Upon adding 2.0 eq. of $NaNO_2$ to a slurry of $^{3/Me}$**[Cu$_2$(OTf)$_2$]**$^{2+}$, the starting material was consumed over the course of 2 hours to afford a dark blue-green solution. Diffusion of Et_2O into a concentrated MeCN solution afforded crystals suitable for X-ray diffraction. The product was identified as the di(μ-κ^1-ONO) macrocycle complex, [$^{3/Me}$PDI$_2$Cu$_2$(ONO)$_2$][OTf]$_2$ ($^{3/Me}$**[Cu$_2$(ONO)$_2$]**$^{2+}$).

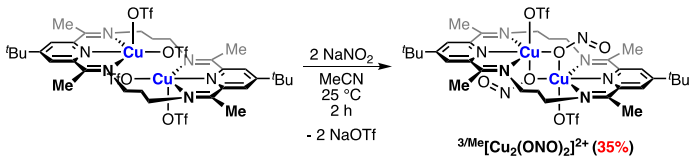

Figure 2.12 Synthesis of $^{3/Me}$**[Cu$_2$(ONO)$_2$]**$^{2+}$ in MeCN.

The solid-state structure of $^{3/Me}$**[Cu$_2$(ONO)$_2$]**$^{2+}$ depicts the macrocyclic ligand enforcing a μ-κ^1-binding of each nitrite anion (Figure 2.13). Limited examples of this

geometry are found for Cu_2(II,II) systems in the literature.[68-71] In $^{3/Me}[Cu_2(ONO)_2]^{2+}$, each copper is found in a distorted octahedral geometry, with the overall structure appearing similar in form to $^{3/Me}[Cu_2(N_3)_2]^{2+}$. The two copper(II) centers are related by a center of symmetry in the crystal lattice and are separated by 3.2553(6) Å. The characteristic Cu(II)-d^9 Jahn-Teller distortions are observed through the elongated Cu–O bond lengths (2.347(1) Å and 2.505(1) Å). Like $^{3/Me}[Cu_2(N_3)_2]^{2+}$, the $Cu_2(ONO)_2$ core displays a larger bridging angle [∠Cu-O-Cu = 94.18(5)°] than that observed in $^{3/Me}[Cu_2Cl_2]^{2+}$. The short equatorial Cu–O bond lengths of 1.904(1) Å account for this difference.

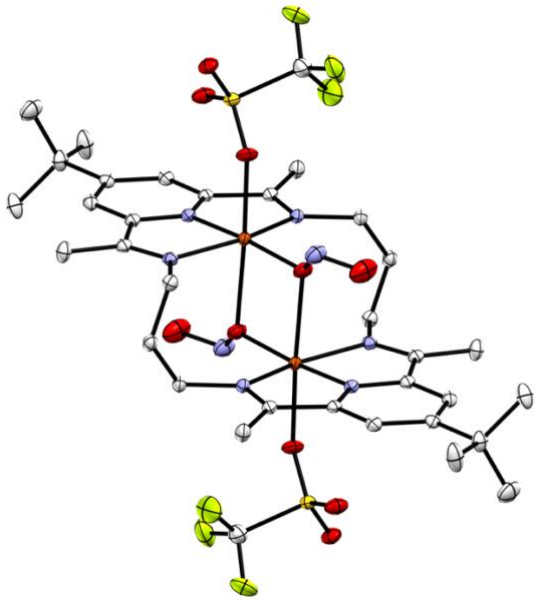

Figure 2.13 Crystal structure of $^{3/Me}[Cu_2(ONO)_2]^{2+}$ (thermal ellipsoids set at 50% probability; hydrogen atoms and nitrite disorder omitted for clarity).

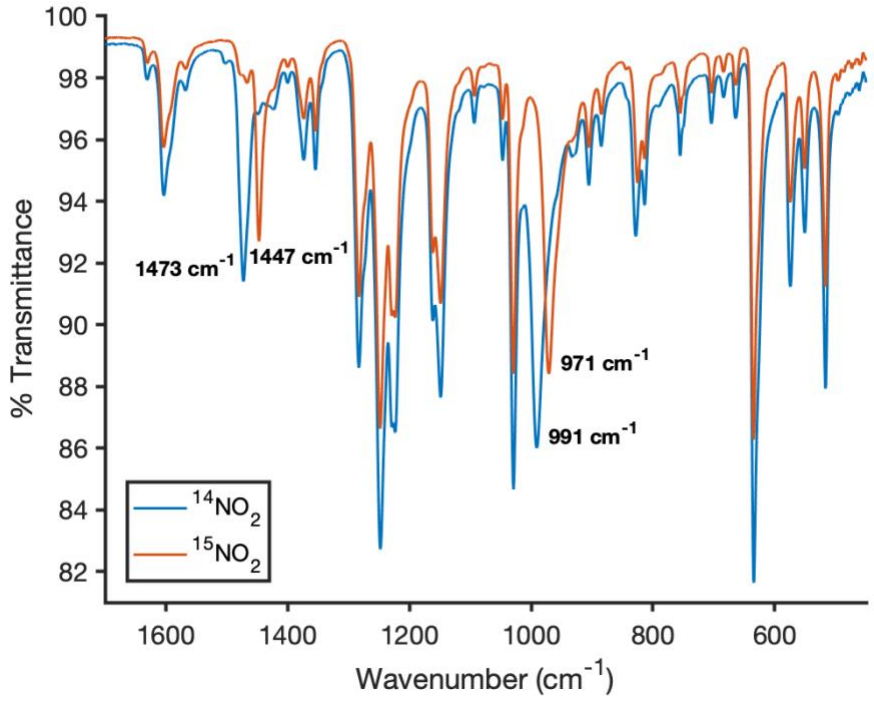

Figure 2.14 Overlay of infrared spectra of $^{3/Me}[Cu_2(O^{14/15}NO)_2]^{2+}$.

The IR spectral data for $^{3/Me}[Cu_2(ONO)_2]^{2+}$ are consistent with the nitrite ligation mode observed crystallographically. IR spectra of Cu_2(II,II) complexes with κ^1-ONO ligands show asymmetric and symmetric stretching modes in the 1400-1100 cm^{-1} region.[68,69] However, the bending and stretching frequencies associated with the macrocyclic ligand convolute the IR spectrum of $^{3/Me}[Cu_2(ONO)_2]^{2+}$. To distinguish the nitrite stretching frequencies from the macrocyclic ligand, the isotopically labeled complex $[^{3/Me}PDI_2Cu_2(O^{15}NO)_2][OTf]_2$ ($^{3/Me}[Cu_2(O^{15}NO)_2]^{2+}$) was prepared. The IR spectrum of $^{3/Me}[Cu_2(ONO)_2]^{2+}$ contains two distinct stretching frequencies at 1473 cm^{-1} and 991 cm^{-1} that shift to lower energies (1447 cm^{-1} and 971 cm^{-1}) when using $^{3/Me}[Cu_2(O^{15}NO)_2]^{2+}$ (Figure 2.14). Thus, the stretching frequencies at 1473 cm^{-1} and 991 cm^{-1} are assigned to the asymmetric and symmetric stretching frequencies of the nitrite ligand.

Bridging alkoxy anions were next targeted as a way of expanding the scope of substitution reactions available to $^{3/Me}$**[Cu$_2$(OTf)$_2$]$^{2+}$**, but Cu$_2$(II,II)-μ-(OR) (R = Me, ^{t}Bu, Ph) macrocyclic species eluded isolation. Instead, substitution was found to be successful when using the trimethylsilanolate anion (Figure 2.15). Upon addition of 2.0 equiv. NaOTMS to a slurry of $^{3/Me}$**[Cu$_2$(OTf)$_2$]$^{2+}$**, a rapid color change from blue to dark orange-brown was observed. Low-temperature crystallization afforded single crystals of the desired complex, [$^{3/Me}$PDI$_2$Cu$_2$(OTMS)$_2$][OTf]$_2$ ($^{3/Me}$**[Cu$_2$(OTMS)$_2$]$^{2+}$**). The crystal structure confirms the presence of two bridging trimethylsilanolate ligands (Figure 2.16). The ligand adopts an unfolded ligand conformation to support the two bridging ligands between the two copper(II) centers. In the case of $^{3/Me}$**[Cu$_2$(OTMS)$_2$]$^{2+}$**, both Cu(II) centers were found to adopt a distorted square pyramidal geometry with the triflate anions lying in the outer coordination sphere (τ_5 = 0.14 for each Cu(II)). The steric encumbrance of the TMS groups may prevent the triflate anions from binding to the metal centers in a manner seen with structurally related complexes presented above.

The Cu$_2$(μ-OTMS)$_2$ diamond core displays a Cu-O-Cu angle of 86.65(5)°, an equatorial Cu–O bond length of 1.8969(14) Å, a distorted axial Cu–O bond length of 2.259(1) Å and a short Cu–Cu distance of 2.8639(4) Å. To date, no structurally-characterized Cu$_2$(II,II)-μ-OTMS complexes have been reported in the CSD. McGeary, Caulton and coworkers previously reported a Cu$_2$(I,I)-*bis*(μ-OSiPh$_3$)-*bis*(diphenylmethylphosphine) cluster.[72] The cluster was found to contain an asymmetric [Cu$_2$(OSiPh$_3$)$_2$] core, with longer Cu–O bond distances of 1.9457(17) and 2.0456(17) Å. The shorter equatorial bond distances observed in $^{3/Me}$**[Cu$_2$(OTMS)$_2$]$^{2+}$** are as expected, considering the higher oxidation states of the metal centers. A longer Cu–Cu distance of 2.9662(7) Å was also observed for the [Cu$_2$(OSiPh$_3$)$_2$] cluster. Compared with $^{3/Me}$**[Cu$_2$(OTMS)$_2$]$^{2+}$**, each copper center in McGeary and Caulton's cluster is more

sterically crowded, owing to the bulky diphenylmethylphopshine ligand. The combined action of the lower oxidation states and increased steric bulk at the metal centers forces a farther copper-copper distance.

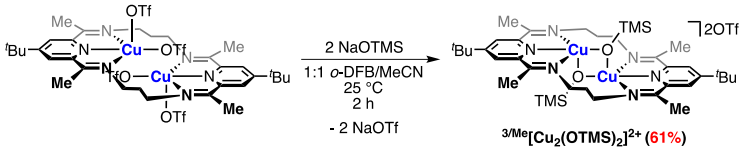

Figure 2.15 Synthesis of $^{3/Me}[Cu_2(OTMS)_2]^{2+}$ *o*-DFB/MeCN.

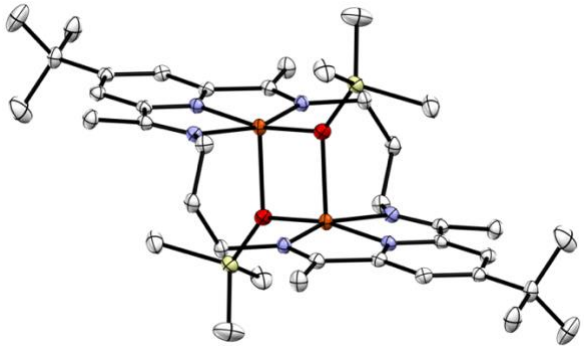

Figure 2.16 Crystal structure of $^{3/Me}[Cu_2(OTMS)_2]^{2+}$ (thermal ellipsoids set at 50% probability; hydrogen atoms and outersphere anions omitted for clarity).

2.3.3 Synthesis of $^{3/Me}[Cu_2OH]^{3+}$

The synthetic protocol for anion-exchange with $^{3/Me}[Cu_2(OTf)_2]^{2+}$ was next implemented with the hydroxide anion. Numerous Cu_2(II,II)-di(μ-OH)-containing complexes exist that are supported with mononucleating, multidentate ligands, such as BDI (BDI = β-diketiminate),[73] Tp^R (Tp = hydrotris(1-pyrazolyl)borate; R = Me, ^{i}Pr)[23,24] and TACN (TACN = 1,4,7-triazacyclononane).[74] However, isolation of a Cu_2(II,II)-di(μ-OH) complex with $^{3/Me}PDI_2$ has remained elusive. Instead, the monohydroxide product $[^{3/Me}PDI_2Cu_2OH][OTf]_3$ ($^{3/Me}[Cu_2OH]^{3+}$) was synthesized through treatment of $^{3/Me}[Cu_2(OTf)_2]^{2+}$ with LiOH, as confirmed by X-ray crystallography (Figure 2.17).

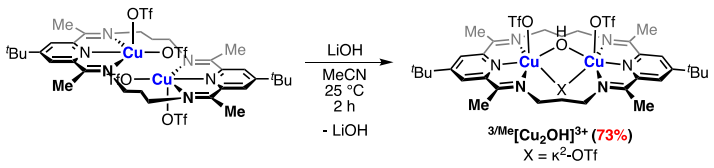

Figure 2.17 Synthesis of $^{3/Me}$**[Cu$_2$OH]$^{3+}$** in MeCN.

Growth of single crystals allowed for structure elucidation of $^{3/Me}$**[Cu$_2$OH]$^{3+}$**. The crystal structure was found to contain a planar macrocyclic ligand (Figure 2.18). Because of this conformation, the Cu–Cu distance lengthens to 3.585(7) Å and 3.618(4) Å (the asymmetric unit contains disordered macrocyclic complexes with distinct metrical parameters). These distances lie at the longer end of the range of Cu–Cu distances observed in the series of *bis*(4-*tert*-butylpyridyldiimine) macrocyclic complexes. Each copper(II) center adopts a distorted octahedral geometry, with weakly-coordinating triflate ligands occupying the axial positions of each copper(II) center. The PDI subunits and a bridging hydroxide ligand occupy the equatorial plane. The Cu–O(H) distances of 1.872(2) and 1.875(5) Å agree well with previously reported Cu$_2$(II,II)-μ-OH complexes (Table 2.2), including Drew and Nelson's [^{Pr}PDI$_2$Cu$_2$OH][ClO$_4$]$_3$·2H$_2$O. However the Cu-O(H)-Cu angle of 149.98(16)° [140.2(2)°] significantly deviates from that of [^{Pr}PDI$_2$Cu$_2$OH][ClO$_4$]$_3$·2H$_2$O [110.3(7)°]. The less-strained $^{3/Me}$**[Cu$_2$OH]$^{3+}$** complex allows for the increased Cu–Cu distance and corresponding increase in the Cu-O(H)-Cu angle. In fact, the observed angle in $^{3/Me}$**[Cu$_2$OH]$^{3+}$** agrees better with the larger complex [^{Oct}PDI$_2$Cu$_2$OH][ClO$_4$]$_3$·H$_2$O reported by Drew and Nelson [141.7(7)°]. As expected, the flexible aliphatic linkers modulate the Cu–Cu distance to allow for variously-sized bridging ligands to be housed between the two metal centers.

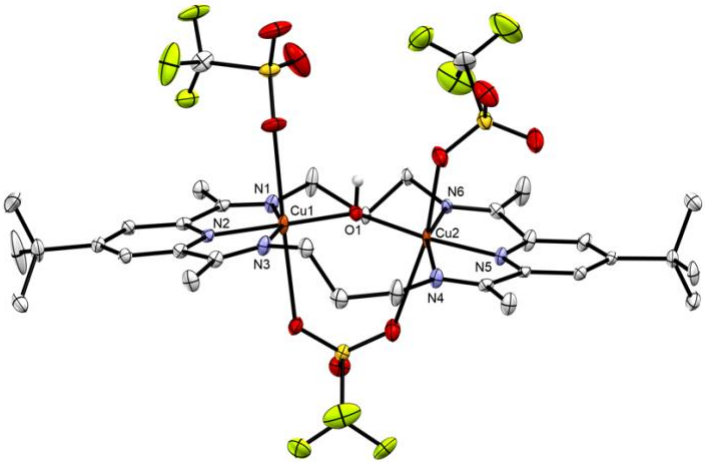

Figure 2.18 Crystal structure of $^{3/Me}[Cu_2OH]^{3+}$ (thermal ellipsoids set at 50% probability; hydrogen atoms, solvent molecules, triflate disorder and macrocycle disorder omitted for clarity).

Table 2.2 Selected bond metrics of copper(II) hydroxide PDI complexes.

	$^{3/Me}[Cu_2OH]^{3+}$	$[^{Et}PDI_2Cu2OH]^{3+}$*b,c*	$[^{Oct}PDI_2Cu_2OH]^{3+}$*c*
Cu(1) – N(1) / Å	2.097(2)	2.066(12)	2.039(11)
Cu(1) – N(2) / Å	1.912(2)	1.916(13)	1.907(16)
Cu(1) – N(3) / Å	2.040(3)	2.061(13)	2.060(9)
Cu(2) – N(4) / Å	2.096*a*	-	2.076(4)
Cu(2) – N(5) / Å	1.926 *a*	-	1.925(12)
Cu(2) – N(6) / Å	2.038 *a*	-	2.059(14)
Cu(1) – O(1) / Å	1.872(2)	1.916(9)	1.866(13)
Cu(2) – O(1) / Å	1.908 *a*	-	1.912(10)
Cu(1) – Cu(2) / Å	3.603 *a*	3.145(4)	3.57
∠Cu(1)-O(1)-Cu(2) / °	145.09*a*	110.3(7)	141.7(7)
Δ / Å	0.196 *a*	0.230	0.147

a – Average values based on disorder of molecule
b – Macrocycle is symmetric; bond metrics are the same for Cu(2)
c – Crystal structure obtained at room temperature

2.4 Summary of Cu_2(II,II) 4-*tert*-butyl-*bis*(pyridyldiimine) Macrocycles

The isolation and characterization of a series of Cu_2(II,II) *bis*(4-*tert*-butylpyridyldiimine) macrocycles was carried out using a new "open-core" macrocycle, $^{3/Me}[Cu_2(OTf)_2]^{2+}$. The triflate complex is a suitable precursor to a host of novel Cu_2(II,II)

macrocycles through anion metathesis reactions. Through this work, a secondary pathway to substituted Cu_2(II,II) macrocycles was also found through a one-pot procedure in which $^{3/Me}$**[Sr]**$^{2+}$ was treated with 2.0 equiv. $Cu(OTf)_2$ and a corresponding source of anion. Either pathway was sufficient to achieve anion metathesis. The macrocycles were found to exhibit greater solubility in lower-polarity organic solvents (THF, DCM, MeCN, etc.) than analogous complexes reported by Drew and Nelson. The solid-state structures of each new macrocyclic complex showed that the conformation of the macrocycle was able to change depending on the number of bridging substituents between the copper(II) centers (Table 2.3). If two bridging ligands were present, the macrocycle adopted an unfolded conformation. If one bridging ligand was present, the macrocycle adopted an arched or planar conformation. The geometric differences were enabled by the flexibility of the macrocyclic aliphatic linkers, an observation also made by Drew and Nelson. The electronic absorption spectra all displayed common features, including d-d transitions, LMCT transitions, and π-π* ligand transitions. The robust synthetic protocol allowed access to different bridging motifs, including a hydroxide anion, which is an ideal intermediate to study in the pursuit of a bridging oxo complex and C-H bond oxidation.

Table 2.3 Summary of Cu_2(II,II) *bis*(4-*tert*-butylpyridyldiimine) macrocycles

	Conformation	Cu-Cu / Å	Cu-$X_{equatorial}$ / Å[a]	Cu-X-Cu / °[a]
$^{3/Me}$**[Cu_2Cl]**$^{2+}$	Unfolded	3.129(1)	2.1860	75.05
$^{2/Me}$**[Cu_2Cl]**$^{2+}$	Unfolded	2.9922[a]	2.2056	70.82
$^{3/Me}$**[Cu_2(NCMe)$_2$]**$^{4+}$	Unfolded	3.3479(7)	1.973	77.64
$^{3/Me}$**[Cu_2Cl]**$^{3+}$	Arched	3.7045(7)	2.2823	108.50
$^{3/Me}$**[Cu_2F]**$^{3+}$	Unfolded	3.7240(4)	1.8620	180.00[b]
$^{3/Me}$**[Cu_2(N_3)$_2$]**$^{2+}$	Unfolded	3.1362(6)	1.936	88.02
$^{3/Me}$**[Cu_2(ONO)$_2$]**$^{2+}$	Unfolded	3.2553(6)	1.904	94.18
$^{3/Me}$**[Cu_2(OTMS)$_2$]**$^{2+}$	Unfolded	2.8639(4)	1.8969	86.65
$^{3/Me}$**[Cu_2OH]**$^{3+}$	Planar	3.603[a]	1.890	145.09

a – Average values.
b – 1-X,1-Y,1-Z

2.5 Experimental

2.5.1 General Considerations

Unless stated otherwise, all reactions were carried out under an inert atmosphere of N_2 using standard Schlenk techniques or a PureLab HE glovebox, then worked up in air. Glassware, stir bars, filter aid (Celite), and 4 Å molecular sieves were dried in an oven at 175 °C for at least one hour prior to use when applicable. Degassed anhydrous solvents (Pentane, Et_2O, THF, DCM, and MeCN) were dried by passage through activated alumina using a Solvent Purification System and stored over 4 Å molecular sieves for at least one day before use. Chloroform-*d* was purchased from Cambridge Isotopes Laboratories, Inc. and was stored over 4 Å molecular sieves for at least one day before use. The macrocyclic precursor $^{2/Me}$**[Sr]**$^{2+}$ was prepared according to a previous reported procedure.[75] Tetrabutylammonium chloride (NBu_4Cl) was purchased from Sigma Aldrich, ground to a fine powder with a mortar and pestle and dried under vacuum over P_2O_5 for one week before use. Tetrabutylammonium bromide (NBu_4Br) was purchased from Sigma Aldrich and dried under vacuum over P_2O_5 for one week before use. Sodium nitrite ($NaNO_2$) was purchased from Fisher Chemicals, ground to a fine powder with a mortar and pestle and flame dried under dynamic vacuum, then stored under N_2 in an inert atmosphere glovebox. ^{15}N-labeled sodium nitrite ($Na^{15}NO_2$) was purchased from Cambridge Isotope Laboratories, Inc., ground to a fine powder with a mortar and pestle, and flame dried under dynamic vacuum. The isotopologue was then stored in the dark, in the glovebox. Sodium trimethylsilanolate was purchased as a 1.0 M solution in THF from Sigma Aldrich in a Sure/Seal^{TM} bottle and was stored under N_2 in the glovebox. All other reagents were purchased from commercial vendors and used as received.

NMR Spectroscopy: NMR spectra were recorded on a NEO 600 spectrometers. All chemical shifts are reported in units of ppm and referenced to the residual proteo-solvent resonance for proton and carbon chemical shifts.

Elemental Analysis: Analytical data were obtained from the CENTC Elemental Analysis Facility at the University of Rochester. Microanalysis samples were weighed with a PerkinElmer Model AD6000 Autobalance and their compositions were determined with a PerkinElmer 2400 Series II Analyzer. Air-sensitive samples were handled in a VAC Atmospheres glovebox and combusted in a tin capsule that was crimp-sealed with a die apparatus. For $^{3/Me}[Cu_2(NCMe)_2]^{2+}$, analytical data was collected using a Costech ECS 4010 analyzer in the Earth & Environmental Science Department at the University of Pennsylvania.

Infrared Spectroscopy: Infrared spectra were recorded using a PerkinElmer Spectrum Two FT-IR spectrometer. Samples were placed on an ATR crystal after collecting a blank spectrum and spectral data was measured over the range of 450-4000 cm^{-1}.

UV-vis-NIR Spectroscopy: Absorption spectra were collected over the range of 200-1000 nm using an Agilent Cary 60 UV-vis-NIR spectrophotometer. Stock solutions (3.0-11.0 mM) were prepared under an N_2 atmosphere in the glovebox. Samples were then diluted to obtain absorption profiles in the linear response range of the spectrophotometer. Each measurement was obtained using a 10 mm path-length quartz cuvette with a screw cap. The temperature of each measurement was maintained at 25 °C using an Unisoku USP-203A cryostat. Five different concentrations were used for Beer's Law analysis of each

peak maxima. The absorption intensities for peak maxima were plotted vs. concentration to ensure a linear fit was obtained ($R^2 > 0.990$).

X-ray Crystallography: X-ray intensity data were collected on a Bruker D8Quest CMOS ($^{3/Me}[Cu_2Cl_2]^{2+}$, $^{2/Me}[Cu_2Cl_2]^{2+}$ and $^{3/Me}[Cu_2OH]^{3+}$) and a Bruker APEXII CCD ($^{3/Me}[Cu_2(OTMS)^{2+}$) area detector diffractomer with graphite-monochromated Mo-Kα radiation (λ = 0.71073 Å) at a temperature of 100 K. X-ray intensity data for $^{3/Me}[Cu_2Cl]^{3+}$, $^{3/Me}[Cu_2F]^{3+}$ and $^{3/Me}[Cu_2(ONO)_2]^{2+}$ were collected on a Rigaku XtaLAB Synergy-S diffractometer equipped with an HPC area detector (Dectris Pilatus3 R 200K) employing confocal multilayer optic-monochromated Mo-Kα radiation (λ = 0.71073 Å) at a temperature of 100 K. X-ray intensity data for $^{3/Me}[Cu_2(N_3)_2]^{2+}$ and $^{3/Me}[Cu_2(NCMe)_2]^{3+}$ were collected on a Rigaku XtaLab Synergy-S diffractometer equipped with an HPC area detector (HyPix-6000HE) employing confocal multilayer optic-monochromated Mo-Kα radiation (λ = 0.71073 Å) ($^{3/Me}[Cu_2(N_3)_2]^{2+}$) or Cu-Kα radiation (λ = 1.54184 Å) ($^{3/Me}[Cu_2(NCMe)_2]^{3+}$) at a temperature of 100 K. Rotation frames were integrated using SAINT or CrysAlisPro, producing a listing of unaveraged F^2 and $\sigma(F^2)$ values. The intensity data were corrected for Lorentz and polarization effects and for absorption using SADABS or SCALE3 ABSPACK. The structures were solved by direct methods using either SHELXT ($^{3/Me}[Cu_2Cl_2]^{2+}$, $^{2/Me}[Cu_2Cl_2]^{2+}$, $^{3/Me}[Cu_2(NCMe)_2]^{3+}$, $^{3/Me}[Cu_2F]^{3+}$, $^{3/Me}[Cu_2(N_3)_2]^{2+}$, $^{3/Me}[Cu_2(ONO)_2]^{2+}$ and $^{3/Me}[Cu_2OH]^{3+}$) or SHELXS-97 ($^{3/Me}[Cu_2(OTMS)^{2+}$) and refined by full-matrix least-squares, based on F^2 using SHELXL-2018. All reflections were used during refinement. Non-hydrogen atoms were refined anisotropically and hydrogen atoms were refined using a riding model. For $^{3/Me}[Cu_2Cl_2]^{2+}$ $^{3/Me}[Cu_2(N_3)_2]^{2+}$, the molecule lies on a crystallographic center-of-symmetry (at ½, ½, ½). For $^{3/Me}[Cu_2(ONO)_2]^{2+}$, the coordinate NO_2 is disordered by a slight rotation about the Cu1-O1 bond with relative occupancies of

0.72/0.28. For $^{3/Me}$**[Cu$_2$(OTMS)]$^{2+}$**, the molecule lies on a crystallographic center-of-symmetry (at 0, 0, 0).

2.5.2 Synthetic Procedures

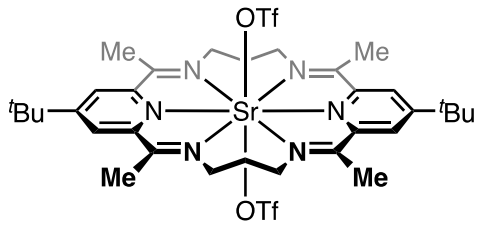

$^{3/Me}$[Sr]$^{2+}$. The following procedure was adapted from the literature report.[75] A 500 mL round bottom flask was charged with 4-*tert*-butyl-2,6-diacetylpyridine (5.1349 g, 23.417 mmol, 2.00 equiv.), Sr(OTf)$_2$ (4.5353 g, 11.757 mmol, 1.00 equiv.), and MeOH (250 mL). The mixture was stirred until all solids were dissolved. To the pale-yellow solution, 1,3-diaminopropane (2.00 mL, 23.9 mmol, 2.04 Eq.) was added. The solution became darker and was heated to reflux (oil bath set to 75 °C) for 16 hours. The volatile materials were then removed under vacuum. The crude product was extracted into *ca*. 25 mL DCM and filtered over a pad of celite to remove insoluble materials. The yellow-orange filtrate was then treated with *ca*. 300-400 mL hexanes to precipitate the product as an off-white powder. The powder was collected via vacuum filtration, washed with an additional *ca*. 500 m L hexanes and dried under vacuum (9.6398 g, 91%). Analytical characterization data matched those previously reported. **^{1}H NMR** ($CDCl_3$, 600 MHz, 298 K): δ = 7.81 (s, 8H), 3.96 (t, J = 6.5 Hz, 8H), 2.46 (s, 12 H), 1.90 (quint, J = 6.5 Hz, 4H), 1.43 (s, 18H) ppm. **^{13}C{^{1}H} NMR** ($CDCl_3$, 151 MHz, 298 K): δ = 167.1, 164.0, 155.6, 121.4, 120.1 (q, J = 319.4 Hz), 46.7, 35.5, 30.67, 28.9, 15.2 ppm. **^{19}F{^{1}H} NMR** ($CDCl_3$, 565 MHz, 298 K): δ = -78.06 ppm.

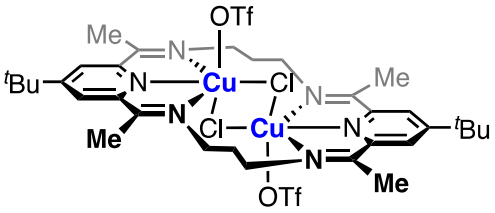

$^{3/Me}[Cu_2Cl_2]^{2+}$. The following procedure was carried out in air. A 100 mL round bottom flask was charged with $^{3/Me}$**[Sr]**$^{2+}$ (553.4 mg, 0.6145 mmol, 1.00 equiv.) and MeOH (15 mL). Once all starting material was dissolved, the golden-yellow solution was treated with a solution of $CuCl_2 \cdot 2H_2O$ (209.8 mg, 1.231 mmol, 2.00 equiv.) in MeOH (10 mL). The reaction mixture immediately became dark green and was stirred for 60 min at room temperature. Solvent was then removed under vacuum. The product was extracted in 20 mL MeCN and filtered over a pad of Celite to remove insoluble byproducts. The dark blue-green filtrate was then layered with 80 mL Et_2O at room temperature. After one day, a crystalline solid was collected via vacuum filtration and rinsed with 50 mL Et_2O. The product was collected as a blue powder and dried under vacuum (517.0 mg, 83%). **Anal. % Calcd.** for $C_{34}H_{46}Cl_2Cu_2F_6N_6O_6S_2$ (1010.88 g/mol): C, 40.40; H, 4.59; N, 8.31. Found: C, 40.06; H, 4.51 N, 8.22. **FT-IR** (ATR): 1597 (C=N) cm^{-1}. **UV-vis-NIR** (MeCN, 298 K): 238 nm (7.71 x 10^4 M^{-1} cm^{-1}), 676 nm (242 M^{-1} cm^{-1}).

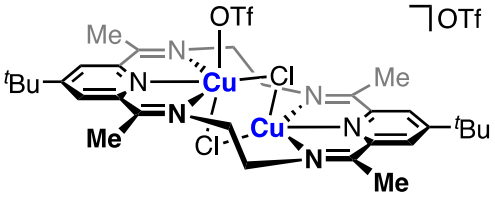

$^{2/Me}[Cu_2Cl_2]^{2+}$. The following procedure was carried out in air. A 100 mL round bottom flask was charged with $^{2/Me}$**[Sr]**$^{2+}$ (520.9 mg, 0.5969 mmol, 1.00 equiv.) and MeOH (15 mL). Once all starting material was dissolved, the golden-yellow solution was treated with a

solution of $CuCl_2 \cdot 2H_2O$ (206.9 mg, 1.214 mmol, 2.03 equiv.) in MeOH (10 mL). The reaction mixture immediately became dark green and was stirred for 60 minutes at room temperature. Solvent was then removed under vacuum. The product was extracted in *ca*. 20 mL MeCN and filtered over a pad of celite to remove insoluble byproducts. The dark blue-green filtrate was then layered with *ca*. 80 mL Et_2O at room temperature. After one day, the crystalline solid was collected via vacuum filtration and rinsed with 50 mL Et_2O. The product was collected as a blue powder and dried under vacuum (481.1 mg, 82%). Crystals suitable for single crystal X-ray crystallography were grown by slow diffusion of Et_2O into a concentrated MeCN solution at room temperature. **Anal. % Calcd.** for $C_{32}H_{42}Cl_2Cu_2F_6N_6O_6S_2$ (982.83 g/mol): C, 39.11; H, 4.31; N, 8.55. Found: C, 38.89; H, 4.19; N, 8.44. **FT-IR** (ATR): 1594 (C=N) cm^{-1}. **UV-vis-NIR** (MeCN, 298 K): 236 nm (5.31 x 10^4 M^{-1} cm^{-1}), 681 nm (228 M^{-1} cm^{-1}).

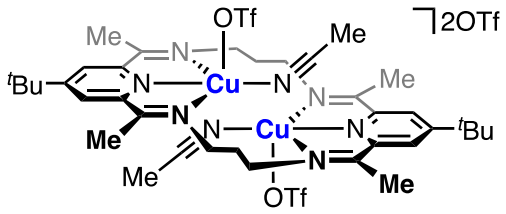

$^{3/Me}[Cu_2(NCMe)_2]^{4+}$. To a 100 mL Schlenk tube, **$[Cu_2Cl_2]^{2+}$** (1.094 g, 1.082 mmol, 1.00 equiv.) and MeCN (24 mL) were added. Once all solids were dissolved, the stirring, dark green solution was cooled to 0 °C and treated dropwise with TMS-OTf (0.790 mL, 4.37 mmol, 4.04 equiv.). The solution immediately turned dark blue and was warmed to room temperature over 30 minutes. Solvent was then removed under vacuum. The crude product was triturated with *ca*. 25 mL Et_2O and concentrated under vacuum to afford a light blue solid. The solid was transferred to the glove box, collected on a fritted glass filter, and washed with 4 x *ca*. 10 mL 1:1 MeCN/Et_2O followed by *ca*. 50 mL Et_2O. The product

was then dried under vacuum. The resulting fine blue powder (1.232 g, 86%) was stored at -35 °C in a glovebox. A sample suitable for X-ray crystallography was grown by slow diffusion of Et_2O into a concentrated MeCN solution at room temperature. From the same batch of isolated material, single crystals of $^{3/Me}[Cu_2Cl]^{3+}$ were grown by slow diffusion of *n*-hexane into a concentrated *o*-F_2-C_6H_4 solution at room temperature. **Anal. % Calcd.** for $C_{40}H_{52}N_8Cu_2F_{12}O_{12}S_4$ (1320.21 g/mol): C, 36.39; H, 3.97; N, 8.49. Found: C, 36.29; H, 4.05; N, 8.70.

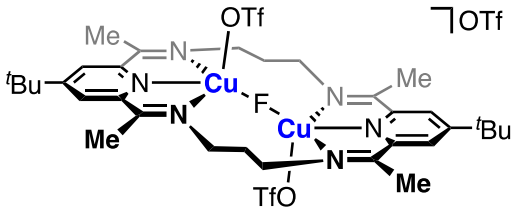

$^{3/Me}[Cu_2F]^{3+}$. A 500 mL round bottom Schlenk flask was charged with $Cu(OTf)_2$ (3.2736 g, 9.0513 mmol, 2.05 equiv.) and DCM (40 mL). The slurry was stirred and treated with a solution of $^{3/Me}[Sr]^{2+}$ (3.9844 g, 4.4246 mmol, 1.00 equiv.) in DCM (40 mL) followed by a solution of $[NBu_4][Ph_3SiF_2]$ (2.6507 g, 4.9099 mmol, 1.11 equiv.) in MeCN (80 mL). The reaction mixture became dark blue and was stirred for 4 hours at room temperature. The solution was filtered through a pad of Celite to remove insoluble materials. The Celite pad was rinsed with an additional 40 mL of 1:1 DCM:MeCN. The dark blue filtrate was then concentrated under vacuum to afford a crude blue oil, which solidified upon standing. The flask was transferred to the glovebox. The crude blue solid was washed with 3 x 30 mL 2:1 Et_2O:THF and collected over a fritted glass filter. The solid was washed with copious amounts of Et_2O followed by 3 x 25 mL THF (a dark impurity was removed). The remaining crystalline blue solid was rinsed with *ca*. 50-60 mL pentane and dried under vacuum to afford the desired product (3.7947 g, 77%). Crystals suitable for single crystal X-ray

crystallography were grown by layering a concentrated MeCN solution with Et_2O at room temperature and letting the two layers diffuse together overnight. **Anal. % Calcd.** for $C_{35}H_{46}Cu_2F_{10}N_6O_9S_3$ (1108.04 g/mol): C, 37.94; H, 4.18; N, 7.58. Found: C, 37.88; H, 4.16; N, 7.58. **FT-IR** (ATR): 1589 (C=N) cm^{-1}. **UV-vis-NIR** (MeCN, 298 K): 228, 667 nm (248 M^{-1} cm^{-1}).

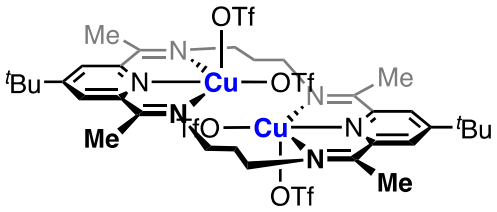

$^{3/Me}[Cu_2(OTf)_2]^{2+}$. To a 100 mL Schlenk tube was added **$^{3/Me}[Cu_2F]^{3+}$** (1.1099 mg, 1.0017 mmol, 1.00 equiv.) and DCM (25 mL). The blue slurry was cooled to -78 °C and treated dropwise with TMS-OTf (0.200 mL, 1.11 mmol, 1.10 equiv.). The mixture was removed from the cold bath and stirred for one hour. Over time, the dark blue slurry became light blue. Solvent was then removed under vacuum affording a light blue solid. The solid was transferred to the glovebox, triturated with *ca*. 100-200 mL Et_2O and collected by vacuum filtration. The product was then washed with *ca*. 100-200 mL pentane and dried under vacuum (1.0966 mg, 88%). **Anal. % Calcd.** for $C_{36}H_{46}Cu_2F_{12}N_6O_{12}S_4$ (1238.11 g/mol): C, 34.92; H, 3.75; N, 6.79. Found: C, 34.09; H, 3.53; N, 6.58.

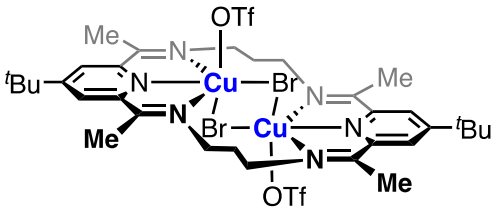

$^{3/Me}[Cu_2Br_2]^{2+}$. To a 100 mL Schlenk tube, $Cu(OTf)_2$ (433.2 mg, 1.198 mmol, 2.04 Eq.) and DCM (5 mL) were added. The slurry was treated with a solution of **$^{3/Me}[Sr]^{2+}$** (529.2 mg, 0.5877 mmol, 1.00 equiv.) in DCM (10 mL). No change occurred upon this addition. A solution of NBu_4Br (379.4 mg, 1.177 mmol, 2.00 equiv.) in DCM (10 mL) was then added. The reaction mixture immediately became dark green. Within minutes, a bright green solid precipitated from solution. The reaction was allowed to proceed for 4 h at room temperature. To the solution, MeCN (35 mL) was added, and the dark green solution was filtered over a pad of celite. The pad was rinsed with an additional 35 mL 1:1 DCM:MeCN, and the filtrate was concentrated under vacuum. The resulting crude solid was triturated with 10 mL THF and collected via vacuum filtration. The product was washed with 3 x 10 mL THF and 50 mL Et_2O. The product was re-dissolved in *ca*. 45 mL MeCN and was layered with 200 mL Et_2O at room temperature. The product powdered out of solution as a light green solid after three days. The solid was collected and rinsed with 50 mL Et_2O before drying under vacuum (487.2 mg, 75%). **Anal. % Calcd.** for $C_{34}H_{46}Br_2Cu_2F_6N_6O_6S_2$ (1099.79 g/mol): C, 37.13; H, 4.22; N, 7.64. Found: C, 37.12; H, 4.04; N, 7.57. **FT-IR** (ATR): 1600 (C=N) cm^{-1}. **UV-vis-NIR** (MeCN, 298 K): 238 nm, 680 nm.

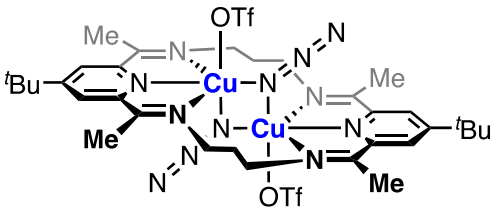

$^{3/Me}[Cu_2(N_3)_2]^{2+}$. To a 100 mL Schlenk tube, $Cu(OTf)_2$ (406.2 mg, 1.123 mmol, 2.02 equiv.) and DCM (5 mL) were added. The slurry was treated with a solution of $^{3/Me}$**[Sr]**$^{2+}$ (501.1 mg, 0.5565 mmol, 1.00 equiv.) in DCM (10 mL). No change occurred upon this addition. A solution of NBu_4N_3 (320.2 mg, 1.126 mmol, 2.02 equiv.) in DCM (10 mL) was then added. The reaction mixture immediately became dark green. Within minutes, a dark green solid precipitated from solution. The reaction was allowed to proceed for 4 hours at room temperature. To the solution, MeCN (25 mL) was added, and the dark green solution was filtered over a pad of celite. The pad was rinsed with an additional 35 mL 1:1 DCM/MeCN, and the filtrate was concentrated under vacuum. The resulting crude solid was triturated with 10 mL THF and collected via vacuum filtration. The product was washed with 3 x 10 mL THF and 50 mL Et_2O. The product was re-dissolved in *ca*. 45 mL MeCN and was layered with 200 mL Et_2O at room temperature. The product crystallized as green needles after three days. The crystals were collected and rinsed with 50 mL Et_2O before drying under vacuum (424.7 mg, 75%). Crystals suitable for single crystal X-ray crystallography were grown by vapor diffusion of Et_2O into a concentrated MeCN solution. **Anal. % Calcd.** for $C_{34}H_{46}Cu_2F_6N_{12}O_6S_2$ (1024.02 g/mol): C, 39.88; H, 4.53; N, 16.41. Found: C, 39.91; H, 4.38; N, 16.25. **FT-IR** (ATR): 2063 (N_3), 1602 (C=N) cm^{-1}. **UV-vis-NIR** (MeCN, 298 K): 227 nm, 365 nm (5.04 x 10^3 M^{-1} cm^{-1}), 661 nm (418 M^{-1} cm^{-1}).

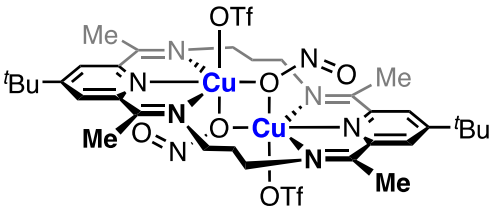

$^{3/Me}[Cu_2(ONO)_2]^{2+}$. In a glovebox, a 20 mL scintillation vial was charged with **$^{3/Me}[Cu(OTf)_2]^{2+}$** (203.9 mg, 0.1647 mmol, 1.00 equiv.), $NaNO_2$ (24.0 mg, 0.348 mmol, 2.11 equiv.) and MeCN (*ca*. 8 mL). The blue slurry was stirred for 2 h at room temperature, at which point the dark blue-green solution appeared homogeneous. The sample was removed from the glovebox and worked up under air. The crude reaction mixture was diluted with DCM (10 mL) and filtered through a pad of celite to remove insoluble materials. Solvent was then removed under vacuum. The crude dark green solid was washed with 3 x 5 mL THF. A blue crystalline solid was collected via vacuum filtration and dried under vacuum to afford the desired product (59.5 mg, 35%). Crystals suitable for single crystal X-ray crystallography were grown by vapor diffusion of Et_2O into a concentrated MeCN solution. **Anal. % Calcd.** for $C_{34}H_{46}Cu_2F_6N_8O_{10}S_2$ (1031.99 g/mol): C, 39.57; H, 4.49; N, 10.86. Found: C, 39.61; H, 4.45; N, 10.72. **FT-IR** (ATR): 1603 (C=N), 1473, 991 (NO_2) cm^{-1}. **UV-vis-NIR** (MeCN, 298 K): 231, 638 nm (248 M^{-1} cm^{-1}).

$^{3/Me}[Cu_2(O^{15}NO)_2]^{2+}$. In the glovebox, a 20 mL scintillation vial was charged with **$^{3/Me}[Cu_2(OTf)_2]^{2+}$** (207.8 mg, 0.1678 mmol, 1.00 equiv.), $Na^{15}NO_2$ (24.6 mg, 0.351 mmol, 2.09 equiv.) and MeCN (*ca*. 8 mL). The blue slurry was stirred for 2 hours at room temperature, at which point the dark blue-green solution appeared homogeneous. The sample was removed from the glovebox and worked up in air. The crude reaction mixture was diluted with DCM (10 mL) and filtered over a pad of celite to remove insoluble materials. Solvent was then removed under vacuum. The crude dark green solid was

washed with 3 x *ca*. 2 mL THF. A blue-green powder was collected via vacuum filtration and dried under vacuum to afford the desired product (136.5 mg, 79%). **FT-IR** (ATR): 1604 (C=N), 1447, 971 (NO_2) cm^{-1}.

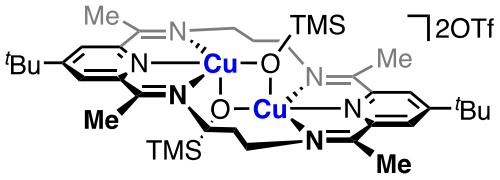

$^{3/Me}[Cu_2(OTMS)_2]^{2+}$. In the glovebox, a 20 mL scintillation vial was charged with **$^{3/Me}[Cu_2(OTf)_2]^{2+}$** (211.4 mg, 0.1707 mmol, 1.00 equiv.), *o*-DFB (*ca*. 5 mL) and MeCN (*ca*. 5 mL MeCN). The blue slurry was stirred at room temperature and treated dropwise with 1.0 M NaOTMS (0.350 mL, 0.350 mmol, 2.05 equiv.). The reaction mixture quickly became dark orange-brown and was stirred for 2 hours. The mixture was then directly filtered over a pad of celite, and the dark orange filtrate was concentrated under vacuum. The crude product was triturated with 3 x *ca*. 2-3 mL THF. The remaining dark blue-green solid was dissolved in minimal MeCN and filtered over celite. The sample was concentrated under vacuum, triturated with *ca*. 15 mL Et_2O and dried under vacuum (116.7 mg, 61%). Crystals suitable for single crystal X-ray crystallography were grown by vapor diffusion of Et_2O into a concentrated MeCN solution at -35 °C. **Anal. % Calcd.** for $C_{40}H_{64}Cu_2F_6N_6O_8S_2Si_2$ (1118.36 g/mol): C, 42.96; H, 5.77; N, 7.51. Found: C, 42.89; H, 5.57**;** N, 7.80. **FT-IR** (ATR): 1603 (C=N) cm^{-1}. **UV-vis-NIR** (MeCN, 298 K): 229 nm (5.51 x 10^4 M^{-1} cm^{-1}), 481 nm (382 M^{-1} cm^{-1}).

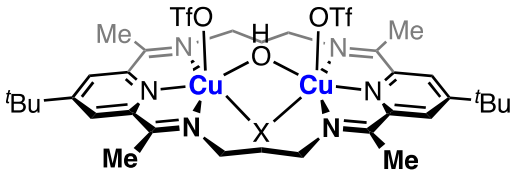

X = κ^2-OTf

$^{3/Me}$[Cu$_2$OH]$^{3+}$. In the glovebox, a 20 mL scintillation vial was charged with $^{3/Me}$**[Cu$_2$(OTf)$_2$]$^{2+}$** (208.1 mg, 0.1681 mmol, 1.00 Eq.), LiOH (4.0 mg, 0.17 mmol, 0.99 Eq.) and MeCN (*ca*. 8 mL). The blue slurry was stirred at room temperature for 2 hours, at which point the dark blue solution appeared homogeneous. The sample was removed from the glovebox and worked up in air. Solvent was removed under vacuum. The product was extracted in *ca*. 5 mL DCM and filtered over celite to remove insoluble materials. The dark blue filtrate was layered with *ca*. 15 mL hexanes. After one day, a blue crystalline solid was isolated and dried under vacuum (134.8 mg, 73%). Crystals suitable for single crystal X-ray crystallography were grown by vapor diffusion of Et_2O into a concentrated THF solution.

2.5.3 NMR Spectra

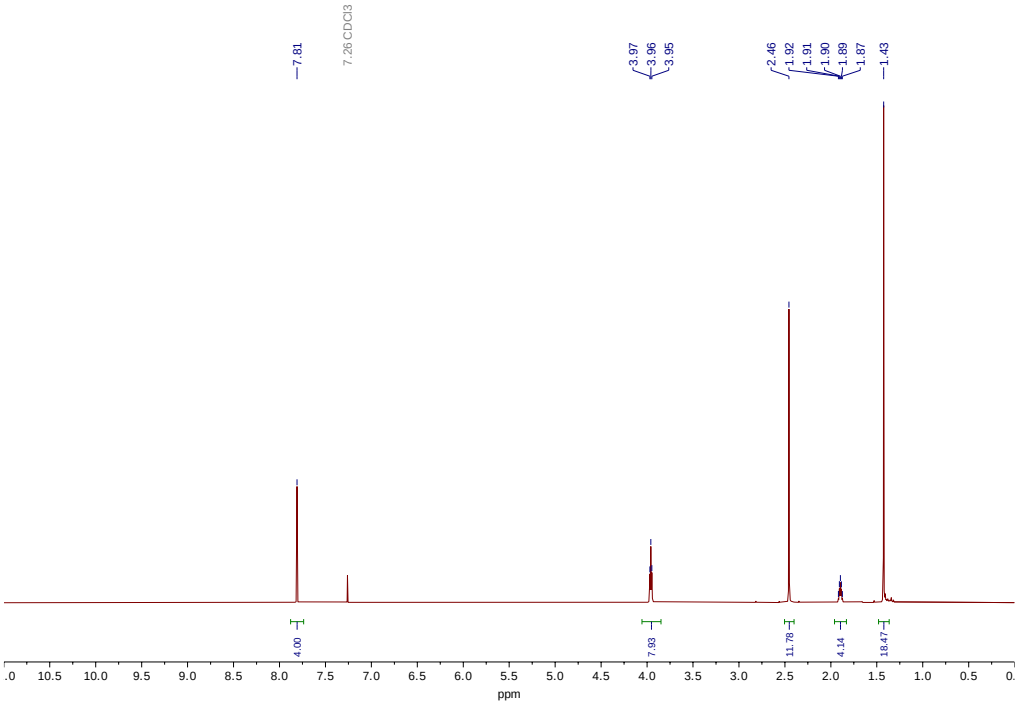

Figure 2.19 ^{1}H NMR spectrum of $^{3/Me}$**[Sr]**$^{2+}$ in $CDCl_3$.

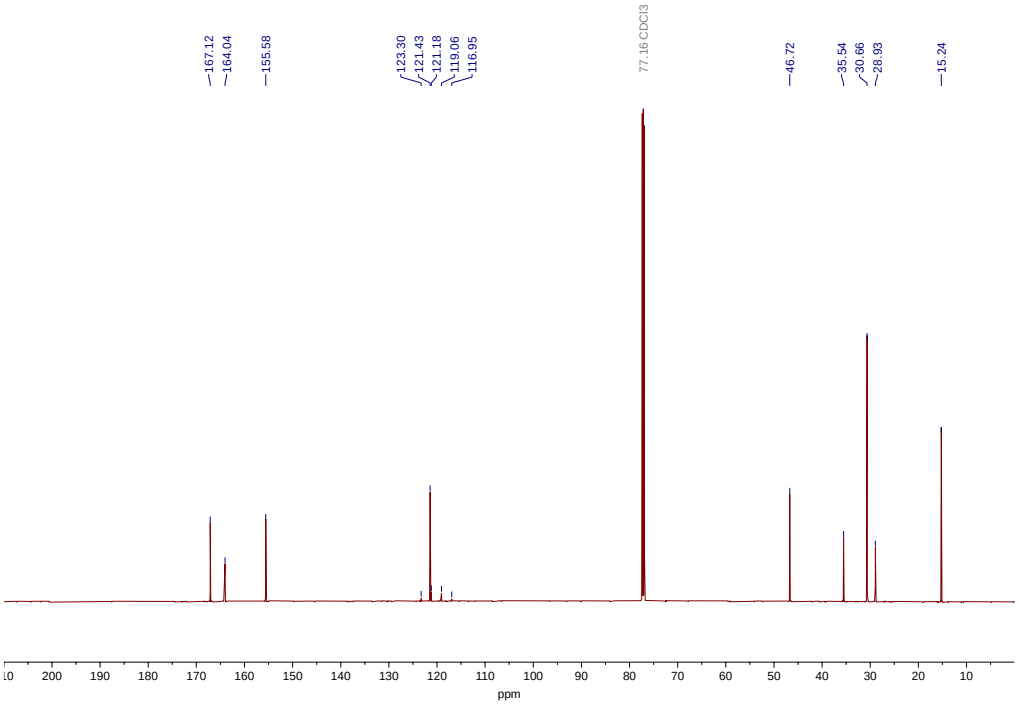

Figure 2.20 ^{13}C{^{1}H} NMR spectrum of $^{3/Me}$**[Sr]**$^{2+}$ in $CDCl_3$.

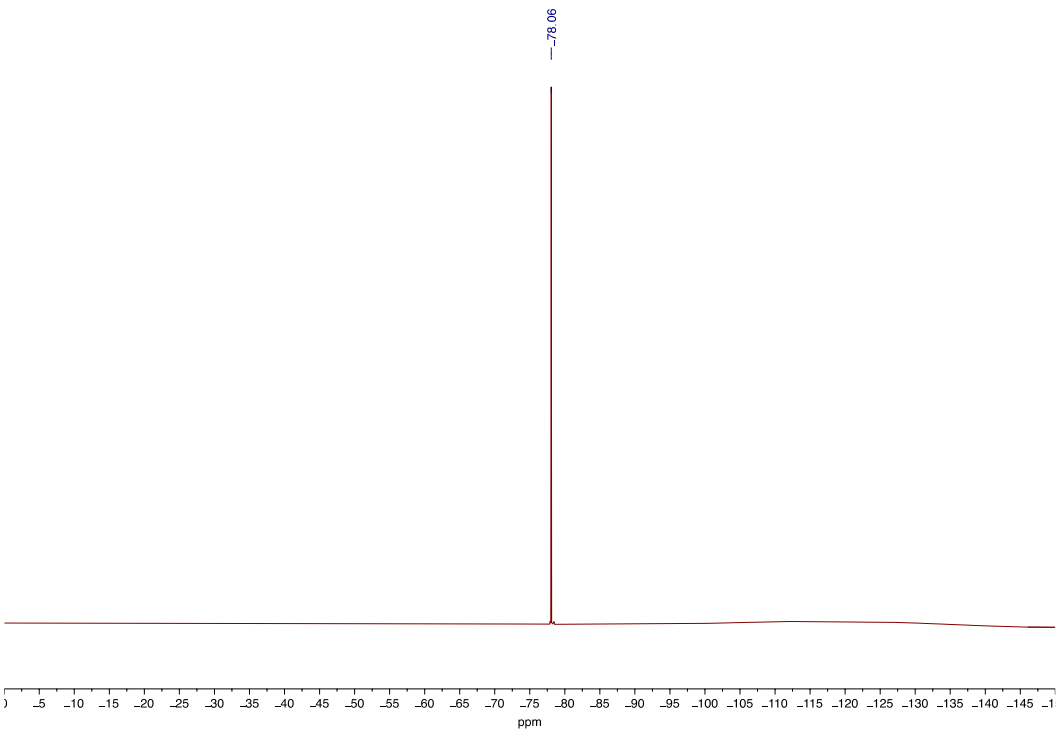

Figure 2.21 $^{19}F\{^{1}H\}$ NMR spectrum of $^{3/Me}$**[Sr]**$^{2+}$ in $CDCl_3$.

2.5.4 Infrared Spectra

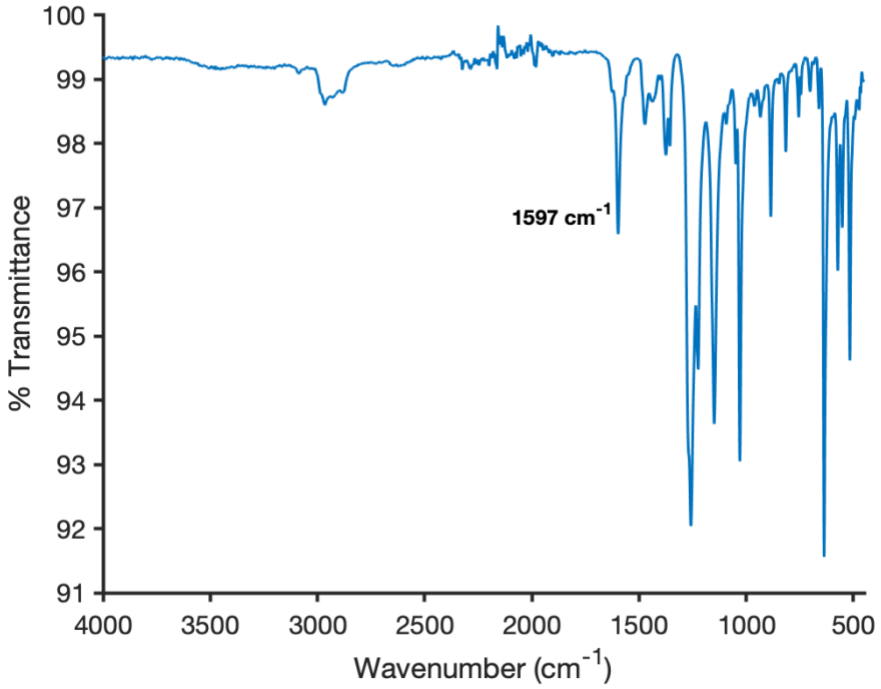

Figure 2.22 Infrared spectrum of $^{3/Me}[Cu_2Cl_2]^{2+}$.

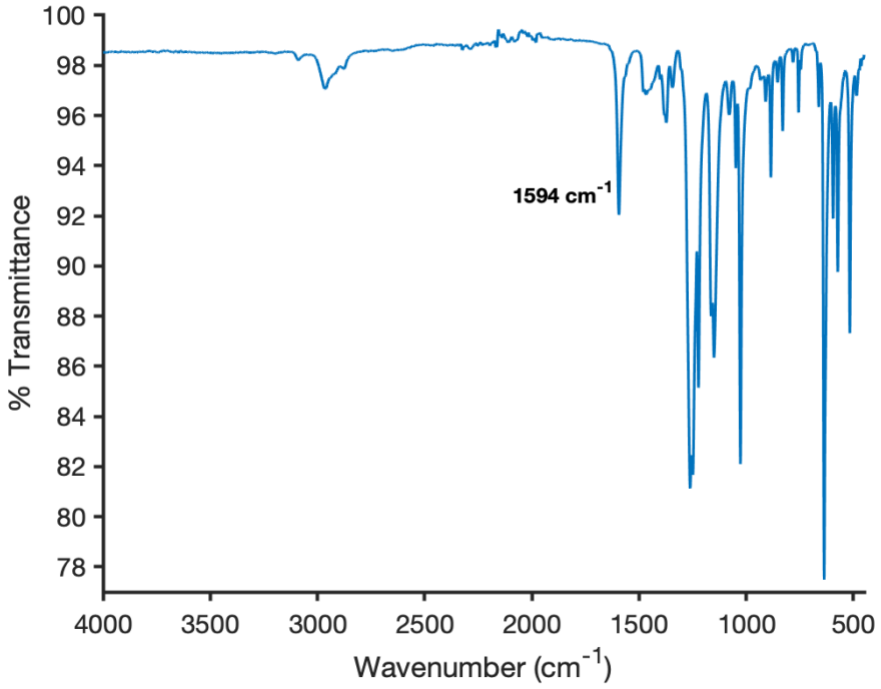

Figure 2.23 Infrared spectrum of $^{2/Me}[Cu_2Cl_2]^{2+}$.

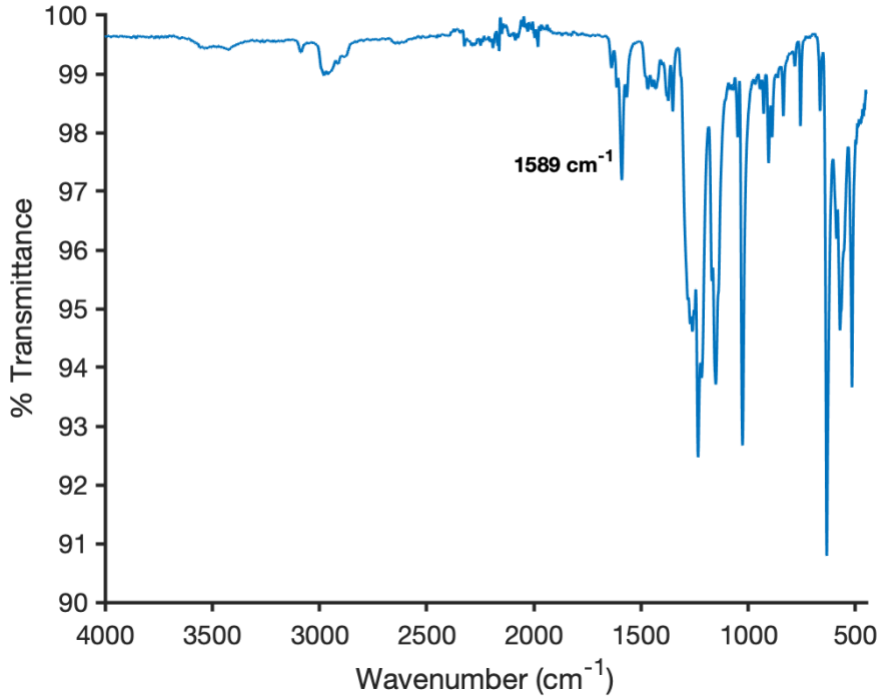

Figure 2.24 Infrared spectrum of $^{3/Me}[Cu_2F]^{3+}$.

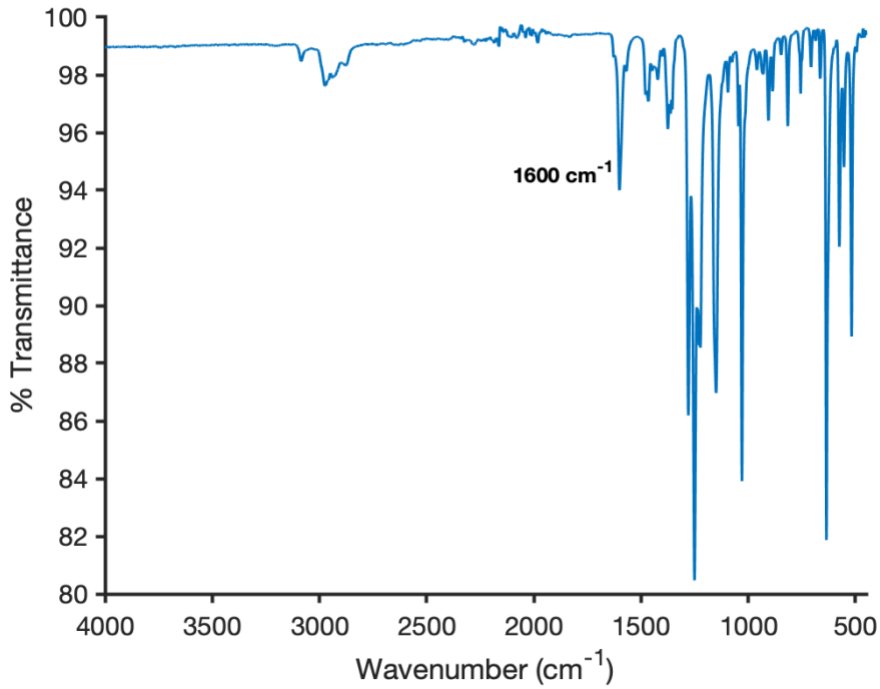

Figure 2.25 Infrared spectrum of $^{3/Me}[Cu_2Br_2]^{2+}$.

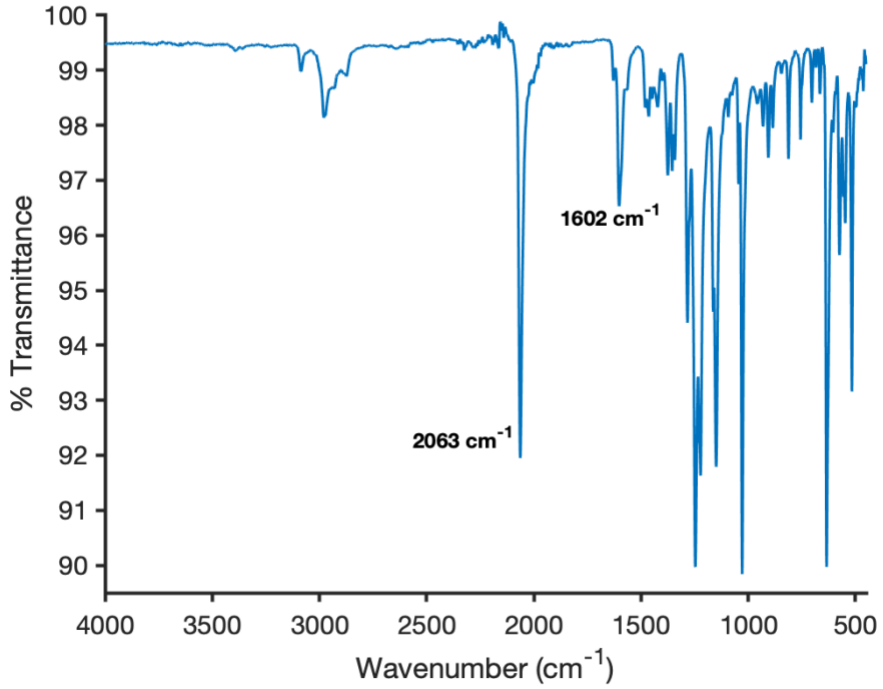

Figure 2.26 Infrared spectrum of $^{3/Me}[Cu_2(N_3)_2]^{2+}$.

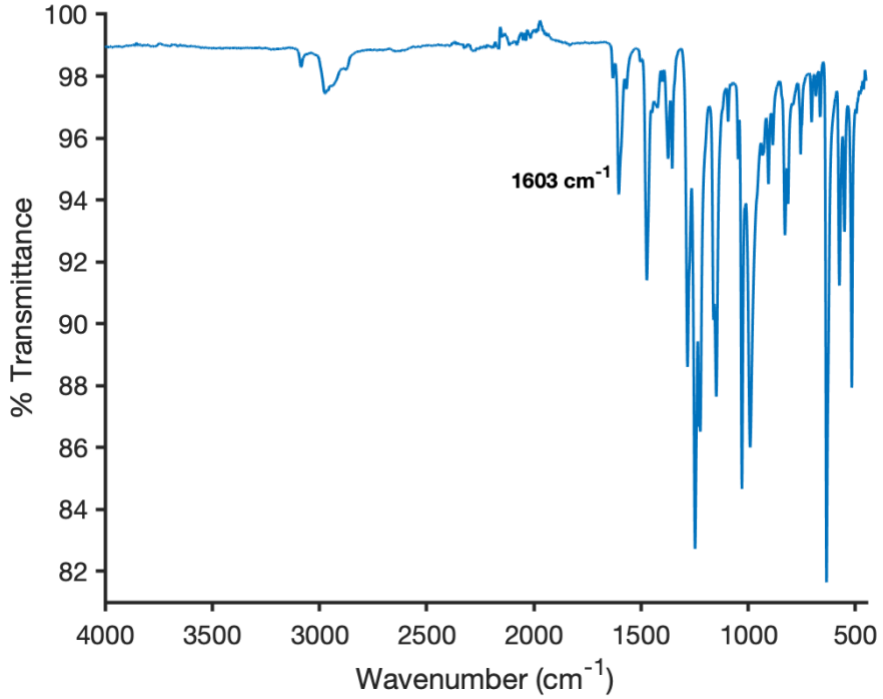

Figure 2.27 Infrared spectrum of $^{3/Me}[Cu_2(ONO)_2]^{2+}$.

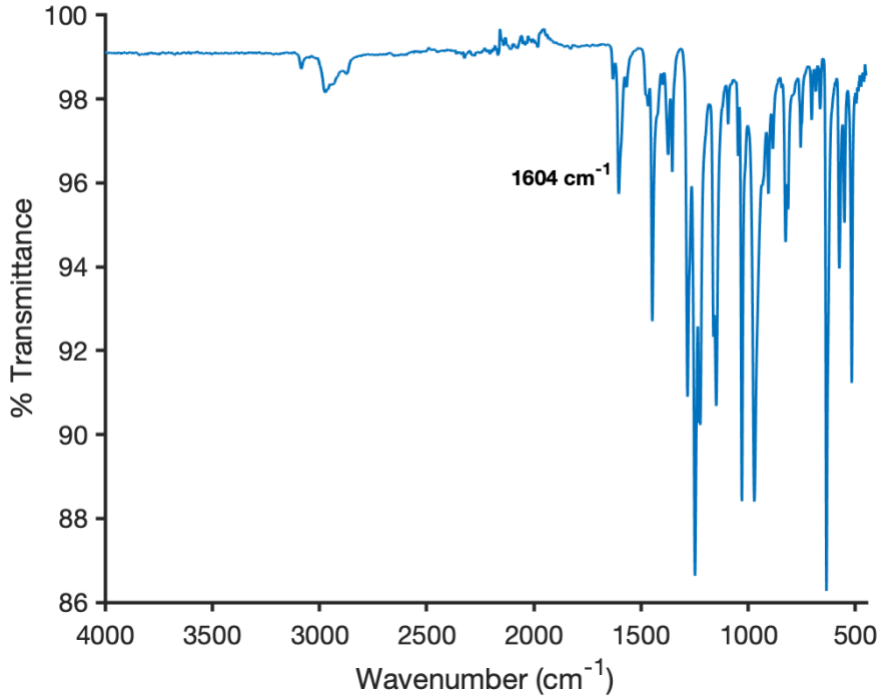

Figure 2.28 Infrared spectrum of $^{3/Me}[Cu_2(O^{15}NO)_2]^{2+}$.

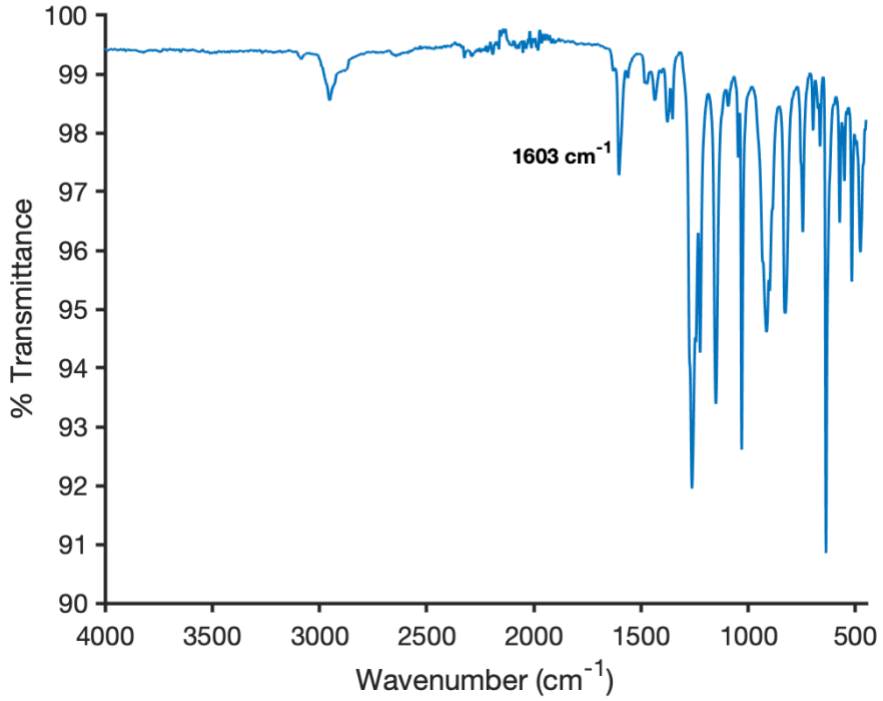

Figure 2.29 Infrared spectrum of $^{3/Me}[Cu_2(OTMS)_2]^{2+}$.

2.5.5 UV-vis-NIR Spectra

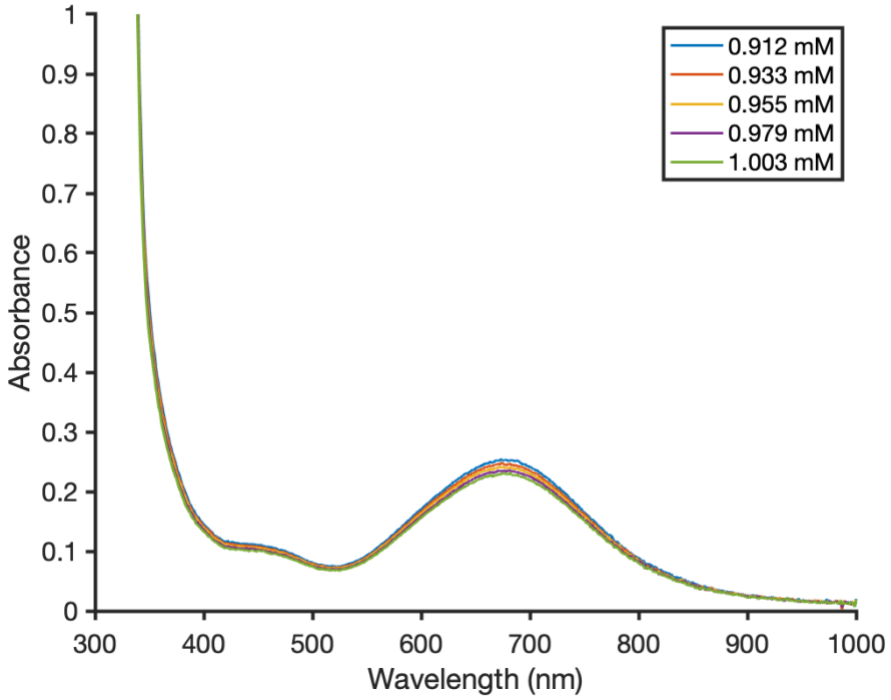

Figure 2.30 Beer's law analysis of $^{3/Me}[Cu_2Cl_2]^{2+}$ at 676 nm.

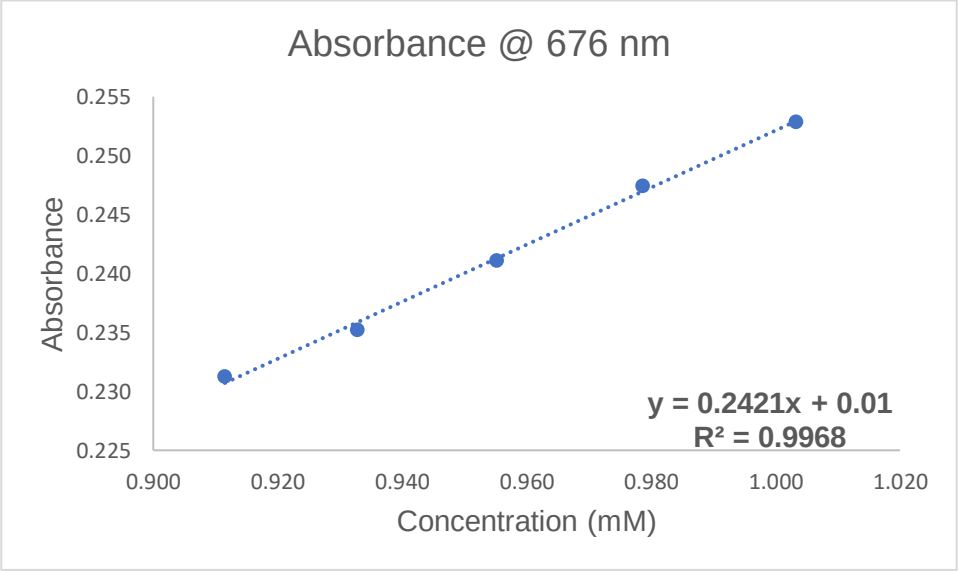

Figure 2.31 Linear fit of $^{3/Me}[Cu_2Cl_2]^{2+}$ absorbance data at 676 nm.

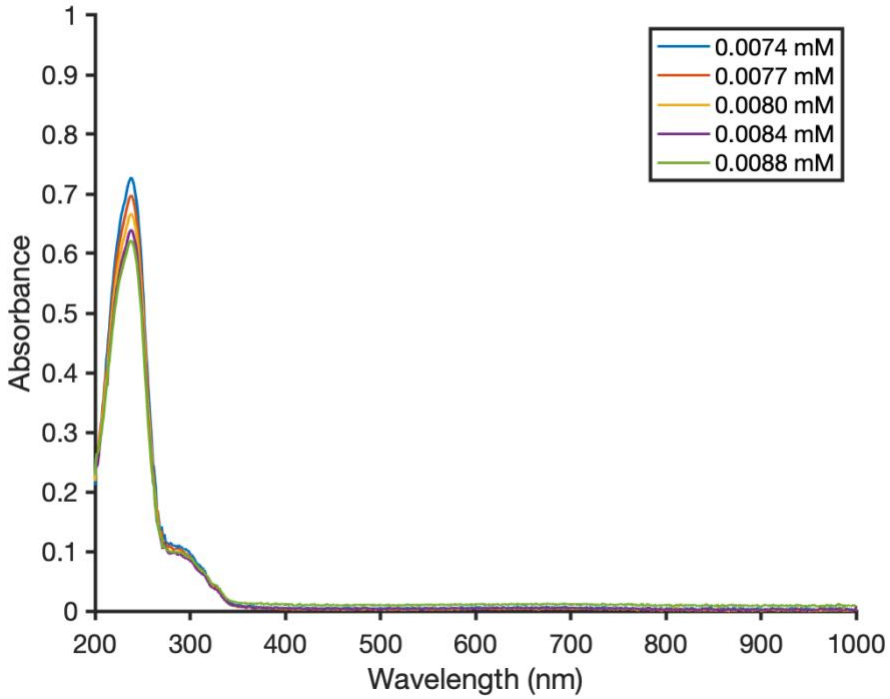

Figure 2.32 Beer's law analysis of $^{3/Me}[Cu_2Cl_2]^{2+}$ at 238 nm.

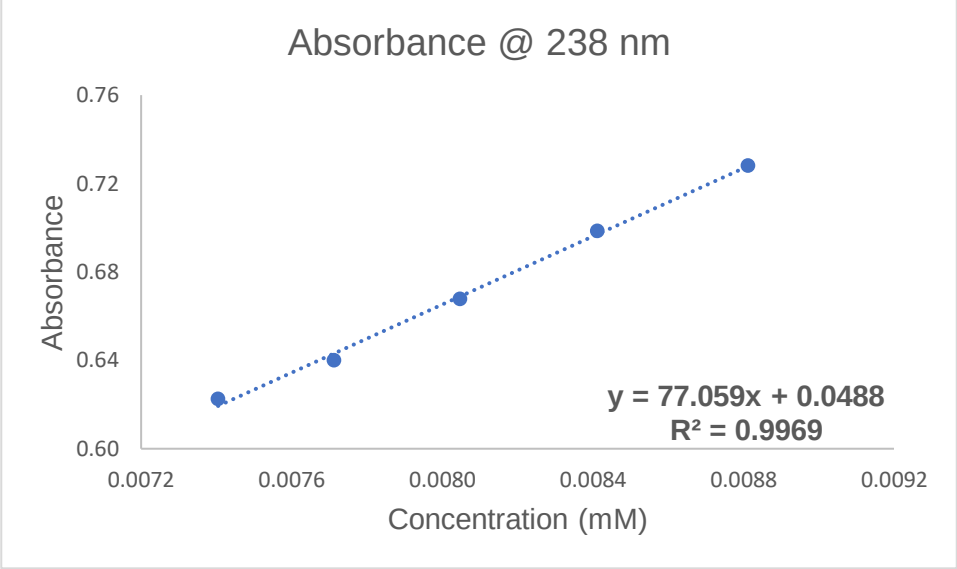

Figure 2.33 Linear fit of $^{3/Me}[Cu_2Cl_2]^{2+}$ absorbance data at 238 nm.

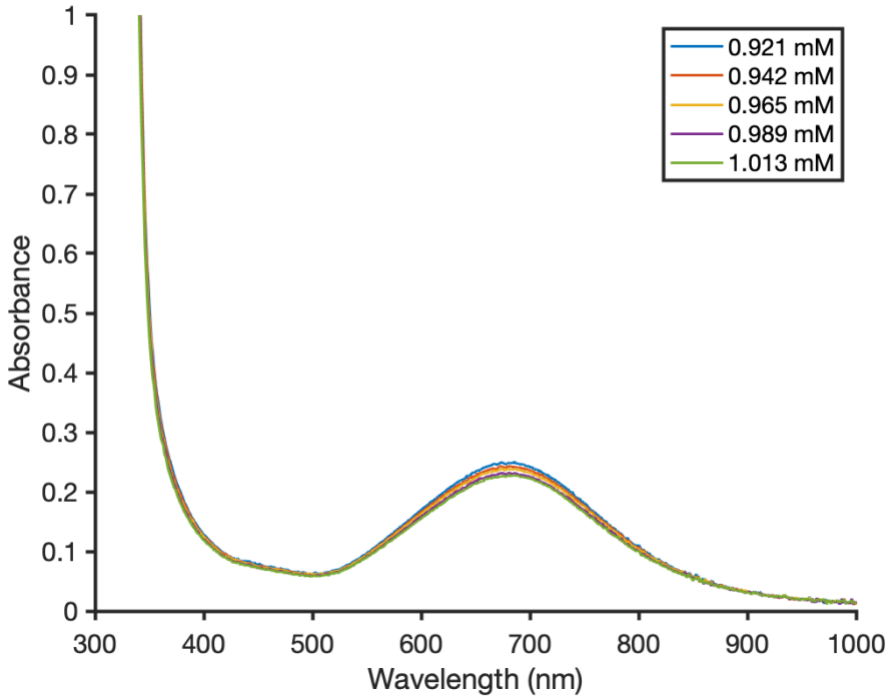

Figure 2.34 Beer's law analysis of $^{2/Me}[Cu_2Cl_2]^{2+}$ at 681 nm.

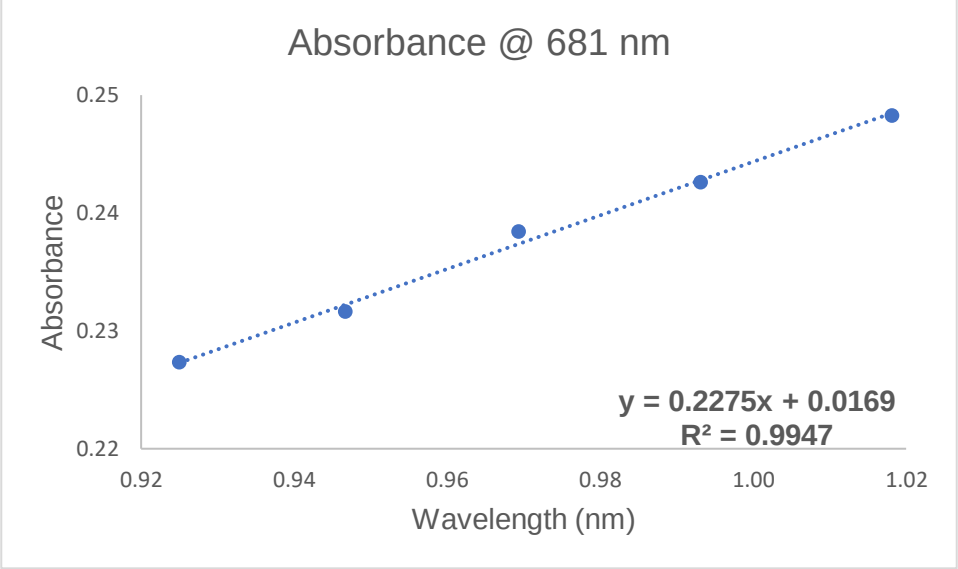

Figure 2.35 Linear fit of $^{3/Me}[Cu_2Cl_2]^{2+}$ absorbance data at 681 nm.

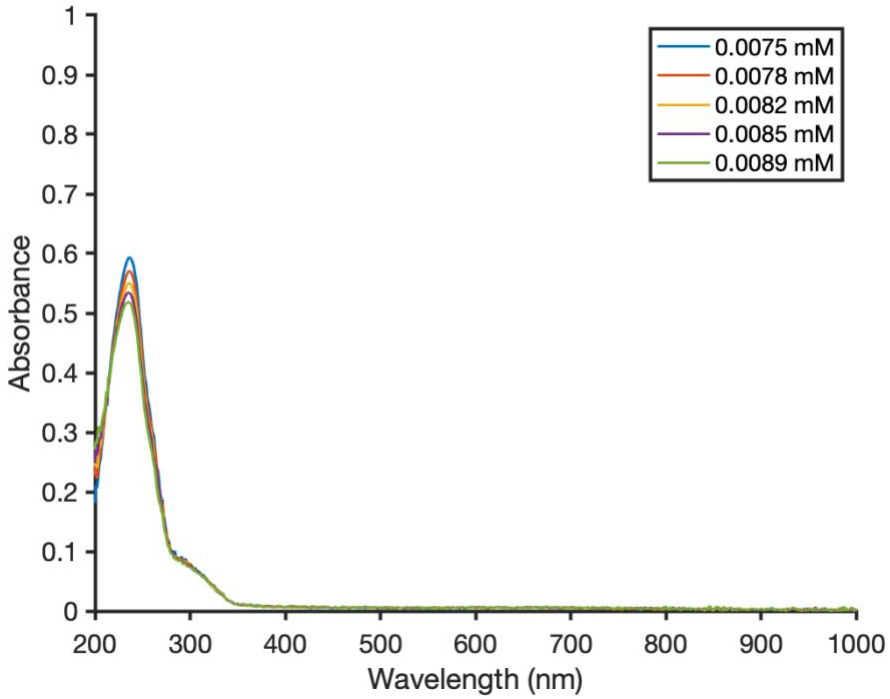

Figure 2.36 Beer's law analysis of $^{2/Me}[Cu_2Cl_2]^{2+}$ at 236 nm.

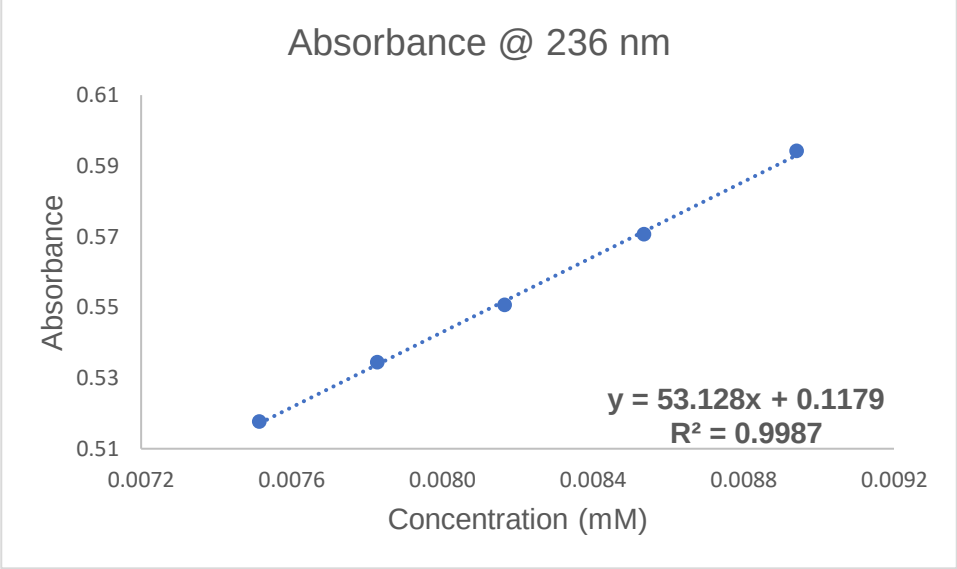

Figure 2.37 Linear fit of $^{2/Me}[Cu_2Cl_2]^{2+}$ at 236 nm.

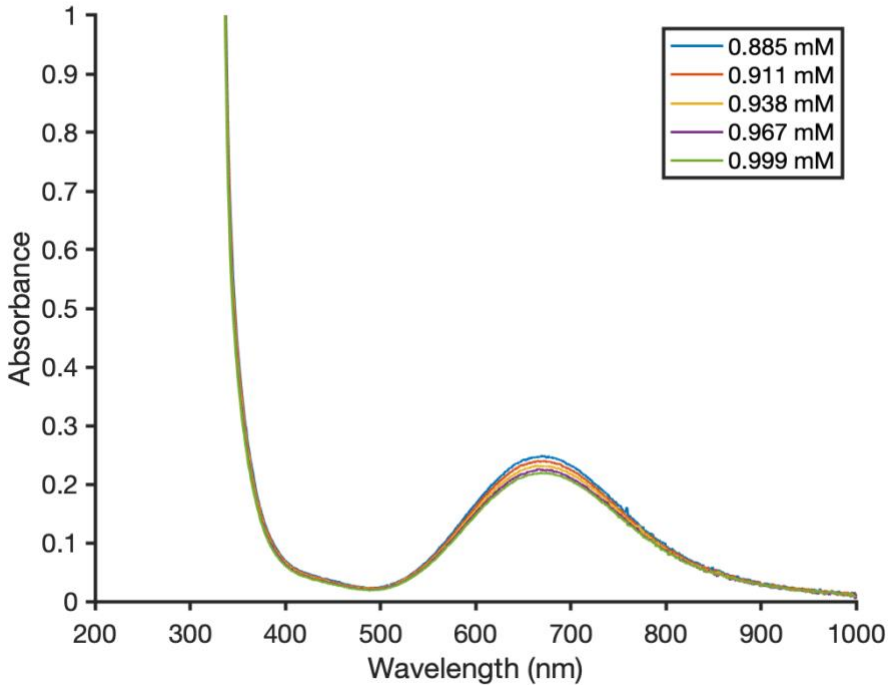

Figure 2.38 Beer's law analysis of $^{3/Me}[Cu_2F]^{3+}$ at 667 nm.

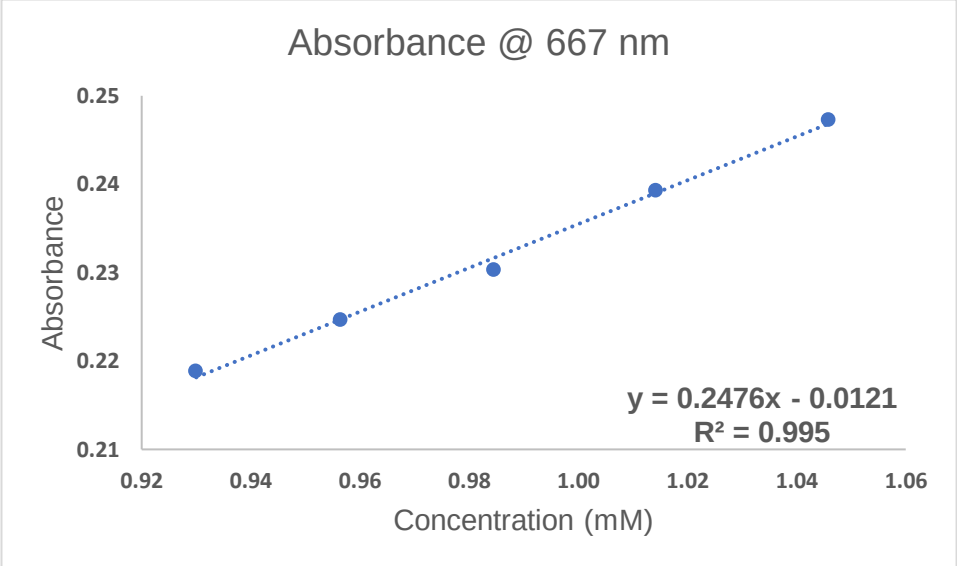

Figure 2.39 Linear fit of $^{3/Me}[Cu_2F]^{3+}$ absorbance data at 667 nm.

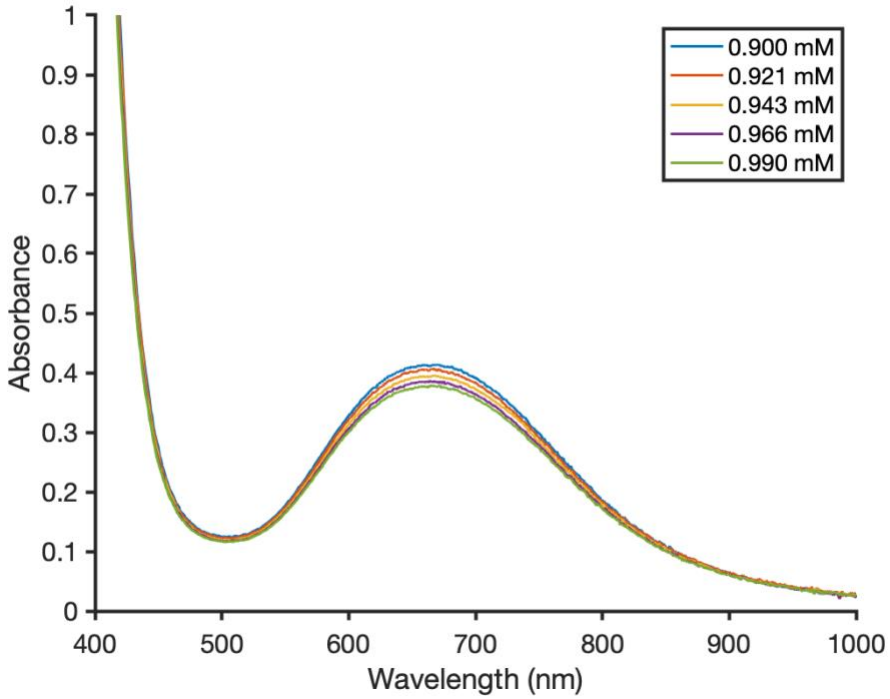

Figure 2.40 Beer's law analysis of $^{3/Me}[Cu_2(N_3)_2]^{2+}$ at 661 nm.

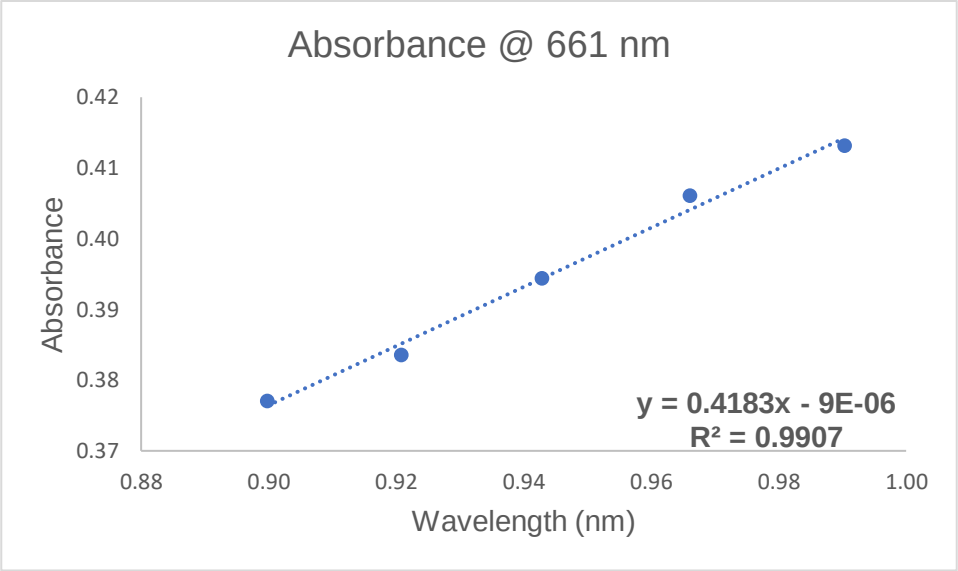

Figure 2.41 Linear fit of $^{3/Me}[Cu_2(N_3)_2]^{2+}$ absorbance data at 661 nm.

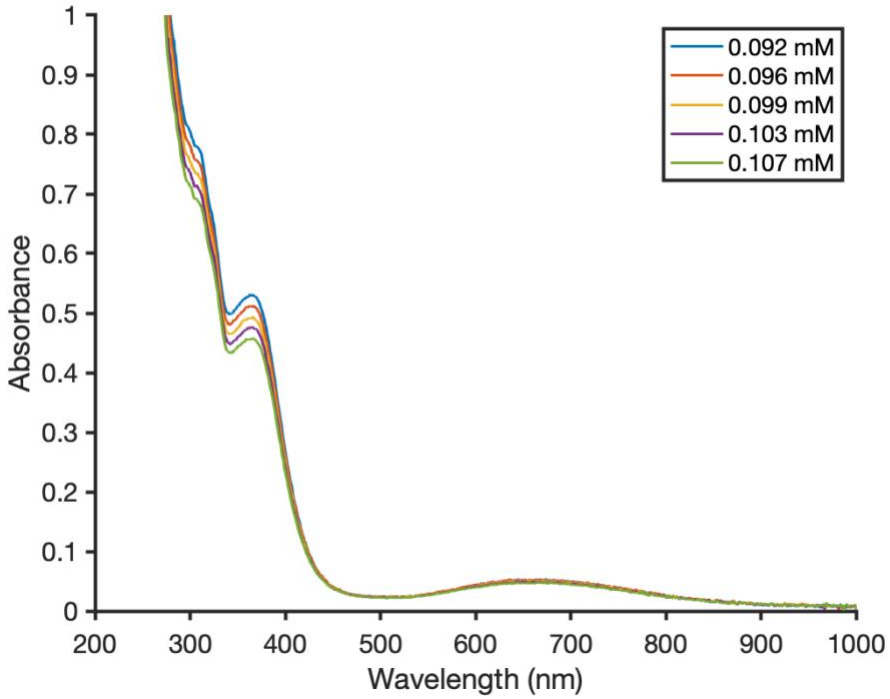

Figure 2.42 Beer's law analysis of $^{3/Me}[Cu_2(N_3)_2]^{2+}$ at 365 nm.

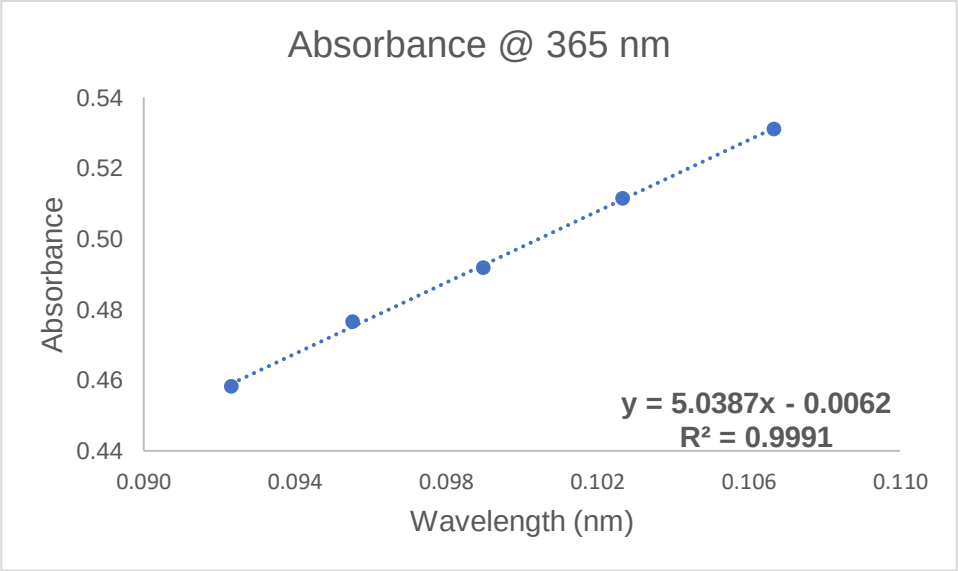

Figure 2.43 Linear fit of $^{3/Me}[Cu_2(N_3)_2]^{2+}$ absorbance data at 365 nm.

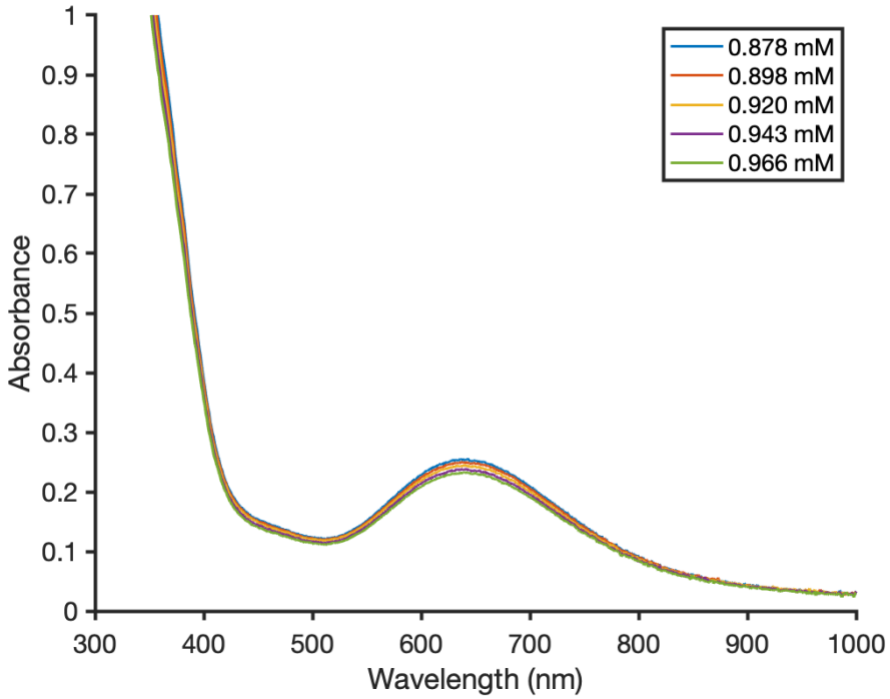

Figure 2.44 Beer's law analysis of $^{3/Me}[Cu_2(ONO)_2]^{2+}$ at 638 nm.

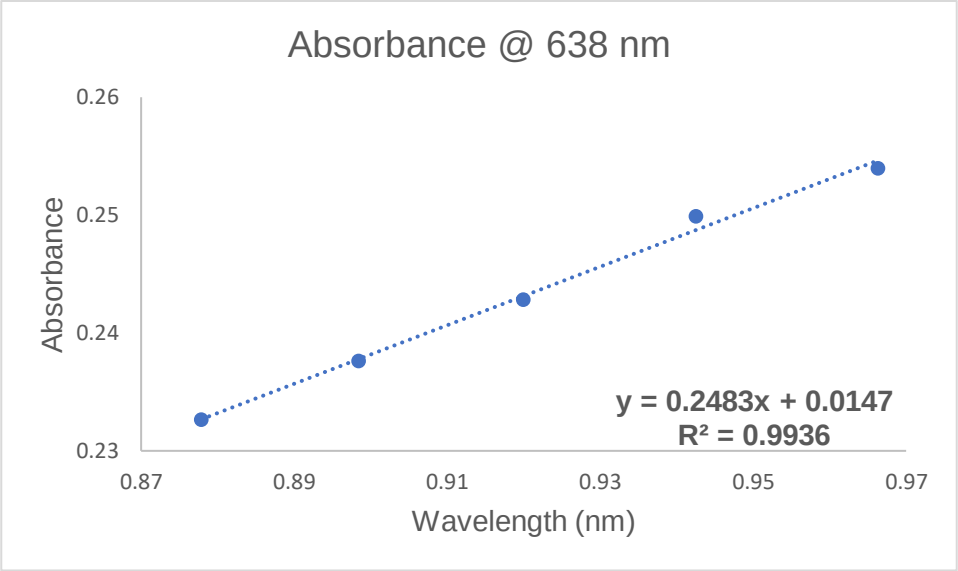

Figure 2.45 Linear fit of $^{3/Me}[Cu_2(ONO)_2]^{2+}$ absorbance data at 638 nm.

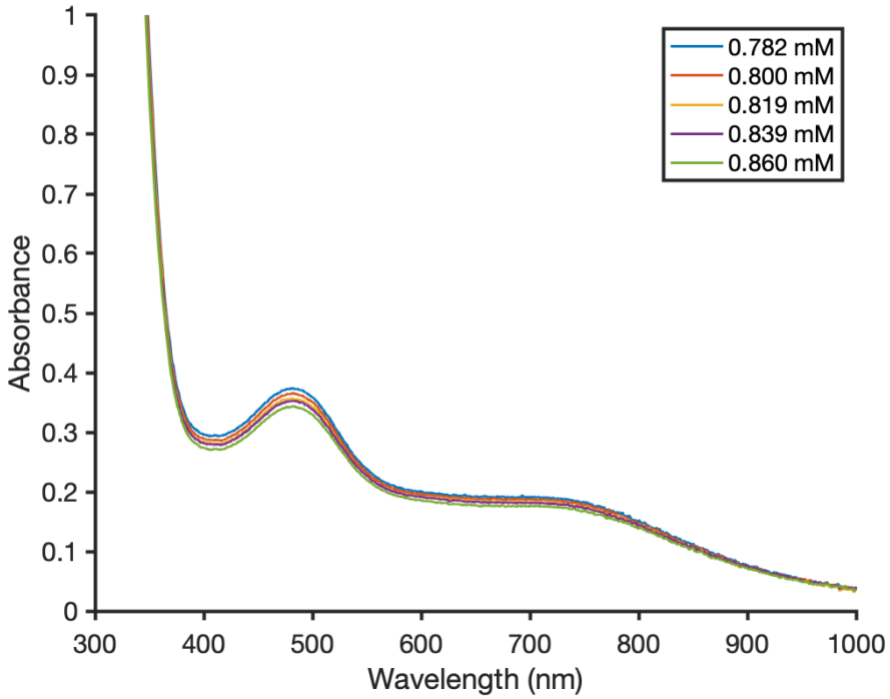

Figure 2.46 Beer's law analysis of $^{3/Me}[Cu_2(OTMS)_2]^{2+}$ at 481 nm.

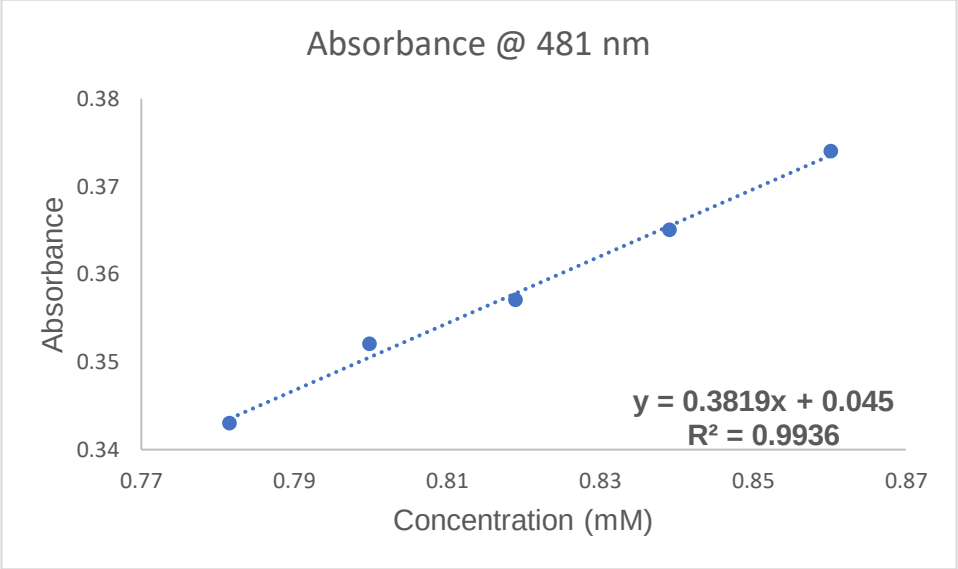

Figure 2.47 Linear fit of $^{3/Me}[Cu_2(OTMS)_2]^{2+}$ absorbance data at 481 nm.

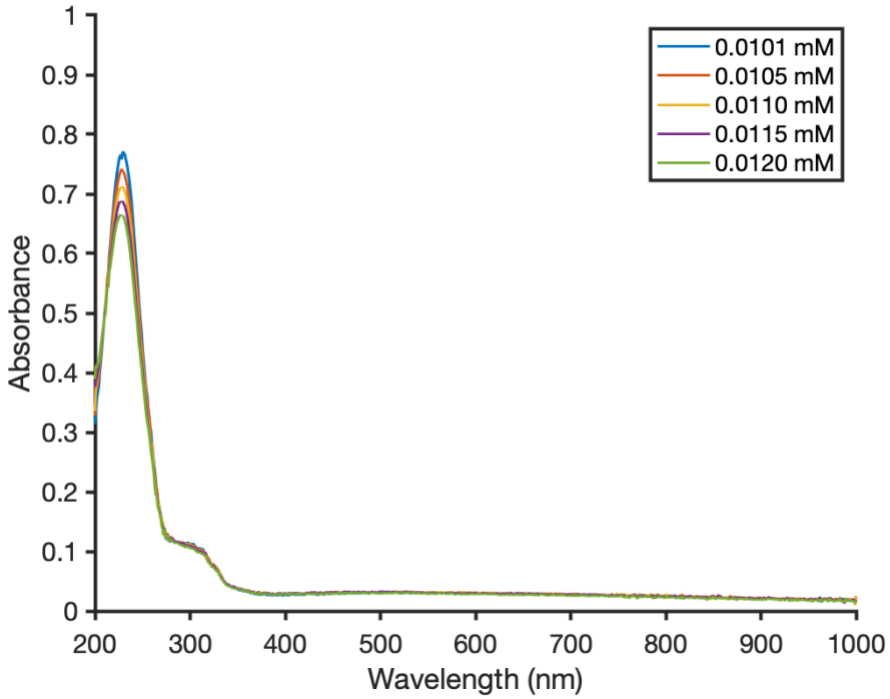

Figure 2.48 Beer's law analysis of $^{3/Me}[Cu_2(OTMS)_2]^{2+}$ at 229 nm.

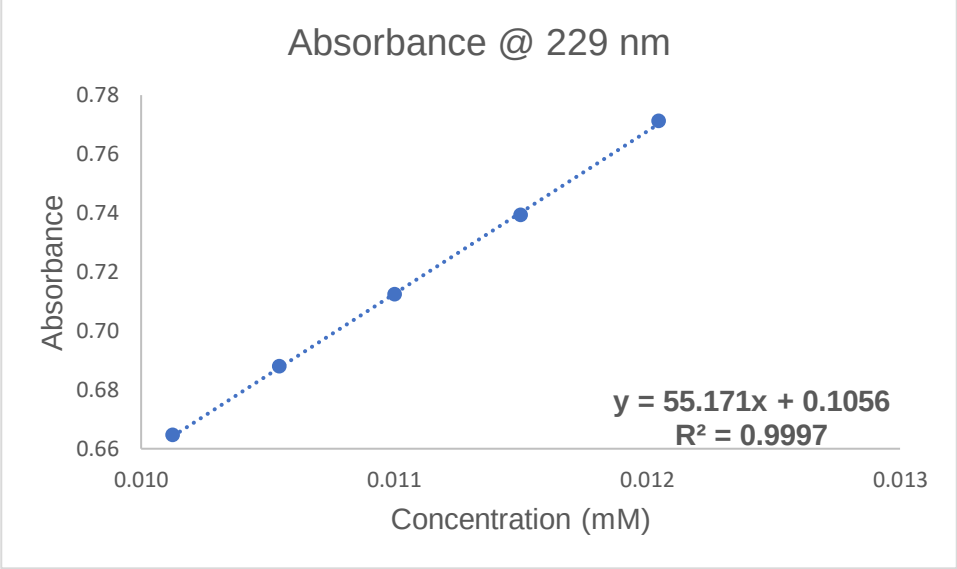

Figure 2.49 Linear fit of $^{3/Me}[Cu_2(OTMS)_2]^{2+}$ absorbance data at 229 nm.

2.5.6 X-ray Crystallography

Table 2.4 Summary of structure determination of $^{3/Me}[Cu_2Cl_2]^{2+}$.

Empirical formula	$C_{34}H_{46}Cl_2Cu_2F_6N_6O_6S_2$
Formula weight	1010.87
Temperature/K	100
Crystal system	monoclinic
Space group	$P2_1/c$
a	12.5444(7)Å
b	15.9671(9)Å
c	11.8223(7)Å
β	117.009(2)°
Volume	2109.7(2)Å^3
Z	2
d_{calc}	1.591 g/cm^3
μ	1.310 mm^{-1}
F(000)	1036.0
Crystal size, mm	0.3 × 0.2 × 0.02
2θ range for data collection	6.272 - 55.24°
Index ranges	-16 ≤ h ≤ 16, -20 ≤ k ≤ 20, -15 ≤ l ≤ 15
Reflections collected	51161
Independent reflections	4881[R(int) = 0.0957]
Data/restraints/parameters	4881/84/339
Goodness-of-fit on F^2	1.051
Final R indexes [I>=2σ (I)]	R_1 = 0.0728, wR_2 = 0.1776
Final R indexes [all data]	R_1 = 0.0970, wR_2 = 0.1998
Largest diff. peak/hole	1.03/-1.28 eÅ^{-3}

Table 2.5 Summary of structure determination of $^{2/Me}[Cu_2Cl_2]^{2+}$.

Empirical formula	$C_{36}H_{48}Cl_2Cu_2F_6N_8O_6S_2$
Formula weight	1064.92
Temperature/K	100
Crystal system	triclinic
Space group	$P\bar{1}$
a	12.6430(12)Å
b	13.7270(13)Å
c	28.579(3)Å
α	79.827(3)°
β	82.354(3)°
γ	68.329(3)°
Volume	4524.4(7)Å^3
Z	4
d_{calc}	1.563 g/cm^3
μ	1.228 mm^{-1}
F(000)	2184.0
Crystal size, mm	0.38 × 0.32 × 0.25
2θ range for data collection	5.772 - 55.138°
Index ranges	-16 ≤ h ≤ 16, -17 ≤ k ≤ 17, -37 ≤ l ≤ 37
Reflections collected	108801
Independent reflections	20849[R(int) = 0.0472]
Data/restraints/parameters	20849/0/1142
Goodness-of-fit on F^2	1.023
Final R indexes [I>=2σ (I)]	R_1 = 0.0664, wR_2 = 0.2072
Final R indexes [all data]	R_1 = 0.0739, wR_2 = 0.2203
Largest diff. peak/hole	1.15/-0.69 eÅ^{-3}

Table 2.6 Summary of structure determination of $^{3/Me}[Cu_2(NCMe)_2]^{4+}$.

Empirical formula	$C_{44}H_{58}Cu_2F_{12}N_{10}O_{12}S_4$
Formula weight	1402.32
Temperature/K	100
Crystal system	triclinic
Space group	$P\bar{1}$
a	9.5549(3)Å
b	12.0215(4)Å
c	13.3759(4)Å
α	103.747(2)°
β	105.331(3)°
γ	91.855(2)°
Volume	1431.84(8)Å^3
Z	1
d_{calc}	1.626 g/cm^3
μ	3.224 mm^{-1}
F(000)	718.0
Crystal size, mm	0.11 × 0.04 × 0.03
2θ range for data collection	7.088 - 148.932°
Index ranges	-11 ≤ h ≤ 11, -12 ≤ k ≤ 15, -16 ≤ l ≤ 16
Reflections collected	18204
Independent reflections	5765[R(int) = 0.0476]
Data/restraints/parameters	5765/0/386
Goodness-of-fit on F^2	1.074
Final R indexes [I>=2σ (I)]	R_1 = 0.0520, wR_2 = 0.1434
Final R indexes [all data]	R_1 = 0.0628, wR_2 = 0.1567
Largest diff. peak/hole	0.66/-0.85 eÅ^{-3}

Table 2.7 Summary of structure determination of $^{3/Me}[Cu_2Cl]^{3+}$.

Empirical formula	$C_{35}H_{46}ClCu_2F_9N_6O_9S_3$
Formula weight	1124.49
Temperature/K	100
Crystal system	monoclinic
Space group	$P2_1/n$
a	15.4647(5)Å
b	11.5756(4)Å
c	25.5577(6)Å
β	96.493(3)°
Volume	4545.8(2)Å^3
Z	4
d_{calc}	1.643 g/cm^3
μ	1.227 mm^{-1}
F(000)	2296.0
Crystal size, mm	0.46 × 0.16 × 0.06
2θ range for data collection	4.584 - 56.564°
Index ranges	-20 ≤ h ≤ 20, -15 ≤ k ≤ 15, -32 ≤ l ≤ 34
Reflections collected	79844
Independent reflections	11270[R(int) = 0.0508]
Data/restraints/parameters	11270/216/651
Goodness-of-fit on F^2	1.033
Final R indexes [I>=2σ (I)]	R_1 = 0.0485, wR_2 = 0.1237
Final R indexes [all data]	R_1 = 0.0618, wR_2 = 0.1309
Largest diff. peak/hole	1.53/-0.75 eÅ^{-3}

Table 2.8 Summary of structure determination of $^{3/Me}[Cu_2F]^{3+}$.

Empirical formula	$C_{35}H_{46}Cu_2F_{10}N_6O_9S_3$
Formula weight	1108.04
Temperature/K	100
Crystal system	monoclinic
Space group	P2/c
a	13.7556(5)Å
b	9.1159(3)Å
c	17.8988(6)Å
β	103.059(4)°
Volume	2186.37(13)Å^3
Z	2
d_{calc}	1.683 g/cm^3
μ	1.218 mm^{-1}
F(000)	1132.0
Crystal size, mm	0.44 × 0.14 × 0.08
2θ range for data collection	4.672 - 56.564°
Index ranges	-18 ≤ h ≤ 17, -10 ≤ k ≤ 12, -23 ≤ l ≤ 23
Reflections collected	42756
Independent reflections	5424[R(int) = 0.0553]
Data/restraints/parameters	5424/0/336
Goodness-of-fit on F^2	1.035
Final R indexes [I>=2σ (I)]	R_1 = 0.0430, wR_2 = 0.1037
Final R indexes [all data]	R_1 = 0.0510, wR_2 = 0.1077
Largest diff. peak/hole	1.88/-1.11 eÅ^{-3}

Table 2.9 Summary of structure determination of $^{3/Me}[Cu_2(N_3)_2]^{2+}$.

Empirical formula	$C_{34}H_{46}Cu_2F_6N_{12}O_6S_2$
Formula weight	1024.03
Temperature/K	100
Crystal system	monoclinic
Space group	$P2_1/c$
a	7.6454(2)Å
b	12.0716(2)Å
c	23.2817(5)Å
β	94.729(2)°
Volume	2141.41(8)Å^3
Z	2
d_{calc}	1.588 g/cm^3
μ	1.175 mm^{-1}
F(000)	1052.0
Crystal size, mm	0.18 × 0.17 × 0.12
2θ range for data collection	3.804 - 56.562°
Index ranges	-10 ≤ h ≤ 9, -16 ≤ k ≤ 16, -31 ≤ l ≤ 31
Reflections collected	42276
Independent reflections	5301[R(int) = 0.0338]
Data/restraints/parameters	5301/0/285
Goodness-of-fit on F^2	1.042
Final R indexes [I>=2σ (I)]	R_1 = 0.0236, wR_2 = 0.0610
Final R indexes [all data]	R_1 = 0.0262, wR_2 = 0.0621
Largest diff. peak/hole	0.42/-0.32 eÅ^{-3}

Table 2.10 Summary of structure determination of $^{3/Me}[Cu_2(ONO)_2]^{2+}$

Empirical formula	$C_{34}H_{46}Cu_2F_6N_8O_{10}S_2$
Formula weight	1031.99
Temperature/K	100
Crystal system	monoclinic
Space group	$P2_1/c$
a	8.1673(3)Å
b	11.6841(4)Å
c	23.3957(7)Å
β	98.843(3)°
Volume	2206.06(13)Å^3
Z	2
d_{calc}	1.554 g/cm^3
μ	1.145 mm^{-1}
F(000)	1060.0
Crystal size, mm	0.26 × 0.16 × 0.09
2θ range for data collection	4.958 - 56.56°
Index ranges	-10 ≤ h ≤ 10, -15 ≤ k ≤ 15, -31 ≤ l ≤ 30
Reflections collected	40925
Independent reflections	5463[R(int) = 0.0814]
Data/restraints/parameters	5463/18/294
Goodness-of-fit on F^2	1.066
Final R indexes [I>=2σ (I)]	R_1 = 0.0304, wR_2 = 0.0745
Final R indexes [all data]	R_1 = 0.0373, wR_2 = 0.0772
Largest diff. peak/hole	0.45/-0.45 eÅ^{-3}

Table 2.11 Summary of structure determination of $^{3/Me}[Cu_2(OTMS)_2]^{2+}$/

Empirical formula	$C_{20}H_{32}CuF_3N_3O_4SSi$
Formula weight	559.17
Temperature/K	100
Crystal system	monoclinic
Space group	$P2_1/n$
a	13.8850(14)Å
b	13.0849(13)Å
c	15.4405(15)Å
β	114.690(2)°
Volume	2548.8(4)Å^3
Z	4
d_{calc}	1.457 g/cm^3
μ	1.038 mm^{-1}
F(000)	1164.0
Crystal size, mm	0.3 × 0.25 × 0.2
2θ range for data collection	4.484 - 55.018°
Index ranges	-18 ≤ h ≤ 17, -16 ≤ k ≤ 17, -20 ≤ l ≤ 20
Reflections collected	46045
Independent reflections	5846[R(int) = 0.0188]
Data/restraints/parameters	5846/18/306
Goodness-of-fit on F^2	1.039
Final R indexes [I>=2σ (I)]	R_1 = 0.0373, wR_2 = 0.0967
Final R indexes [all data]	R_1 = 0.0405, wR_2 = 0.0995
Largest diff. peak/hole	1.32/-1.22 eÅ^{-3}

Table 2.12 Summary of structure determination of $^{3/Me}[Cu_2OH]^{3+}$.

Empirical formula	$C_{39}H_{55}Cu_2F_9N_6O_{11}S_3$
Formula weight	1178.15
Temperature/K	100
Crystal system	triclinic
Space group	$P\bar{1}$
a	12.1466(12)Å
b	14.6587(16)Å
c	14.8914(16)Å
α	67.013(4)°
β	81.872(4)°
γ	83.338(4)°
Volume	2411.0(4)Å^3
Z	2
d_{calc}	1.623 g/cm^3
μ	1.110 mm^{-1}
F(000)	1212.0
Crystal size, mm	0.41 × 0.33 × 0.05
2θ range for data collection	5.976 - 55.158°
Index ranges	-15 ≤ h ≤ 15, -19 ≤ k ≤ 19, -19 ≤ l ≤ 19
Reflections collected	67617
Independent reflections	11091[R(int) = 0.0686]
Data/restraints/parameters	11091/259/753
Goodness-of-fit on F^2	1.127
Final R indexes [I>=2σ (I)]	R_1 = 0.0564, wR_2 = 0.0903
Final R indexes [all data]	R_1 = 0.0800, wR_2 = 0.0977
Largest diff. peak/hole	0.94/-0.59 eÅ^{-3}

CHAPTER 3 : *BIS*(PYRIDYLDIIMINE) MACROCYCLIC LIGAND DEVELOPMENT

3.1 Introduction

Pyridyldiimine (PDI) ligands are versatile molecules used in synthetic and catalytic applications.[76,77] Known initially for influencing the catalytic activity of iron and cobalt toward the polymerization of ethylene,[78,79] PDI ligands have now been shown to stabilize a plethora of transition metal, main group, lanthanide, and actinide complexes.[42] Tuning the PDI unit through synthetic tailoring shows striking differences in the redox properties of the ligands and their resulting complexes. Considering the now well-known capacity of the PDI moiety to serve as a redox non-innocent ligand in metal complexes, tuning the redox properties of the PDI unit has the potential to dramatically affect the overall reactivity of PDI-supported metal system.[80]

Numerous syntheses of substituted PDI ligands have been reported by way of functionalization either at the 4-position of the pyridyl ring or at the imino moieties appended to the 2- and 6-positions of the central pyridyl group. Importantly, these synthetic routes are not general, highlighting the challenge of identifying a common method for modifying the steric and electronic profile of the PDI ligand. Nocera and coworkers have reported significant improvements with respect to the preparation of 4-substituted-2,6-diacetylpyridine precursors (*vide infra*), but these lack generality in the substitution pattern at the imino group. Herein, previous synthetic routes to 2,6-pyridyldiketone precursors and PDI ligands are highlighted. Taking inspiration from these synthetic methods, we have developed new derivatives of the *bis*(pyridyldiimine) macrocycle used in Chapter 2. Moreover, a new, scalable, tunable synthetic route to 4-aryl-2,6-dibenzoylpyridines is demonstrated, which allows for facile steric/electronic modifications to the PDI units of the macrocyclic ligands.

3.1.1 General Approach to the Synthesis of PDI Ligands

Typical synthetic pathways to either mononucleating PDI ligands or dinucleating macrocyclic PDI-based ligands involve the use of 2,6-pyridyldialdehyde or 2,6-pyridyldiketone starting materials. With an appropriate amine, an imine condensation results in the formation of the corresponding PDI unit. Early examples of this reactivity were demonstrated by Lions and Martin as well as Figgins and Busch.[81,82] In both cases, 2,6-diformylpyridine was converted to the corresponding 2,6-dialdiminopyridine using aniline, benzylamine, or methylamine (Figure 3.1, left and right). The respective ligands were found to bind Fe, Co, Ni and Cu in 2:1 stoichiometries. Following these preliminary works, Alyea and Merrell showed 2,6-diacetylpyridine to be a suitable precursor to 2,6-diiminopyridine using a similar protocol.[83] The PDI ligands were isolated following an imine condensation with aniline, *p*-anisidine, or benzylamine (Figure 3.1, bottom). Unlike the dialdehyde starting material, 2,6-diacetylpyridine required elevated reaction temperatures and an acid catalyst to achieve optimal yields. Notably, Ni and Zn complexes were synthesized in a 1:1 or 2:1 stoichiometry depending on the quantity of ligand used in the reaction mixture. The initial synthetic reports paved the way for a multitude of PDI derivatives containing an aldimino or methyl-substituted ketimino moiety.

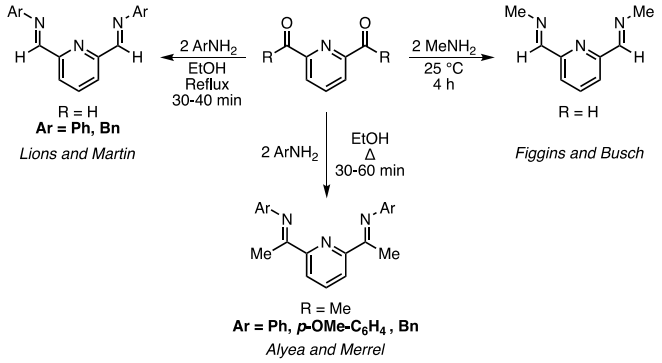

Figure 3.1 Early synthetic routes of PDI Ligands using imine condensations.

3.1.2 Substitution at the 4-Position of the PDI Unit

Substituents at the 4-position of PDI ligands are commonly introduced through 4-substituted-2,6-diacetylpyridine precursors. Examples of direct substitution of PDI derivatives are known but less common. Typically, alkylation,[84-86] halogenation,[87-92] oxidation,[93] or C–H activation[94] pathways are invoked to modify the 4-position of the pyridyl unit. An overview of select methods focusing on the above pathways follows herein.

Alkylation at the 4-position of 2,6-diacetylpyridine and related PDI ligands may be achieved through radical-based Minisci reactions,[84] organometallic manganese reagents[85,86] or metal-free photocatalysis.[95] Initially reported by Burger and coworkers, the *tert*-butylation of 2,6-diacetylpyridine was carried out under Minisci conditions in water/chlorobenzene (Figure 3.2, top). The *tert*-butyl group was found to improve the solubility of Rh and Ir PDI complexes in nonpolar solvents. Inspired by Burger's report and the previous *tert*-butylation of dimethyl-2,6-pyridinedicarboxylate in water,[96] our lab recently developed a two-step, greener preparation of 4-*tert*-butyl-2,6-diacetylpyridine (Figure 3.2, bottom).[75]

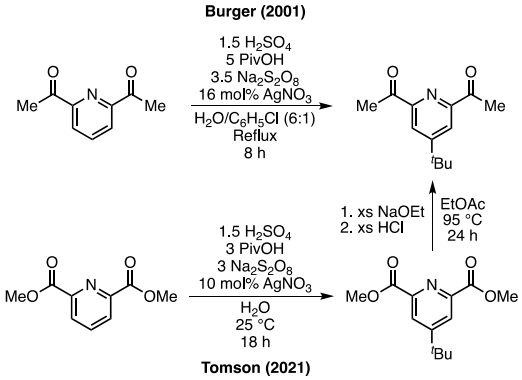

Figure 3.2 Preparation of 4-*tert*-butyl-2,6-diacetylpyridine.

Considering the successful *tert*-butylation of PDI precursors, the Minisci reaction is highly dependent on the stability of the alkyl radical. The limited scope of alkylation reactions led Cámpora and coworkers to develop a new alkylation procedure of PDI

ligands by using dialkylmanganese(II) reagents (Figure 3.3). Treating $^{i\text{Pr}}$PDI with MnR_2 (R = CH_2MePh, Bn, CH_2CHCH_2) followed by methanolysis, afforded a mixture of the 4-alkylated products and 1,4-dihydropyridines. Subjecting the crude product to oxidizing conditions allowed for full conversion to the desired 4-alkylated $^{i\text{Pr}}$PDI products. Cámpora proposed an alkyl migration mechanism as a means of generating the observed organic products.

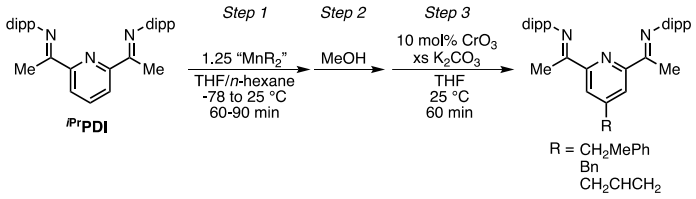

Figure 3.3 Alkylation of ^{iPr}PDI using alkyl manganese reagents.

Nocera and coworkers introduced a scalable synthesis of 4-substituted-2,6-pyridyldiketones for the synthesis of PDI ligands.[97] Using commercially available 4-substituted pyridines, a Minisci reaction was conducted using pyruvic acid to install acyl groups at the 2- and 6-positions. The method avoids the use of harsh halogenation conditions and eliminates the need for certain pyrophoric/toxic reagents used in other procedures.

Halogenation offers another route to functionalization. A common means of introducing halides to the 4-position of PDI ligands is first through the chlorination/bromination of chelidamic acid (4-hydroxy-2,6-pyridinedicarboxylic acid). Previous reports have established a routine procedure for chlorinating chelidamic acid using $SOCl_2$ or PCl_5.[87-89] The resulting chlorinated product, 4-chloro-2,6-pyridinedicarbonyl dichloride is subsequently converted to the appropriate 2,6-pyridyldiketone, which can be condensed with an amine. Chirik and coworkers reported this route was suitable for the synthesis of ^{iPr}PDI derivatives with 4-dimethylamino and 4-trifluoromethyl substitutions (Scheme 3.1).[90]

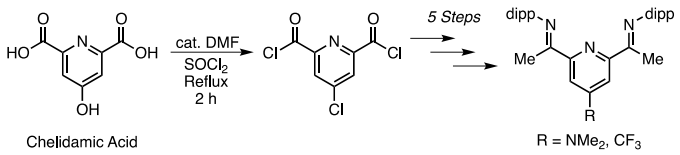

Scheme 3.1 Preparation of 4-substituted $^{i\text{Pr}}$PDI derivatives.

The bromination of chelidamic acid was first reported by Takalo and Kankare, in which PBr_5 was generated *in situ* and heated with chelidamic acid to afford 4-bromo-2,6-pyridinedicarbonyl dibromide.[92] Ivchenko and coworkers later introduced the bromination procedure in the preparation of a 4-*p*-tolyl-2,6-diacetylpyridine (Scheme 3.2).[91] The addition of pyrrolidine to 4-bromo-2,6-pyridinedicarbonyl dibromide afforded the diamide 4-bromo-2,6-*bis*(1-pyrrolydinylcarbonyl)pyridine, which was then coupled to *p*-tolylboronic acid using Suzuki conditions. Reduction of the cross-coupled product to 4-*p*-tolyl-2,6-diacetylpyridine was carried out using an excess of MeMgCl. Through regioselective bromination, a simple means of installing aryl groups at the 4-position of 2,6-diacetylpyridine was achieved.

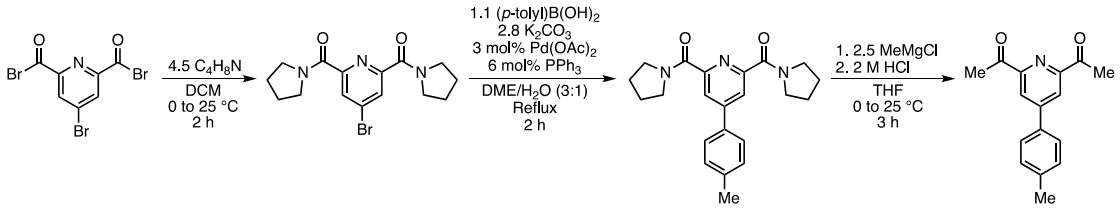

Scheme 3.2 Ivchenko's bromination and cross-coupling procedure.

More recently, Burger and coworkers developed a one-pot borylation procedure for both 2,6-diacetylpyridine (Scheme 3.3) and PDI derivatives.[94] The C–H activation pathway was selective for the 4-position of the pyridine ring, allowing easy access to borylated starting materials using B_2pin_2 (B_2pin_2 = *bis*(pinacolatodiboron). The products were then suitable for Suzuki cross-coupling reactions with various fused arenes to afford *bis*(2,6-diacetylpyridine) or dinucleating *bis*(PDI) compounds.

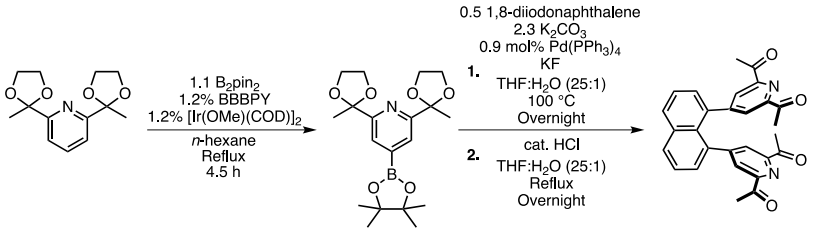

Scheme 3.3 Burger's borylation and cross-coupling procedure (BBBPY = 4,4'-di-*tert*-butyl-2,2'-bipyridine).

3.1.2 Substitution at the Imino Carbon of the PDI Unit

Another site at which substitution may influence the reactivity of a PDI ligand is the imino moiety. The most common substitutions include a proton or methyl group. Several examples have demonstrated unique approaches to generate 2,6-pyridyldiketones with new imino carbon functionality, including the addition of phenyl,[98] *tert*-butyl,[99] amino, ether and thioether substituents.[100] In particular, the synthesis of 2,6-dibenzoylpyridine was carried out by Esteruelas and coworkers in the pursuit of a phenyl-substituted PDI ligand for chromium(III). A Friedel-Crafts alkylation procedure was carried out using 2,6-pyridinedicarbonyl dichloride, benzene and $AlCl_3$ (Figure 3.4). Alternatively, the phenyl-substituted Gilman reagent ($LiCuPh_2$) may be used in the preparation of 2,6-dibenzoylpyridine.[101] The Friedel-Crafts synthetic pathway has displayed more versatility, as other aryl groups were tolerated under the reaction conditions (bromobenzene and 2-methylanisole).[102,103]

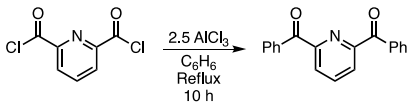

Figure 3.4 Synthesis of 2,6-dibenzoylpyridine.

3.2 Retrosynthetic Analysis

The current work aims to further macrocyclic ligand design for use in the generation of reactive Cu_2(II,II)-μ-oxo macrocyclic complexes. Tuning the electronics of

the macrocycle is desirable, as the ligand will play an important role in dictating the basicity and oxidizing strength of the Cu_2(II,II)-μ-oxo moiety (see Chapter 4 for more details). We sought to identify a modular ligand synthesis in which facile changes to the steric/electronic profiles of the PDI units can be made. The development of this synthesis focused on the incorporation of aryl substituents on the pyridyl and imino moieties of the PDI units; numerous substituted (electron-rich/poor) arenes are commercially available and eliminate the need for divergent syntheses to introduce bulky, electronic-donating or electron-withdrawing groups to the PDI unit.

The macrocyclic ligand (**5**) intended for this study is shown in Figure 3.5. Each PDI unit contains a phenyl group at the pyridyl and imino moieties. To synthesize **5,** a [2+2] imine condensation of 4-phenyl-2,6-dibenzoylpyridine (**4**) with 1,3-diaminopropane could afford the desired macrocycle in analogous fashion to our previous macrocycle syntheses. The formation of **4** would be accessible from the reduction of 4-phenyl-2,6-*bis*(1-pyrrolidinylcarbonyl)pyridine (**3**) using PhMgBr. Installation of a phenyl group at the 4-position of 3 was envisioned using a Suzuki cross-coupling reaction with phenylboronic acid and 4-bromo-2,6-*bis*(1-pyrrolidinylcarbonyl)pyridine (**2**). (Both the Grignard reduction and Suzuki coupling steps are points at which substituted arenes could be introduced.) Ivchenko and coworkers have previously reported the two-step synthesis of **2** from 4-bromopyridine-2,6-dicarbonyl dibromide (**1**), which was prepared from the commercial reagent chelidamic acid.

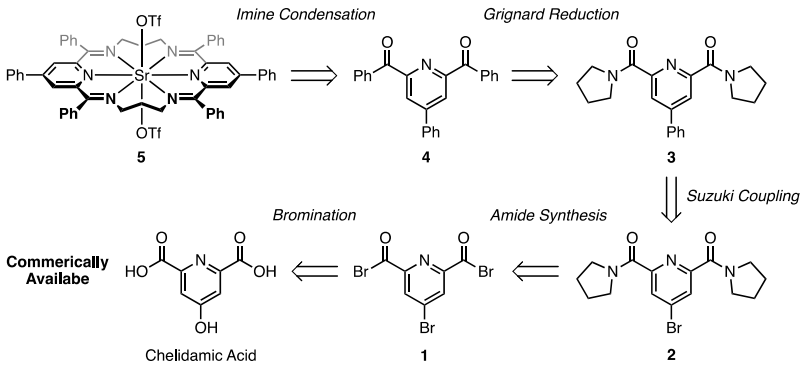

Figure 3.5 Retrosynthetic analysis of Macrocycle **5**.

3.3 Macrocyclic Ligand Synthesis

3.3.1 Synthesis of a Cross-Coupling Partner

Initial efforts were directed at the synthesis of **2** using the procedure developed by Ivchenko and coworkers. However, attempts at repeating the regioselective bromination were met with intractable mixtures at scale. To circumvent this issue, we modified the retrosynthetic pathway to include an iridium-catalyzed C–H borylation step (Figure 3.6). The synthesis of 2,6-*bis*(1-pyrrolidinylcarbonyl)pyridine-4-boronic acid pinacol ester (**7**) would arise from the borylation of 2,6-bis(1-pyrrolidinylcarbonyl)pyridine (**6**) with B_2pin_2 (B_2pin_2 = *bis*(pinacolato)diboron). The borylation procedure proved quite robust, as **7** was isolated in near-quantitative yield (Figure 3.7). The conversion of starting material was evident by ^{1}H NMR spectroscopy, as only a singlet at 8.13 ppm is present in the aromatic region, indicating one set of equivalent pyridyl protons. Additionally, a singlet at 1.31 ppm corresponds to the CH_3 groups on the newly installed Bpin moiety.

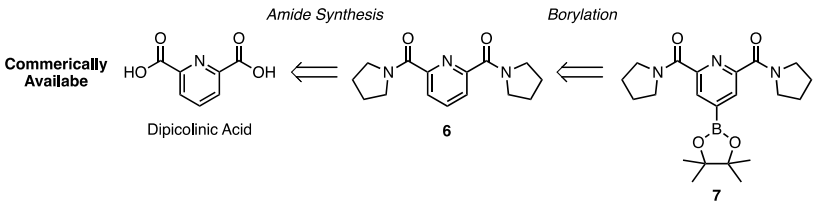

Figure 3.6 Modified retrosynthetic pathway**.**

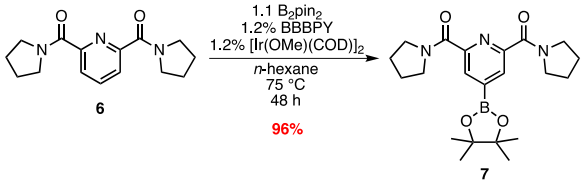

Figure 3.7 Synthesis of borylated diamide **7**.

3.3.2 Synthesis of 4-aryl-2,6-dibenzoylpyridine Derivatives

To install a phenyl group at the 4-position of pyridine ring, Suzuki cross-coupling conditions were optimized through reaction screening. A high-throughput experimental (HTE) study was carried out using **7** and bromobenzene. Twenty-four reactions were performed with variations in solvent, base and palladium (pre)catalyst (Figure 3.8). The best conditions, presented in Figure 3.9, were found to include DME (DME = 1,2-dimethoxyethane) as the solvent, potassium carbonate as the base, and SPhos Pd G2 as the palladium precatalyst. Using optimized conditions, the coupling of a phenyl group at the 4-position of the pyridine ring was achieved in 81% yield on gram-scale.

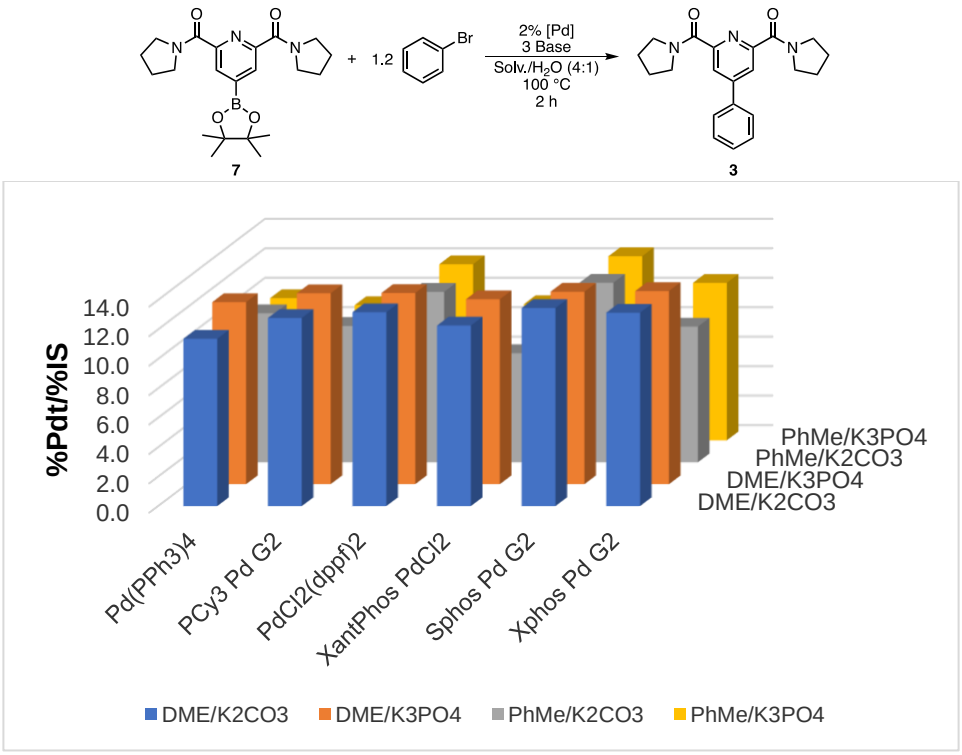

Figure 3.8 HTE screen of **7** and bromobenzene cross-coupling reaction (IS = Internal Standard = 4,4'-di-*tert*-butylbiphenyl).

The optimized conditions were then applied to other aryl bromides to introduce new substituents on the pyridyl unit. In some instances, a lower loading of catalyst was found to improve the reaction outcome. A range of electron-donating and -withdrawing aryl groups were well tolerated in the cross-coupling reaction. Coupling of 4-bromoanisole with **7** afforded 4-methoxyphenyl-substituted **8** in good yield. (HTE optimization was also carried out on the coupling of **7** to bromoanisole and is outlined in section 3.5.4). Fluorinated derivatives were also explored and led to incorporation of fluoro or trifluoromethyl substitution (**9** and **10**). Moreover, use of the electron-deficient 3,5-*bis*(trifluoromethyl)bromobenzene yielded the desired coupling product with ease (**11**).

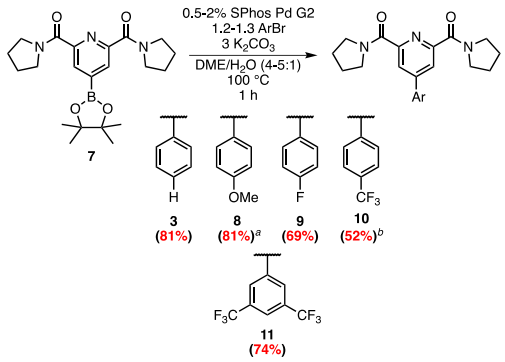

Figure 3.9 Suzuki cross-coupling reactions with **7** (*a* = K_3PO_4 was used as the base; *b* = $Pd(PPh_3)_4$ was used as the catalyst).

Following the cross-coupling step, the synthesis of **4** was carried out by treating **3** with an excess of PhMgBr. The desired triphenyl-substituted diketone was formed in 61% yield. Upon acidic workup, **4** precipitates from solution, offering a convenient way to isolate the product by filtration. In general, **4** was found to be fairly insoluble in common organic solvents. The procedure was extended to other phenyl Grignard reagents, allowing for the generation of a new series of triaryl-substituted 2,6-pyridyldiketones in moderate to good yield (Figure 3.10, **12-18**). Both electron-donating (*p*-tolylphenyl and *p*-methoxyphenyl) and electron-withdrawing (*p*-fluorophenyl) aryl Grignard reagents were implemented and afforded a diverse series of electron-rich and electron-poor triaryl-substituted diketones. Notably, the procedure allowed for the construction of mixed-aryl substrates, in which the aryl group at the 4-position of the pyridyl unit is different from the aryl group at the imino moiety.

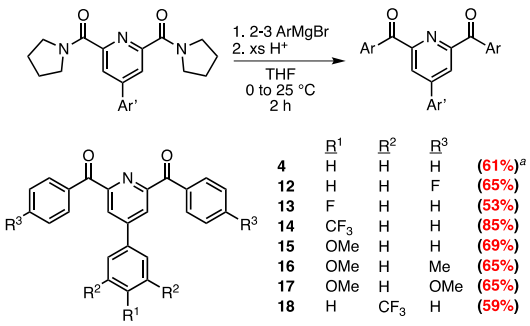

Figure 3.10 Synthesis of 4-aryl-2,6-dibenzoyl pyridine derivatives (*a* = PhMgBr was added at -78 °C and then mixture was warmed to room temperature).

3.3.3 Macrocyclization Examples

As depicted in Figure 3.7, the synthesis of macrocycle **5** was envisioned to occur from macrocyclization of **4**. Typically, *bis*(pyridyldiimine) macrocycles are synthesized through a [2+2] imine condensation reaction using an alkaline-earth metal(II) template ion. Using **4,** $Sr(OTf)_2$ and 1,3-diaminopropane, **5** was synthesized in 87% yield (Figure 3.11). The formation of the desired macrocyclic product was evidenced by ^1H NMR spectroscopy, in which the propylene linker protons were observed as a broad singlet at 3.93 ppm (8 protons) and a quintuplet at 1.77 ppm (4 protons). Additionally, a singlet appears at 7.28 ppm (corresponding to the 4 pyridyl protons), which lies upfield from the chemical shift observed for **4** (8.51 ppm).

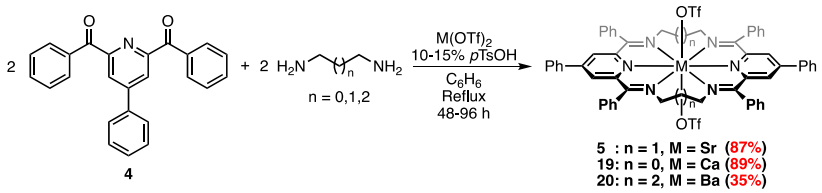

Figure 3.11 Synthesis of alkaline-earth metal triflate macrocycles.

The solid-state structure of **5** was determined using single-crystal X-ray crystallography (Figure 3.12). The structure is similar to $^{3/Me}$**[Sr]**$^{2+}$, in that the two PDI subunits are linked by propylene units and a $Sr(OTf)_2$ unit lies at the center of the macrocyclic cavity. The major difference is the phenyl substitution at both the pyridyl and

imino moieties; each phenyl group is rotated out of the PDI plane. As expected for the alkaline-earth metal(II) macrocycles, the ligand carries a neutral charge, as indicated by the Δ parameter of 0.188 Å.

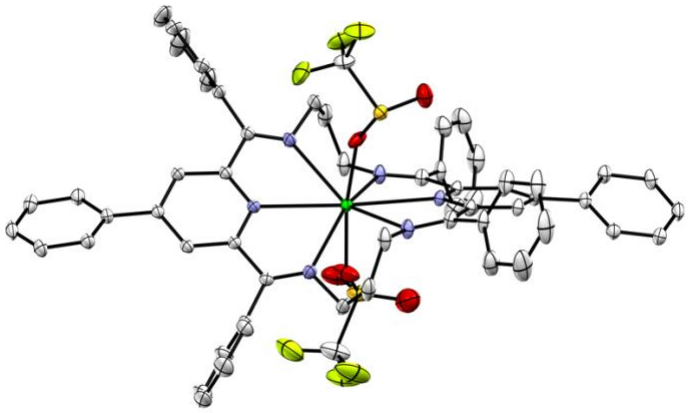

Figure 3.12 Crystal structure of **5** (thermal ellipsoids set at 50% probability; hydrogen atoms, disorder and solvent molecules omitted for clarity).

Previous work by our lab has demonstrated the isolation and synthesis of a series of alkaline-earth metal triflate macrocycles using the *bis*(4-*tert*-butylpyridyldiimine) macrocyclic ligand.[75] Using $MOTf_2$ salts (M = Ca, Sr, Ba) and alkyl diamines varying in carbon length, macrocycles of different sizes were prepared. The same approach was used in the preparation of smaller and larger macrocycle variants based on **4** (Figure 3.11). The use of $Ca(OTf)_2$/ethylenediamine and $Ba(OTf)_2$/1,4-diaminobutane allowed for the direct synthesis of macrocycles **19** and **20**, respectively. Macrocycle formation was confirmed by ^{1}H NMR spectroscopy, as the pyridyl singlet is shifted upfield in both cases (7.36 ppm for **19** and 7.30 ppm for **20**). The ethylene linker protons are observed as a singlet at 3.71 ppm (8 protons), while the butylene protons appear as two broadened singlets at 3.76 ppm and 1.98 ppm (each corresponding to 8 protons). The synthesis of macrocycles **5**, **19**, and **20** allows for direct comparison to be made between size and reactivity (see Chapter 4 for further details using Cu_2(II,II) macrocyclic complexes).

In addition to changing the size of the macrocycle, the substituents on the PDI units were varied. Any of the 4-aryl-2,6-dibenzoypyridines in Figure 3.11 are viable candidates for macrocyclization. As a proof of concept, substrates **12** and **13** were used in the preparation of fluorinated macrocycle derivatives (Figure 3.13). These diketones were chosen to demonstrate macrocyclization with substituents at either the pyridyl or imino moieties. Using the same synthetic protocol, macrocycles **21** (top) and **22** (bottom) were prepared in good yield.

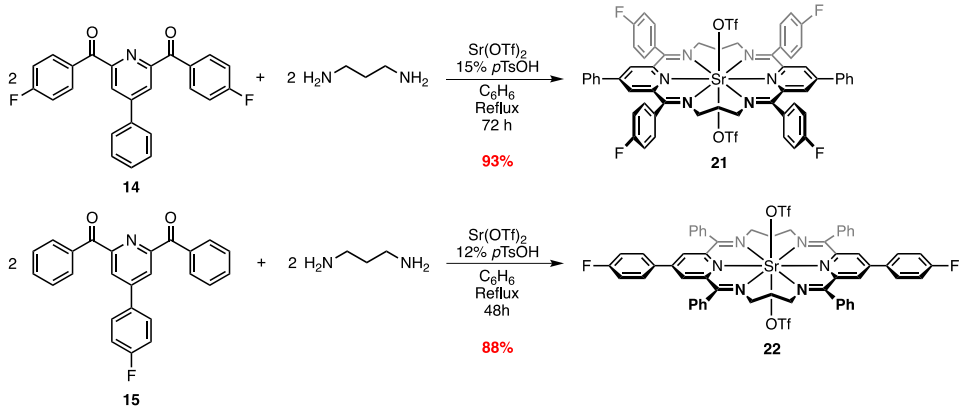

Figure 3.13 Synthesis of fluorinated macrocycle analogues.

3.4 Summary

A new modular synthetic route was developed for the synthesis of 4-aryl-2,6-dibenzoylpyridines. The five-step synthesis was scalable, and a range of aryl substituents were tolerated at the pyridyl and imino moieties. Macrocyclization was demonstrated using diketone **4**. Additionally, macrocycles of different size were prepared using different diamine linkers and alkaline-earth metal triflate template salts (**19** and **20**). Fluorinated analogues **21** and **22** were also prepared using the macrocycle synthesis. Good yields were obtained in all cases. The new diketones offer a range of options for PDI-based chemistry and allow for easy tuning of the steric/electronics of the resulting transition metal

complexes if desired. In this case, macrocycles **5** and **19** will be further explored in Chapter 4 in the pursuit of Cu_2(II,II)-μ-oxo complexes for hydrocarbon oxidation.

3.5 Experimental

3.5.1 General Considerations

Unless stated otherwise, all reactions were carried out under an inert atmosphere of N_2 using standard Schlenk techniques and worked up in air. Glassware, stir bars, filter aid (Celite) and 4 Å molecular sieves, were dried in an oven at 175 °C for at least one hour prior to use when applicable. Benchtop solvents (Pentane, Hexanes, Et_2O, Benzene, Toluene, THF, DCM, $CHCl_3$ and DMF) were purchased from Fisher Chemical or Millipore Sigma and used directly. Degassed anhydrous solvents (*n*-hexane, DME, THF and DCM) were dried by passage through activated alumina using a Solvent Purification System and stored over 4 Å molecule sieves for at least one day before use. Chloroform-*d* was purchased from Cambridge Isotopes Laboratories, Inc. and stored over 4 Å molecular sieves for at least one day before use. Thionyl chloride was purchased from Millipore Sigma in a Sure/Seal™ bottle. The Grignard reagents phenylmagnesium bromide (3.0 M in Et_2O) and 4-fluorophenylmagnesium bromide (2.0 M in Et_2O) were purchased from Millipore Sigma in Sure/Seal™ bottles and stored between 2-8 °C. Both *p*-tolylmagnesium bromide and 4-methoxyphenylmagnesium bromide were prepared as the lithium chloride adducts in THF (1.0 M) and used directly.[104] All other reagents were purchased from typical commercial vendors and used directly as received.

NMR Spectroscopy: ^{1}H, ^{13}C and ^{19}F NMR spectra were recorded on either a Bruker AVII 400 MHz or a Bruker NEO 600 MHz spectrometer. All chemical shifts are reported in units

of ppm, with references to the residual proteo-solvent resonance for proton and carbon chemical shifts.

X-ray Crystallography: X-ray intensity data for **5** were collected on a Rigaku XtaLab Synergy-S diffractometer equipped an HPC area detector (Dectris Pilatus3 R 200K) employing confocal multilayer optic-monochromated Mo-Kα radiation at a temperature of 100K. Rotation frames were integrated using CrysAlisPro, producing a listing of unaveraged F^2 and $\sigma(F^2)$ values. The intensity data were corrected for Lorentz and polarization effects and for absorption using SCALE3 ABSPACK. The structures were solved by dual methods using SHELXT and refined by full-matrix least-squares, based on F^2 using SHELXL-2018. All reflections were used during refinement. Non-hydrogen atoms were refined anisotropically and hydrogen atoms were refined using a riding model.

3.5.2 Synthetic Procedures

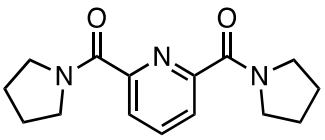

2,6-*bis*(1-pyrrolidinylcarbonyl)pyridine (6). The following procedure was adapted from the literature.[91] A 250 mL round bottom Schlenk flask was charged with pyridine-2,6-dicarboxylic acid (10.6 g, 63.4 mmol, 1.00e equiv.), $SOCl_2$ (20.0 mL, 274 mmol, 4.32 equiv.), and DMF (0.050 mL, 0.65 mmol, 1.0 mol %). The mixture was heated to reflux (oil bath set to 90 °C) for 2 h. Excess $SOCl_2$ was then removed under vacuum. The remaining red oil was treated with PhMe (50 mL) and concentrated under vacuum to remove residual $SOCl_2$. The crude di(acid chloride) was dissolved in DCM (25 mL) and cooled to 0 °C. A

solution of pyrrolidine (22.0 mL, 268 mmol, 4.22 equiv.) in DCM (25 mL) was then added dropwise to the cooled solution. The flask was removed from the cold bath and stirred for 2 h while warming to room temperature. The red-orange reaction mixture was then treated with 100 mL of 5% HCl. The organic layer was separated, and the aqueous layer was washed with 3 x 30 mL DCM. The organic materials were combined and washed with 100 mL of sat. Na_2CO_3, then dried over Na_2SO_4 and concentrated under vacuum to afford a beige solid. The product was triturated with pentane and collected via vacuum filtration. The product was dried under vacuum and used without further purification (15.2 g, 88%). NMR spectroscopic data matched those previously reported. **^{1}H NMR** ($CDCl_3$, 600 MHz, 298 K): δ = 7.84-7.75 (m, 3H), 3.66-3.51 (m, 8H), 1.90-1.79 (m, 8H) ppm. **^{13}C NMR** ($CDCl_3$, 151 MHz, 298 K): δ = 165.9, 152.9, 137.7, 124.7, 49.0, 46.8, 26.5, 23.9 ppm.

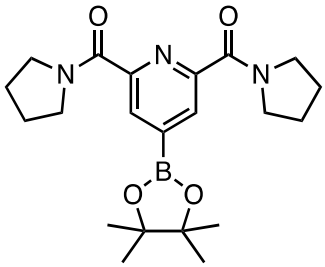

2,6-*bis*(1-pyrroldinylcarbonyl)pyridine-4-boronic acid pinacol ester (7). To a 500 mL Schlenk round bottom flask, was added $[Ir(COD)(OMe)]_2$ (515.3 mg, 0.7774 mmol, 1.06 mol%), 4,4'-di-*tert*-butyl-2,2'-bipyridine (223.6 mg, 0.8331 mmol, 1.13 mol%), B_2pin_2 (20.5770 g, 81.031 mmol, 1.10 equiv.), and *n*-hexane (*ca*. 250 mL). After stirring the dark red solution for one hour at room temperature, 2,6-bis(1-pyrrolidinecarbonyl)pyridine (20.1098 g, 73.571 mmol, 1.00 equiv.) was added. The mixture was refluxed (oil bath set to 75 °C) for 48 h. The heterogeneous mixture was directly filtered over fritted glass, and the filtrand was rinsed with copious amounts of *n*-hexane. The tan solid was collected and

dried under vacuum (28.1 g, 96%). **^{1}H NMR** ($CDCl_3$, 400 MHz, 298 K): δ = 8.13 (s, 2H), 3.62 (dt, *J* = 29.9, 6.4 Hz, 8H), 1.95-1.82 (m, 8H), 1.31 (s, 12H) ppm. **^{13}C NMR** ($CDCl_3$, 151 MHz, 298 K): δ = 166.4, 152.5, 129.4, 84.7, 48.9, 46.6, 26.4, 24.8, 24.0 ppm.

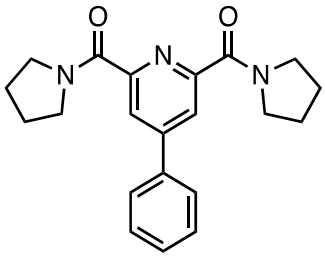

4-phenyl-2,6-*bis*(1-pyrrolidinylcarbonyl)pyridine (3). A 500 mL two-neck Schlenk round bottom flask was charged with 2,6-bis(1-pyrrolidinylcarbonyl)pyridine-4-boronic acid pinacol ester (5.077 g, 12.71 mmol, 1.00 equiv.), SPhos Pd G2 (187.6 mg, 0.2603 mmol, 2.0 mol%), bromobenzene (1.70 mL, 16.1 mmol, 1.27 equiv.), DME (125 mL), and a solution of K_2CO_3 (5.2849 g, 38.24 mmol, 3.01 equiv.) in H_2O (25 mL). The mixture was then refluxed (oil bath set to 100 °C) for one hour. After the reaction mixture had cooled, the mixture was diluted with 100 mL brine and extracted with 100 mL DCM. The organic layer was separated, and the aqueous layer was washed with 2 x 100 mL DCM. Organics were combined, dried over $MgSO_4$, and concentrated under vacuum. The resulting red-orange oil was purified via flash column chromatography (Biotage Isolera, 100 g Sfär column, 50% - 100% EtOAc/hexanes). The product was collected as a white solid and dried under vacuum (3.5795 g, 81%). **^{1}H NMR** ($CDCl_3$, 600 MHz, 298 K): δ = 8.08 (s, 2H), 7.69 (d, *J* = 7.3 Hz, 2H), 7.48-7.41 (m, 3H), 3.70-3.68 (m, 8H), 1.95-1.88 (m, 8H) ppm. **^{13}C NMR** ($CDCl_3$, 151 MHz, 298 K): δ = 166.3, 153.8, 150.4, 137.2, 129.7, 129,3, 127.2, 122.7, 49.3, 47.0, 26.8, 24.2 ppm.

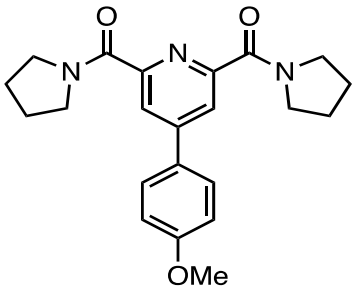

4-(4-methoxyphenyl)-2,6-*bis*(1-pyrrolidinylcarbonyl)pyridine (8). The reaction of **7** with 4-bromoanisole was carried out in similar fashion to the synthesis of **3**. Modifications were made as follows, **7** (5.0499 g, 12.647 mmol, 1.00 equiv.), 4-bromoanisole (1.90 mL, 15.2 mmol, 1.20 equiv.), K_3PO_4 (8.9188 g, 42.0 mmol, 3.32 equiv.) and SPhos Pd G2 (49.5 mg, 0.0687 mmol, 0.543 mol%), DME (100 mL) and H_2O (25 mL). The product was afforded as a white powder (3.87 g, 81%). **^{1}H NMR** ($CDCl_3$, 400 MHz, 298 K): δ = 8.05 (s, 2H), 7.68 (d, *J* = 8.8 Hz, 2H), 6.99 (d, *J* = 8.9 Hz, 2H), 3.86 (s, 3H), 3.70 (t, *J* = 6.7 Hz, 8H), 2.00-1.86 (m, 8H) ppm.

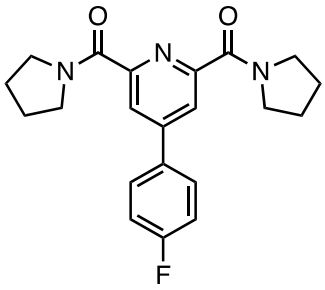

4-(4-fluorophenyl)-2,6-*bis*(1-pyrrolidinylcarbonyl)pyridine (9). The reaction of **7** with 4-fluorobromobenzene was carried out in similar fashion to the synthesis of **3**. Modifications were made as follows, **7** (2.1910 g, 5.487 mmol, 1.00 equiv.), 4-fluorobromobenzene (0.730 mL, 6.66 mmol, 1.21 equiv.), K_2CO_3 (2.2930 g, 16.59 mmol, 3.02 equiv.) and SPhos Pd G2 (20.0 mg, 0.0278 mmol, 0.506 mol%), DME (40 mL) and H_2O (10 mL). Following flash column chromatography, the product was recrystallized from

1:1 hexanes/EtOAc. The product was afforded as a white powder (1.3953 g, 69%).**^{1}H NMR** ($CDCl_3$, 400 MHz, 298 K): δ = 8.03 (s, 2H), 7.67 (dd, *J* = 8.6, 5.4 Hz, 2H), 7.15 (t, *J* = 8.5 Hz, 2H), 3.73-3.62 (m, 8H), 1.96-1.86 (m, 8H) ppm. **^{19}F NMR** ($CDCl_3$, 376 MHz, 298 K): δ = -111.6 ppm (unreferenced).

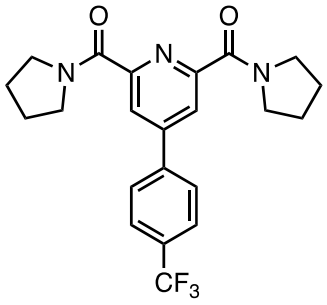

4-(4-trifluoromethylphenyl)-2,6-*bis*(1-pyrrolidinylcarbonyl)pyridine (10). The reaction of **7** with 4-bromobenzotrifluoride was carried out in similar fashion to the synthesis of **3**. Modifications were made as follows, **7** (2.5107 g, 6.2878 mmol, 1.00 equiv.), 4-bromobenzotrifluoride (1.10 mL, 7.86 mmol, 1.25 equiv.), K_2CO_3 (2.6796 g, 19.39 mmol, 3.08 equiv.) and $Pd(PPh_3)_4$ (154.1 mg, 0.1334 mmol, 2.12 mol%), DME (39 mL) and H_2O (13 mL). Following flash column chromatography, the product was triturated with EtOAc to remove a soluble yellow impurity. The product was afforded as an off-white powder (1.3681 g, 52%) **^{1}H NMR** ($CDCl_3$, 400 MHz, 298 K): δ = 8.12 (s, 2H), 7.82 (d, *J* = 8.2 Hz, 2H), 7.75 (d, *J* = 8.3 Hz, 2H), 3.71 (q, *J* = 6.2 Hz, 8H), 2.02-1.87 (m, 8H) ppm. **^{19}F NMR** ($CDCl_3$, 376 MHz, 298 K): δ = -62.8 ppm (unreferenced).

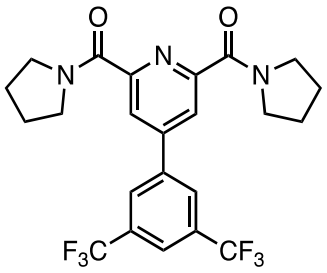

4-(3,5-bis(trifluoromethyl)phenyl)-2,6-*bis*(1-pyrrolidinylcarbonyl)pyridine (11). The reaction of **7** with 3,5-*bis*(trifluoromethyl)bromobenzene was carried out in similar fashion to the synthesis of **3**. Modifications were made as follows, **7** (2.5970 g, 6.5039 mmol, 1.00 equiv.), 3,5-*bis*(trifluoromethyl)bromobenzene (1.30 mL, 7.54 mmol, 1.16 equiv.), K_2CO_3 (2.6940 g, 19.493 mmol, 3.00 equiv.) and SPhos Pd G2 (23.8 mg, 0.0330 mmol, 0.508 mol%), DME (49 mL) and H_2O (13 mL). **^{1}H NMR** ($CDCl_3$, 600 MHz, 298 K): δ = 8.15 (s, 2H), 8.13 (s, 2H), 7.94 (s, 1H), 3.70 (dt, 13.9, 6.5 Hz, 8H), 1.98-1.88 (m, 8H) ppm. **^{13}C{^{1}H} NMR** ($CDCl_3$, 151 MHz, 298 K): δ = 165.6, 147.2, 139.4, 132.9 (q, *J* = 33.7 Hz) ppm, 127.4 (d, *J* = 3.8 Hz), 123.2 (quint, *J* = 3.6 Hz), 123.1 (q, *J* = 273.0 Hz), 122.9, 49.3, 47.2, 26.7, 24.0 ppm. **^{19}F NMR** ($CDCl_3$, 565 MHz, 298 K): δ = -62.9 ppm (unreferenced).

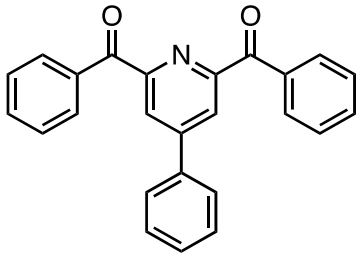

4-phenyl-2,6-dibenzoylpyridine (4). A 250 mL round bottom Schlenk flask was charged with THF (150 mL) and 3.0 PhMgBr (26.0 mL, 78.0 mmol, 2.47 equiv., in Et_2O). The light-yellow solution was cooled to -78 °C and treated slowly with a solution of **3** (11.0 g, 31.6 mmol, 1.00 equiv.) in THF (50 mL). The reaction mixture became dark red-orange and

was removed from the cold bath. After stirring for 2 hours, the mixture was re-cooled and slowly quenched by the dropwise addition of 2 M HCl. The product precipitated from solution as a yellow solid. The solid was collected by vacuum filtration and rinsed with copious amounts of water followed by copious amounts of Et_2O. The remaining off-white solid was collected and dried under vacuum (7.0 g, 61%). **^{1}H NMR** ($CDCl_3$, 600 MHz, 298 K): δ = 8.51 (s, 2H), 8.18 (d, *J* = 6.9 Hz, 4H), 7.82 (d, *J* = 7.0 Hz, 2H), 7.59-7.55 (m, 4H), 7.53-7.51 (m, 1H), 7.43 (t, *J* = 7.8, 4H) ppm. **^{13}C{^{1}H} NMR** ($CDCl_3$, 151 MHz, 298 K): δ = 192.9, 154.7, 151.1, 137.0, 136.2, 133.2, 131.3, 130.1, 129.6, 128.2, 127.4, 124.7 ppm.

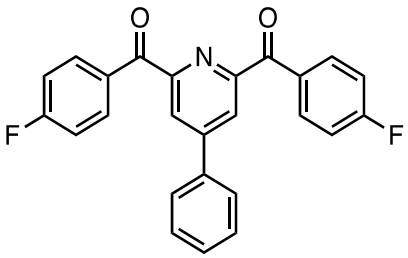

4-phenyl-2,6-*bis*(4-fluorophenylmethanone)pyridine (12). A 250 mL two-neck round bottom Schlenk flask was charged with THF (10 mL) and 2.0 M 4-fluorophenylmagnesium bromide (4.00 mL, 8.00 mmol, 2.44 equiv., in Et_2O). The solution was cooled to 0 °C and treated dropwise with a solution of **3** (1.1474 g, 3.2836 mmol, 1.00 equiv.) in THF (25 mL). The flask was removed from the cold bath. The solution was stirred for 2 hours while warming to room temperature. The mixture was then re-cooled and quenched with 100 mL sat. NH_4Cl. The biphasic mixture was extracted with 100 mL DCM, and the organic layer was separated. The remaining aqueous layer was washed with 2 x 50 mL DCM. The organic materials were combined, dried over $MgSO_4$ and concentrated under vacuum. The resulting yellow product was recrystallized from hot 2:1 PhMe/Et_2O and then triturated with 30 mL Et_2O to remove a soluble impurity. The product was collected as an off-white

powder and was dried under vacuum (846.6 mg, 65%). **^{1}H NMR** ($CDCl_3$, 600 MHz, 298 K): δ = 8.52 (s, 2H), 8.25 (dd, *J* = 8.8, 5.5 Hz, 4H), 7.81 (d, *J* = 6.8 Hz, 2H), 7.58-7.54 (m, 2H), 7.54-7.50 (m, 1H), 7.10 (t, *J* = 8.6 Hz, 4H) ppm. **^{13}C{^{1}H}** ($CDCl_3$, 151 MHz, 298 K): δ = 191.0, 165.9 (d, $^{1}J_{CF}$ = 255.6 Hz), 154.4, 151.3, 136.8, 134.1 (d, $^{3}J_{CF}$ = 9.2 Hz), 132.4 (d, $^{4}J_{CF}$ = 2.9 Hz), 130.2, 129.6, 127.3, 124.9, 115.4 (d, $^{2}J_{CF}$ = 21.7 Hz) ppm. **^{19}F NMR** ($CDCl_3$, 565 MHz, 298 K): δ = -104.5 ppm (unreferenced).

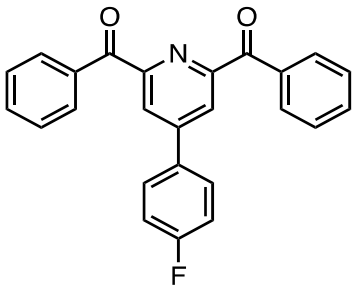

4-(4-fluorophenyl)-2,6-dibenzoylpyridine (13). The reaction of **9** with PhMgBr was carried out in similar fashion to the synthesis of **12**. Modifications were made as follows, **9** (1.3563 g, 3.6914 mmol, 1.00 equiv.) in THF (30 mL) and 3.0 M PhMgBr (3.00 mL, 9.00 mmol, 2.44 equiv., in Et_2O) in THF (20 mL). After aqueous workup, the crude yellow product was recrystallized from hot PhMe. The product was afforded as an off-white powder (741.6 mg, 53%). **^{1}H NMR** ($CDCl_3$, 400 MHz, 298 K): δ = 8.56 (s, 2H), 8.27 (d, *J* = 7.0 Hz, 4H), 7.90 (dd, *J* = 8.8, 5.2 Hz, 2H), 7.72-7.63 (m, 2H), 7.52 (t, *J* = 7.8 Hz, 4H), 7.39-7.30 (m, 2H) ppm. **^{19}F NMR** ($CDCl_3$, 376 MHz, 298 K): δ = -110.9 ppm (unreferenced).

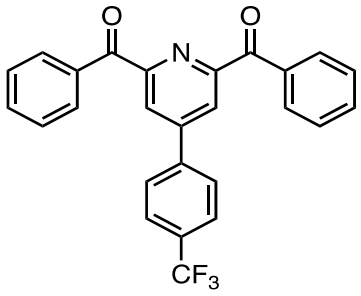

4-(4-trifluoromethylphenyl)-2,6-dibenzoylpyridine (14). The reaction of **10** with PhMgBr was carried out in similar fashion to the synthesis of **12**. Modifications were made as follows, **10** (1.3611 g, 3.2607 mmol, 1.00 equiv.) in THF (24 mL) and 3.0 M PhMgBr (3.70 mL, 8.10 mmol, 2.48 equiv., in Et_2O). In this instance, the Grignard solution was directly added dropwise to a chilled solution of **10** in THF. The reaction was quenched with 28 mL 2 M HCl. After aqueous workup, the yellow product was dried under vacuum. The product was afforded as a yellow powder (1.1944 g, 85%). **^{1}H NMR** ($CDCl_3$, 400 MHz, 298 K): δ = 8.52 (s, 2H), 8.18 (d, *J* = , 4H), 7.93 (d, *J* = 8.2 Hz, 2H), 7.83 (d, *J* = 8.2 Hz, 2H), 7.64-7.54 (m, 2H), 7.43 (t, *J* = 7.8 Hz, 4H) ppm. **^{19}F NMR** ($CDCl_3$, 376 MHz, 298 K): δ = -62.8 ppm (unreferenced).

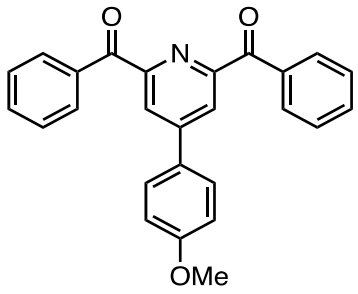

4-(4-methoxyphenyl)-2,6-dibenzoylpyridine (15). The reaction of **8** with PhMgBr was carried out in similar fashion to the synthesis of **12**. Modifications were made as follows, **8** (1.3994 g, 3.6879 mmol, 1.00 equiv.) in THF (30 mL) and 3.0 M PhMgBr (2.80 mL, 8.40 mmol, 2.28 equiv., in Et_2O). In this instance, the Grignard solution was directly added

dropwise to a chilled solution of **8** in THF. The reaction was quenched with 31 mL 2 M HCl. After aqueous workup, the crude yellow product was recrystallized from acetone. The product was afforded as a light yellow powder (1.0062 g, 69%). **^{1}H NMR** ($CDCl_3$, 400 MHz, 298 K): δ = 8.47 (s, 2H), 8.17 (d, *J* = 6.9 Hz, 4H), 7.79 (d, *J* = 8.8 Hz, 2H), 7.57 (t, *J* = 7.2 Hz, 2H), 7.42 (t, *J* = 7.8 Hz, 4H), 7.07 (d, *J* = 8.7 Hz, 2H), 3.90 (s, 3H) ppm.

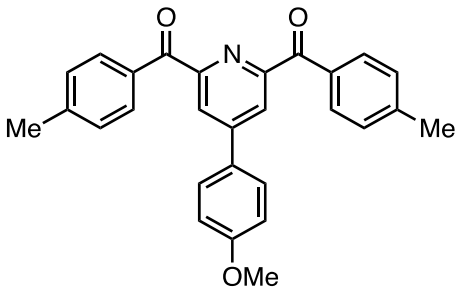

4-(4-methoxyphenyl)-2,6-*bis*(4-*p*-tolylmethanone)pyridine (16). The reaction of **8** with *p*-tolylmagnesium bromide was carried out in similar fashion to the synthesis of **12**. Modifications were made as follows, **8** (1.0731 g, 2.8280 mmol, 1.00 equiv.) in THF (15 mL) and 0.9 M *p*-tolylmagnesium bromide (7.30 mL, 6.57 mmol, 2.32 equiv., in THF). The aqueous workup was performed with EtOAc, from which the crude product was recrystallized at -20 °C. After filtering off the recrystallized product, the filtrate was concentrated under vacuum to afford a yellow-white solid. A second crop of material was obtained upon triturating the solid with acetone to remove a soluble impurity. This crop of material was combined with the recrystallized material, affording the product as afforded as an off-white powder (773.0 mg, 65%). **^{1}H NMR** ($CDCl_3$, 600 MHz, 298 K): δ = 8.39 (s, 2H), 8.10 (d, *J* = 8.0 Hz, 4H), 7.77 (d, *J* = 8.8 Hz, 2H), 7.23 (d, *J* = 7.9 Hz), 4H), 7.05 (d, *J* = 8.8 Hz, 2H), 3.88 (s, 3H), 2.43 (s, 6H) ppm. **^{13}C{^{1}H} NMR** ($CDCl_3$, 151 MHz, 298 K): δ = 192.8, 161.3, 155.0, 150.3, 144.0, 133.6, 131.5, 129.2, 129.0, 128.6, 123.7, 114.9, 55.6, 21.9 ppm.

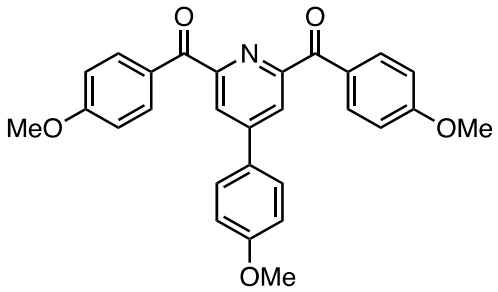

4-(4-methoxyphenyl)-2,6-*bis*(4-methoxyphenylmethanone)pyridine (17). The reaction of **8** with *p*-methoxyphenylmagnesium bromide was carried out in similar fashion to the synthesis of **12**. Modifications were made as follows, **8** (786.7 g, 2.073 mmol, 1.00 equiv.) in THF (17 mL) and 0.8 M *p*-methoxyphenylmagnesium bromide (8.0 mL, 6.40 mmol, 3.09 equiv., in Et_2O). After aqueous workup, the crude product was recrystallized from hot acetone. The desired product was afforded as an off-white powder (697.0 mg, 65%). **^{1}H NMR** ($CDCl_3$, 600 .4MHz, 298 K): δ = 8.37 (s, 2H), 8.24 (d, *J* = 8.5 Hz, 4 H), 7.76 (d, *J* = 8.4 Hz, 2H), 7.05 (d, *J* = 8.4 Hz, 2H), 6.92 (d, *J* = 8.4 Hz, 4H), 3.88 (s, 3H), 3.87 (s, 6H) ppm. **^{13}C{^{1}H} NMR** ($CDCl_3$, 151 MHz, 298 K): δ = 191.5, 163.8, 161.3, 155.2, 150.3, 133.9, 129.3, 129.1, 128.6, 123.6, 114.9, 113.5, 55.6, 55.6 ppm.

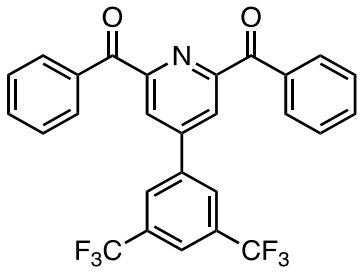

4-(3,5-*bis*(trifluoromethyl)phenyl)-2,6-dibenzoylpyridine (18). The reaction of **11** with PhMgBr was carried out in similar fashion to the synthesis of **12**. Modifications were made as follows, **11** (2.2277 g, 4.5891 mmol, 1.00 equiv.) in THF (20 mL) and 3.0 M PhMgBr

(3.60 mL, 10.8 mmol, 2.35 equiv., in Et_2O) in THF (20 mL). In this instance, the Grignard solution was added to a chilled solution of **11**. The reaction was quenched with 38 mL 2 M HCl. After aqueous workup, the product was recrystallized from 1:1 hexanes/Et_2O at -20 °C. The product was afforded as an off-white powder (1.3566 g, 59%). **^{1}H NMR** ($CDCl_3$, 600 MHz, 298 K): δ = 8.54 (s, 2H), 8.23 (s, 2H), 8.18 (d, *J* = 7.8 Hz, 4H), 8.05 (s, 1H), 7.60 (t, *J* = 7.4 Hz, 2H), 7.43, *J* = 7.7 Hz, 4H) ppm. **^{13}C{^{1}H} NMR** ($CDCl_3$, 151 MHz, 298 K): δ = 192.2, 155.1, 148.2, 139.4, 135.8, 133.4, 133.2 (q, *J* = 33.8 Hz), 131.3, 128.3, 127.6 (d, *J* = 3.8 Hz), 124.7, 123.6 (quint, *J* = 3.8 Hz), 123.1 (q, *J* = 273.0 Hz) ppm. **^{19}F NMR** ($CDCl_3$, 565 MHz, 298 K): δ = -62.8 ppm (unreferenced).

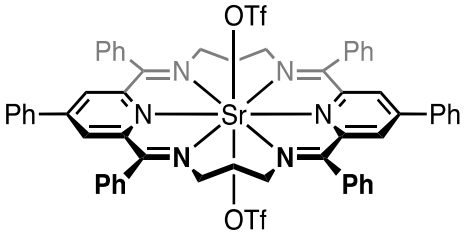

^{3Ph}[Sr]$^{2+}$ (5). A 500 mL round bottom flask was charged with **4** (3.2433 g, 8.9244 mmol, 2.00 equiv.), $Sr(OTf)_2$ (1.7222 mg, 2.4645 mmol, 1.00 equiv.), *p*TsOH (78.3 mg, 0.455 mmol, 10.2 mol%), 1,3-diaminopropane (0.750 mL, 8.97 mmol, 2.01 equiv.) and C_6H_6 (250 mL). The flask was equipped with a Dean-Stark apparatus and refluxed (oil bath set to 110 °C) for 48 hours. Solvent was removed under vacuum. The crude product was extracted in minimal (*ca*. 30-40 mL) DCM and filtered over a pad of celite to remove insoluble materials. The filtrate was treated with hexanes until the product precipitated from solution. The product was collected by vacuum filtration, rinsed with copious amounts of hexanes, and dried under vacuum (4.6052 mg, 87%). **^{1}H NMR** ($CDCl_3$, 400 MHz, 298 K): δ = 7.60-7.48 (m, 12 H), 7.46-7.38 (m, 8H), 7.39-7.32 (m, 6H), 7.28 (s, 4H), 7.24-7.17

(m, 4H), 3.93 (s, 8H), 1.80-1.73 (m, 4H) ppm. **^{19}F NMR** ($CDCl_3$, 376 MHz, 298 K): δ = -78.1 ppm (unreferenced).

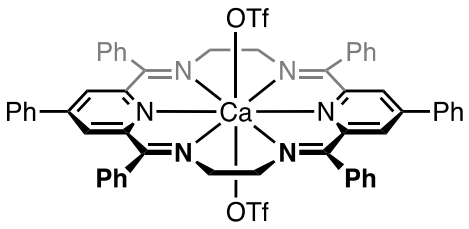

$^{2/Ph}$[Ca]$^{2+}$ (19). A 500 mL round bottom flask was charged with **4** (2.4926 g, 6.8587 mmol, 2.00 equiv.), $Ca(OTf)_2$ (1.2924 mg, 1.114 mmol, 1.11 equiv.), *p*TsOH (88.8 mg, 0.516 mmol, 15.0 mol%), ethylenediamine (0.460 mL, 6.88 mmol, 2.01 equiv.) and C_6H_6 (250 mL). The flask was equipped with a Dean-Stark apparatus and refluxed (oil bath set to 120 °C) for 96 hours. Solvent was removed under vacuum. The crude product was extracted in $CHCl_3$ (25 mL) and filtered over a pad of celite to remove insoluble materials. The filtrate was concentrated under vacuum to afford a grey solid. The solid was triturated with THF (25 mL) and collected by vacuum filtration. The filtrand was rinsed with 200 mL pentane. The product, an off-white solid, was then dried under vacuum (3.4034 g, 89%). **^{1}H NMR** ($CDCl_3$, 600 MHz, 298 K): δ = 7.59-7.47 (m, 12H), 7.43-7.33 (m, 18H), 7.30-7.25 (m, 4H), 3.72 (s, 8H) ppm. **^{13}C{^{1}H} NMR** ($CDCl_3$, 151 MHz, 298 K): δ = 169.9, 154.7, 152.1, 136.9, 134.6, 129.9, 129.7, 129.5, 129.3, 127.5, 127.2, 125.1, 120.2 (q, *J* = 319.4 Hz), 54.4 ppm.

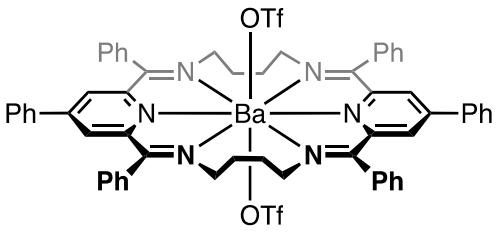

$^{4/Ph}$[Ba]$^{2+}$ (20). A 500 mL round bottom flask was charged with **4** (1.6059 g, 4.4189 mmol, 2.00 equiv.), $Ba(OTf)_2$ (1.0670 mg, 2.4503 mmol, 1.11 equiv.), *p*TsOH (58.1 mg, 0.337 mmol, 15.3 mol%), 1,4-diaminobutane (0.450 mL, 4.48 mmol, 2.03 equiv.) and C_6H_6 (250 mL). The flask was equipped with a Dean-Stark apparatus and refluxed (oil bath set to 120 °C) for 72 hours. Solvent was removed under vacuum. The crude product was extracted in minimal $CHCl_3$ and filtered over a pad of celite to remove insoluble materials. The filtrate was treated with hexanes until the product precipitated from solution. The product was collected by vacuum filtration, rinsed with copious amounts of hexanes, and dried under vacuum (990.8 mg, 35%). **^{1}H NMR** ($CDCl_3$, 600 MHz, 298 K): δ = 7.58-7.43 (m, 12H), 7.41-7.35 (m, 8H), 7.35-7.30 (m, 6H), 7.29 (s, 4H), 7.20-7.14 (m, 4H), 3.76 (s, 8H), 1.98 (s, 8H) ppm. **^{13}C{^{1}H} NMR** ($CDCl_3$, 151 MHz, 298 K): δ = 171.3, 156.3, 151.4, 137.0, 135.9, 129.4, 129.29, 129.26, 127.4, 127.1, 126.4, 120.5 (q, J_{CF} = 319.9 Hz), 53.8, 27.6 ppm. **^{19}F NMR** ($CDCl_3$, 565 MHz, 298 K): δ = -78.1 ppm (unreferenced).

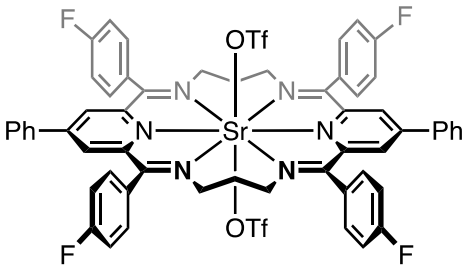

$^{3/PhF}$[Sr]$^{2+}$ (21). A 250 mL round bottom flask was charged with **12** (823.4 mg, 2.062 mmol, 2.00 equiv.), $Sr(OTf)_2$ (438.7 mg, 1.137 mmol, 1.10 equiv.), *p*TsOH (25.8 mg, 0.150 mmol, 14.5 mol%), 1,3-diaminopropane (0.180 mL, 2.15 mmol, 2.09 equiv.) and C_6H_6 (100 mL). The flask was equipped with a Dean-Stark apparatus and refluxed (oil bath set to 120 °C) for 72 hours. Solvent was removed under vacuum. The crude product was extracted in minimal DCM and filtered over a pad of celite to remove insoluble materials. The filtrate was treated with hexanes until the product precipitated from solution. The product was collected by vacuum filtration, rinsed with copious amounts of hexanes, and dried under vacuum (1.2087 g, 93%). **^{1}H NMR** ($CDCl_3$, 600 MHz, 298 K): δ = 7.45-7.36 (m, 14H), 7.31-7.25 (m, 10H), 7.23 (dd, *J* = 7.8, 1.8 Hz, 4H), 3.92 (s, 8H), 1.77 (quint., *J* = 6.6 Hz, 4H) ppm. **^{19}F NMR** ($CDCl_3$, 376 MHz, 298 K): δ = -78.2, -110.3 ppm (unreferenced).

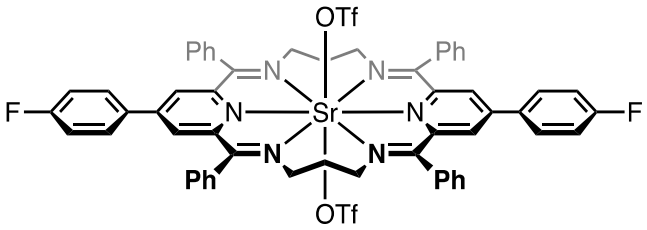

$^{3/PhF/Ph}$[Sr]$^{2+}$ (22). A 250 mL round bottom flask was charged with **13** (730.4 mg, 1.915 mmol, 2.00 equiv.), $Sr(OTf)_2$ (377.5 mg, 0.9786 mmol, 1.02 equiv.), *p*TsOH (19.2 mg, 0.111 mmol, 11.6 mol%), 1,3-diaminopropane (0.160 mL, 1.91 mmol, 2.00 equiv.) and C_6H_6 (100 mL). The flask was equipped with a Dean-Stark apparatus and refluxed (oil bath

set to 120 °C) for 48 hours. Solvent was removed under vacuum. The crude product was extracted in minimal DCM and filtered over a pad of celite to remove insoluble materials. The filtrate was treated with hexanes until the product precipitated from solution. The product was collected by vacuum filtration, rinsed with copious amounts of hexanes, and dried under vacuum (1.0266 g, 88%). **^{1}H NMR** ($CDCl_3$, 400 MHz, 298 K): δ = 7.61-7.49 (m, 12H), 7.47-7.38 (m, 8H), 7.23 (s, 4H), 7.18 (dd, *J* = 8.8, 5.2 Hz, 4H), 7.04 (t, *J* = 8.6 Hz, 4H), 3.92 (s, 8H), 1.81-1.73 (m, 4H) ppm. **^{19}F NMR** ($CDCl_3$, 376 MHz, 298 K): δ = -78.2, -110.9 ppm (unreferenced).

3.5.3 NMR Spectra

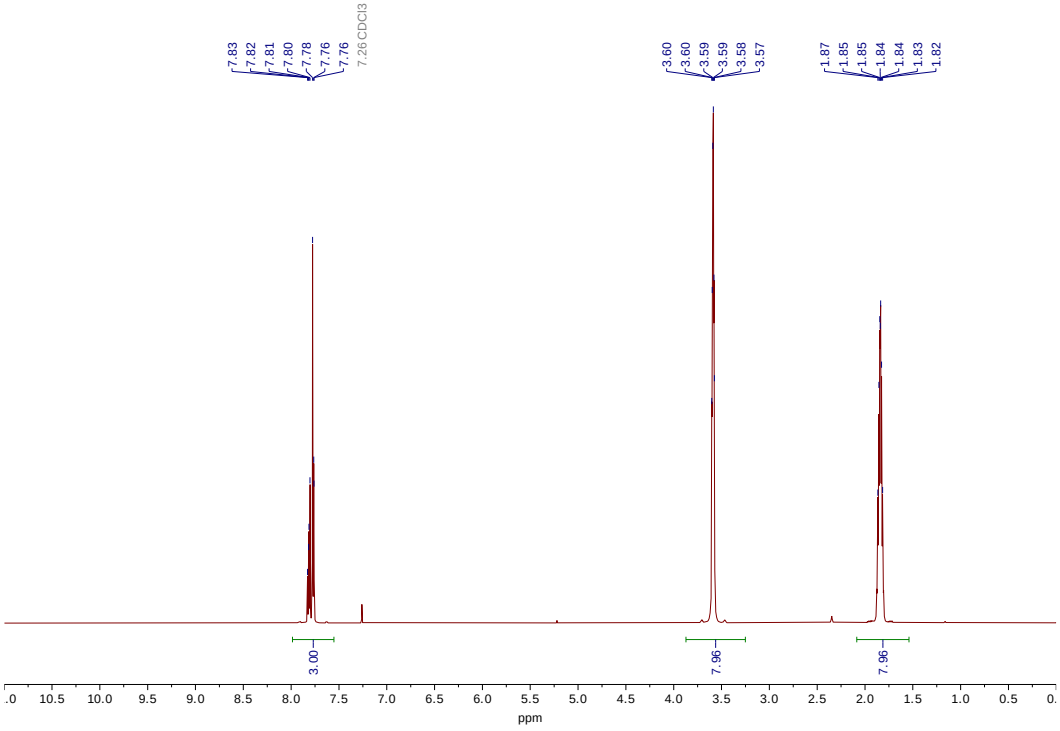

Figure 3.14 ^{1}H NMR spectrum of **6** in $CDCl_3$.

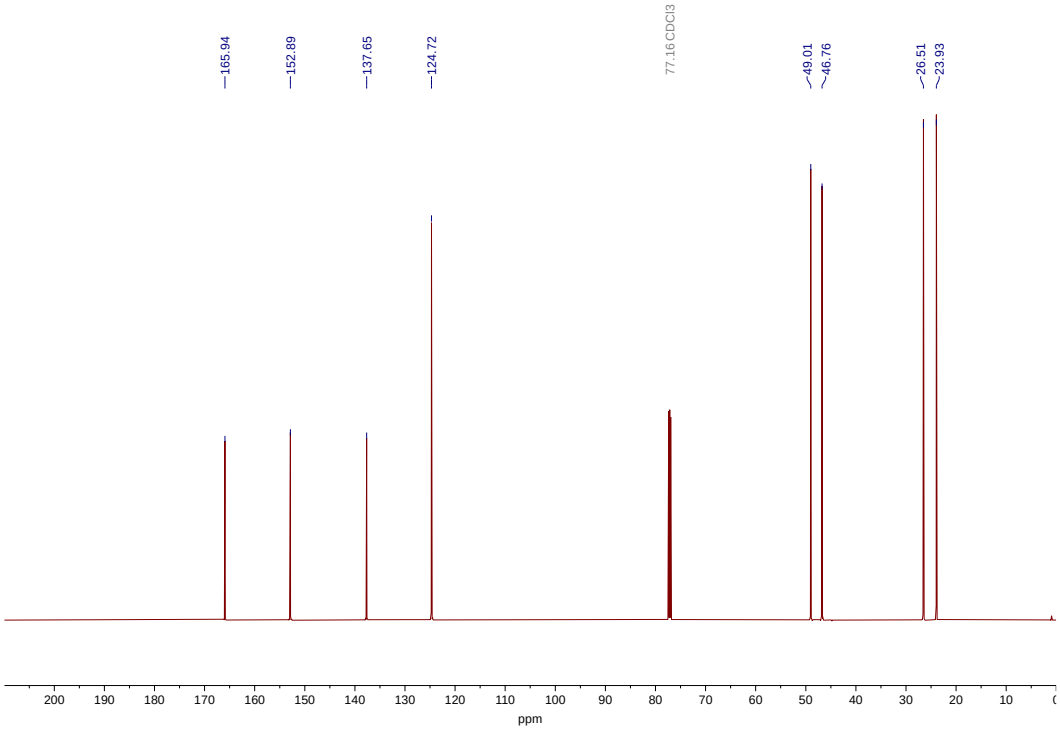

Figure 3.15 $^{13}C\{^{1}H\}$ NMR spectrum of **6** in $CDCl_3$.

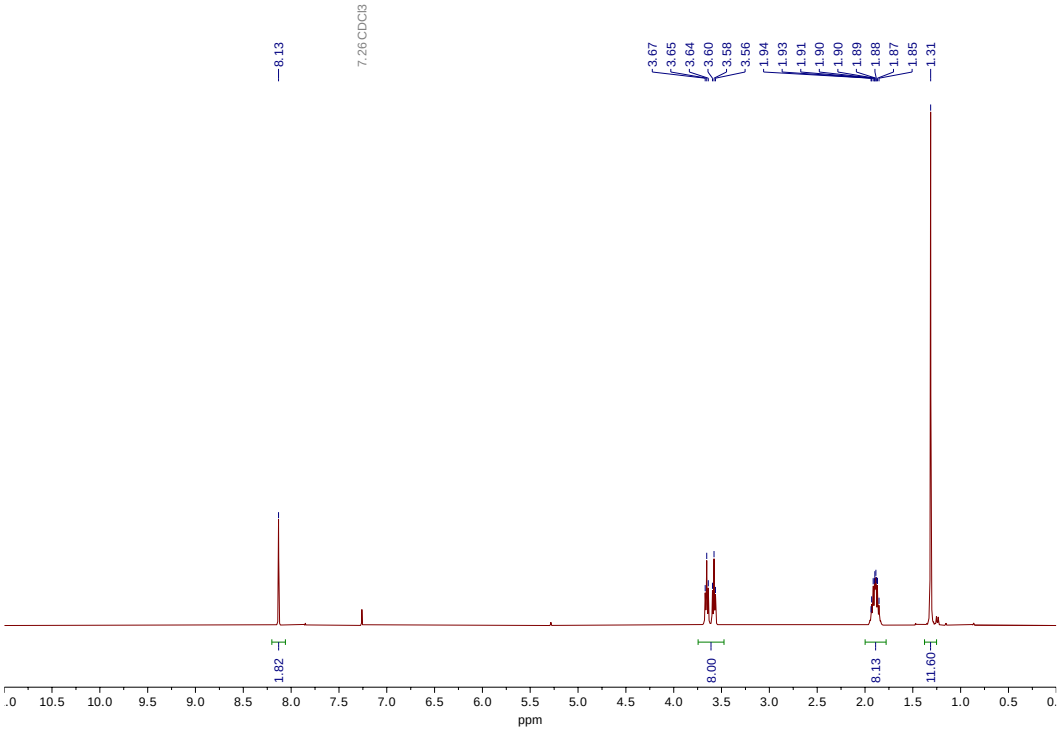

Figure 3.16 ^{1}H NMR spectrum of **7** in $CDCl_3$.

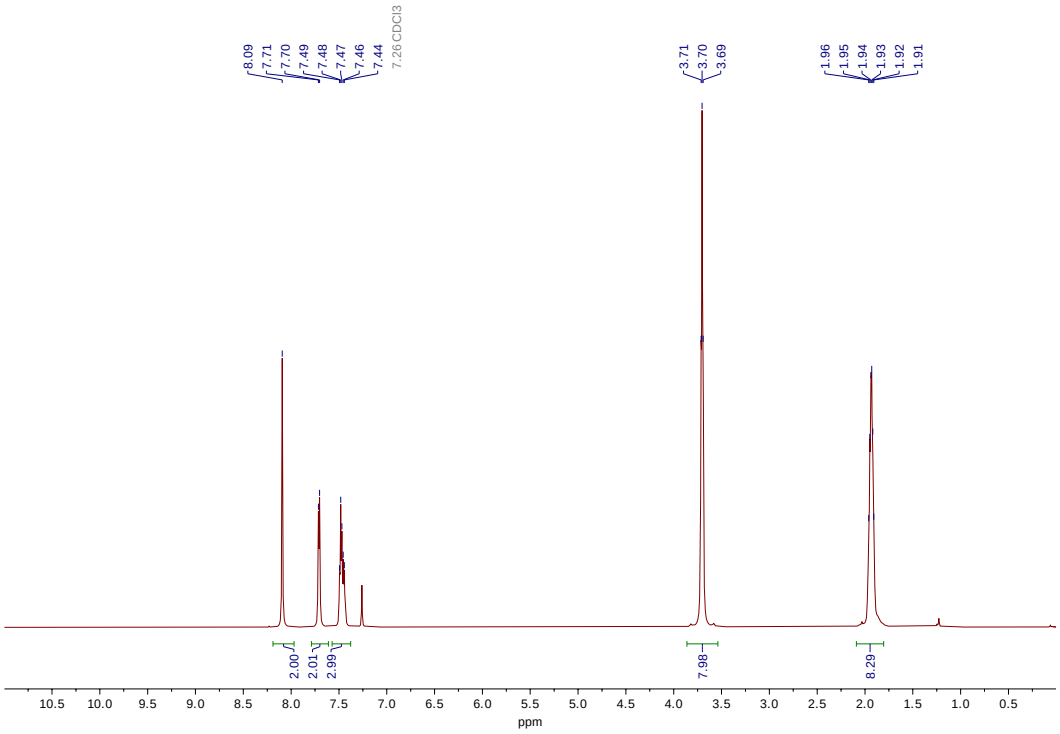

Figure 3.17 ^{1}H NMR spectrum of **3** in $CDCl_3$.

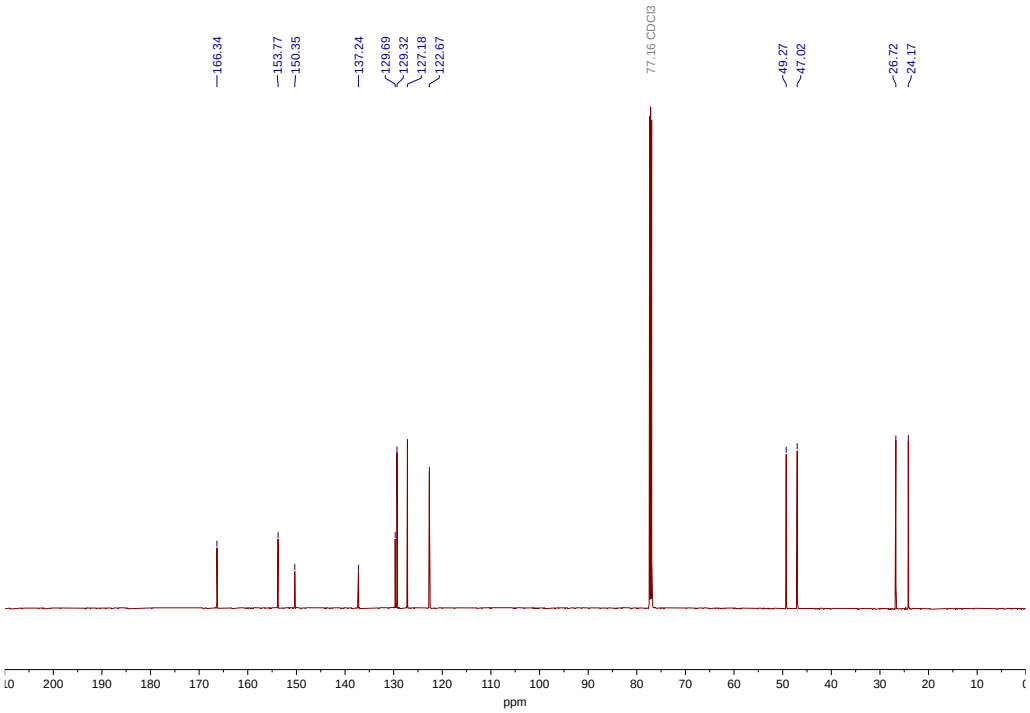

Figure 3.18 $^{13}C\{^{1}H\}$ NMR spectrum of **3** in $CDCl_3$.

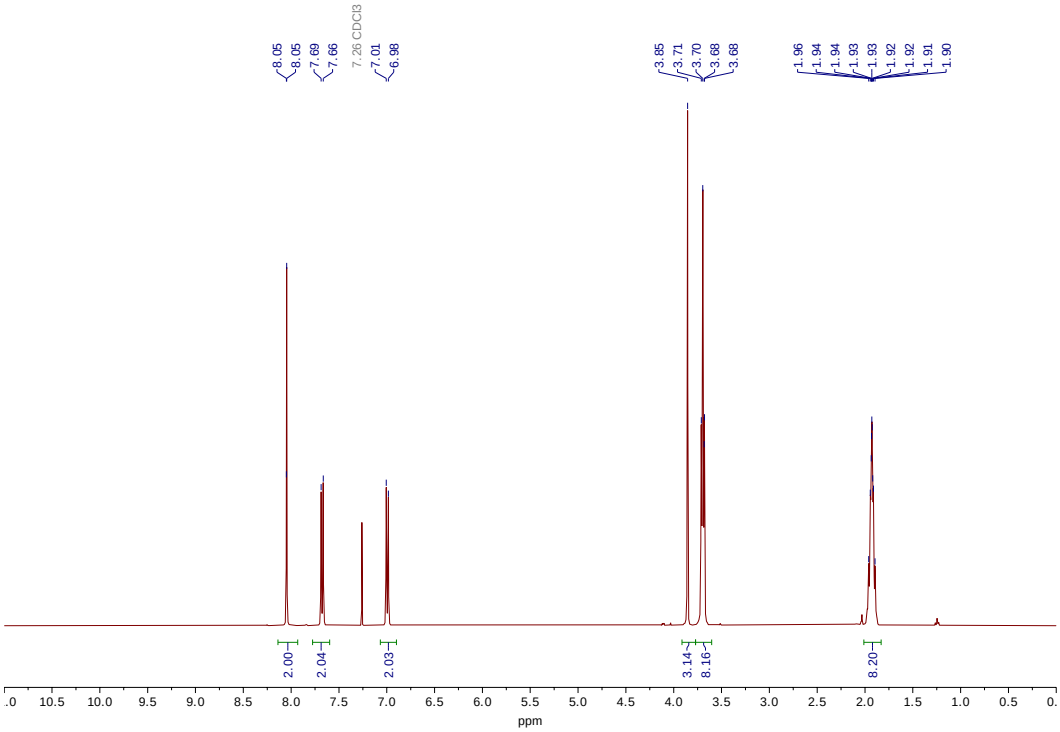

Figure 3.19 ^{1}H NMR spectrum of **8** in $CDCl_3$.

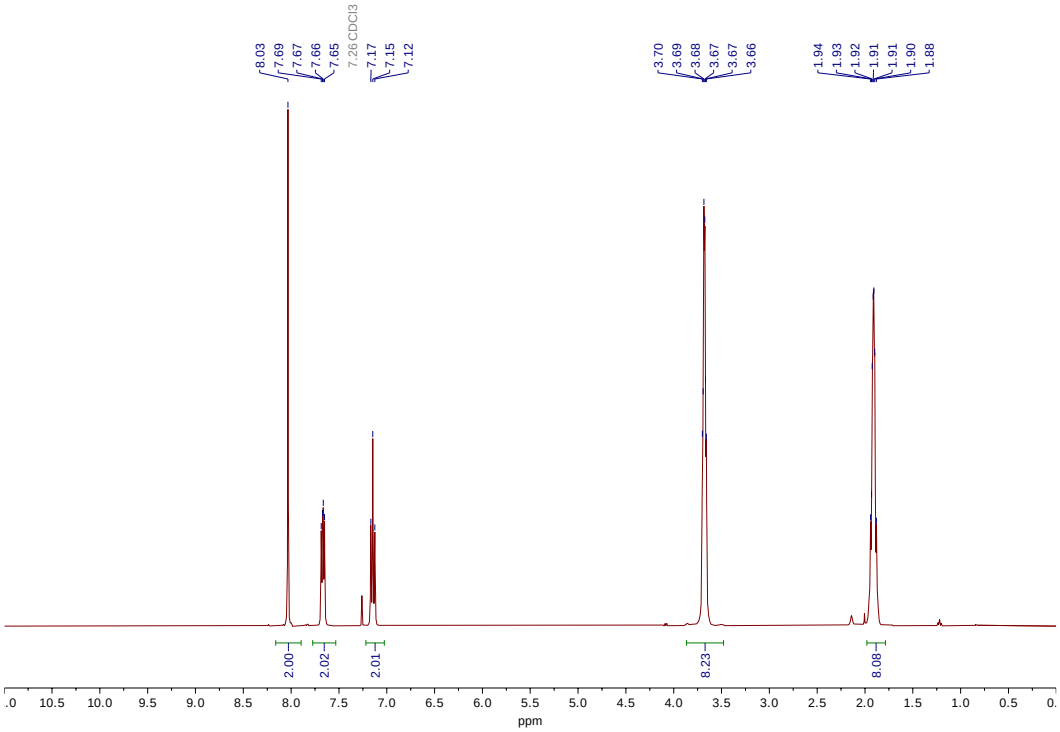

Figure 3.20 ^{1}H NMR spectrum of **9**.

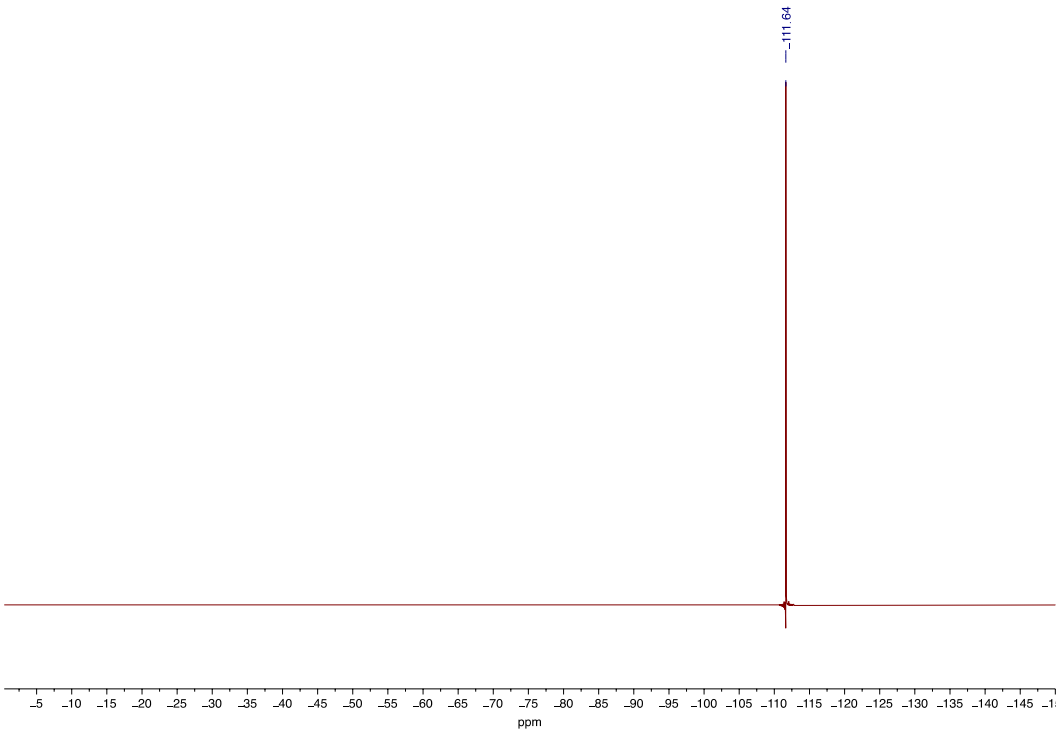

Figure 3.21 $^{19}F\{^{1}H\}$ NMR spectrum of **9**.

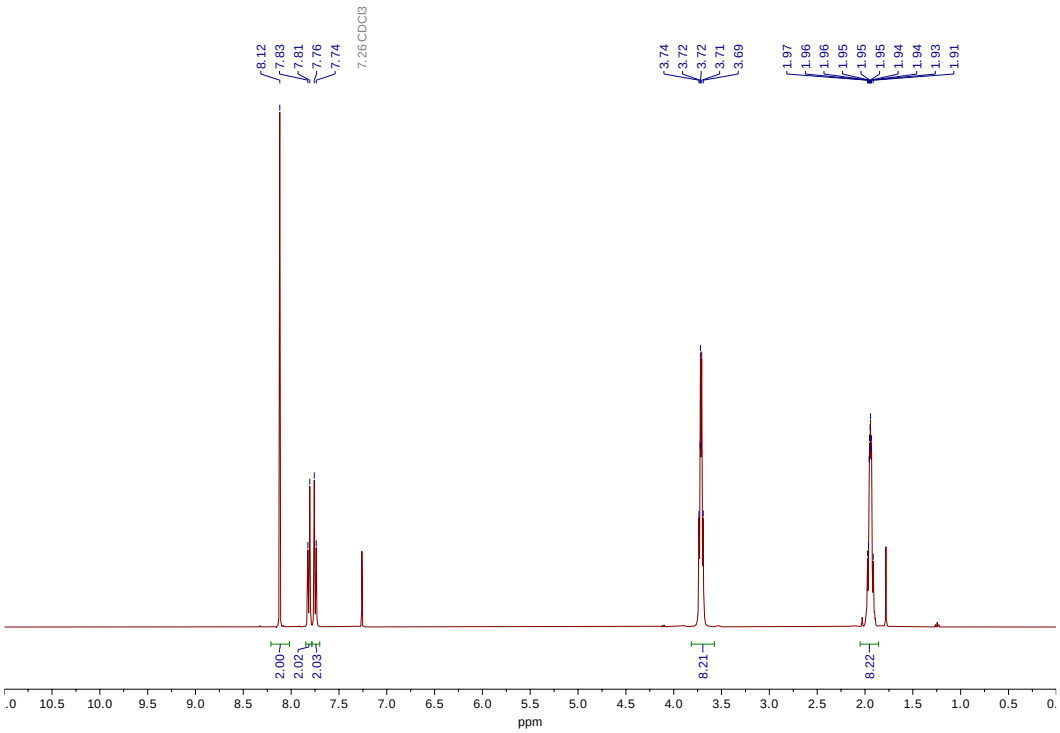

Figure 3.22 ^{1}H NMR spectrum of **10** in $CDCl_3$.

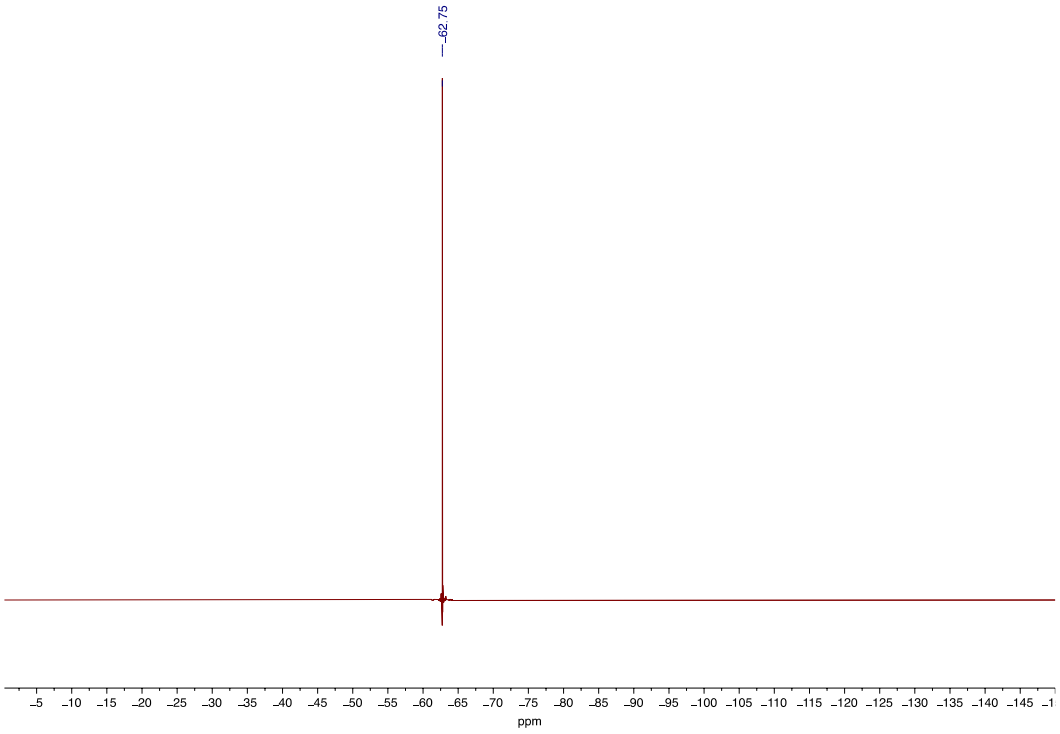

Figure 3.23 $^{19}F\{^{1}H\}$ NMR spectrum of **10** in $CDCl_3$.

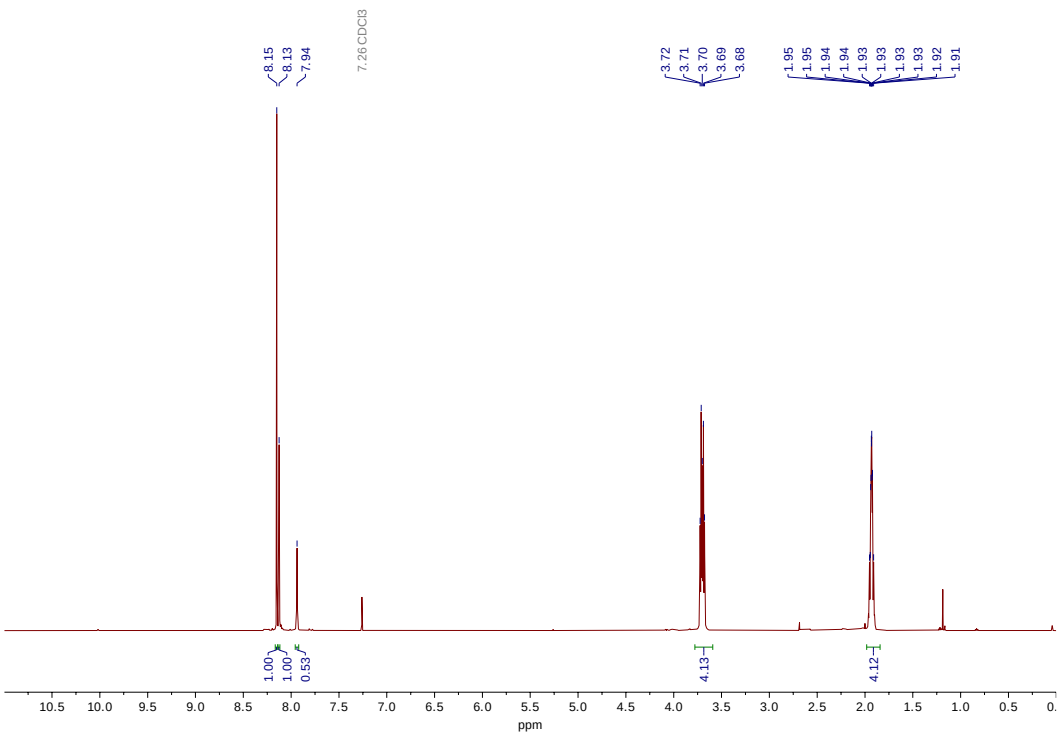

Figure 3.24 ^{1}H NMR spectrum of **11** in $CDCl_3$.

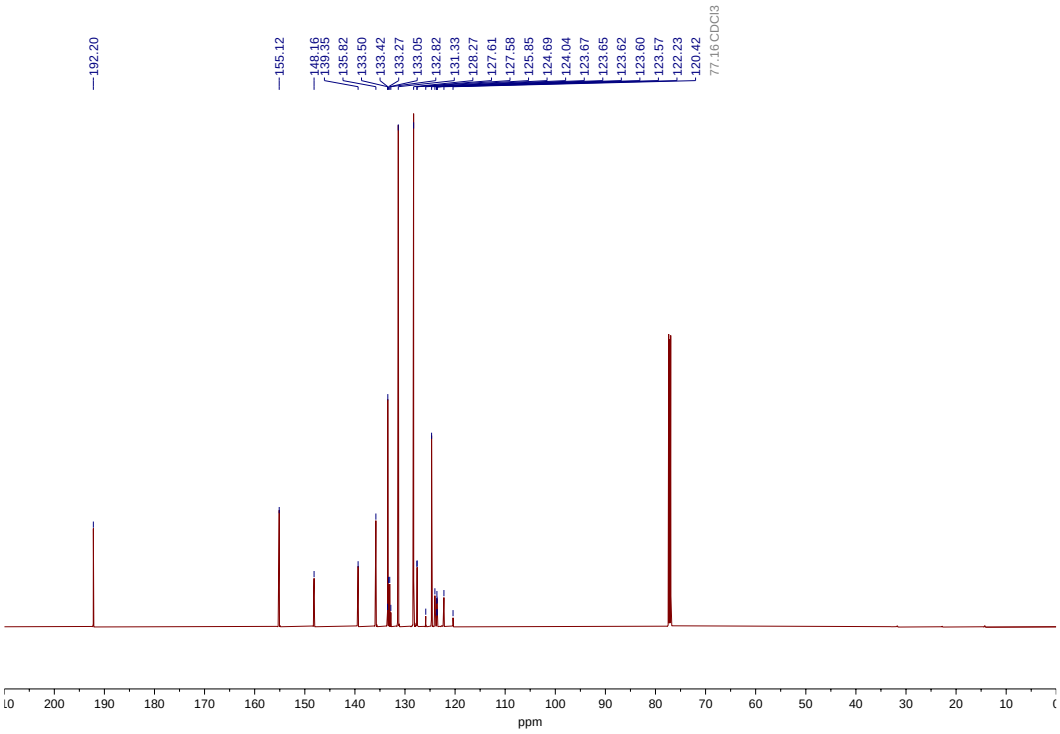

Figure 3.25 $^{13}C\{^{1}H\}$ NMR spectrum of **11** in $CDCl_3$.

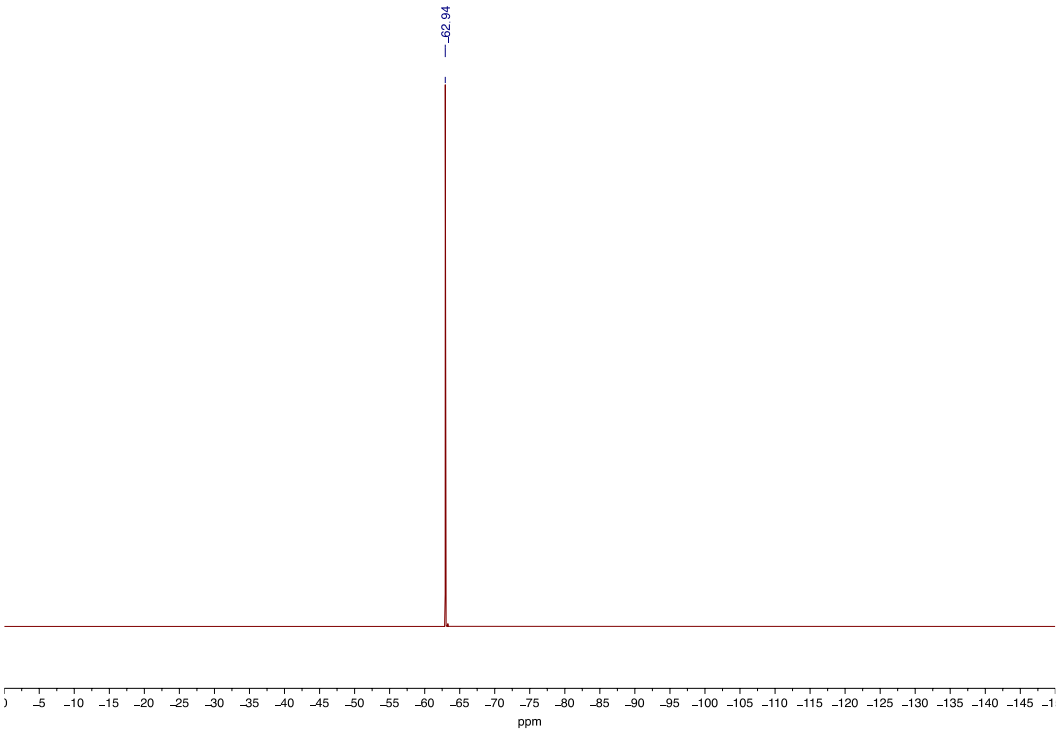

Figure 3.26 ^{19}F NMR spectrum of **11** in $CDCl_3$.

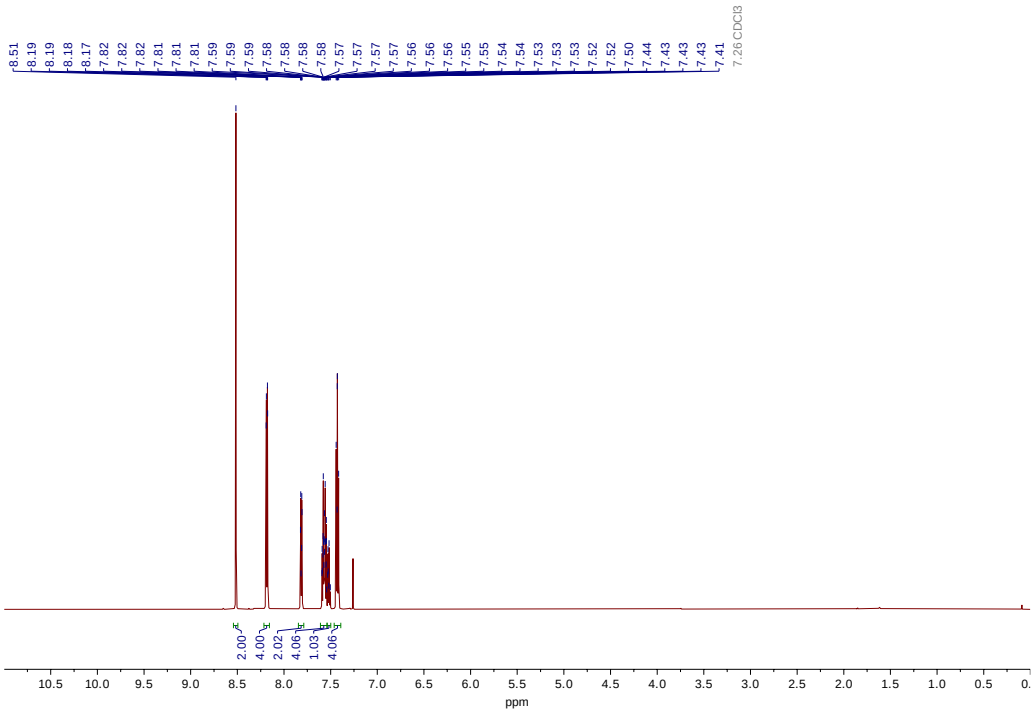

Figure 3.27 ^{1}H NMR spectrum of **4** in $CDCl_3$.

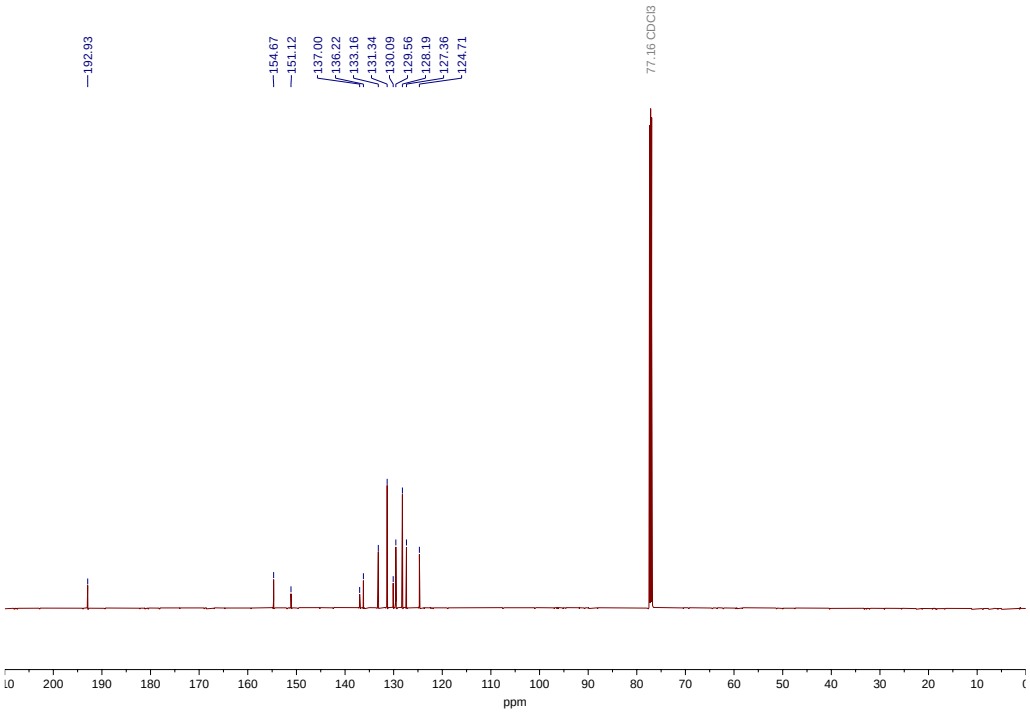

Figure 3.28 $^{13}C\{^{1}H\}$ NMR spectrum of **4** in $CDCl_3$.

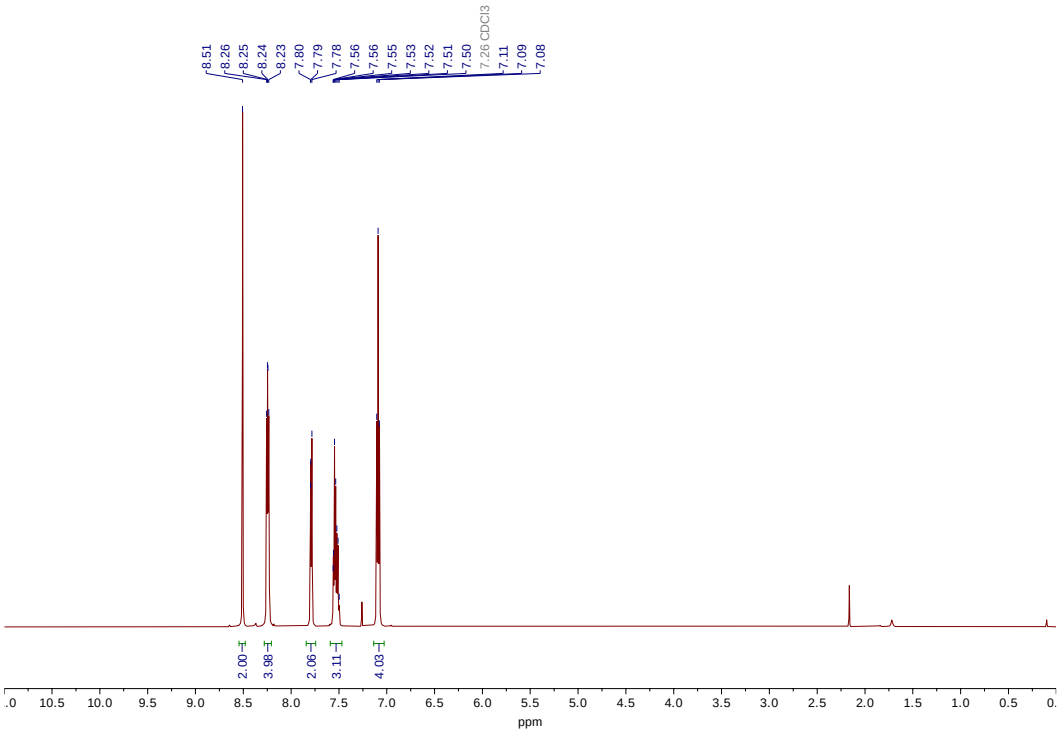

Figure 3.29 ^{1}H NMR spectrum of **12** in $CDCl_3$.

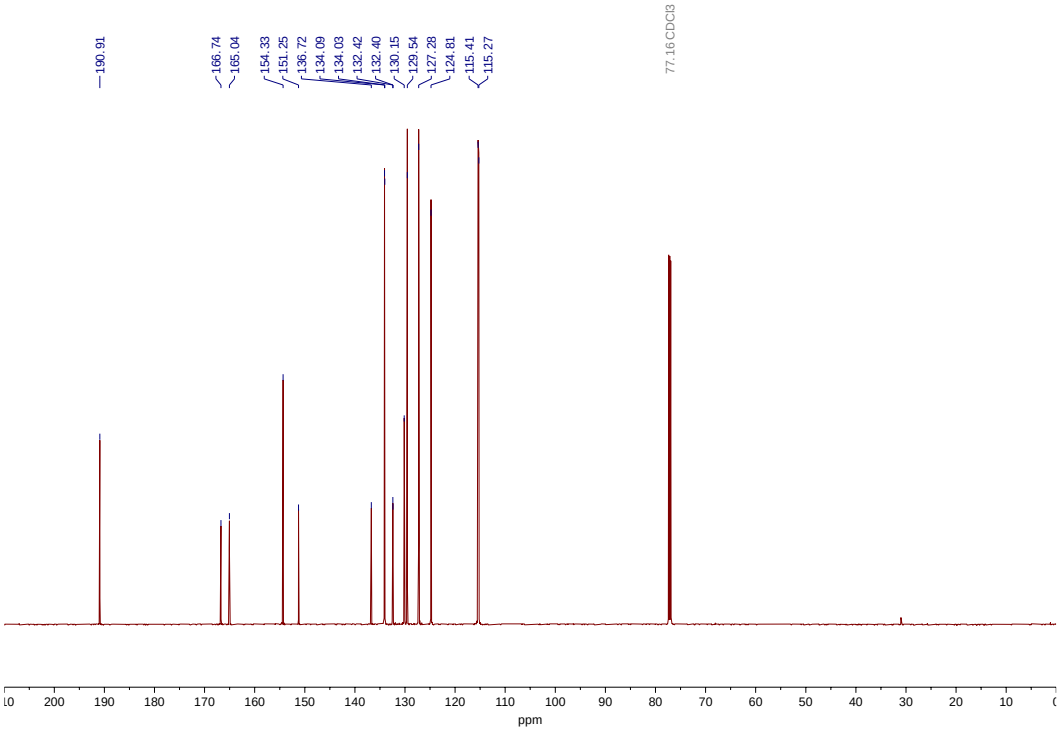

Figure 3.30 $^{13}C\{^{1}H\}$ NMR spectrum of **12** in $CDCl_3$.

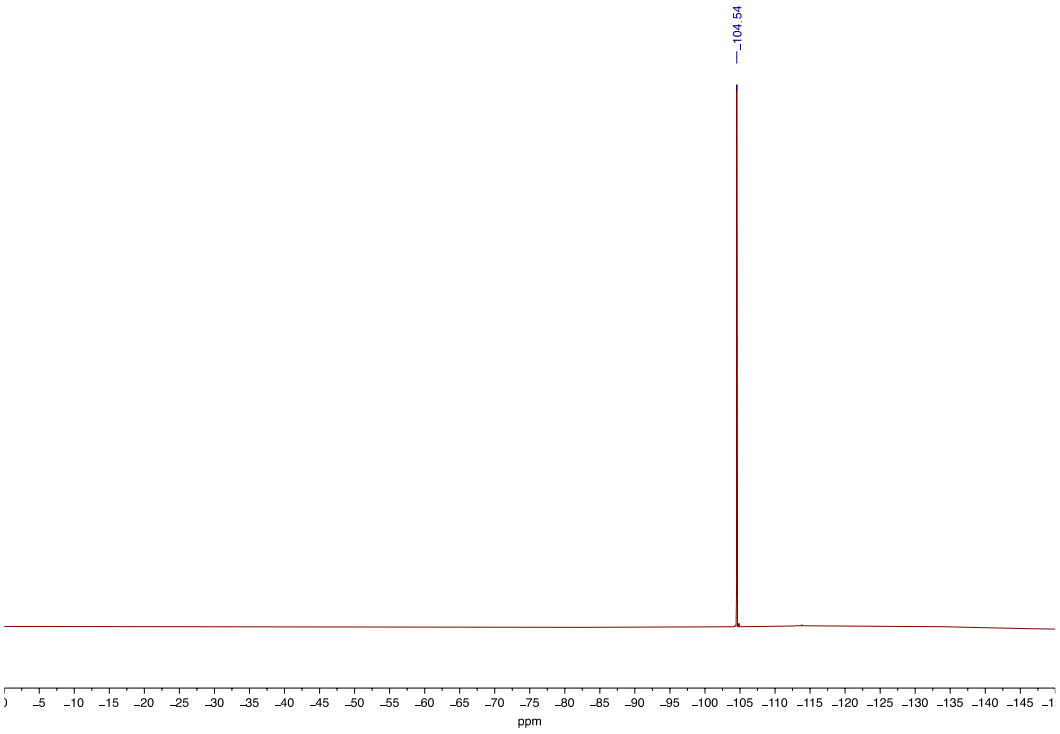

Figure 3.31 ^{19}F NMR spectrum of **12** in $CDCl_3$.

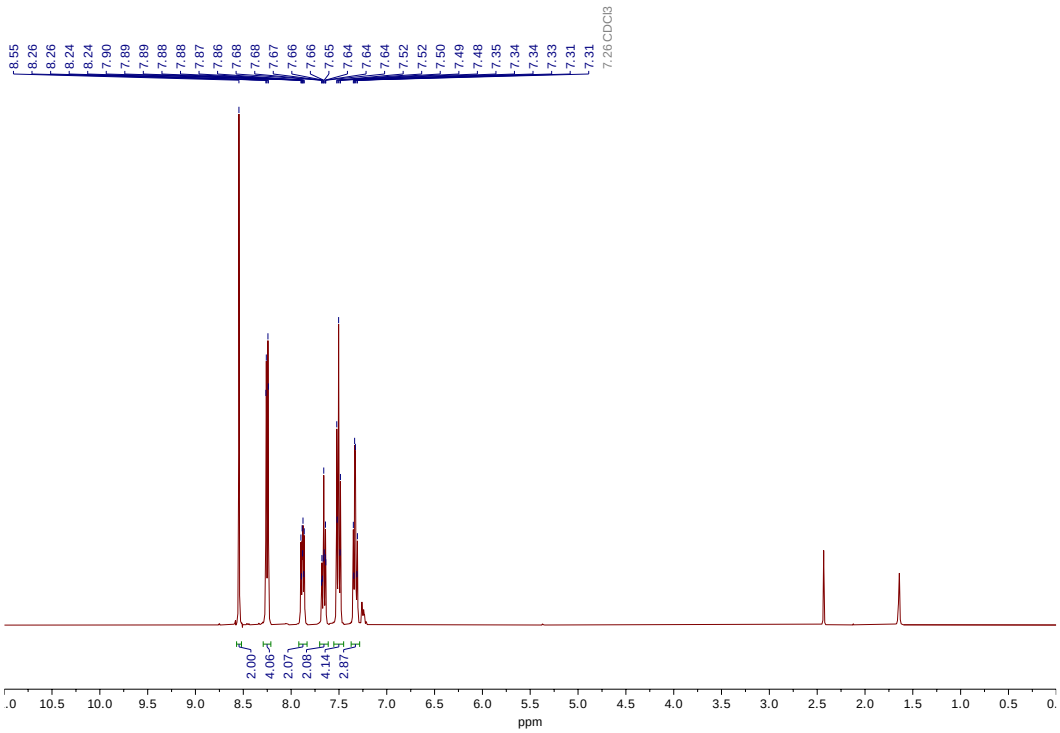

Figure 3.32 ^{1}H NMR spectrum of **13** in $CDCl_3$.

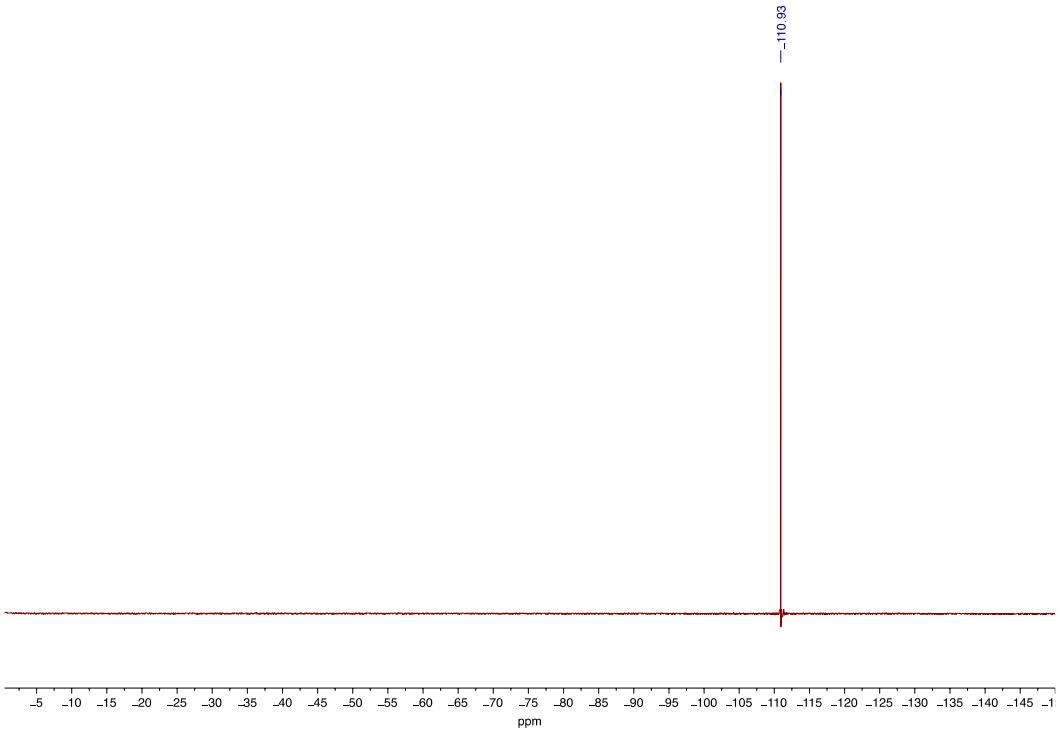

Figure 3.33 $^{19}F\{^{1}H\}$ NMR spectrum of **13** in $CDCl_3$.

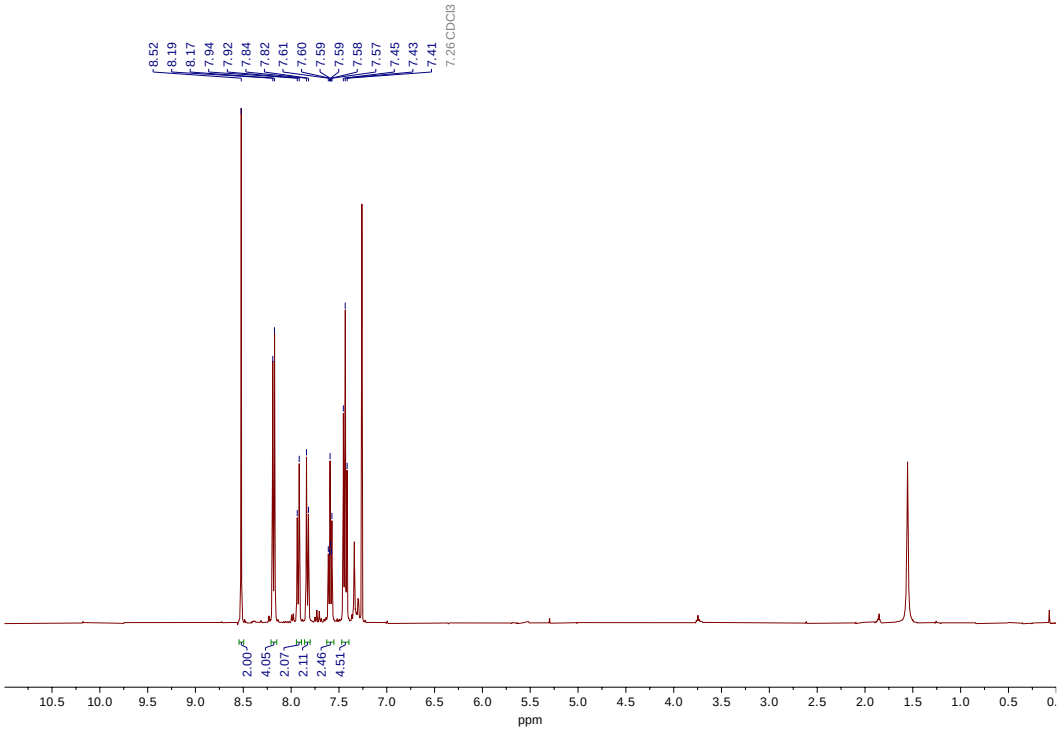

Figure 3.34 ^{1}H NMR spectrum of **14** in $CDCl_3$.

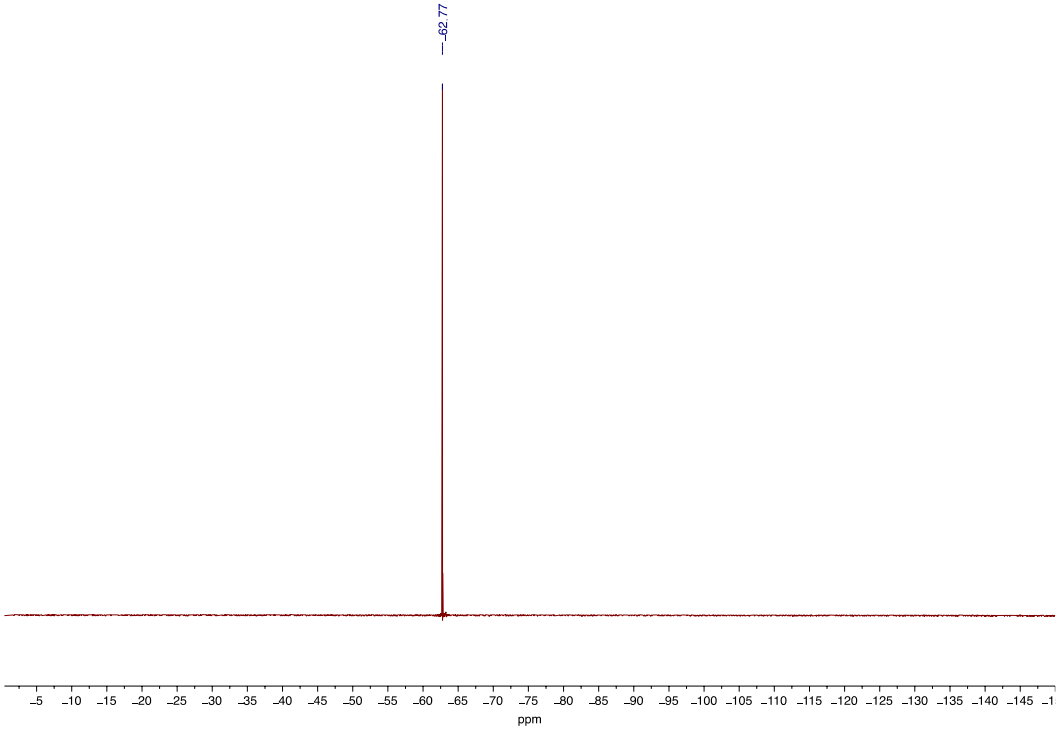

Figure 3.35 $^{19}F\{^{1}H\}$ NMR spectrum of **14** in $CDCl_3$.

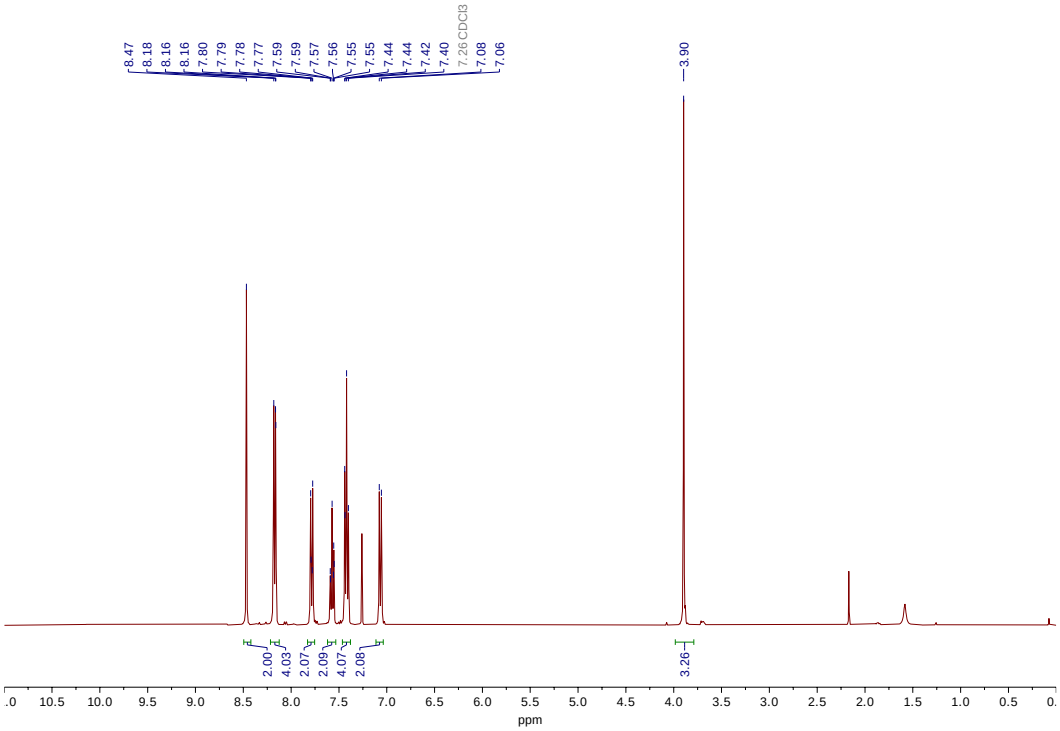

Figure 3.36 ^{1}H NMR spectrum of **15** in $CDCl_3$.

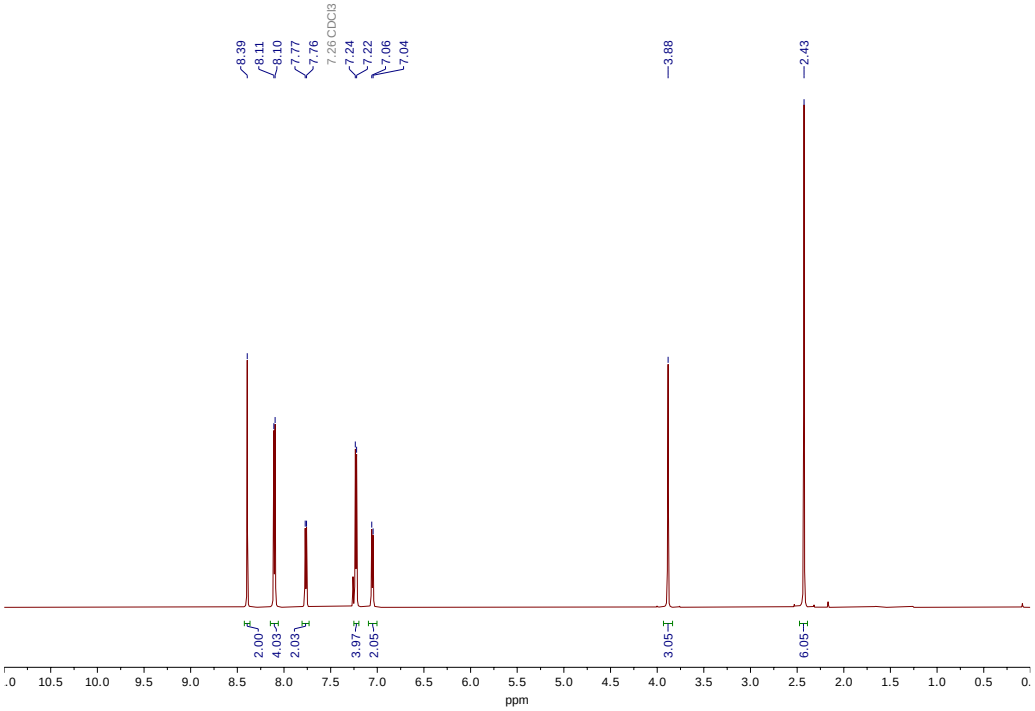

Figure 3.37 ^{1}H NMR spectrum of **16** in $CDCl_3$.

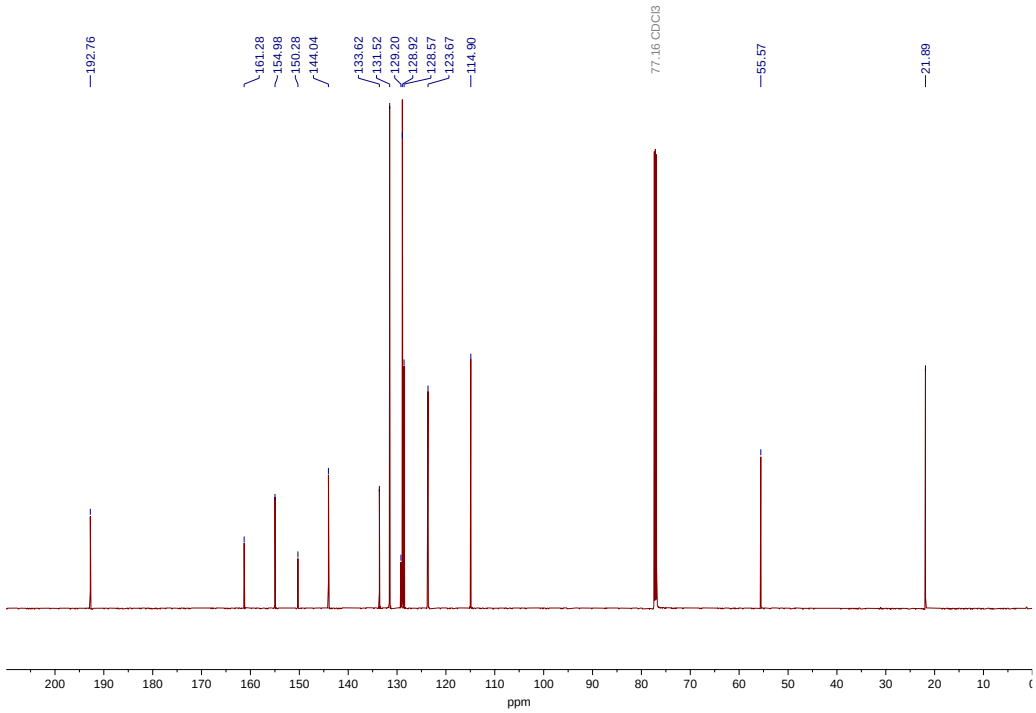

Figure 3.38 $^{13}C\{^{1}H\}$ NMR spectrum of **16** in $CDCl_3$.

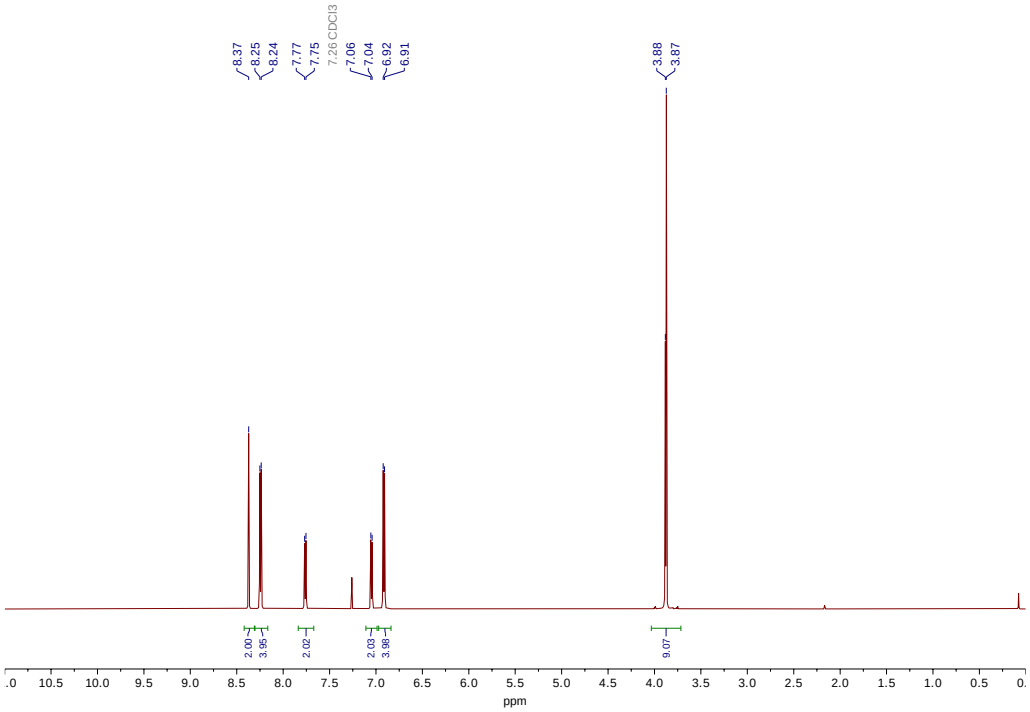

Figure 3.39 ^{1}H NMR spectrum of **17** in $CDCl_3$.

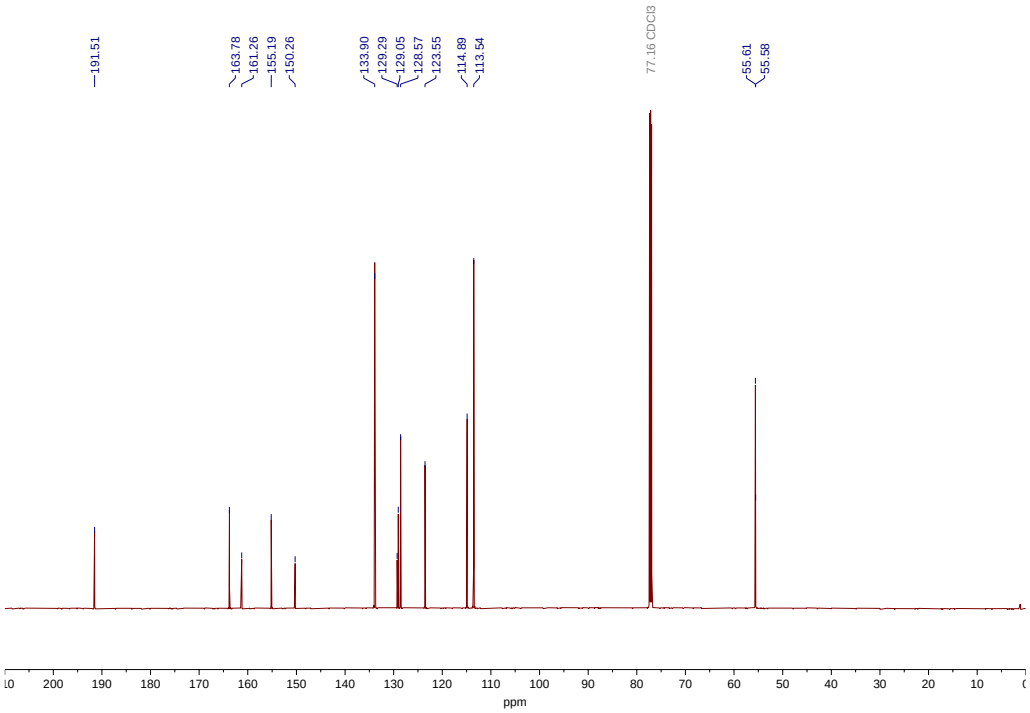

Figure 3.40 $^{13}C\{^{1}H\}$ NMR spectrum of **17** in $CDCl_3$.

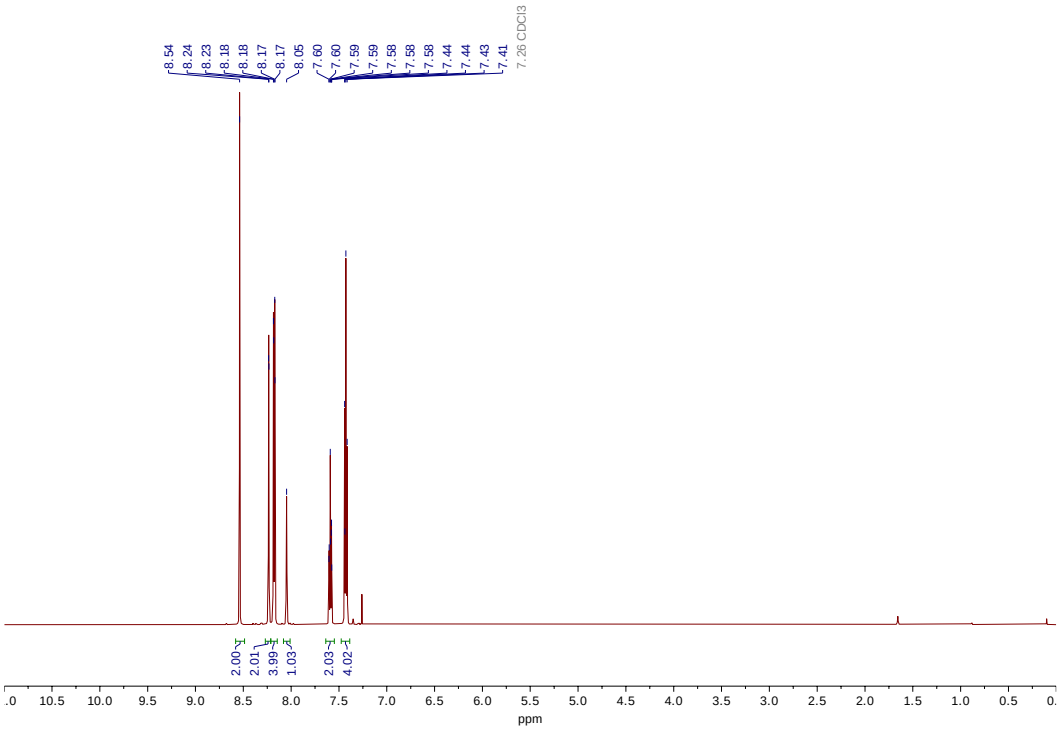

Figure 3.41 ^{1}H NMR spectrum of **18** in $CDCl_3$.

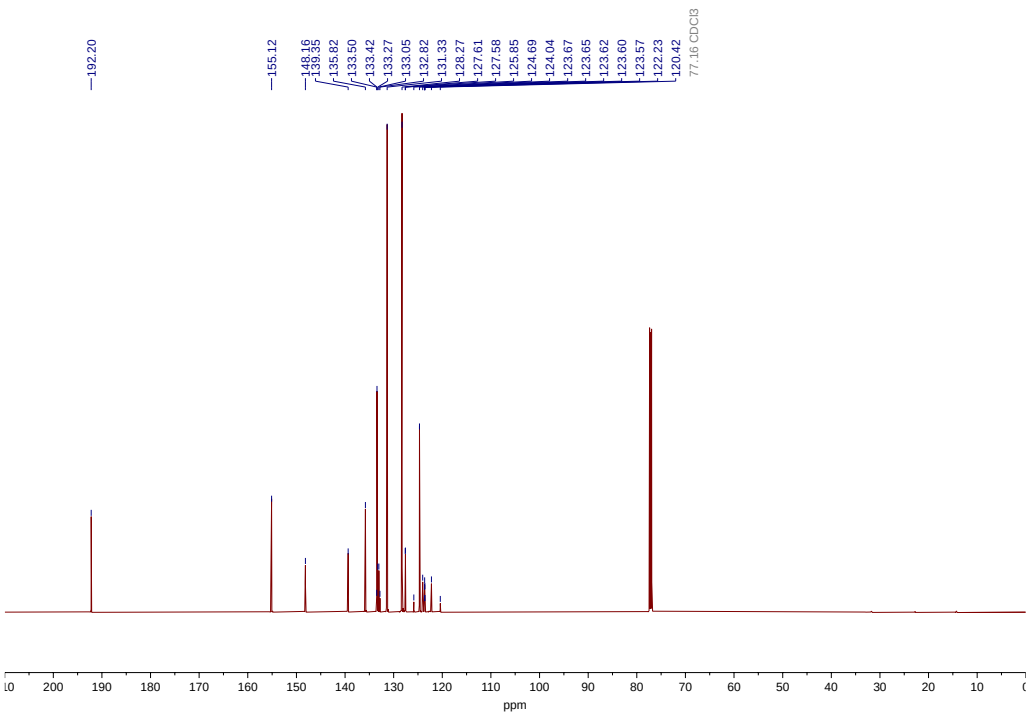

Figure 3.42 $^{13}C\{^{1}H\}$ NMR spectrum of **18** in $CDCl_3$.

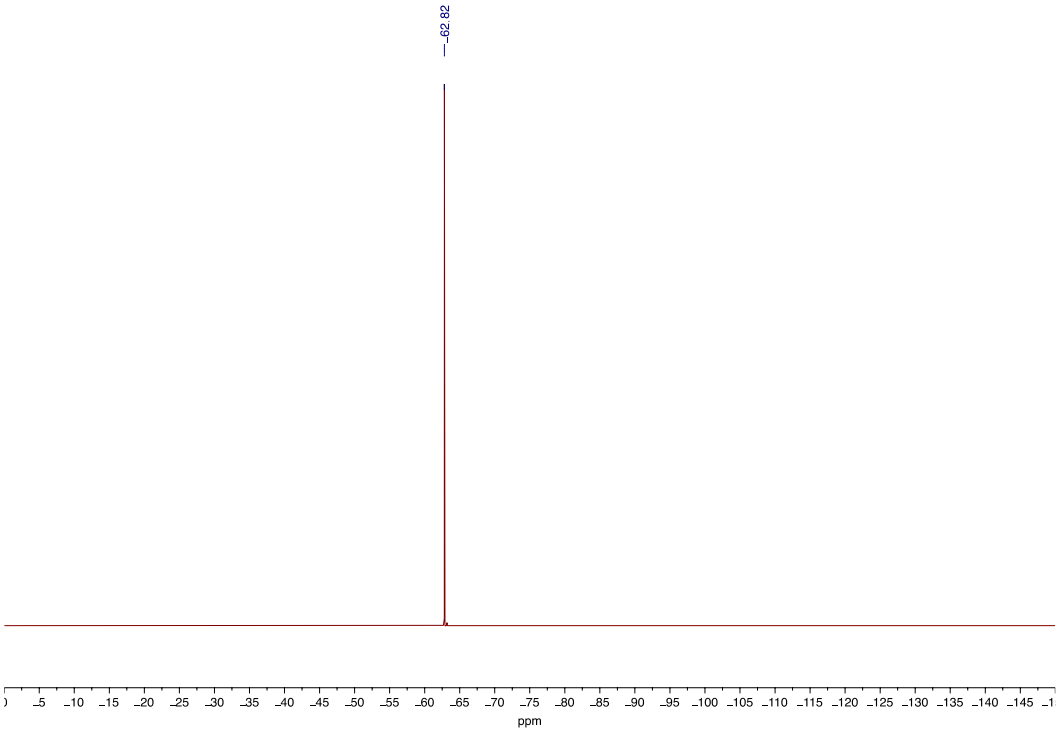

Figure 3.43 ^{19}F NMR spectrum of **18** in $CDCl_3$.

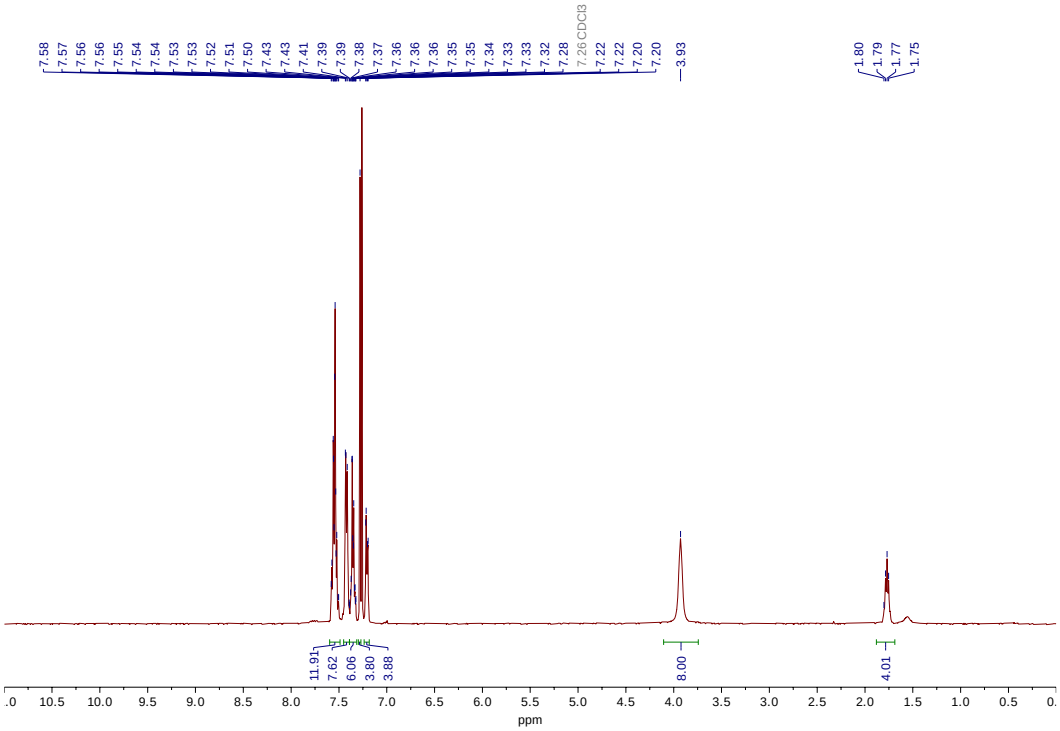

Figure 3.44 ^{1}H NMR spectrum of **5** in $CDCl_3$.

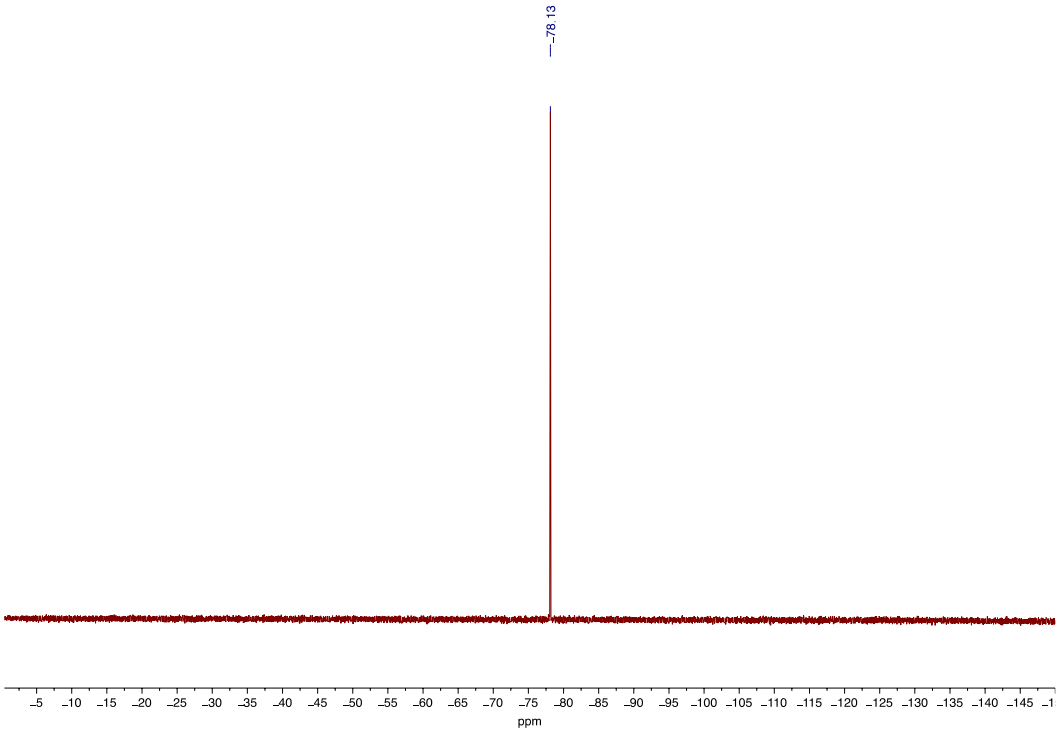

Figure 3.45 $^{19}F\{^{1}H\}$ NMR spectrum of **5** in $CDCl_3$.

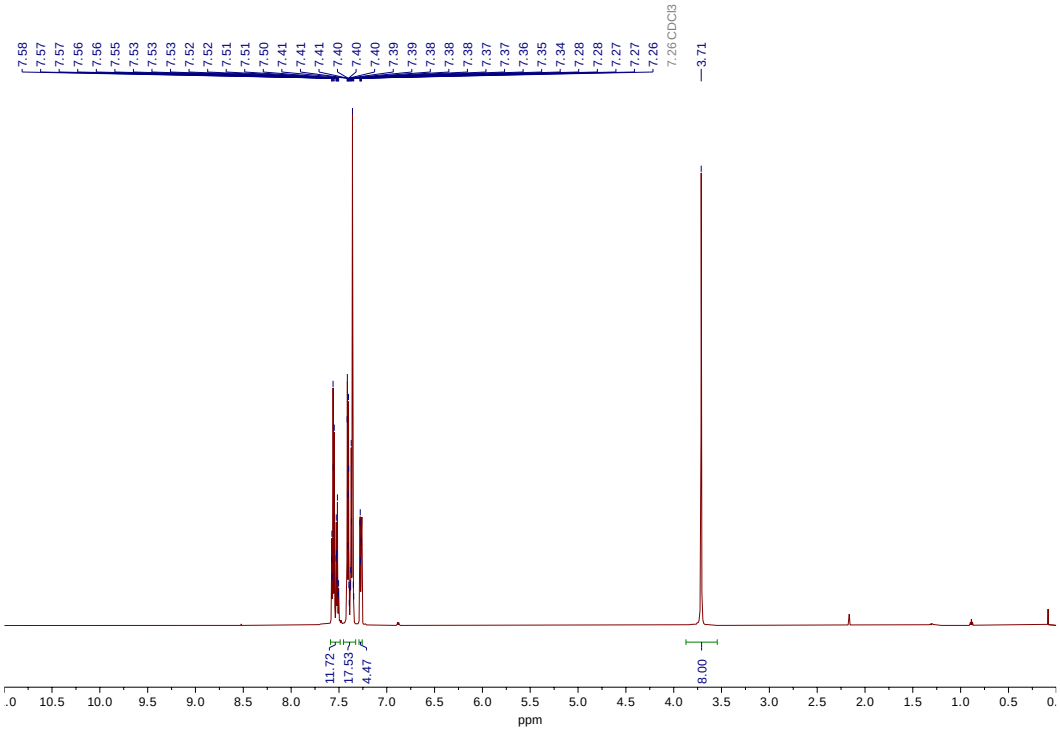

Figure 3.46 ^{1}H NMR spectrum of **19** in $CDCl_3$.

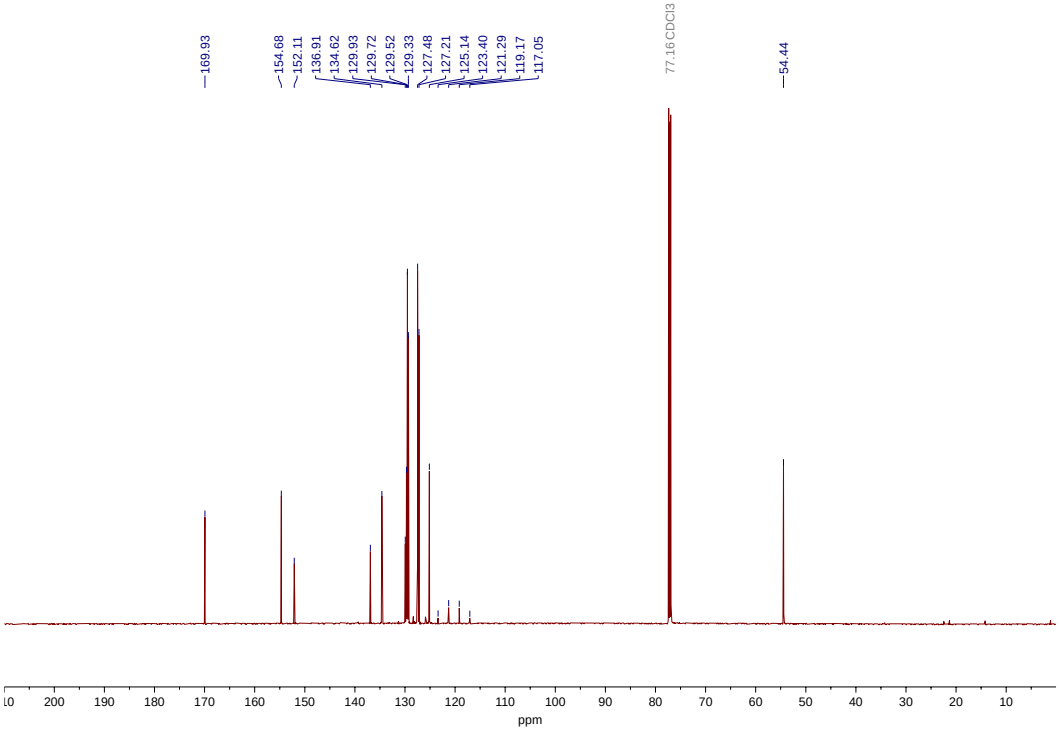

Figure 3.47 $^{13}C\{^{1}H\}$ NMR spectrum of **19** in $CDCl_3$.

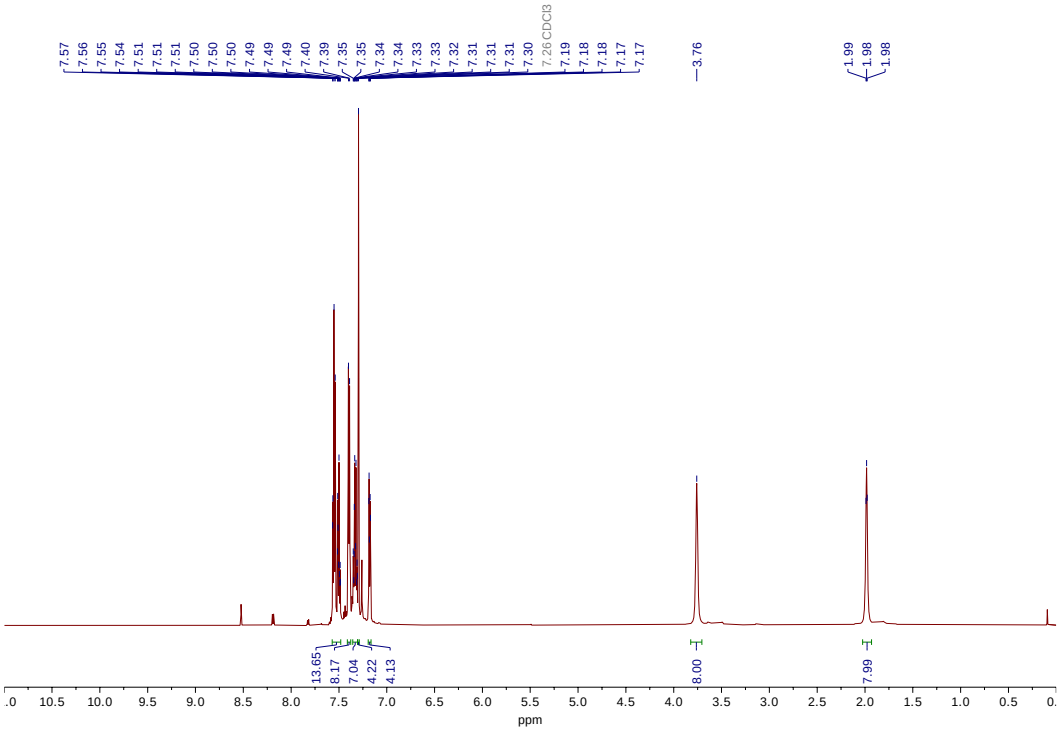

Figure 3.48 ^{1}H NMR spectrum of **20** in $CDCl_3$.

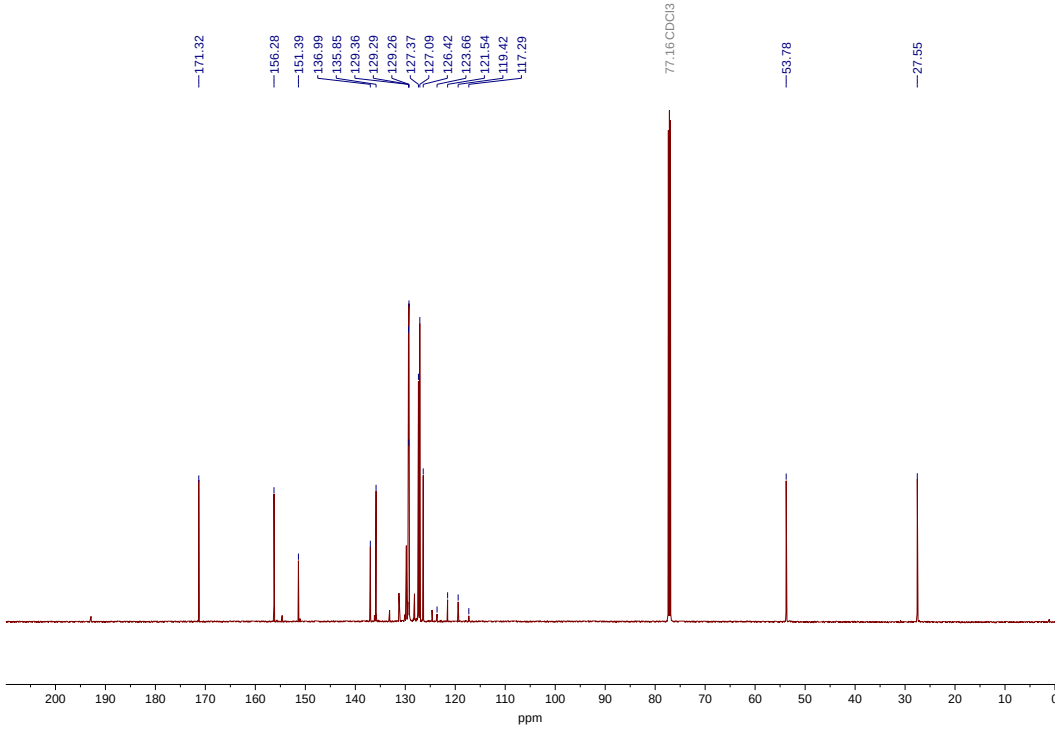

Figure 3.49 $^{13}\{^{1}H\}$ NMR spectrum of **20** in $CDCl_3$.

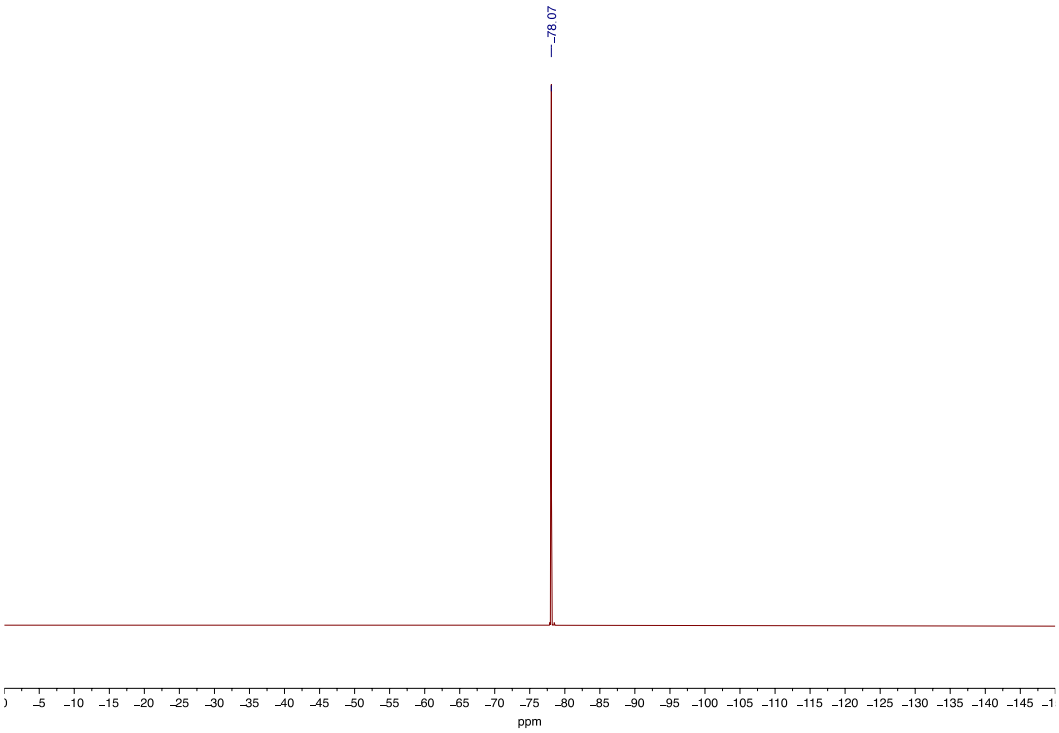

Figure 3.50 ^{19}F NMR spectrum of **20** in $CDCl_3$.

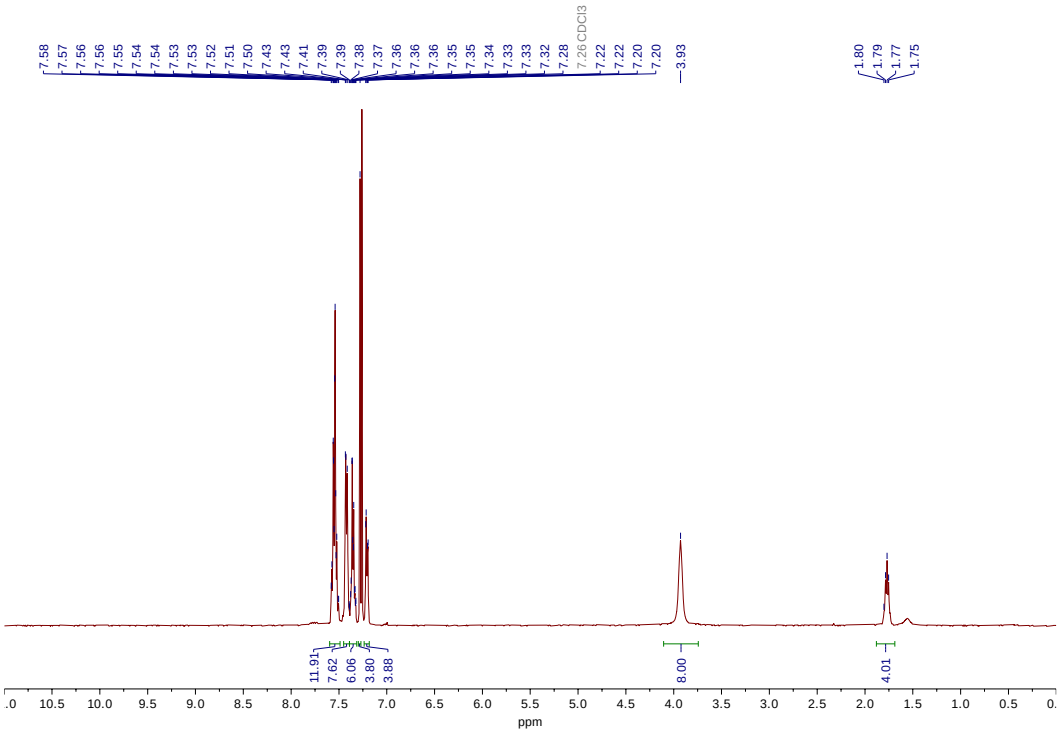

Figure 3.51 ^{1}H NMR spectrum of **21** in $CDCl_3$.

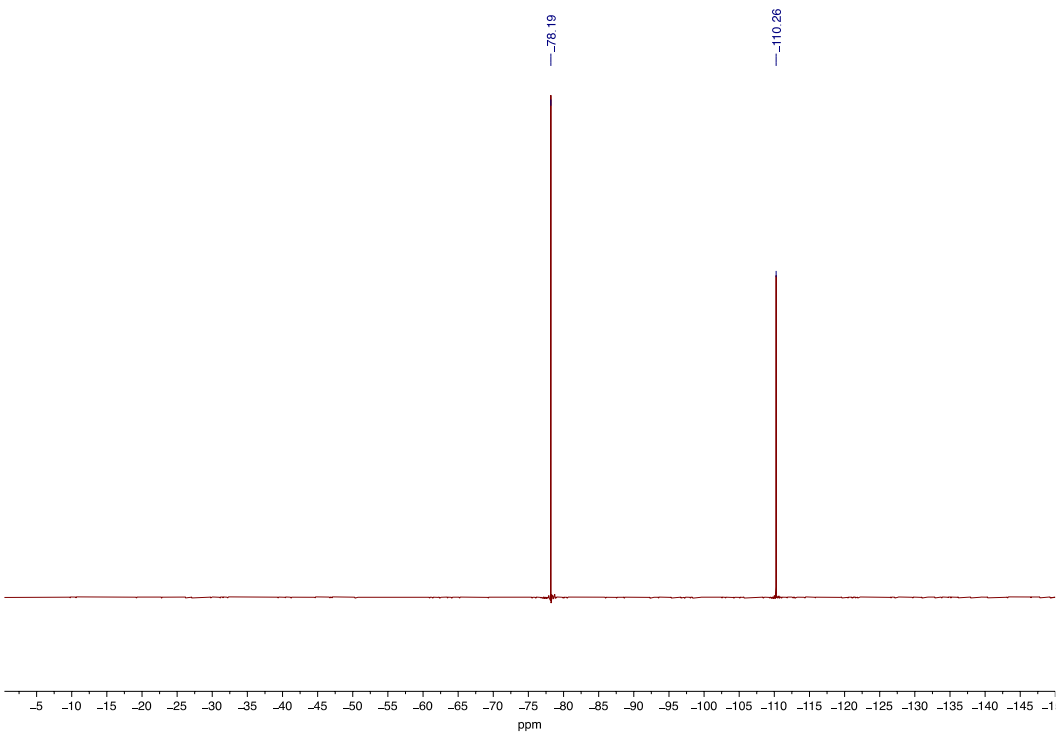

Figure 3.52 $^{19}F\{^{1}H\}$ NMR spectrum of **21** in $CDCl_3$.

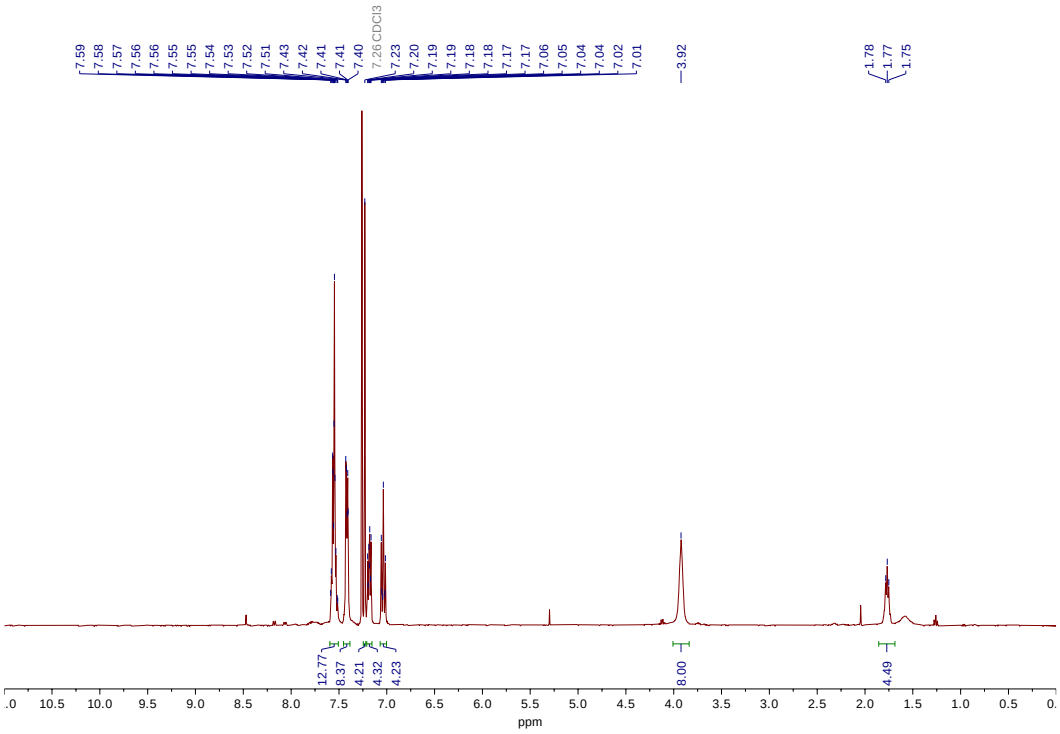

Figure 3.53 ^{1}H NMR spectrum of **22** in $CDCl_3$.

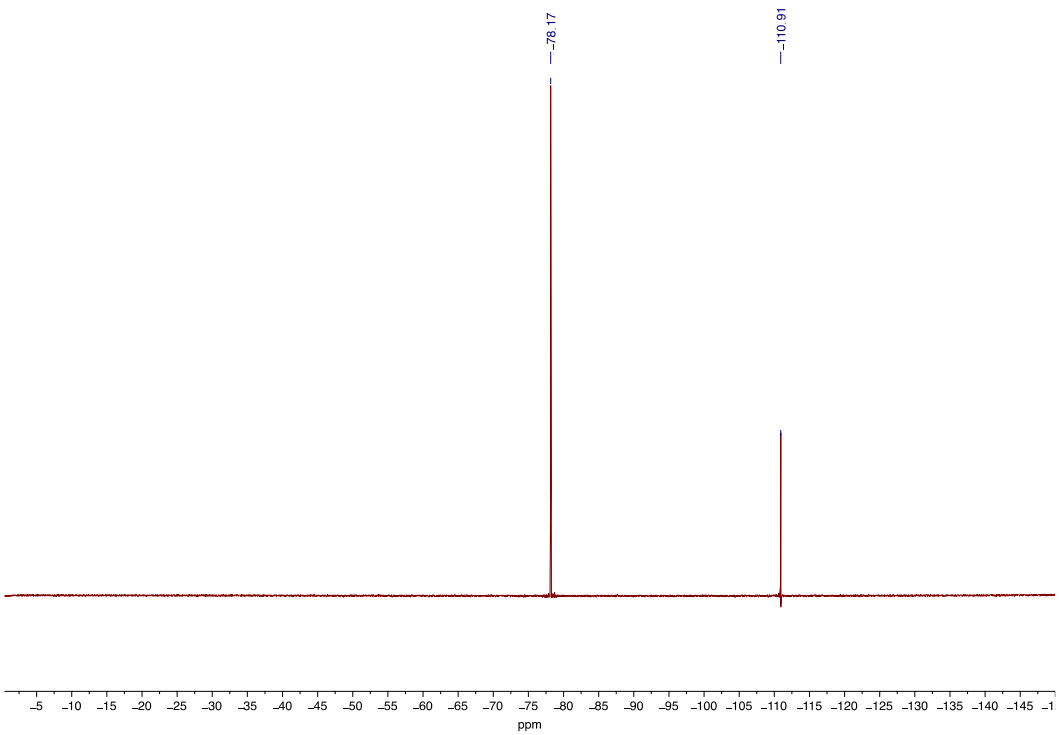

Figure 3.54 $^{19}F\{^{1}H\}$ NMR spectrum of **22** in $CDCl_3$.

3.5.4 High-Throughput Experimental Screening

Optimization of the cross-coupling of **7** and bromobenzene was carried out using a 24-well plate reaction block. Variations in Pd (pre)catalyst, base and solvent were screened amongst the 24 reactions. Reactions were carried out at on a 0.1 mmol scale (respect to **7**) at 100 °C for 2 hours. Following, the crude reactions were analyzed by LC-MS with a 4,4'-di-*tert*-butylbiphenyl internal standard (IS). The ratio of the liquid chromatography area percent (LACP) **3**:IS was used to compare the performance of each set of reagents (Table 3.1).

Table 3.1 HTE optimization of cross-coupling of **7** and bromobenzene.

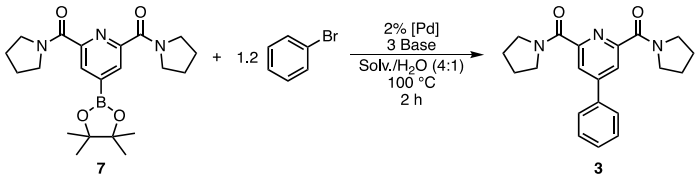

7 3

	$Pd(PPh_3)_4$	PCy_3 Pd G2	$PdCl_2$(dppf)	XantPhos $PdCl_2$	SPhos Pd G2	XPhos Pd G2
DME/K_2CO_3	11.4	12.8	13.2	12.3	13.5	13.1
DME/K_3PO_4	12.4	13.0	13.0	12.6	13.1	13.1
PhMe/K_2CO_3	10.1	9.3	11.6	7.4	12.2	9.2
DME/K_3PO_4	9.7	9.2	12.0	9.2	12.5	10.7

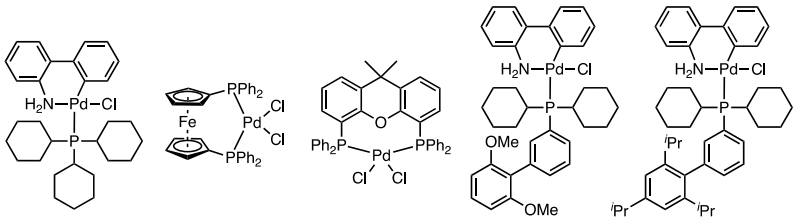

PCy_3 Pd G2 **$PdCl_2$(dppf)** **XantPhos $PdCl_2$** **SPhos Pd G2** **XPhos Pd G2**

From the reaction screen, all the combinations of reagents afforded **3** in some capacity. The best conditions of the screen (which also gave the cleanest LC-MS profile) included DME as the solvent, K_2CO_3 as the base, and SPhos Pd G2 as the Pd precatalyst. These conditions were then applied to a bench-scale reaction, in which **3** was prepared

on a 5 g scale in 81% yield (see section 3.5.2). Monitoring on large-scale showed full consumption of **7** by ^{1}H NMR spectroscopy after one hour. Of note, applying other reagent combinations to bench-scale work, albeit in lower yields. For example, when $Pd(PPh_3)_4$ is used in place of SPhos Pd G2, the yield drops to 75% on a 2 g scale. While this is a modest decrease in yield, SPhos Pd G2 remained the best performing catalyst of the series.

The same optimization was carried out, in parallel, using 4-bromoanisole in place of bromobenzene. Again, all combinations of reagents afforded the desired product **9**. The most productive combination included DME as the solvent, K_3PO_4 and SPhos Pd G2 as the Pd precatalyst. Notably, K_2CO_3 was also a suitable base in the synthesis of **9**. However, the optimal conditions afforded the cleanest LC-MS profile and were applied to bench-scale with slight modifications (see section 3.5.2).

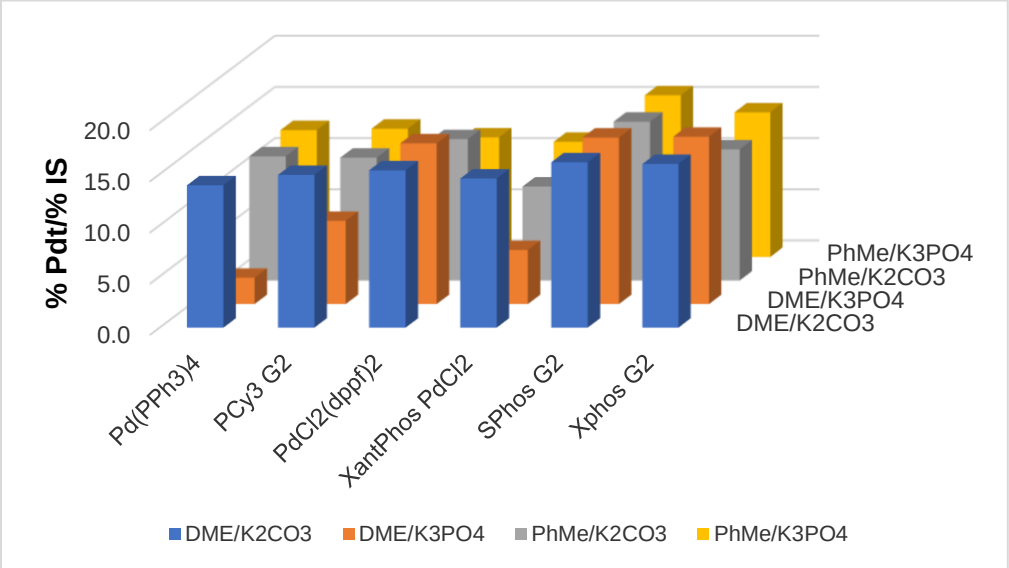

Figure 3.55 HTE screen of **7** and 4-bromoanisole cross-coupling reaction.

Table 3.2 HTE optimization of cross-coupling of **9** and 4-bromoanisole.

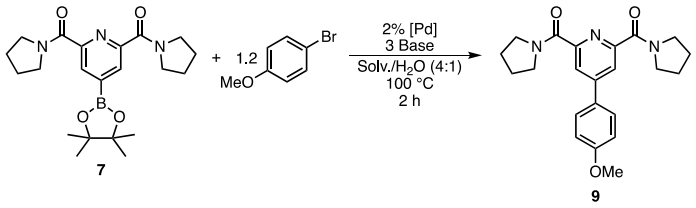

7 9

	$Pd(PPh_3)_4$	PCy_3 Pd G2	$PdCl_2$(dppf)	XantPhos $PdCl_2$	SPhos Pd G2	XPhos Pd G2
DME/K_2CO_3	13.9	14.9	15.4	14.6	16.2	16.0
DME/K_3PO_4	2.6	8.1	15.7	5.3	16.3	16.3
PhMe/K_2CO_3	12.1	12.0	13.8	9.2	15.5	12.8
DME/K_3PO_4	12.4	12.5	11.7	11.3	15.8	14.1

3.5.5 X-ray Crystallography

Table 3.3 Summary of structure determination of **5**.

Empirical formula	$C_{74.4}H_{64.4}F_{8.2}N_6O_{6.8}S_2Sr$
Formula weight	1458.86
Temperature/K	100
Crystal system	monoclinic
Space group	C2/c
a	22.1685(4)Å
b	15.3758(3)Å
c	20.8854(4)Å
β	108.228(2)°
Volume	6761.7(2)$Å^3$
Z	4
d_{calc}	1.433 g/cm^3
μ	0.942 mm^{-1}
F(000)	3004.0
Crystal size, mm	0.24 × 0.24 × 0.15
2θ range for data collection	4.76 - 56.562°
Index ranges	-29 ≤ h ≤ 29, -20 ≤ k ≤ 20, -27 ≤ l ≤ 27
Reflections collected	81775
Independent reflections	8328[R(int) = 0.0397]
Data/restraints/parameters	8328/258/585
Goodness-of-fit on F^2	1.035
Final R indexes [I>=2σ (I)]	R_1 = 0.0353, wR_2 = 0.0965
Final R indexes [all data]	R_1 = 0.0394, wR_2 = 0.0992
Largest diff. peak/hole	0.53/-0.63 $eÅ^{-3}$

CHAPTER 4 : E-H BOND (E = C, N) ACTIVATION BY LOW-TEMPERATURE STABLE DICOPPER(II,II)-μ-OXO MACROCYCLIC COMPLEXES

4.1 Introduction

The reactive Cu_2(II,II)-μ-oxo site within Cu(II)-ZSM-5 is capable of selectively oxidizing methane to methanol (see Chapter 1). Radical trapping experiments have lent evidence for a HAT mechanism, in which the μ-oxo abstracts a hydrogen atom from methane to form a Cu_2(I,II)-μ-hydroxide core that undergoes radical rebound with the methyl radical. Solomon and coworkers provided a thorough computational analysis supporting the HAT mechanism. From these computations, the driving force of the HAT reaction is the formation of the strong O–H bond (90 kcal/mol) in the generation of the mixed-valent hydroxide core.

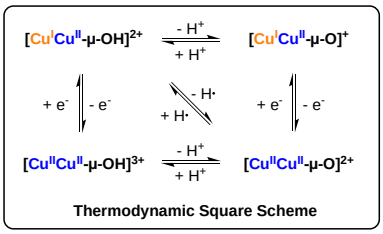

Figure 4.1 Generalized thermodynamic square scheme for a Cu_2(II,II)-μ-oxo.

Identifying copper complexes that mimic the activity of the Cu_2(II,II)-μ-oxo in Cu(II)-ZSM-5 requires an understanding of the thermodynamics of HAT processes for molecular (di)copper-oxygen complexes. Yet, it is difficult to directly measure the strength of a chemical bond. Rather, the thermodynamic square scheme approach is used to estimate bond dissociation free energies (BDFEs) in molecular examples (Figure 4.1).[105,106] The diagonal of the square scheme represents the overall BDFE associated with hydrogen atom loss/addition, which may also be viewed as separate proton and electron transfer steps. The Bordwell relationship (eq. 1) defines the BDFE of the bond of interest in terms of the relevant values of pK_a, E^0 (redox potential under standard state

conditions – 1 M and 25 °C) and C_G (a solvent dependent constant referring to the free energy change associated with H^+ reduction), which are experimentally derived thermodynamic quantities. Thus, in the case of a Cu_2(II,II)-μ-oxo, both the basicity of the unit and its oxidizing strength are important factors to consider when designing complexes for hydrogen atom abstraction.

$$\textbf{BDFE (O–H)} = 1.37p\boldsymbol{K}_a + 23.06\boldsymbol{E}^0 + \boldsymbol{C}_G \qquad (1)$$

Herein, the thermodynamic square scheme approach is applied to new Cu_2(II,II)-μ-OH complexes bearing the newly developed $^{n/Ph}PDI_2$ (n = 2,3) ligand (see Chapter 3). Although the thermodynamic square scheme has been invoked for numerous transition metal systems, few (di)copper-oxygen complexes have been studied using this approach (see sections 4.1.1 – 4.1.3). By using the modularity of the present system to develop an understand of the factors that govern hydrogen atom transfer in these complexes, this work will aid in identifying new systems that are capable of oxidizing substrates with strong C–H bonds.

4.1.1 Estimation of a Monocopper(III)-hydroxide O–H BDE

A limited number of examples are known of copper-oxygen systems with experimentally determined BDFEs. Tolman and coworkers were the first to use the Bordwell relationship in describing hydrogen atom abstraction thermodynamics by a copper-oxygen species.[107] Upon treating the copper(II) acetonitrile complex ^{PDA}**[Cu(NCMe)]^0** (PDA = N,N'-*bis*(2,6-diisopropylphenyl)-2,6-pyridinedicarboxamide) with NBu_4OH, the anionic hydroxide complex ^{PDA}**[CuOH]$^-$** was isolated. Accessing the one-electron oxidation of ^{PDA}**[CuOH]$^-$** was possible with $FcPF_6$, allowing for the generation of the formally copper(III) hydroxide complex ^{PDA}**[CuOH]^0**. ^{PDA}**[CuOH]^0** was found to react with 9,10-dihydroanthracene (DHA, C–H $BDFE_{DMSO}$ = 72.9 kcal/mol) *via* rapid C–H

activation to afford anthracene in 85% GC yield and the corresponding copper(II)-aqua complex ^{PDA}**[CuOH$_2$]^0**.

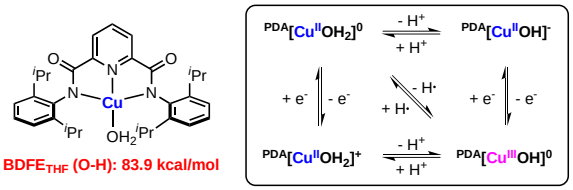

Figure 4.2 Thermodynamic square Scheme of Tolman's copper(III)-hydroxide complex (Note: BDFE was determined using C_G for THF – 59.9 kcal/mol).

The three complexes, ^{PDA}**[CuOH]$^-$**, ^{PDA}**[CuOH]^0** and ^{PDA}**[CuOH$_2$]^0** are related by part of the thermodynamic square scheme presented in Figure 4.2. Recognizing this relationship, Tolman identified the $E^{1/2}$ for ^{PDA}**[CuOH]$^-$** oxidation and pK_a of ^{PDA}**[CuOH$_2$]^0** for use in the Bordwell relationship (eq. 1).[108] A reversible one-electron oxidation event at -0.074 V (THF, vs. Fc/Fc$^+$) was observed by cyclic voltammetry (CV) at fast scan rates. Additionally, titration of ^{PDA}**[CuOH]$^-$** with [HNEt$_3$][OTf] (pK_a in THF = 12.5) allowed for determination of the pK_a of ^{PDA}**[CuOH$_2$]^0** as 18.8 ± 1.8. Together, the thermodynamic quantities were used in the calculation of the O–H BDFE of ^{PDA}**[CuOH$_2$]^0** as 83.9 ± 3 kcal/mol. (In Tolman's initial report, a solution bond dissociation enthalpy (BDE) was reported as 90 ± 3 kcal/mol under the assumption that entropic contributions were minor.)

The hydrogen atom abstraction reactivity of ^{PDA}**[CuOH]^0** was extended to substrates with C–H bond strengths varying over the range of 77-99 kcal/mol. Of note, both THF (C–H BDE = 92 kcal/mol) and cyclohexane (C–H BDE = 99 kcal/mol) underwent hydrogen atom transfer reactions with ^{PDA}**[CuOH]^0**. The methodology was later extended to 4-substituted-phenols (4-NMe$_2$, -OMe, -Me, -H, -Cl), which allowed for hydrogen atom abstraction to be observed over a broad O–H BDFE range (BDFE$_{DMSO}$ = 75.6 – 85.6 kcal/mol).[109]

Investigations into the influence of ligand substitution on the resulting O–H BDE of the hydroxyl group in ^{PDA}**[CuOH]^{0}** were also carried out by Tolman.[110, 111] Varying the electron-donating or -withdrawing ability of the PDA ligand significantly influenced the $Cu^{II/III}$ redox potential, but the experimental BDEs were largely unchanged with respect to the parent species (Figure 4.3). It was found that while the electronics of the ligand led to predictable changes in $E^{1/2}$, these changes were countered by shifts in the associated pK_a values, such that more oxidizing complexes are less basic and *vice versa*. This is known as a scaling relationship and represents a major barrier to catalyst optimization in this field of study (*vide infra*).

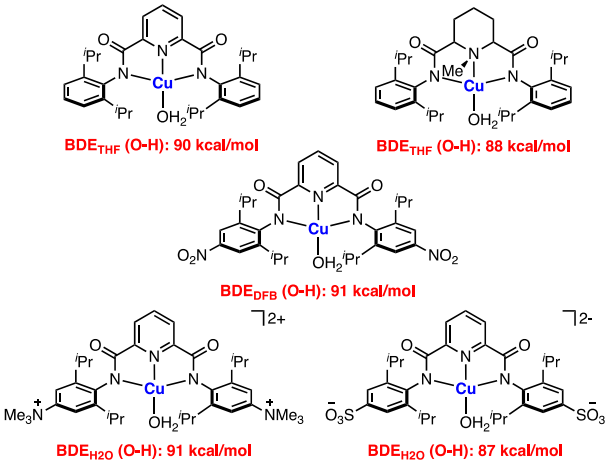

Figure 4.3 Derivatives of PDA ligand with respective BDEs (Note: Tolman and coworkers reported BDEs in all reports).

4.1.2 Cu_2(II,II)-μ-Peroxide/Hydroperoxide Couples with Estimated O–H BDFEs

Dinuclear copper-dioxygen complexes have also garnered interest with respect to hydrogen atom transfer thermodynamics. Meyer and coworkers were the first to report an estimated BDFE for the O–H bond in an electrophilic Cu_2(II,II)-μ-OOH complex. Their work made use of the pyrazolate/triazacyclononane ligand and invoked the thermodynamic square scheme shown in Figure 4.4.

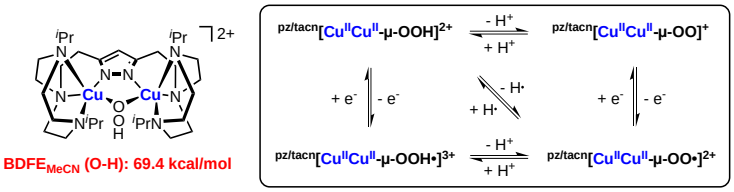

Figure 4.4 Thermodynamic square scheme of Meyer's hydroperoxide complex.

Meyer's analysis began with evidence for reversible protonation of the Cu_2(II,II)-μ-(1,2-peroxide) complex $^{pz/tacn}$**[Cu$_2$OO]$^+$**.[112] Full protonation of $^{pz/tacn}$**[Cu$_2$OO]$^+$** was achieved using 2,6-lutidinium triflate (pK_a = 14.16 in MeCN). The product, $^{pz/tacn}$**[Cu$_2$OOH]$^{2+}$**, was structurally and spectroscopically characterized. The pK_a of $^{pz/tacn}$**[Cu$_2$OOH]$^{2+}$** was determined by monitoring the treatment of the hydroperoxide complex with tetramethylguanidine (TMG, pK_{aH} = 23.35 in MeCN) with UV-vis-NIR spectroscopy. Equilibrium mixtures were observed upon titrating increasing amounts of TMG into a solution of $^{pz/tacn}$**[Cu$_2$OOH]$^{2+}$**, allowing for a pK_a estimate of 22.2 ± 0.3 to be obtained. This value is indicative of a basic peroxide unit in MeCN. Electrophilic reactivity of $^{pz/tacn}$**[Cu$_2$OOH]$^{2+}$** was also observed through the quantitative conversion of PPh_3 to PPh_3O.

Electrochemical analysis was also performed on $^{pz/tacn}$**[Cu$_2$OOH]$^{2+}$**.[113] Its cyclic voltammogram revealed a reversible one-electron oxidation feature at $E^{1/2}$ = -0.59 ± 0.02 V. The oxidation event was chemically accessible with an equivalent of $AgBF_4$, generating the superoxide species $^{pz/tacn}$**[Cu$_2$OO·]$^{2+}$** at -20 °C. The superoxide was characterized by X-ray crystallography, UV-vis-NIR, Resonance Raman and EPR spectroscopy. With both the pK_a and $E^{1/2}$ measurements, Meyer and coworkers used eq. 1 to estimate the O–H BDFE of $^{pz/tacn}$**[Cu$_2$OOH]$^{2+}$** as 69.4 ± 1.1 kcal/mol.

In line with the complex's reported O–H BDFE, $^{pz/tacn}$**[Cu$_2$OOH]$^{2+}$** was found to react with the 2,4,6-tri-*tert*-butylphenoxyl radical (2,4,6-tri-*tert*-butylphenol O–H BDFE$_{MeCN}$

= 74.8 kcal/mol) to afford $^{pz/tacn}$**[Cu$_2$OO·]$^{2+}$**. The superoxide complex was found, in turn, to be reactive towards the weaker E-H bonds of TEMPOH (O–H BDFE$_{MeCN}$ = 66.0 kcal/mol) and phenylhydrazine (N–H BDFE$_{MeCN}$ = 67.3 kcal/mol). The steric profiles of both $^{pz/tacn}$**[Cu$_2$OO·]$^{2+}$** and the HAT reagents were postulated to play a major role in the kinetics of the HAT reactions. Although the N–H BDFE of phenylhydrazine is higher than the O–H BDFE of TEMPOH, HAT was found to occur ~6 times faster for phenylhydrazine, presumably due to its decreased steric profile.

More recently, Karlin and coworkers reported an analogous study on a Cu$_2$(II,II)-μ-OOH unit supported by the XYLO ligand framework (XYLO = 2,6-*bis*(2-{2-pyridyl}ethyl)amine)phenolate).[114] The complex ^{XYLO}**[Cu$_2$OOH]$^{2+}$** sits on a thermodynamic square scheme like Meyer's system (Figure 4.5) with related, accessible μ-peroxide (^{XYLO}**[Cu$_2$OO]$^{+}$**) and μ-superoxide (^{XYLO}**[Cu$_2$OO·]$^{2+}$**) complexes. A full deprotonation of ^{XYLO}**[Cu$_2$OOH]$^{2+}$** to ^{XYLO}**[Cu$_2$OO]$^{+}$** was achieved using the strong base EtP$_2$(dma) (dma = dimethylamino, EtP$_2$(dma) = (dma)$_3$P=NP(=NC$_2$H$_5$)(dma)$_2$), pK_a = 28.1 in THF). Deprotonation was found to be reversible, as mild acids such as [HDBU][B(C$_6$F$_5$)$_4$] (pK_a = 19.1 in THF) were suitable for reforming ^{XYLO}**[Cu$_2$OOH]$^{2+}$**. An equilibrium mixture was observed when using the milder base ^{t}BuP$_1$(pyrr) (pyrr = pyrrole, ^{t}BuP$_1$(pyrr) = (pyrr)$_3$P=N^{t}Bu, pK_a = 22.8 in THF). Spectroscopic titration afforded equilibrium mixtures that allowed for an estimated pK_a for ^{XYLO}**[Cu$_2$OOH]$^{2+}$** in MeTHF of 24.0 ± 0.6.

The interconversion between ^{XYLO}**[Cu$_2$OO]$^{+}$** and ^{XYLO}**[Cu$_2$OO·]$^{2+}$** was demonstrated through a chemical oxidation using dimethylferrocenium or octamethylferrocenium salts at -125 °C in MeTHF. Both oxygen-containing species were extensively characterized using UV-vis-NIR, resonance Raman, EPR and extended X-ray absorption fine structure spectroscopy. Treating ^{XYLO}**[Cu$_2$OO]$^{+}$** with a milder oxidant, the decamethylferrocenium (Cp*$_2$Fe$^+$) cation, afforded an equilibrium mixture with the oxidized ^{XYLO}**[Cu$_2$OO·]$^{2+}$**

product. A UV-vis-NIR spectroscopic titration of $Cp^*_2Fe^+$ into a solution of ^{XYLO}**[Cu$_2$OO]$^+$** afforded an estimate of $E^{1/2}$ as -0.525 ± 0.01 V. Together with the pK_a, this value was used in eq. 1 to estimate the O–H BDFE of 80.7 ± 1.5 kcal/mol.

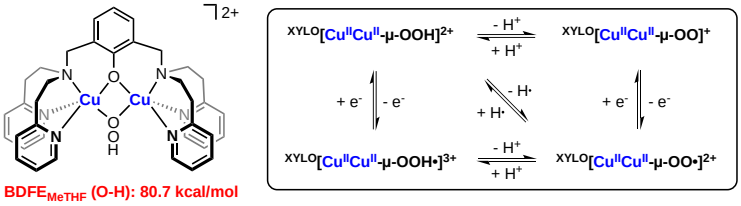

Figure 4.5 Thermodynamic square scheme of Karlin's hydroperoxide complex.

The reported O–H BDFE is relatively high for a copper-dioxygen-based system. The HAT chemistry was explored by Karlin and ^{XYLO}**[Cu$_2$OO·]$^{2+}$** was found to react with a range of substrates with varying O–H (65.4-82.0 kcal/mol) and C–H (71.1-77.6 kcal/mol) bond strengths. A substrate of note from this study is *p*-methoxyphenol (O–H BDFE$_{THF}$ = 82.0 kcal/mol). The formation of ^{XYLO}**[Cu$_2$OOH]$^{2+}$** from a substrate with a higher O-H BDFE than the value for ^{XYLO}**[Cu$_2$OOH]$^{2+}$** determined by the square scheme analysis described above lent support to the notion that the true O–H BDFE of ^{XYLO}**[Cu$_2$OOH]$^{2+}$** was similar to or higher than the phenolic O–H BDFE value. The O–H BDFE of ^{XYLO}**[Cu$_2$OOH]$^{2+}$** was further bracketed, as ^{XYLO}**[Cu$_2$OO·]$^{2+}$** was not found to react with 4-methylphenol (O–H BDFE$_{THF}$ = 85.3 kcal/mol). The higher reactivity of ^{XYLO}**[Cu$_2$OO·]$^{2+}$** compared to Meyer's $^{pz/tacn}$**[Cu$_2$OO·]$^{2+}$** was thought to be driven by the higher basicity of the superoxide ligand.

4.1.3 A Cu$_2$(II,II)-μ-O and Related HAT Reactivity

To date, the sole example of an experimentally derived O–H BDFE of a Cu$_2$(I,II)-μ-OH unit, like the one proposed to evolve in Cu-ZSM-5 during methane oxidation, involves the *in situ* generation of a Cu$_2$(II,II)-μ-oxo species. Kieber-Emmons and coworkers reported the thermodynamic square scheme shown in Figure 4.6, using the TMPA (TMPA = *tris*(2-pyridylmethyl)amine) ligand framework.[26] The Cu$_2$(II,II)-μ-OH

complex $^{TMPA}[Cu_2OH]^{3+}$ was found to be a suitable entry point into their thermodynamic analysis. Using this study, Kieber-Emmons built upon the foundation outlined in Chapter 1 (see sections 1.3 and 1.4) and found the μ-oxo complex $^{TMPA}[Cu_2O]^{2+}$ suitable for HAT chemistry.

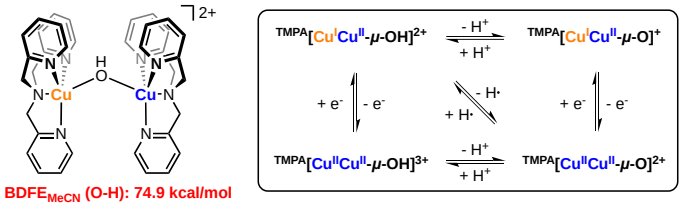

Figure 4.6 Thermodynamic square scheme of Kieber-Emmons's oxo complex.

Electrochemical measurements on $^{TMPA}[Cu_2OH]^{3+}$ were performed using cyclic voltammetry at -30 °C. Two notable redox events were observed in the cyclic voltammogram. A one-electron reversible reduction event at -0.48 V followed by an irreversible reduction event at -0.70 V. These two features were assigned as the Cu(II,II)/Cu(I,II) and Cu(I,II)/Cu(I,I) redox couples. Thus, the event at -0.48 V gave a reasonable estimate of $E^{1/2}$ for the Bordwell relationship, as the one-electron reduction of $^{TMPA}[Cu_2OH]^{3+}$ would afford $^{TMPA}[Cu_2OH]^{2+}$ on the thermodynamic square scheme.

Deprotonation of $^{TMPA}[Cu_2OH]^{3+}$ was achieved using Verkade's base, 2,8,9-triisobutyl-2,5,8,9-tetraaza-1-phosphabicyclo[3.3.3]undecane (pK_a = 33.53 in MeCN) to afford $^{TMPA}[Cu_2O]^{2+}$. The deprotonation was found to be reversible, as $^{TMPA}[Cu_2OH]^{3+}$ was formed upon treating $^{TMPA}[Cu_2O]^{2+}$ with 2,6-lutidinium triflate. Like other Cu_2(II,II)-μ-oxo complexes, $^{TMPA}[Cu_2O]^{2+}$ was EPR silent and displayed an NMR spectrum with resonances in the typical "diamagnetic" region. Using a milder base, a pK_a for $^{TMPA}[Cu_2OH]^{3+}$ was determined through spectroscopic titration measurements. In this case, DBU was found to be a suitable base for producing equilibrium mixtures of $^{TMPA}[Cu_2OH]^{3+}$ and $^{TMPA}[Cu_2O]^{2+}$. The estimated pK_a was reported as 24.3 ± 1.9, and the

corresponding O–H BDFE of $^{TMPA}[Cu_2OH]^{2+}$ was estimated as 74.9 ± 2.3 kcal/mol. The reactivity of $^{TMPA}[Cu_2O]^{2+}$ was evaluated using TEMPOH and 1,4-cyclohexadiene. $^{TMPA}[Cu_2O]^{2+}$ reacted slowly with 1,4-CHD ($BDFE_{MeCN}$ = 72.9 kcal/mol) to afford benzene in 75% yield, while quantitative formation of TEMPO was observed by EPR spectroscopy.

Kieber-Emmons later extended the analysis of $^{TMPA}[Cu_2OH]^{3+}$ by directly measuring the BDFE of the Cu_2(II,II)-μ-OH complex in MeCN (thermodynamic square scheme depicted in Figure 4.7).[115] Electrochemical measurements of *in situ* generated $^{TMPA}[Cu_2O]^{2+}$ revealed an irreversible one-electron oxidation event at 0.76 V (quasi-reversible on the square wave voltammetry timescale). Assigning this oxidation event to the formally $Cu^{II}Cu^{II}/Cu^{II}Cu^{III}$ couple, an O–H BDFE of 103.4 ± 2.6 kcal/mol was estimated for $^{TMPA}[Cu_2OH]^{3+}$ using the previously determined pK_a of 24.3 ± 1.9. Attempts at observing the mixed-valent Cu_2(II,III)-μ-oxo $^{TMPA}[Cu_2O]^{3+}$ were met with difficulty, as oxidation reactions solely afforded $^{TMPA}[Cu_2OH]^{3+}$, most likely due to $^{TMPA}[Cu_2O]^{3+}$ rapidly abstracting a hydrogen atom from the solvent.

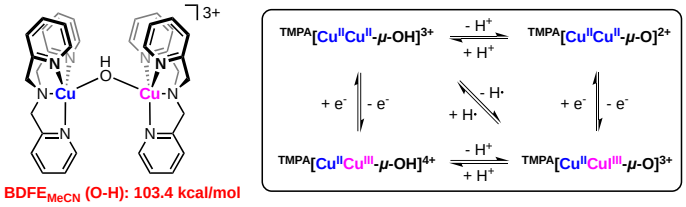

Figure 4.7 Extension of Kieber-Emmons's thermodynamics square scheme.

4.2 Synthesis of $^{3/Ph}[Cu_2OH]^{3+}$

We sought to target the isolation of a discrete Cu_2(II,II)-μ-OH complex that would provide entry into a thermodynamic square scheme analysis centered on the capacity for a Cu_2(II,II)-μ-O species to perform a hydrogen atom abstraction reaction to form a mixed-valent Cu_2(I,II)-μ-OH product. We initially approached the synthesis by applying the methods outlined Chapter 2. Treatment of a methanolic solution of $[^{3/Ph}PDI_2Sr][OTf]_2$

($^{3/Ph}$**[Sr]**$^{2+}$) with 2.0 equiv. $CuCl_2 \cdot 2H_2O$ afforded a deep green solution. Upon workup and crystallization, the green, macrocycle-supported dicopper complex [$^{3/Ph}$PDI$_2$Cu$_2$Cl$_2$][OTf]$_2$ ($^{3/Ph}$**[Cu$_2$Cl$_2$]**$^{2+}$) was isolated in good yield (Figure 4.8). Compared with the analogous species $^{3/Me}$**[Cu$_2$Cl$_2$]**$^{2+}$ (see section 2.2.1), the new phenyl derivative was less soluble in common organic solvents.

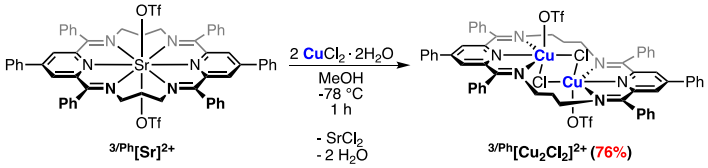

Figure 4.8 Synthesis of $^{3/Ph}$**[Cu$_2$Cl$_2$]**$^{2+}$ in MeOH.

The crystal structure of $^{3/Ph}$**[Cu$_2$Cl$_2$]**$^{2+}$ depicts the macrocyclic ligand in an unfolded conformation (as expected based on the observations in Chapter 2) with two molecules occupying the asymmetric unit (Figure 4.9). In each case, the copper(II) centers are bridged by two chloride ligands, one occupying an equatorial position and one occupying an axial position on each metal. The metals adopt distorted octahedral geometries, with elongated axial Cu–Cl (avg. 2.973(1) Å) and Cu–O (avg. 2.4308(12) Å) bond lengths due to strong Jahn-Teller distortions. The average equatorial Cu–Cl distance of 2.1997(12) Å agrees well that from $^{3/Me}$**[Cu$_2$Cl$_2$]**$^{2+}$, as does the Cu-Cl-Cu angle (avg. 77.46(4)°). In line with other isolated Cu$_2$(II,II) *bis*(pyridyldiimine) macrocycles, the average Cu–Cu distance of 3.2920(10) Å falls in the expected range (Table 2.3). The average Δ parameter of 0.185 Å also agrees with the values reported for the Cu$_2$(II,II) macrocycles described in Chapter 2, supporting a neutral ligand assignment.

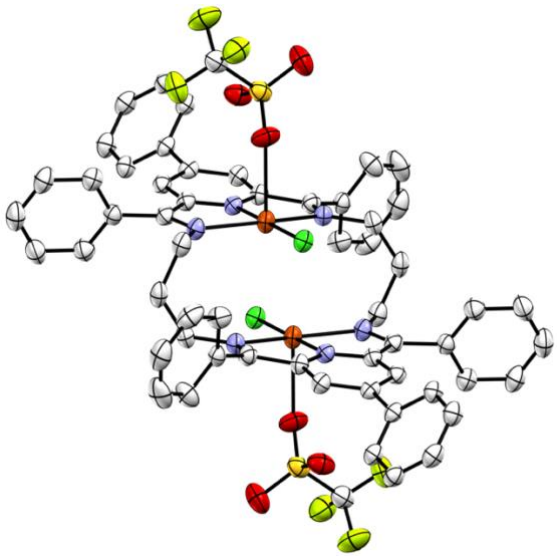

Figure 4.9 Crystal structure of $^{3/Ph}$**[Cu$_2$Cl$_2$]$^{2+}$** (thermal ellipsoids set at 50% probability; hydrogen atoms, phenyl and triflate disorder and macrocycle disorder omitted for clarity).

In pursuit of a Cu_2(II,II)-μ-OH complex, the removal of the chloride ligands was attempted to promote metathesis chemistry between the metal centers. The addition of an excess of TMS-OTf to a green acetonitrile slurry of $^{3/Ph}$**[Cu$_2$Cl$_2$]$^{2+}$** affords an insoluble, light-green macrocycle-containing material. Single crystals of the product were obtained by diffusion of Et_2O into a saturated MeCN solution. The product was identified as the Cu_2(II,II)-μ-Cl species $[^{3/Ph}PDI_2Cu_2Cl][OTf]_3$ ($^{3/Ph}$**[Cu$_2$Cl]$^{2+}$**) (Figure 4.10). As observed in Chapter 2, incomplete chloride abstraction occurred, even in the presence of excess TMS-OTf.

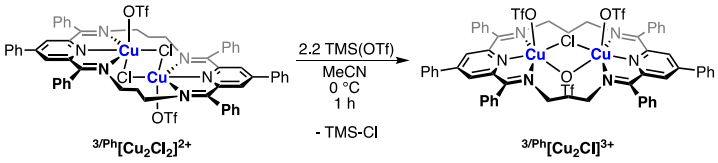

$^{3/Ph}$[Cu$_2$Cl$_2$]$^{2+}$ $^{3/Ph}$[Cu$_2$Cl]$^{3+}$

Figure 4.10 Attempt at halide abstraction from $^{3/Ph}$**[Cu$_2$Cl$_2$]$^{2+}$** in MeCN.

The crystal structure of $^{3/Ph}$**[Cu$_2$Cl]$^{3+}$** is almost identical to that of $^{3/Me}$**[Cu$_2$Cl]$^{3+}$**, except for the phenyl substitutions (Figure 4.11). The macrocycle adopts an arched conformation to accommodate the Cu_2Cl core, which exhibits a Cu–Cu distance of

3.7205(7) Å, a Cu-Cl-Cu angle of 109.00(3)°, and Cu–Cl distances of 2.2851(5) Å, which are longer than those observed in the dichloride complex $^{3/Ph}$**[Cu$_2$Cl$_2$]$^{2+}$**. A neutral ligand is assigned based on the Δ parameter of 0.184 Å.

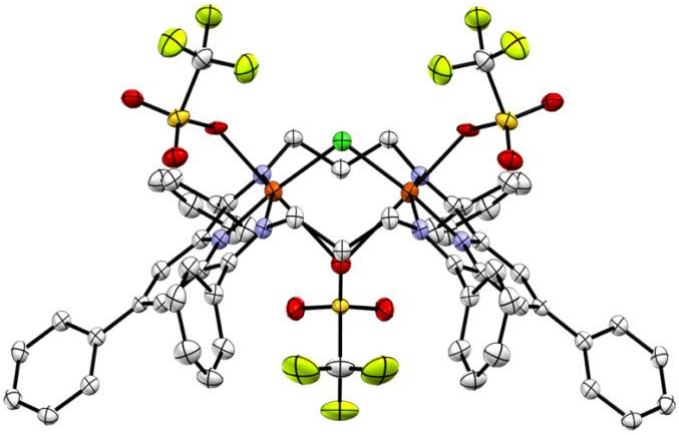

Figure 4.11 Crystal structure of $^{3/Ph}$**[Cu$_2$Cl]$^{3+}$** (thermal ellipsoids set at 50% probability; hydrogen atoms, solvent molecules, triflate disorder and macrocycle disorder omitted for clarity).

The desired hydroxide complex [$^{3/Ph}$PDI$_2$Cu$_2$OH][OTf]$_3$ ($^{3/Ph}$**[Cu$_2$OH]$^{3+}$**) was synthesized using a one-pot procedure by combining $^{3/Ph}$**[Sr]$^{2+}$**, Cu(OTf)$_2$ and NBu$_4$OH in stoichiometric ratios (Figure 4.12). The new hydroxide complex was crystallized from DCM and hexanes, affording dark green crystals that were suitable for crystallographic analysis. The solid-state structure is similar to that of $^{3/Ph}$**[Cu$_2$Cl]$^{3+}$**, with *pseudo*-C_{2v} symmetry and the two copper(II) centers residing in distorted octahedral geometries (Figure 4.13). Each is bound by axially ligated triflate anions (avg. Cu–O distance is 2.452(2) Å), with the PDI and hydroxide units occupying the equatorial plane positions. Moreover, the Cu–O(H) distances of 1.9135(14) and 1.9156(14) Å fall within the expected bond distance range for Cu$_2$(II,II)-μ-OH complexes. The ligand adopts an arched conformation to accommodate the bent dinuclear core and the Cu–Cu distance of 3.3936(7) Å. The bridging hydroxide unit is displaced from the Cu–Cu vector, creating a Cu-O(H)-Cu angle of 124.80(8)°. The Δ parameter of 0.181 Å supports a neutral ligand. Identification of the bridging hydroxide

unit as such was further supported by the observation of a low intensity, sharp stretch at 3662 cm^{-1} in the IR spectrum for this material. This features results from the O–H stretching mode and falls in the correct range for Cu_2(II,II)-μ-OH complexes.

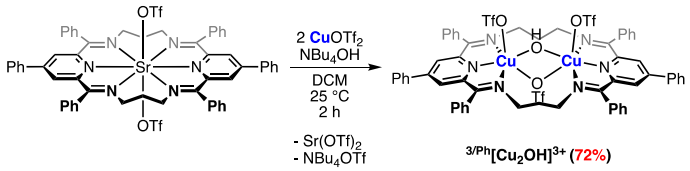

Figure 4.12 One-pot synthesis of $^{3/Ph}$**[Cu$_2$OH]$^{3+}$** in DCM.

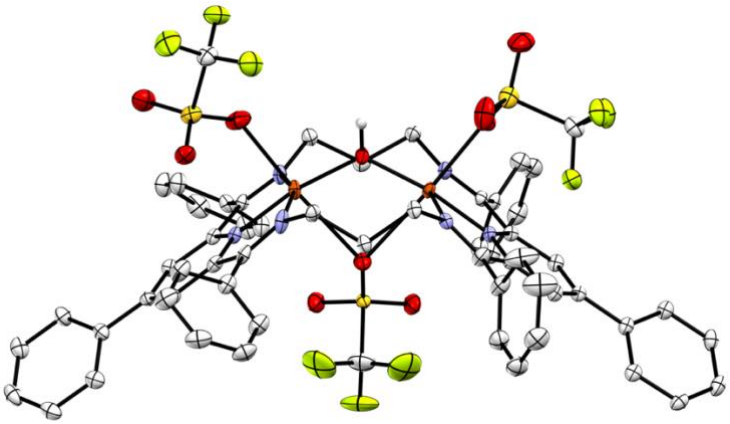

Figure 4.13 Crystal structure of $^{3/Ph}$**[Cu$_2$OH]$^{3+}$**(thermal ellipsoids set at 50% probability; hydrogen atoms, solvent molecules, and macrocycle disorder omitted for clarity).

The ^{1}H NMR spectrum of $^{3/Ph}$**[Cu$_2$OH]$^{3+}$** displays broadened and shifted resonances that likely result from the paramagnetic character of the Cu_2(II,II) species (see section 4.9.3). A shifted, broad resonance was observed as far downfield as 50.63 ppm. The UV-vis-NIR spectrum displayed an absorption profile commonly associated with Cu_2(II,II) *bis*(pyridyldiimine) complexes. A low intensity absorption band was observed at 759 nm and assigned as a d→d transition, based on its energy and intensity profiles. For similar reasons, an intense feature at 316 nm is assigned as an OH→Cu(II) LMCT transition. An intense feature were also observed at 203 nm and likely results from ligand-based π→π* transitions, based on previous studies.

4.3 Reduction of $^{n/Ph}[Cu_2OH]^{3+}$ Complexes

4.3.1 Cyclic Voltammetry Studies

A thermodynamic square scheme centered on the capacity of a *bis*(pyridyldiimine)-supported Cu_2(II,II)-μ-O species to form a mixed-valent Cu_2(I,II)-μ-OH product requires determination of both the pK_a of $^{3/Ph}[Cu_2OH]^{3+}$ and the potential of the $^{3/Ph}[Cu_2OH]^{3+/2+}$ redox couple. Cyclic voltammetry was carried out in MeCN; scanning cathodically revealed two irreversible reduction events (Figure 4.14, see section 4.8.5 for more details). The first peak ($E_{p,c1}$), at -0.510 V vs. Fc/Fc^+, was assigned as the reduction of Cu_2(II,II) to Cu_2(I,II) and the second ($E_{p,c2}$), at -0.845 V vs. Fc/Fc^+, as the reduction of Cu_2(I,II) to Cu_2(I,I). These assignments agree with Kieber-Emmons' related $^{TMPA}[Cu_2OH]^{3+}$ complex (reversible Cu_2(II,II)/Cu_2(I,II) = -0.48 V and irreversible Cu_2(I,II)/Cu_2(I,I) = -0.70 V).

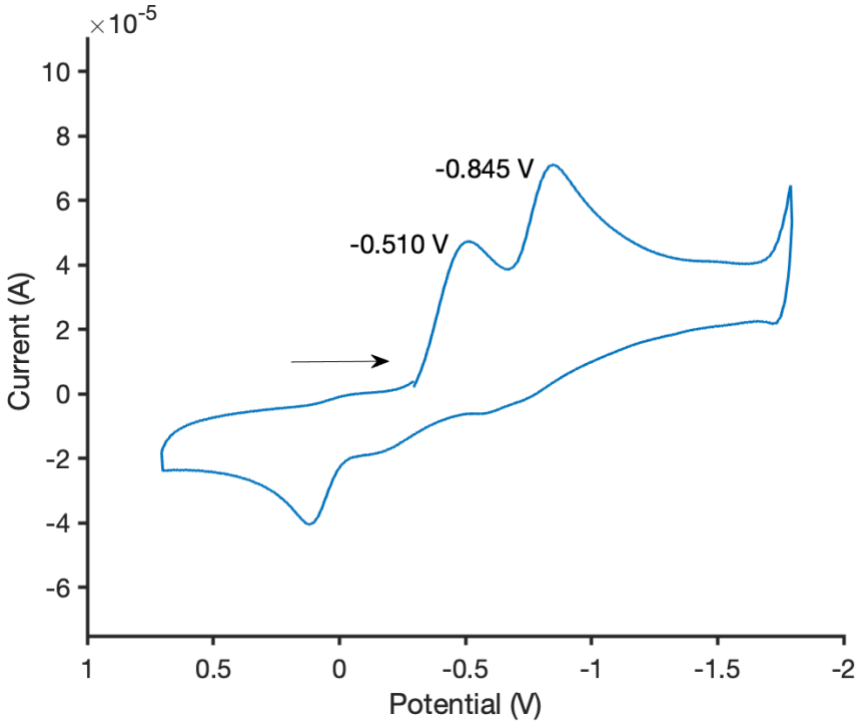

Figure 4.14 Cyclic voltammogram of $^{3/Ph}[Cu_2OH]^{3+}$ (initial Scan, 1000 mV/s scan rate).

In terms of the thermodynamic square scheme and Bordwell relationship, more positive values of E^0 would lead to larger O–H BDFEs for the mixed-valent Cu_2(I,II)-μ-OH complex $^{3/Ph}$**[Cu$_2$OH]$^{2+}$**, provided the pK_a remains the same. A useful approximation of E^0 is $E^{1/2}$ (half-wave potential) under nonstandard conditions. However, the irreversibility of the first reduction event prevents an adequate estimate of $E^{1/2}$ for the Cu_2(II,II)/Cu_2(I,II) couple. Rather, we can use $E_{p,c1}$ as a lower bound for $E^{1/2}$, meaning the BDFE derived from this square scheme analysis would represent an underestimate of the actual BDFE. The uncertainty of using irreversible redox features in the determination of BDFEs has been previously highlighted by Bordwell and coworkers and has led to an estimated ~0.6 kcal/mol uncertainty in experimentally derived BDFEs when using $E_{p,c}$/$E_{p,a}$ in place of E_0 in eq. 1.[116]

4.3.2 Chemical Reduction Studies

To identify the one-electron reduced product associated with the first reduction event, the chemical reduction of $^{3/Ph}$**[Cu$_2$OH]$^{3+}$** was carried out with Cp^*_2Fe, resulting in a dark yellow solution at -45 °C that turned deep red in color on warming. Upon crystallization of the dark red product, the monocopper(I) complex [$^{3/Ph}$PDI$_2$Cu][OTf] (**$^{3/Ph}$[Cu]$^+$**) was identified by X-ray crystallography (Figures 4.15 and 4.16). The solid-state structure depicts a unique example of a copper(I) PDI complex. The macrocyclic ligand twists in an uncharacteristic conformation to bind the Cu(I) center. Each PDI unit binds κ^2 to the metal center, with one unbound imino moiety on each pyridyl unit pointed away from the macrocyclic cavity. Because of the macrocyclic twisting, the Cu(I) center adopts a see-saw geometry (τ_4 = 0.64)[117] with an observed average Cu(I)–N bond length of 2.0438 Å. The Cu(I) oxidation state is supported by the presence of one outersphere triflate anion and a neutral ligand (Δ = 0.185 Å). Gilberton's copper(I) PDI complexes are the only

reported examples of PDI stabilizing a Cu(I) center; however, the geometries of these complexes are quite different than observed for $^{3/Ph}$**[Cu]**$^{+}$ (four-coordinate distorted square planar and five-coordinate square pyramidal).[51]

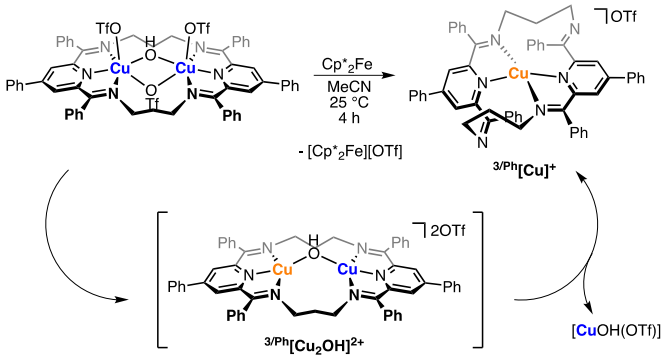

Figure 4.15 Chemical reduction of $^{3/Ph}$**[Cu$_2$OH]**$^{3+}$ in MeCN with proposed intermediate $^{3/Ph}$**[Cu$_2$OH]**$^{2+}$.

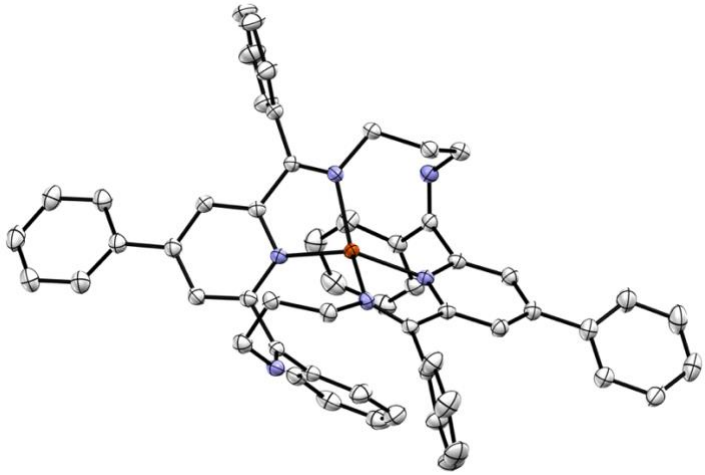

Figure 4.16 Crystal structure of $^{3/Ph}$**[Cu]**$^{+}$ (thermal ellipsoids set at 50% probability; hydrogen atoms and triflate anion omitted for clarity).

Given the formation of a Cu(I) complex from this reduction reaction, along with the color change observed at low temperature, we hypothesized that an initial reduction to a Cu$_2$(I,II)-μ-OH complex was occurring prior to irreversible loss of a [Cu(II)OH] unit to an unidentified byproduct. Analogous reactivity with $^{3/Ph}$**[Cu$_2$Cl]**$^{2+}$ was initially observed. At room temperature, the one-electron reduction of $^{3/Ph}$**[Cu$_2$Cl]**$^{2+}$ with Cp*$_2$Fe afforded the dark red $^{3/Ph}$**[Cu]**$^{+}$. Yet, in the presence of PPh$_3$, the orange macrocyclic complex

[$^{3/Ph}$PDI$_2$Cu$_2$Cl$_2$(PPh$_3$)][OTf] (**$^{3/Ph}$[Cu$_2$Cl$_2$]$^+$**) was isolated and demonstrates a mixed-valent Cu$_2$(I,II) core is accessible (Figure 4.17). Attempts at purifying the mixed-valent Cu$_2$(I,II)-di(μ-Cl) species were met with unsatisfactory combustion analysis results and purification remains an ongoing pursuit. However, single crystals were grown that informed on the geometry of the dinuclear complex.

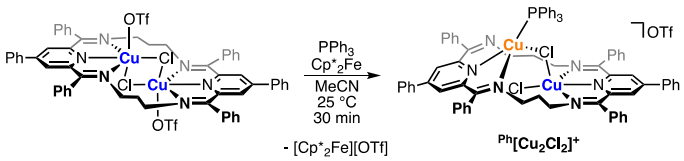

Figure 4.17 Synthesis of **$^{3/Ph}$[Cu$_2$Cl$_2$]$^+$** in MeCN.

The structure of **$^{3/Ph}$[Cu$_2$Cl$_2$]$^+$** was elucidated using X-ray crystallography (Figure 4.18). A unique macrocyclic conformation was observed, in which the macrocycle twists to accommodate the mixed-valent Cu$_2$(I,II) core. The metal-based reduction was supported by the neutral macrocyclic ligand (Δ = 0.184 Å). The Cu(I) center sits above the macrocyclic pocket, capped by the PPh$_3$ ligand (Cu(I)–P = 2.1940(7) Å), in a distorted trigonal pyramidal geometry (τ_4 = 0.75). To accommodate the Cu(I) geometry, one of the imino moieties bends away from the macrocyclic pocket and remains uncoordinated. The other imino group and pyridyl nitrogen bind to the Cu(I) center along with a μ-Cl ligand to compose the base of the trigonal pyramid (Cu(I)–Cl = 2.23415(8) Å). The Cu(II) center adopts a distorted square pyramidal geometry (τ_4 = 0.09), with an elongated axial Cu(II)–Cl bond of 2.4410(7) Å. The equatorial Cu(II)–Cl bond (2.239(1) Å) is the shortest of the Cu–Cl bonds. The twisting of the ligand enforces a long Cu(I)–Cu(II) distance of 4.1103(5) Å (the longest observed Cu–Cu distance of any macrocyclic complex presented in Chapter 2 and Chapter 4). Upon reduction of **$^{3/Ph}$[Cu$_2$Cl]$^{2+}$**, the di(μ-Cl) interactions are disrupted. The Cu(I)-Cl-Cu(II) angle increases to 118.50(3) (from 77.46(4) observed for

$^{3/Ph}$**[Cu$_2$Cl$_2$]$^{2+}$**). One chloride bridges the two metal centers instead of two, as the Cu(I) sits 4.4122(8) Å away from the second chloride ligand bound to the Cu(II) site.

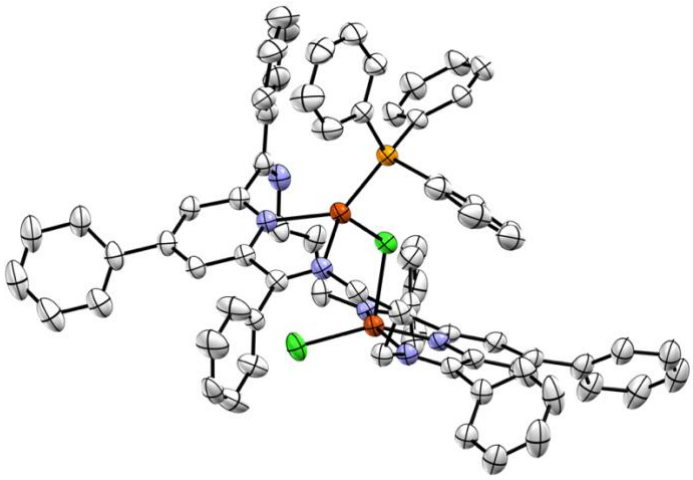

Figure 4.18 Crystal structure of $^{3/Ph}$**[Cu$_2$Cl$_2$]$^{+}$** (thermal ellipsoids set at 50% probability; hydrogen atoms, solvent molecules and triflate anion omitted for clarity).

Despite successful trapping of $^{3/Ph}$**[Cu$_2$Cl$_2$]$^{+}$,** similar attempts (using PPh_3 or 2,6-dimethylphenyl isocyanide) with $^{3/Ph}$**[Cu$_2$OH]$^{3+}$** afforded $^{3/Ph}$**[Cu]$^{+}$**. Low-temperature UV-vis-NIR spectroscopic studies were employed to provide a more quantitative analysis of the reaction progress (see section 4.8.6). At -65 °C, the UV-vis-NIR spectrum of $^{3/Ph}$**[Cu$_2$OH]$^{3+}$** in isobutyronitrile (IBN) showed a broad d-d absorption band at 759 nm (Figure 4.17). Treating $^{3/Ph}$**[Cu$_2$OH]$^{3+}$** with Cp^*_2Fe afforded a new spectral feature at 445 nm. Warming the reaction mixture to room temperature led to the growth of a new peak at 503 nm, with concomitant loss of the peak at 445 nm. An isosbestic point was not observed during this decomposition, suggesting a complicated pathway with intermediate complexes involved. The thermal decomposition product was identified independently as $^{3/Ph}$**[Cu]$^{+}$**, and remained even when heated to higher temperatures (95 °C) or when re-cooled to -65 °C.

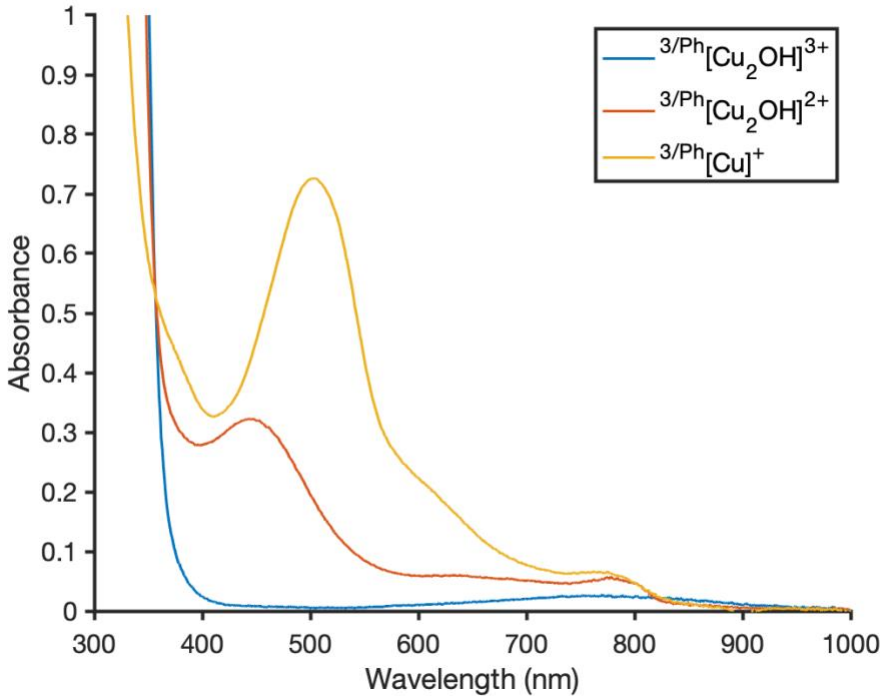

Figure 4.19 Spectral traces of identified intermediates in the one-electron reduction of $^{3/Ph}$**[Cu$_2$OH]$^{3+}$** ($^{3/Ph}$**[Cu$_2$OH]$^{3+}$** at -65 °C, $^{2/Ph}$**[Cu$_2$OH]$^{2+}$** at -65 °C and $^{3/Ph}$**[Cu]$^{+}$** at 95 °C; 0.1 mM; small peak at 776 nm corresponds to [Cp*$_2$Fe][OTf]).

The low-temperature stable 445 nm feature associated with the one-electron reduction of $^{3/Ph}$**[Cu$_2$OH]$^{3+}$** is assigned to the mixed-valent Cu$_2$(I,II)-μ-OH complex $^{3/Ph}$**[Cu$_2$OH]$^{2+}$** (Figure 4.19). Monitoring the absorbance of the spectral feature at 445 nm through the titration of $^{3/Ph}$**[Cu$_2$OH]$^{3+}$** with Cp*$_2$Fe at -65 °C yielded the plot shown in Figure 4.20. The exponential curve supports an equilibrium reduction reaction of $^{3/Ph}$**[Cu$_2$OH]$^{3+}$** with Cp*Fe$_2$. Based on the titration data, we expected the stronger reductant Cp$_2$Co[118] to allow for the full formation of $^{3/Ph}$**[Cu$_2$OH]$^{2+}$**. Surprisingly, the addition of an equiv. of Cp$_2$Co to $^{3/Ph}$**[Cu$_2$OH]$^{3+}$** led to a mixture of the one- and two-electron reduced species (see section 4.8.6).

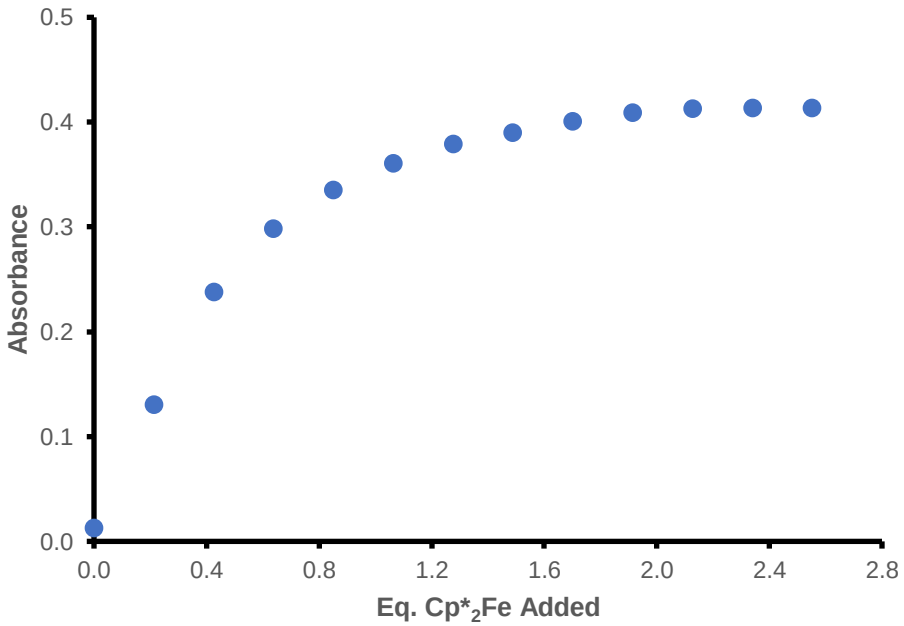

Figure 4.20 Titration of $^{3/Ph}$**[Cu$_2$OH]$^{3+}$** with increasing quantities of Cp*$_2$Fe at -30 °C.

4.4 Determination of the pK_a the Hydroxide Unit

In accordance with the Bordwell relationship, both E^0 and a pK_a are necessary components for estimating an O–H BDFE. To first demonstrate deprotonation of $^{3/Ph}$**[Cu$_2$OH]$^{3+}$** in MeCN, DBU (pK_a = 24.31 in MeCN)[119] was used. Treatment of $^{3/Ph}$**[Cu$_2$OH]$^{3+}$** with DBU at room temperature afforded a deep red solution. The formation of the conjugate acid [H-DBU][OTf] was observed by the ^{1}H NMR spectroscopy (see section 4.8.7). Full consumption of $^{3/Ph}$**[Cu$_2$OH]$^{3+}$** was also noted by the disappearance of the paramagnetically-shifted signal at 50.63 ppm. Intriguingly, the isolated macrocyclic product from the deprotonation reaction was $^{3/Ph}$**[Cu]$^+$**, the same product obtained from the one-electron reduction of $^{3/Ph}$**[Cu$_2$OH]$^{3+}$**.

The similar product of both reduction and deprotonation suggested that the deprotonated species may be reacting to form $^{3/Ph}$**[Cu$_2$OH]$^{2+}$** and then decomposing to $^{3/Ph}$**[Cu]$^+$**. To avoid this possibility, we turned to studying the deprotonation event using

variable temperature ^{1}H NMR spectroscopy (see section 4.8.7). The deprotonation of $^{3/Ph}$**[Cu$_2$OH]$^{3+}$** with DBU was carried out at -25 °C. Significant broadening of all resonances was observed. Of note, the paramagnetically shifted $^{3/Ph}$**[Cu$_2$OH]$^{3+}$** resonances were still present, suggesting an equilibrium reaction with DBU. Treating the reaction mixture with 2,6-lutidinium triflate re-formed $^{3/Ph}$**[Cu$_2$OH]$^{3+}$**, demonstrating reversible protonation of the deprotonated species.

Further analysis of the deprotonation reaction was carried out using low temperature UV-vis-NIR spectroscopy. To avoid an equilibrium mixture and ensure complete deprotonation, DBU was replaced with the strong Verkade base 2,8,9-triisopropyl-2,5,8,9-tetraaza-1-phosphabicyclo[3.3.3]undecane (Verkade^{iPr}, pK_a = 33.63 in MeCN).[120] Deprotonation of $^{3/Ph}$**[Cu$_2$OH]$^{3+}$** at -65 °C afforded minor changes to the UV-vis-NIR spectrum (Figure 4.21). An isosbestic point was observed at 352 nm, indicating a 1:1 transformation without the buildup of an intermediate species. As the sample was warmed to room temperature, the growth of the characteristic 503 nm feature for $^{3/Ph}$**[Cu]$^{+}$** occurred, in line with the room temperature NMR spectroscopic observations. Together, these data indicate that at low temperature, the deprotonation of $^{3/Ph}$**[Cu$_2$OH]$^{3+}$** occurs to form the Cu$_2$(II,II)-μ-O species $^{3/Ph}$**[Cu$_2$O]$^{2+}$**, which thermally decomposes to give the same product as that observed on chemical reduction of $^{3/Ph}$**[Cu$_2$OH]$^{3+}$**.

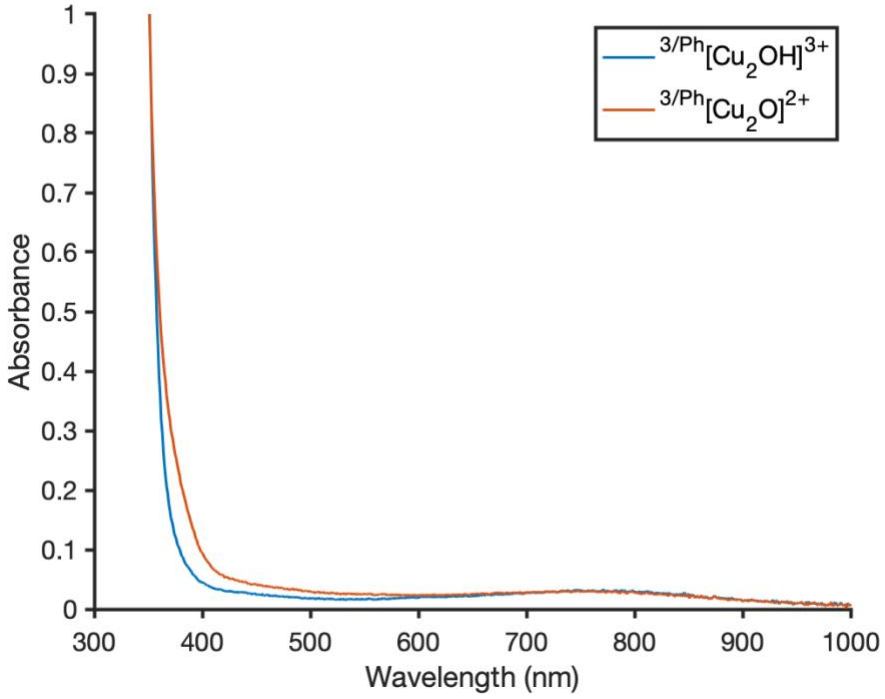

Figure 4.21 Deprotonation of **$^{3/Ph}$[Cu$_2$OH]$^{3+}$** with Verkade^{iPr} at -65 °C (0.1 mM).

Due to the temperature instability of the deprotonated product, the pK_a of **$^{3/Ph}$[Cu$_2$OH]$^{3+}$** was obtained using low temperature ^{1}H NMR spectroscopy (see section 4.8.7). The base, 1,8-*bis*(tetramethylguanidino)naphthalene (pK_a = 24.92 in MeCN) was found to afford an equilibrium mixture with **$^{3/Ph}$[Cu$_2$OH]$^{3+}$** at -30 °C in CD_3CN. The bulky, substituted proton sponge has previously been identified as a suitable base for pK_a determination due to slow proton exchange on the NMR timescale. Titration of 1,8-*bis*(tetramethylguanidino)naphthalene into a CD_3CN solution of **$^{3/Ph}$[Cu$_2$OH]$^{3+}$** at -30 °C allowed for the determination of a pK_a of 24.4 ± 0.4.

4.5 Hydrogen Atom Transfer Reactivity

The thermodynamic quantities determined in the previous sections are those needed for determining the O–H BDFE of **$^{3/Ph}$[Cu$_2$OH]$^{2+}$**. Use of the pK_a value of 24.4 ± 0.4 for **$^{3/Ph}$[Cu$_2$OH]$^{3+}$**, along with the lower-bound of its redox potential $E_{p,c1}$ = -0.510 V, in

eq. 1 allowed us to estimate the BDFE for the O–H bond in $^{3/Ph}$**[Cu$_2$OH]$^{2+}$** as equal to 74.3 ± 1.4 kcal/mol. Given the inherent uncertainty associated with this value, we next sought to assess the HAT chemistry of $^{3/Ph}$**[Cu$_2$O]$^{2+}$** both to bracket the BDFE of the O–H bond in $^{3/Ph}$**[Cu$_2$OH]$^{2+}$** and to gain support for the BDFE value that was estimated by the square scheme analysis.

Full deprotonation of $^{3/Ph}$**[Cu$_2$OH]$^{3+}$** to $^{3/Ph}$**[Cu$_2$O]$^{2+}$** was carried out using an equivalent of Verkade$^{i\text{Pr}}$ and monitored by UV-vis-NIR spectroscopy. An initial reactivity study was conducted using an equivalent of 9-cyanoxanthene as a hydrogen atom donor. This substrate was chosen for its weak C–H bond (C–H BDFE$_{DMSO}$ = 63.7 kcal/mol).[121] The addition of 9-cyanoxanthene to the solution of $^{3/Ph}$**[Cu$_2$O]$^{2+}$** at -65 °C led to a sharp change in the mixture's UV-vis-NIR spectrum, as two new features were observed to grow in at 455 nm and 632 nm over 15 minutes; isosbestic points were observed at 380 and 765 nm (Figure 4.22). The peak at 455 nm overlays well with the spectrum of $^{3/Ph}$**[Cu$_2$OH]$^{2+}$** generated in the low temperature, one-electron reduction reaction (see section 4.8.7), indicating that the hydrogen atom transfer reaction was successful.

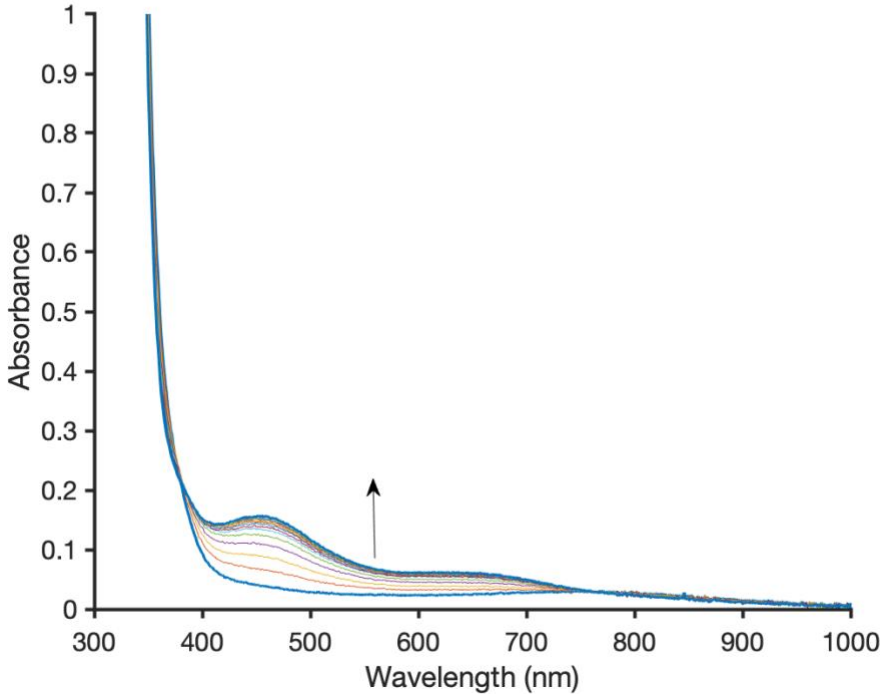

Figure 4.22 Time course of $^{3/Ph}$**[Cu$_2$O]$^{2+}$** + 9-cyanoxanthene at -65 °C (15 x 1 min. scans; 0.1 mM; bolded traces represent start and finish).

In line with the estimated BDFE value, $^{3/Ph}$**[Cu$_2$O]$^{2+}$** was also observed to react with phenylhydrazine (N–H BDFE$_{DMSO}$ = 67.3 kcal/mol) to afford the same HAT product ($^{3/Ph}$**[Cu$_2$OH]$^{2+}$**) as in the reaction with 9-cyanoxanthene, based on the appearance of a spectral feature at 455 nm (Figure 4.68). However, stronger E–H bonds that would be expected to react with $^{3/Ph}$**[Cu$_2$O]$^{2+}$** were found to be unreactive. Xanthene (C–H BDFE$_{DMSO}$ = 70.2 kcal/mol), DHA (C–H BDFE$_{DMSO}$ = 72.9 kcal/mol) and 1,4-cyclohexadiene (C–H BDFE$_{MeCN}$ = 72.9 kcal/mol) afforded no changes to the UV-vis-NIR profile of the system, even when introduced in large excess and upon warming (aside from background decomposition). While thermodynamically accessible, the lack of reactivity suggests either the substrates are kinetically inaccessible for HAT or that the O–H BDFE for $^{3/Ph}$**[Cu$_2$OH]$^{2+}$** is overestimated.

To further bracket the O–H BDFE of $^{3/Ph}$**[Cu$_2$OH]$^{2+}$**, we sought to abstract a hydrogen atom from $^{3/Ph}$**[Cu$_2$OH]$^{2+}$** by treatment with a hydrogen atom acceptor. As expected, no reaction was observed upon treatment of $^{3/Ph}$**[Cu$_2$OH]$^{2+}$** with TEMPO (TEMPOH, O–H BDFE$_{MeCN}$ = 66.5 kcal/mol) at low temperature. Based on the reactivity of $^{3/Ph}$**[Cu$_2$O]$^{2+}$** with phenylhydrazine, the O–H bond formed is stronger than 67.3 kcal/mol and thus TEMPO is not capable of abstracting a hydrogen atom from $^{3/Ph}$**[Cu$_2$OH]$^{2+}$**. The stronger hydrogen atom abstracting agent, 2,4,6-tri-*tert*-butylphenoxyl radical (2,4,6-^{t}Bu$_3$PhOH, O-H BDFE$_{MeCN}$ = 74.8 kcal/mol), however, was found to react with $^{3/Ph}$**[Cu$_2$OH]$^{2+}$**, leading to the loss of the feature at 445 nm and loss of a sharp feature at 405 nm that are associated with the phenol product. The observed reactivity supports the notion that the O–H BDFE of $^{3/Ph}$**[Cu$_2$OH]$^{2+}$** is less than 74.8 kcal/mol. Thus, the experimental O–H BDFE of $^{3/Ph}$**[Cu$_2$OH]$^{2+}$** falls between 67.3 – 70.2 kcal/mol based upon the reactivity observed with HAT reagents.

4.6 Preliminary Investigation into $^{2/Ph}$[Cu$_2$OH]$^{3+}$

Enhancement of the HAT reactivity was desirable due to the limited bond activation demonstrated by the $^{3/Ph}$**[Cu$_2$O]$^{2+}$** system. A folded macrocyclic ligand may provide both a more oxidizing and basic Cu$_2$(II,II)-μ-oxo moiety for the activation of stronger bonds. Through ligand folding, the orbital overlap between the copper centers and ligand is expected to decrease causing a lowering of the d_{x2-y2} manifold (LUMO). The Cu$_2$(II,II)-μ-oxo complex would thus be easier to reduce. Moreover, as the ligand folds, the oxygen will be displaced from the Cu–Cu vector, enhancing the basicity of oxo unit. Typically, strong bases are poor oxidants and strong oxidants are poor bases. However, ligand folding may effectively break this scaling relationship, allowing for hydrogen atom

abstraction from strong E–H bonds. Thus, we next targeted the synthesis of the smaller Cu_2(II,II)-μ-OH variant $^{2/Ph}$**[Cu$_2$OH]$^{2+}$**.

The synthesis of [$^{2/Ph}$PDI$_2$Cu$_2$OH][OTf]$_3$ ($^{2/Ph}$**[Cu$_2$OH]$^{3+}$**) was carried out in an analogous fashion to $^{3/Ph}$**[Cu$_2$OH]$^{3+}$**. A one-pot reaction was carried out in which a mixture of [$^{2/Ph}$PDI$_2$Ca][OTf]$_2$ ($^{2/Ph}$**[Ca]$^{2+}$**) and 2.0 equiv. Cu(OTf)$_2$ were treated slowly with NBu_4OH. The desired product was afforded as large blue-green blocks following crystallization (Figure 4.23). Like $^{3/Ph}$**[Cu$_2$OH]$^{3+}$**, $^{2/Ph}$**[Cu$_2$OH]$^{3+}$** displayed a low intensity, sharp O–H stretching frequency in the IR spectrum (3679 cm^{-1}). The complex displayed broadened, shifted resonances in the ^{1}H NMR spectrum, most likely due to the paramagnetic nature of $^{2/Ph}$**[Cu$_2$OH]$^{3+}$**.

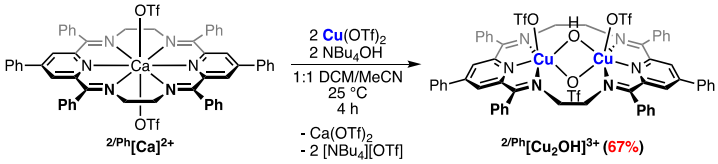

Figure 4.23 Synthesis of $^{2/Ph}$**[Cu$_2$OH]$^{3+}$** in DCM/MeCN.

The crystal structure of $^{2/Ph}$**[Cu$_2$OH]$^{3+}$** depicts the macrocyclic ligand in a folded conformation (Figure 4.24). The copper(II) centers each adopt a distorted octahedral geometry, with all three triflate anions bound in axial positions by the dinuclear core (Jahn-Teller distortions are evidenced by the elongated Cu–O bonds; avg. Cu–O distance is 2.495(3) Å). The equatorial plane of each copper(II) center consists of a PDI unit and a hydroxide ligand. The hydroxide bridges the two copper(II) centers with Cu–O(H) distances of 1.898(2) and 1.884(2) Å; these distances are slightly shorter than the distances observed for $^{3/Ph}$**[Cu$_2$OH]$^{3+}$** but agree well with the literature. The short ethylene linker accompanied by the folding of the macrocyclic ligand enforces a Cu–Cu distance of 2.8910(5) Å, which is ~0.5 Å shorter than the Cu–Cu distance in $^{3/Ph}$**[Cu$_2$OH]$^{3+}$**. The close copper(II) centers, in turn, force the hydroxide further away from the Cu–Cu vector than in

$^{3/Ph}$**[Cu$_2$OH]$^{3+}$**, leading to a Cu-O(H)-Cu angle of 99.72(10)°. The angle is 25° smaller than that observed for $^{3/Ph}$**[Cu$_2$OH]$^{3+}$**. The Δ parameter of 0.192 Å lends support for a neutral *bis*(pyridyldiimine) macrocyclic ligand.

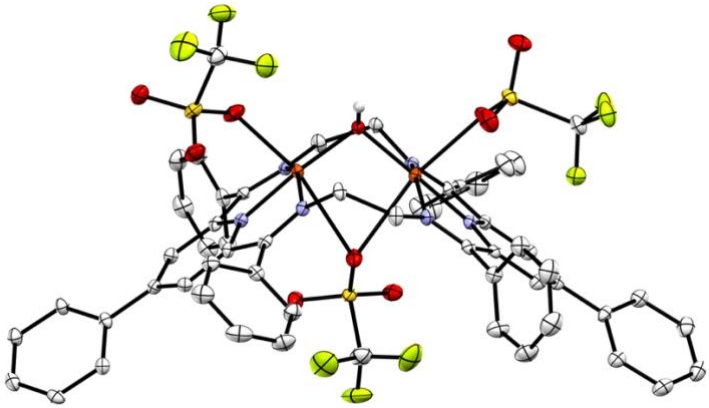

Figure 4.24 Crystal structure of $^{2/Ph}$**[Cu$_2$OH]$^{3+}$** (thermal ellipsoids set at 50% probability; hydrogen atoms and solvent molecules omitted for clarity).

Following the methodology used in analyzing the thermodynamic square scheme for $^{3/Ph}$**[Cu$_2$OH]$^{3+}$**, analysis of $^{2/Ph}$**[Cu$_2$OH]$^{3+}$** began with electrochemical studies (Figure 4.25). As observed for $^{3/Ph}$**[Cu$_2$OH]$^{3+}$**, two irreversible reduction events appeared in the cyclic voltammogram of $^{2/Ph}$**[Cu$_2$OH]$^{3+}$**. The two features were shifted anodically (-0.377 V and -0.595 V vs. Fc/Fc$^+$) from those observed for the larger macrocycle variant (-0.510 V and -0.845 V vs. Fc/Fc$^+$). Continuous cathodic scans showed loss of intensity and coalescence of the two features (analogous to $^{3/Ph}$**[Cu$_2$OH]$^{3+}$**). Due to the similar behavior, the two cathodic features are assigned as the reduction of a Cu^{II}Cu^{II} core to Cu^{I}Cu^{II} ($E_{p,c1'}$ = -0.375 V) and a Cu^{I}Cu^{II} core to Cu^{I}Cu^{I} ($E_{p,c2'}$ = -0.595 V). Thus, the first irreversible reduction feature at -0.377 V is, again, a lower-bound approximation of $E^{1/2}$ on the thermodynamic square scheme.

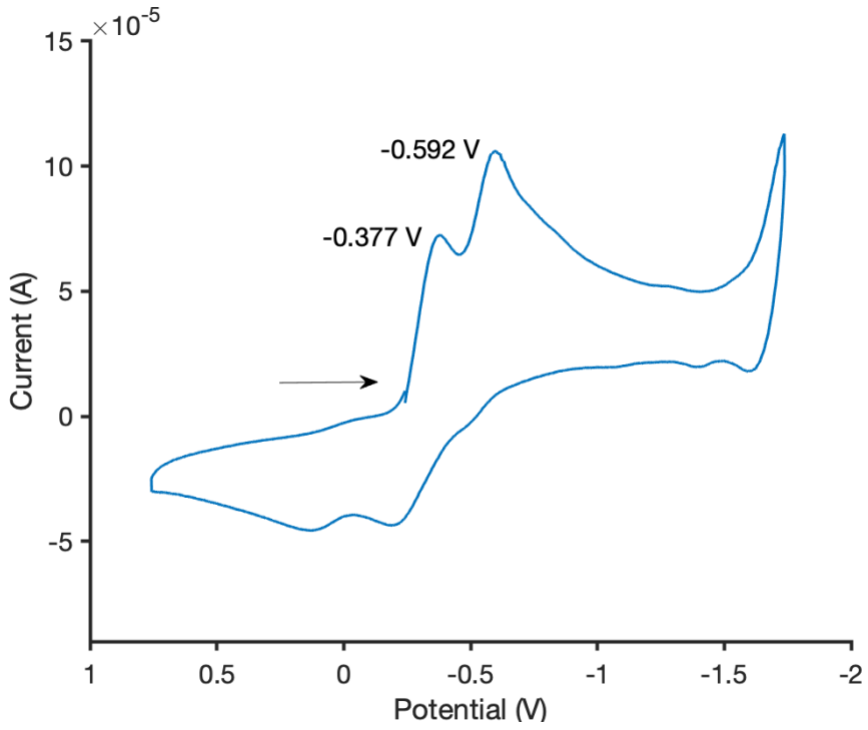

Figure 4.25 Cyclic voltammogram of $^{3/Ph}$**[Cu$_2$OH]$^{3+}$** (initial Scan, 1000 mv/s scan rate).

The deprotonation of $^{2/Ph}$**[Cu$_2$OH]$^{3+}$** was next explored using low-temperature UV-vis-NIR spectroscopy. Full deprotonation of $^{2/Ph}$**[Cu$_2$OH]$^{3+}$** with an equiv. of Verkade^{iPr} in IBN at -30 °C led to minor changes in the UV-vis-NIR spectrum. As the solution sat for 90 minutes, a new feature slowly grew in at 479 nm, indicating the deprotonated species was unstable at this temperature (see section 4.8.7). Performing the deprotonation at -65 °C addressed this issue, as no decomposition was noted (Figure 4.26). Based on the similar spectral changes as observed for $^{3/Ph}$**[Cu$_2$OH]$^{3+}$** at -65 °C, the deprotonated species is assigned to the Cu$_2$(II,II)-μ-oxo species $^{2/Ph}$**[Cu$_2$O]$^{2+}$**.

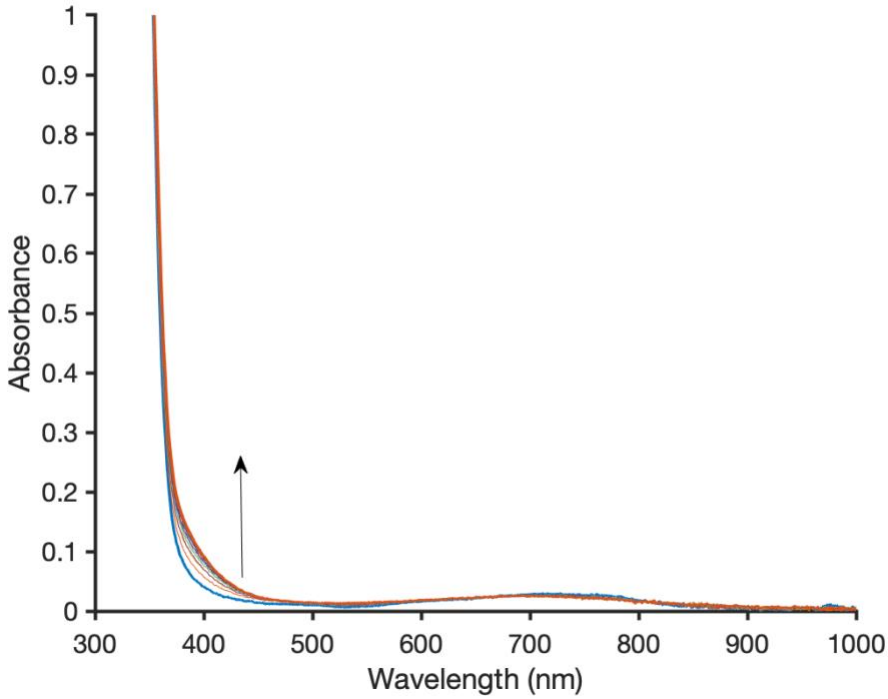

Figure 4.26 Time course of $^{2/Ph}$**[Cu$_2$OH]$^{3+}$** + Verkade^{iPr} at -65 °C (30 x 1 min. scans; 0.1 mM; bolded traces represent start and finish).

The determination of the pK_a of $^{2/Ph}$**[Cu$_2$OH]$^{3+}$** was carried out using the titration method employed for $^{3/Ph}$**[Cu$_2$OH]$^{3+}$** at -30 °C in CD_3CN. Although $^{2/Ph}$**[Cu$_2$O]$^{2+}$** slowly decomposes at this temperature, an estimate of the pK_a of $^{2/Ph}$**[Cu$_2$OH]$^{3+}$** was obtained successfully using 1,8-*bis*(tetramethylguanidino)naphthalene. The pK_a of 25.6 ± 0.5 is an order of magnitude more basic than for the larger macrocycle variant (24.4 ± 0.4). The increased basicity of $^{2/Ph}$**[Cu$_2$O]$^{2+}$** compared with $^{3/Ph}$**[Cu$_2$O]$^{2+}$** may arise from macrocycle conformation differences (*vide supra*).

Together, the estimated pK_a of $^{2/Ph}$**[Cu$_2$OH]$^{3+}$** and its irreversible redox couple -0.377 V were used in eq. 1 to estimate the O–H BDFE of the mixed valent Cu_2(I,II)-μ-OH complex $^{2/Ph}$**[Cu$_2$OH]$^{2+}$**. The O–H BDFE of 79.0 ± 1.5 kcal/mol is ~5 kcal/mol higher than observed for the $^{3/Ph}$**[Cu$_2$OH]$^{2+}$** (74.3 ± 1.4 kcal/mol). The anodic shift of the redox potential accompanied with an increase in basicity of the μ-oxo moiety are thought to arise from an

increase in the extent of folding of the macrocycle ligand. The positive shift in both thermodynamic quantities demonstrates a breaking of the scaling relationship between oxidizing strength and basicity. Like the estimated O–H BDFE of $^{3/Ph}[Cu_2OH]^{2+}$, the O–H BDFE of $^{2/Ph}[Cu_2OH^{2+}$ has an inherent uncertainty associated with the irreversible redox process.

To probe if the $^{2/Ph}[Cu_2O]^{2+}$ system is more reactive, we next explored the hydrogen atom transfer reactivity of the system. At -30 °C, $^{2/Ph}[Cu_2O]^{2+}$ was found to quickly react with 9-cyanoxanthene over 15 minutes to afford a new spectral feature at 476 nm (Figure 4.27). An isosbestic point at 715 nm was observed during this transformation, indicating a 1:1 transformation. Through an independent redox titration of $^{2/Ph}[Cu_2OH]^{3+}$ with Cp^*_2Fe, we assign the feature at 476 nm to the mixed-valent $^{2/Ph}[Cu_2OH]^{2+}$ (see section 4.8.6). This assignment supports a hydrogen atom transfer reaction between $^{2/Ph}[Cu_2O]^{2+}$ and 9-cyanoxanthene.

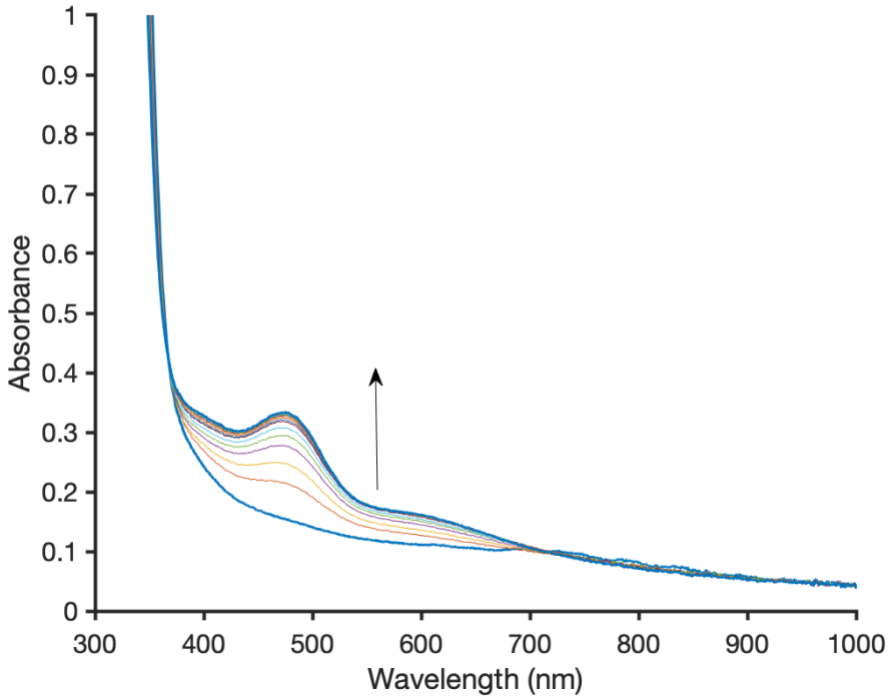

Figure 4.27 Time course of $^{2/Ph}$**[Cu$_2$O]$^{2+}$** + 9-cyanoxanthene at -30 °C (15 x 1 min. scans; 0.1 mM; bolded traces represent start and finish).

Substrates with stronger C–H bonds, xanthene and DHA, were next assessed. While DHA was found unreactive, $^{2/Ph}$**[Cu$_2$O]$^{2+}$** was found to react slowly with xanthene over 15 minutes to afford the spectral feature at 476 nm. This reactivity contrasts with the larger macrocyclic complex $^{3/Ph}$**[Cu$_2$O]$^{2+}$**, which did not react with xanthene. The HAT reactivity of $^{2/Ph}$**[Cu$_2$O]$^{2+}$** suggests a stronger O–H bond is forming and the O–H BDFE of $^{2/Ph}$**[Cu$_2$OH]$^{2+}$** is higher than $^{3/Ph}$**[Cu$_2$OH]$^{3+}$**. Further investigations with other HAT reagents are necessary to effectively bracket the O–H BDFE of $^{2/Ph}$**[Cu$_2$OH]$^{2+}$** and define the origin of the enhanced reactivity.

4.7 Summary

A new Cu$_2$(II,II)-μ-OH complex $^{3/Ph}$**[Cu$_2$OH]$^{3+}$** was synthesized and studied using the thermodynamic square scheme approach. Estimates for $E^{1/2}$ (more positive than -

0.510 V) and pK_a (24.1 ± 0.4) were obtained through cyclic voltammetry and low temperature ^{1}H NMR spectroscopic titrations, respectively, and used to estimate an O–H BDFE = 74.3 ± 1.4 kcal/mol for the mixed-valent hydroxide complex $^{3/Ph}$**[Cu$_2$OH]$^{2+}$**.

A rare example of Cu$_2$(II,II)-μ-O species, $^{3/Ph}$**[Cu$_2$O]$^{2+}$**, was generated by deprotonation of $^{3/Ph}$**[Cu$_2$OH]$^{3+}$** and found to be suitable for HAT from substrates with weak E–H bonds (9-cyanoxanthene, phenylhydrazine) to generate $^{3/Ph}$**[Cu$_2$OH]$^{2+}$**. The O–H BDFE was bracketed to fall within the lower bound of 67.3 kcal/mol and upper bound of 70.2 kcal/mol. The current system offers a new addition to the limited number of copper-oxygen-based complexes with measurable O–H BDFEs.

Additionally, the methods used for analysis of $^{3/Ph}$**[Cu$_2$OH]$^{3+}$** were applied to the smaller macrocycle variant $^{2/Ph}$**[Cu$_2$OH]$^{3+}$**. The estimates for $E^{1/2}$ (more positive than -0.377 V) and pK_a (25.6 ± 0.5) were used to estimate the O–H BDFE = 79.0 ± 1.5 kcal/mol for the mixed-valent hydroxide complex $^{2/Ph}$**[Cu$_2$OH]$^{2+}$**. The increase in redox potential and pK_a suggest that a ligand conformation change may aid in increasing the oxidizing strength and basicity of the corresponding μ-oxo complex $^{2/Ph}$**[Cu$_2$O]$^{2+}$**. Enhanced reactivity of $^{2/Ph}$**[Cu$_2$O]$^{2+}$** towards C–H bonds was demonstrated through a hydrogen atom transfer reaction with xanthene. Ongoing studies are aimed defining the origin of reactivity enhancement of $^{2/Ph}$**[Cu$_2$O]$^{2+}$** in comparison to $^{3/Ph}$**[Cu$_2$O]$^{2+}$**.

4.8 Experimental

4.8.1 General Considerations

Unless stated otherwise, all reactions were carried out under an inert atmosphere of N_2 using standard Schlenk techniques and worked up in air. Glassware, stir bars, filter aid (Celite) and 4 Å molecular sieves, were dried in an oven at 175 °C for at least one hour prior to use when applicable. Benchtop solvents (Pentane, Hexanes, Et_2O, THF and DCM, MeCN and MeOH) were purchased from Fisher Chemicals and used directly. Degassed anhydrous solvents (THF, DCM, IBN and MeCN) were dried by passage through activated alumina using a Solvent Purification System and stored over 4 Å molecule sieves for at least one day before use. Acetonitrile-d_3 was purchased from Cambridge Isotopes Laboratories and was dried over CaH_2, degassed by three freeze-pump-thaw cycles, and stored over 4 Å molecular sieves under N_2 for at least one day prior to use. DBU was dried over CaH_2 and vacuum distilled prior to use. Tetrabutylammonium hydroxide (1.0 M in MeOH) was purchased from MilliporeSigma in a Sure/Seal™ bottle. Tetrabutylammonium hydroxide (40 wt. % in H_2O) was purchased from TCI Chemicals. Decamethylferrocene and $Cu(OTf)_2$ were purchased from Strem Chemicals and were stored in the glovebox at room temperature. 1,8-*bis*(tetramethylguanidino)naphthalene was purchased from Santa Cruz Biotech, dried under vacuum, and stored in the glovebox at room temperature. 2,8,9-Triisopropyl-2,5,8,9-tetraaza-1-phosphabicyclo[3,3,3]undecane was purchased from Millipore Sigma and stored in the glovebox at -35 °C. All other chemicals were purchased from typical commercial vendors and used directly as received.

NMR Spectroscopy: ^{1}H NMR spectra were recorded on either a Bruker DMX 500 or a Bruker DRX 500 spectrometer. All chemical shifts are reported in units of ppm, with reference to the residual proteo-solvent resonance proton chemical shifts.

Elemental Analysis: Analytical data were obtained from the CENTC Elemental Analysis Facility at the University of Rochester. Microanalysis samples were weighed with a PerkinElmer Model AD6000 Autobalance and their compositions were determined with a PerkinElmer 2400 Series II Analyzer. Air-sensitive samples were handled in a VAC Atmospheres glovebox and combusted in a tin capsule that was crimp-sealed with a die apparatus.

Infrared Spectroscopy: Infrared spectra were recorded using a PerkinElmer Spectrum Two FT-IR spectrometer. Samples were placed on an ATR crystal after collecting a blank spectrum and spectral data were measured over the range of 450-4000 cm^{-1}.

UV-vis-NIR Spectroscopy: Absorption spectra were collected over the range of 200-1000 nm using an Agilent Cary 60 UV-vis-NIR spectrophotometer. Each air/moisture-free measurement was obtained using a 10 mm path-length quartz cuvette with screw cap. Variable temperature experiments were conducted using an Unisoku USP-203A cryostat to maintain the desired temperature. Absorption profiles of interest were collected in the linear response range of the instrument (< 1.0 absorbance units). All $^{n/Ph}[Cu_2OH]^{3+}$ (n = 2,3) stock solutions were prepared in isobutyronitrile (1.5-1.9 mM). Samples were then diluted to 0.1 mM for absorption measurements.

Cyclic Voltammetry: Cyclic voltammetry measurements were obtained with a CH Instruments 620D potentiostat using a 3 mm glassy carbon working electrode, a platinum wire auxilliary electrode, and a Ag wire quasi-reference electrode. CV measurements were taken with a 0.005 V sample interval. All electrochemical measurements were taken in MeCN using *n*-propylammonium *tetrakis*[3,5-*bis*(trifluoromethyl)phenyl]borate ([*n*Pr_4N][BAr^F_4] electrolyte (100 mM). The concentration of the analyte was *ca*. 2 mM in all cases. All potentials were referenced to the Fc/Fc^+ couple, measured by adding a known amount of ferrocene to the solution.

X-ray Crystallography: X-ray intensity data for $^{3/Ph}$**[Cu_2Cl_2]$^{2+}$**, $^{3/Ph}$**[Cu_2Cl]$^{3+}$**, $^{3/Ph}$**[Cu_2Cl]$^{2+}$** and $^{2/Ph}$**[Cu_2OH]$^{3+}$** were collected on a Rigaku XtaLab Synergy-S diffractometer equipped with an HPC area detector (HyPix-6000He) employing confocal multilayer-monochromated Mo-Kα radiation (λ = 0.71073 Å) ($^{2/Ph}$**[Cu_2OH]$^{3+}$**) or Cu-Kα radiation (λ=1.54184 Å) ($^{3/Ph}$**[Cu_2Cl_2]$^{2+}$**, $^{3/Ph}$**[Cu_2Cl]$^{3+}$** and $^{3/Ph}$**[Cu_2Cl]$^{2+}$)** at a temperature of 100 K. X-ray intensity data for $^{3/Ph}$**[Cu_2OH]$^{3+}$** and $^{3/Ph}$**[Cu]$^{+}$** were collected on a Rigaku XtaLab Synergy-S diffractometer equipped with an HPC area detector (Dectris Pilatus3 R 200K) employing confocal multilayer optic-monochromated Mo-Kα radiation (λ = 0.71073 Å) at a temperature of 100 K. Rotation frames were integrated using CrysAlisPro, producing a listing of unaveraged F^2 and $\sigma(F^2)$ values. The intensity data were corrected for Lorentz and polarization effects and for absorption using SCALE3 ABSPACK. The structures were solved by direct or dual ($^{3/Ph}$**[Cu_2Cl_2]$^{2+}$**) methods using SHELXT and refined by full-matrix least-squares, based on F^2 using SHELXL-2018. All reflections were used during refinement. Non-hydrogen atoms were refined anisotropically and hydrogen atoms were refined using a riding model. For $^{3/Ph}$**[Cu_2Cl_2]$^{2+}$**, there are two crystallographically independent molecules, each of which lies on a crystallographic center-of-symmetry (at ½, ½, ½ and 0, ½, 0). For $^{3/Ph}$**[Cu_2Cl]$^{3+}$**, the

complex lies on a crystallographic mirror plane (at x, ¼, z); the mirror passes through Cl(1), C(9), C(11), S(4), O(4) and F(4) of the bidentate triflate ligand. For $^{3/Ph}$**[Cu$_2$OH]$^{3+}$**, the C(18)-C(19)-C(20)-N(1) moiety is disordered by twisting of the chain in a 58/42 proportion. For $^{3/Ph}$**[Cu]$^{+}$**, the Cu(I) ion lies on a crystallographic 2-fold axis (at ½, y, ¼).

4.8.2 Synthetic Procedures

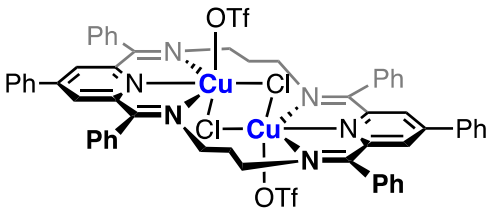

$^{3/Ph}$**[Cu$_2$Cl$_2$]$^{2+}$**. A 500 mL round-bottom flask was charged with ^{3Ph}**[Sr]$^{2+}$** (1.5428 g, 1.2978 mmol, 1.00 equiv.) and MeOH (500 mL). The flask was equipped with an addition funnel and cooled to -78 °C. The yellow-orange solution was treated dropwise with a solution of $CuCl_2 \cdot 2H_2O$ (443.0 mg, 2.599 mmol, 2.00 equiv.) in MeOH (50 mL). An additional 50 mL of MeOH were used to rinse the funnel to ensure quantitative transfer of the starting material. The reaction flask was removed from the cold bath, and the solution was stirred for an additional hour while warming to room temperature. Over time, a color change to dark green was observed. Solvent was removed under vacuum to afford a green solid. The product was extracted in *ca*. 80-90 mL MeCN and filtered through a pad of Celite to remove the $SrCl_2$ byproduct. The pad was rinsed until no color remained. The dark green filtrate was then layered with 350 mL Et_2O at room temperature. Mixing of the layers over 3 days afforded green, crystalline, solid. The product was collected, rinsed with 2 x 100 mL Et_2O, and dried under vacuum. The product was collected as a green powder (1.2821, 76%). Single crystals suitable for X-ray crystallography were grown by vapor diffusion of Et_2O into a concentrated MeCN solution.

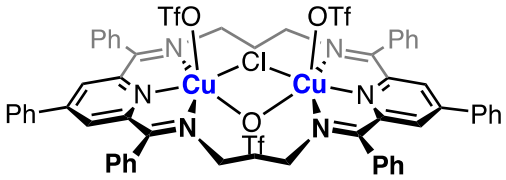

$^{3/Ph}$[Cu$_2$Cl]$^{3+}$. To a 100 mL Schlenk tube, **$^{3/Ph}$[Cu$_2$Cl$_2$]$^{2+}$** (350.1 mg, 0.2695 mmol, 1.00 equiv.) and MeCN (10 mL) were added. The dark green solution was cooled to 0 °C and treated slowly with a solution of TMS-OTf (0.050 mL, 0.277 mmol, 1.03 equiv.) in MeCN (10 mL). The solution was removed from the cold bath and stirred for 30 minutes while warming to room temperature. During this time, the solution became lighter. Solvent was then removed under vacuum to afford a light green powder. The powder was triturated with Et_2O and dried under vacuum (369.7 mg, 97%). Single crystals suitable for X-ray crystallography were grown by vapor diffusion of Et_2O into a concentrated MeCN solution. The undesired **$^{3/Ph}$[Cu$_2$Cl]$^{3+}$** was identified. No further purification was attempted as the one-pot procedure was found to afford **$^{3/Ph}$[Cu$_2$OH]$^{3+}$** cleanly in good yield.

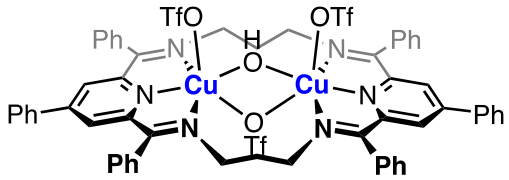

$^{3/Ph}$[Cu$_2$OH]$^{3+}$. To a 250 mL round bottom Schlenk flask was added **^{3Ph}[Sr]$^{2+}$** (4.0765 g, 3.4292 mmol, 1.00 Eq.), $Cu(OTf)_2$ (2.4979 g, 6.9066 mmol, 2.01 Eq.), and DCM (100 mL). The resulting pale orange slurry was stirred and treated dropwise with 1.0 M NBu_4OH in MeOH (3.45 mL, 3.45 mmol, 1.01 Eq.). The reaction mixture quickly became dark green and was stirred for an additional 2 h at room temperature. The mixture was then directly

filtered through a pad of Celite to remove all insoluble materials. The Celite cake was rinsed with an additional 24 mL of DCM, then the filtrate was concentrated under vacuum to afford the crude product as a green solid. After washing the crude product with 3 x 30 mL 2:1 Et_2O/THF, the product was exposed to air and re-dissolved in 150 mL DCM. The dark green solution was filtered through a pad of Celite and layered with *ca*. 350 mL hexanes. After 2 days, crystals suitable for single crystal X-ray crystallography were grown and collected via vacuum filtration. The crystals were rinsed with *ca*. 200-300 mL hexanes and then were dried at 100 °C to remove residual DCM from the crystal lattice; the crystals were intermittently crushed with a spatula to aid in this process. Once complete, the product was isolated as a green powder (3.4415 g, 72%). **^{1}H NMR** (CD_3CN, 500 MHz, 298 K): δ = 50.63 (br s), 8.48 (br s), 8.13 (t, *J* = 7.3 Hz), 8.03 (d, *J* = 7.6 Hz), 7.94 (br s), 6.94 (t, *J* = 7.5 Hz), 6.37 (d, 7.1 Hz) ppm. **Anal. % Calcd.** for $C_{59}H_{47}Cu_2F_9N_6O_{10}S_3$ (1394.31 g/mol): C, 50.82; H, 3.40; N, 6.03. Found: C, 50.58; H, 3.19; N, 6.21. **FTIR** (ATR): 3662 (O-H), 1592 (C=N) cm^{-1}.

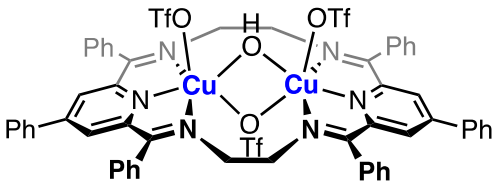

$^{2/Ph}$[Cu_2OH]$^{3+}$. A 250 mL round bottom Schlenk flask was charged with **$^{2/Ph}$[Ca]$^{2+}$** (3.4034 g, 3.0574 mmol, 1.00 equiv.), $Cu(OTf)_2$ (2.2818 g, 6.3091 mmol, 2.06 equiv.) and DCM (50 mL). The slurry was stirred and treated with MeCN (50 mL). The solution became dark green and was stirred for a few minutes before the dropwise addition of NBu_4OH (2.10 mL, 3.15 mmol, 1.03 equiv., 40 wt. % in H_2O). The solution turned dark blue and was stirred for 4 h at room temperature. The reaction mixture was then directly filtered through

a pad of Celite to remove insoluble materials. The Celite cake was rinsed with an additional 35 mL DCM. The volatile materials were removed from the dark blue filtrate under vacuum. The resulting blue solid was triturated with 3 x 30 mL of 2:1 Et_2O/THF, then dissolved in *ca*. 75 mL DCM. The DCM solution was layered with 150 mL hexanes and stored at room temperature. The layers were allowed to mix over 2 days, resulting the in the formation of blue crystals suitable for crystallographic analysis. The crystals were collected by vacuum filtration and rinsed with 100 mL pentane. The crystals were then dried under vacuum at 100 °C to remove DCM from the crystal lattice, affording the desired product as a dark green powder (2.8079 g, 67%). **^{1}H NMR** (CD_3CN, 500 MHz, 298 K): δ = 74.53 (br s), 71.39 (s), 9.05 (br s), 8.90 (br s), 8.54 (d, *J* = 7.6 Hz), 8.48 (t, *J* = 7.4 Hz), 8.28 (br s), 8.14 (br s), 6.86 (t, *J* = 7.2 Hz), 5.39 (t, *J* = 7.1 Hz) ppm. **Anal. % Calcd.** for $C_{57}H_{43}Cu_2F_9N_6O_{10}S_3$ (1366.26 g/mol): C, 50.11; H, 3.17; N, 6.15. Found: C, 49.89; H, 3.10; N, 6.08. **FTIR** (ATR): 3679 (O-H), 1586 (C=N) cm^{-1}.

4.8.3 NMR Spectra

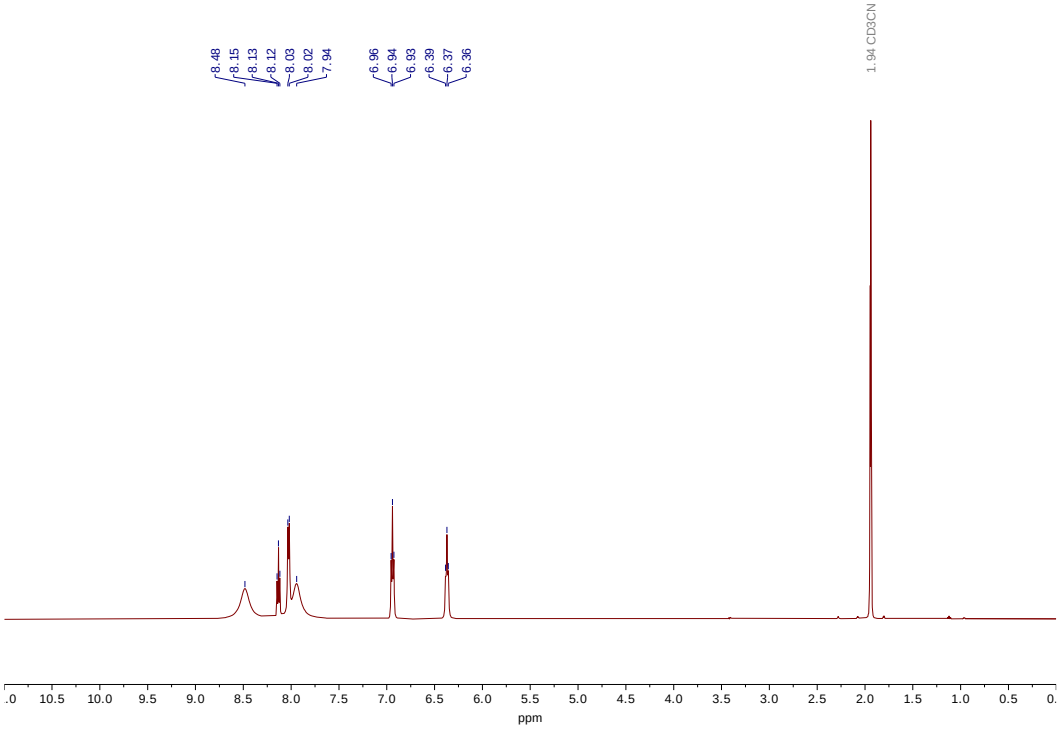

Figure 4.28 ^{1}H NMR spectrum of $^{3/Ph}$**[Cu$_2$OH]$^{3+}$** in CD_3CN.

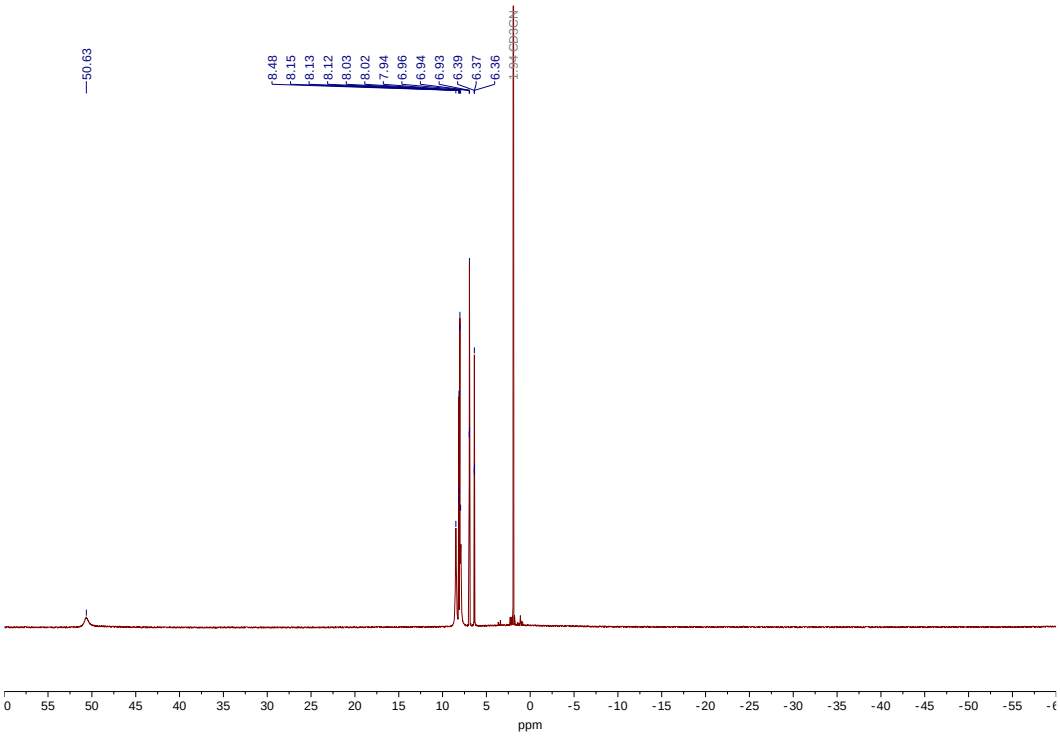

Figure 4.29 Wider window of ^{1}H NMR spectrum of $^{3/Ph}$**[Cu$_2$OH]$^{3+}$** in CD_3CN.

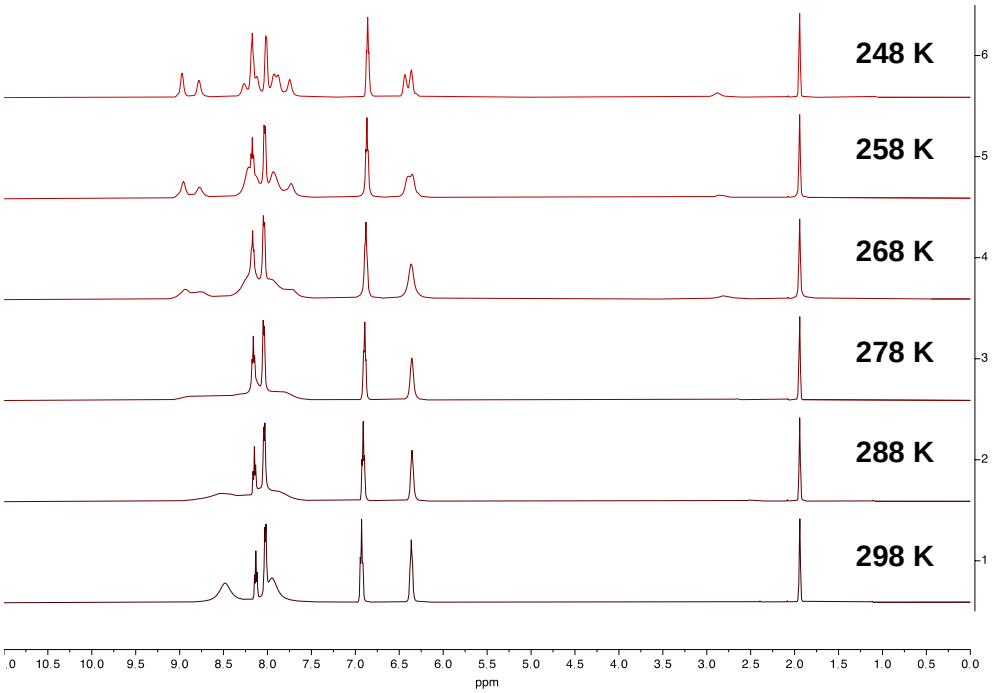

Figure 4.30 Variable temperature ^{1}H NMR spectra of $^{3/Ph}$**[Cu$_2$OH]$^{3+}$** in CD_3CN.

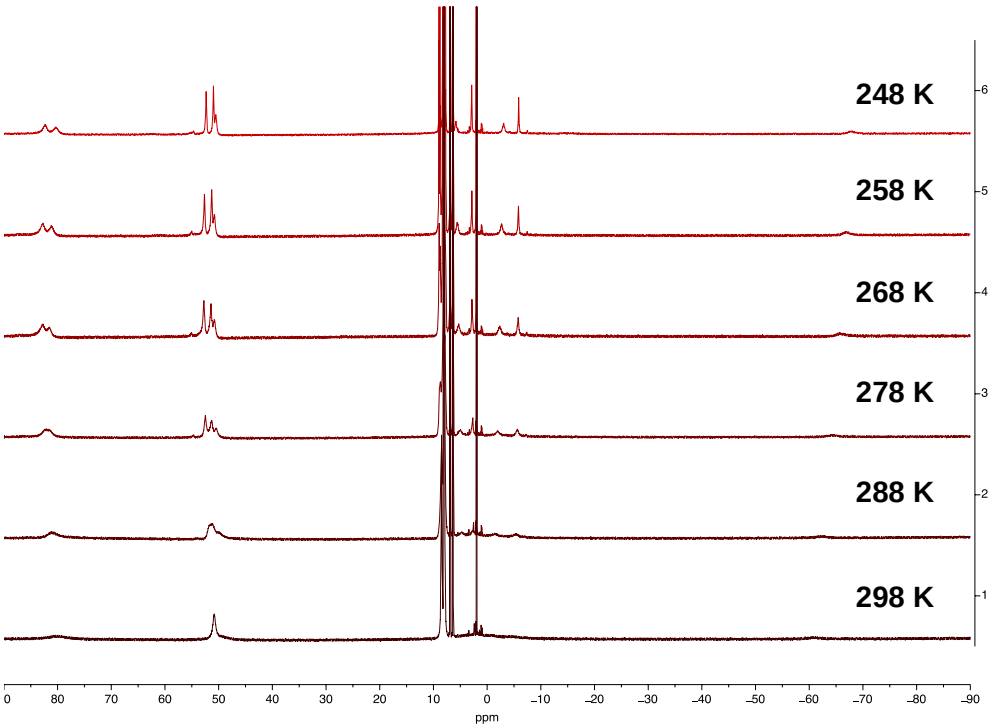

Figure 4.31 Wider window of variable temperature ^{1}H NMR spectra of $^{3/Ph}$**[Cu$_2$OH]$^{3+}$** in CD_3CN.

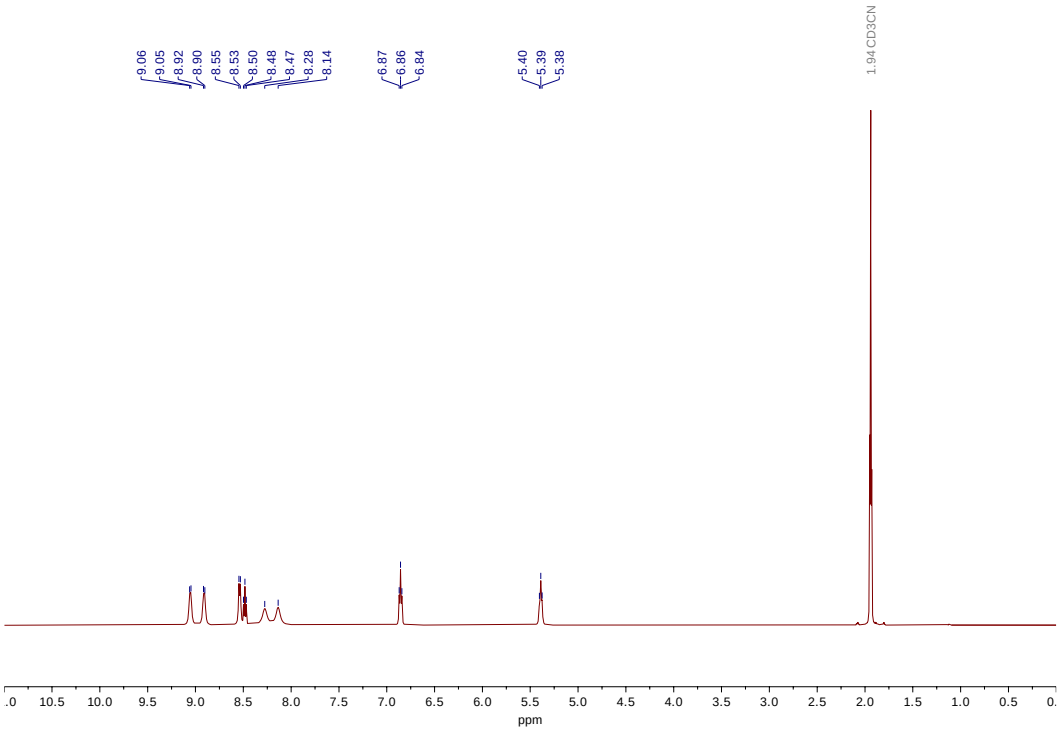

Figure 4.32 ^{1}H NMR spectrum of $^{2/Ph}$**[Cu$_2$OH]$^{3+}$** in CD_3CN.

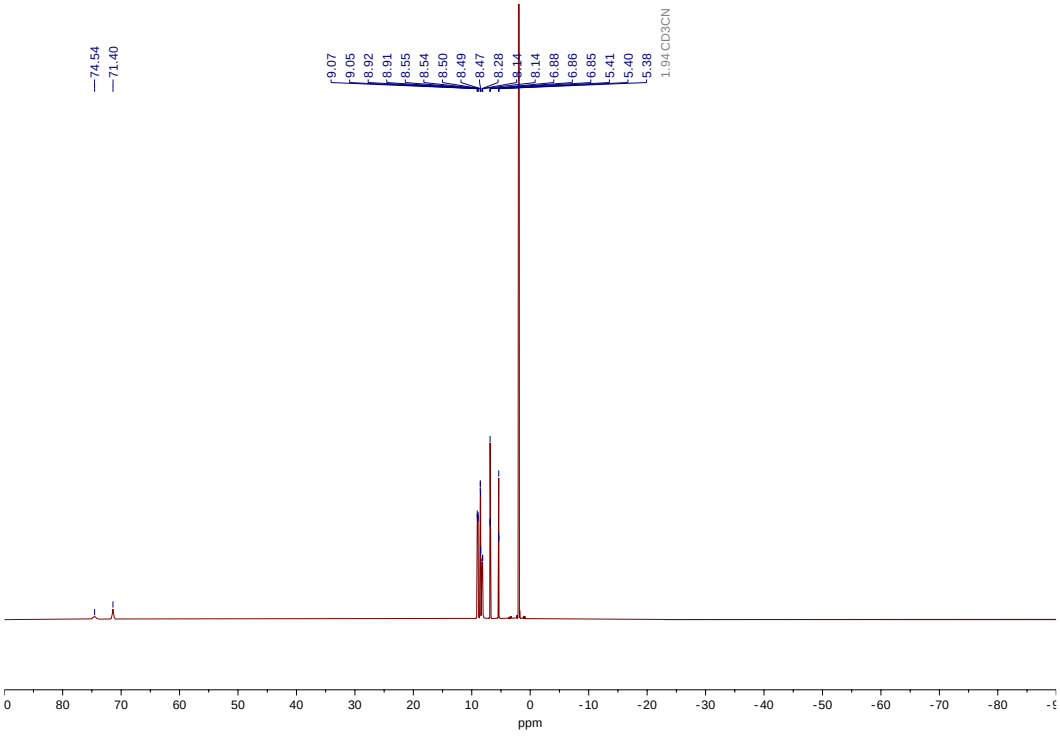

Figure 4.33 Wider window of ^{1}H NMR spectrum of $^{2/Ph}$**[Cu$_2$OH]$^{3+}$** in CD_3CN.

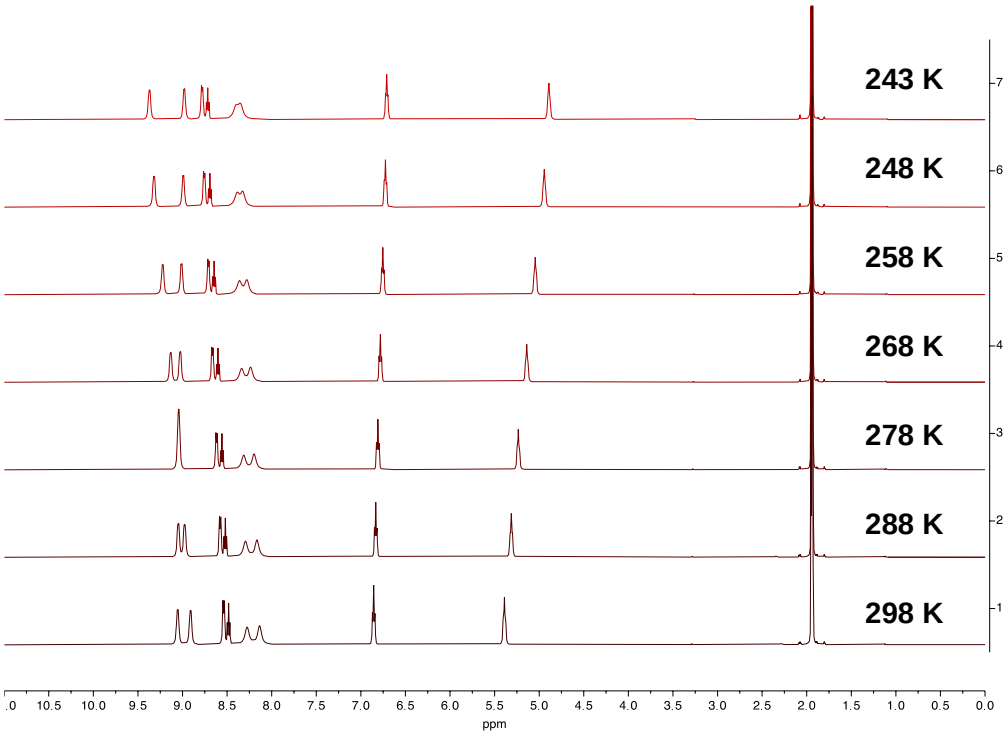

Figure 4.34 Variable temperature ^{1}H NMR spectra of $^{2/Ph}$**[Cu$_2$OH]$^{3+}$** in CD_3CN

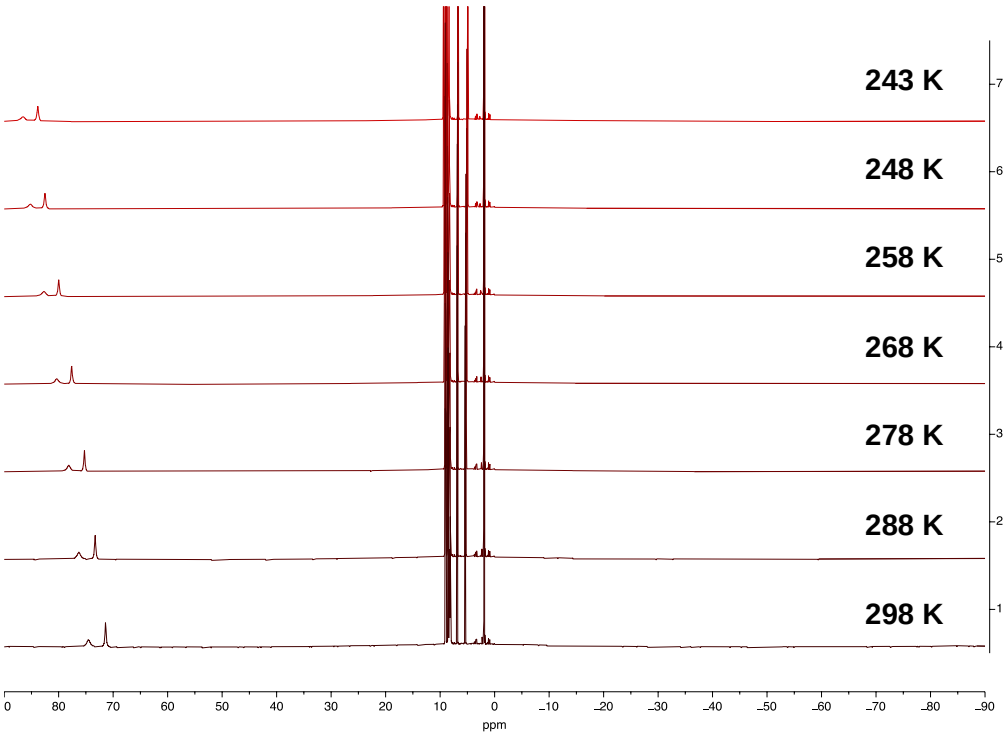

Figure 4.35 Wider window of Figure 4.34.

4.8.4 Infrared Spectra

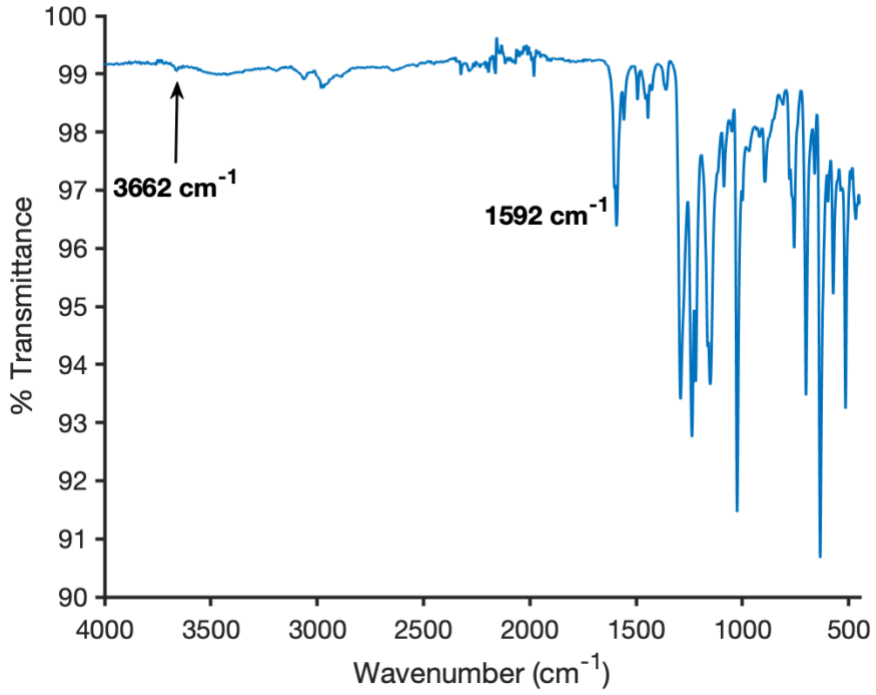

Figure 4.36 Infrared spectrum of $^{3/Ph}[Cu_2OH]^{3+}$.

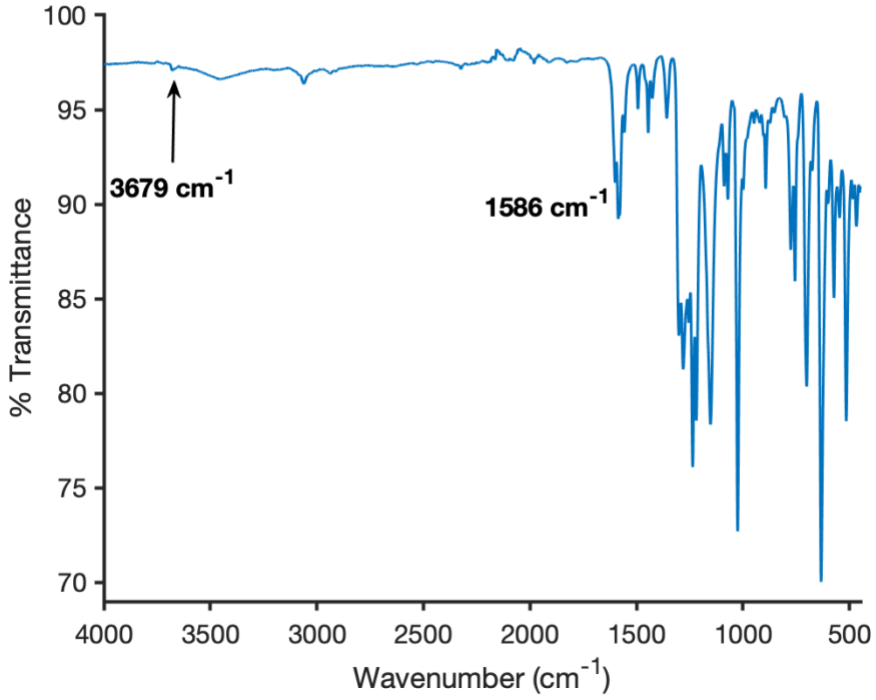

Figure 4.37 Infrared spectrum of $^{2/Ph}[Cu_2OH]^{3+}$.

4.8.5 Electrochemical Measurements of $^{n/Ph}[Cu_2OH]^{3+}$ (n = 2,3) Complexes

Cyclic Voltammetry of $^{3/Ph}[Cu_2OH]^{3+}$

As multiple scans were performed (1000 mV/s scan rate), the initial reduction features lost intensity, beginning to coalesce into one feature (Figure 4.38). The coalescence was more pronounced at slower scan rates (100 mV/s). A single reduction feature was observed in this instance ($E_{p,c}$ = -0.92 V vs. Fc/Fc^+, Figure 4.39). Attempting to observe the two irreversible reduction features, the scan rate was further increased to 2000 mv/S. However, the single reduction feature remained (Figure 4.40). Upon rinsing the working glassy carbon electrode with fresh solvent, the two irreversible features reappeared in the CV (1000 mV/s scan rate, Figure 4.41). Again, the signals coalesced over time. The loss and reappearance of signal suggests the product formed upon the irreversible reduction events adheres to the electrode surface. Due to this behavior, the calculation of the O–H BDFE of $^{3/Ph}[Cu_2OH]^{2+}$ used the $Cu_2(II,II)/Cu_2(I,II)$ irreversible reduction feature from the initial scan of the first CV measurement (before any intensity was lost).

Cyclic Voltammetry of $^{2/Ph}[Cu_2OH]^{3+}$

As observed for $^{3/Ph}\mathbf{[Cu_2OH]^{3+}}$, the two irreversible reduction features lost intensity over time in the CV of $^{2/Ph}\mathbf{[Cu_2OH]^{3+}}$ (Figure 4.42). The two features began to coalesce over the course of multiple measurements at 1000 mV/s with different potential windows (example shown in Figure 4.43). Because of the similar behavior, the calculation of the O–H BDFE of $^{3/Ph}\mathbf{[Cu_2OH]^{2+}}$ used the $Cu_2(II,II)/Cu_2(I,II)$ irreversible reduction feature from the initial scan of the first CV measurement (before any intensity was lost).

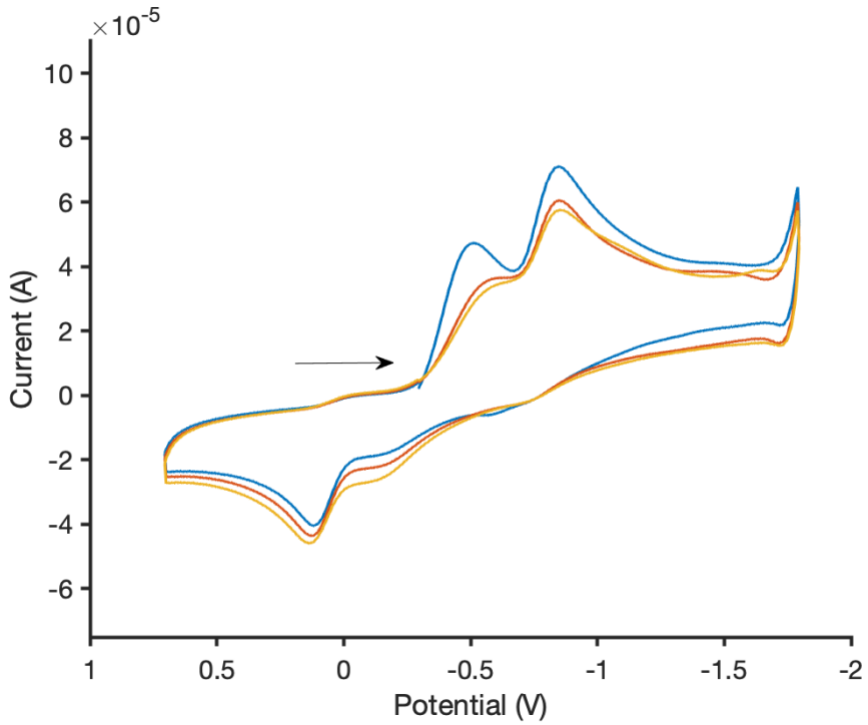

Figure 4.38 Cyclic voltammograms of $^{3/Ph}$**[Cu$_2$OH]$^{3+}$** at 1000 mV/s scan rate.

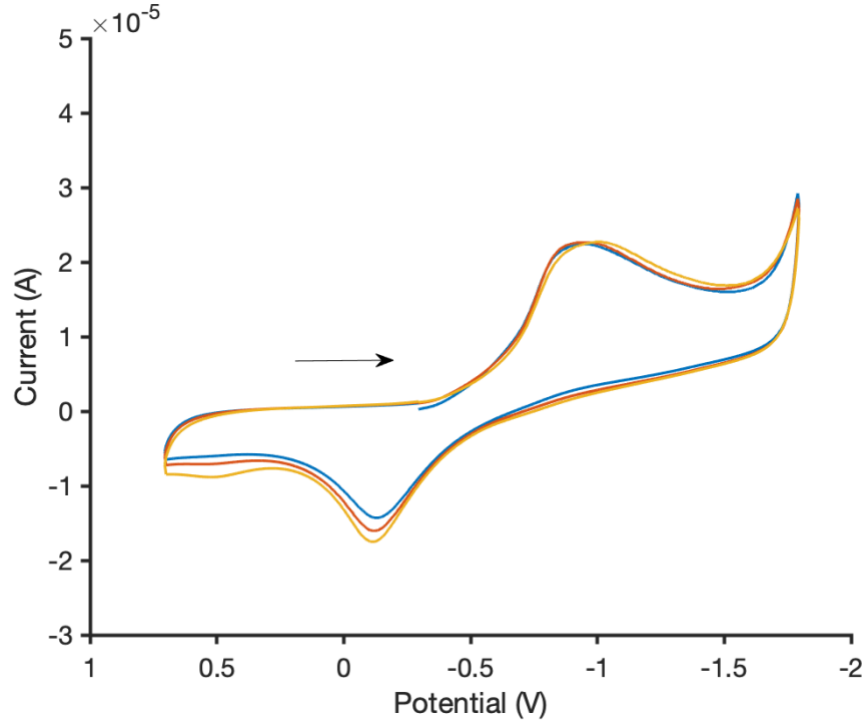

Figure 4.39 Cyclic voltammograms of $^{3/Ph}$**[Cu$_2$OH]$^{3+}$** at 100 mV/s scan rate.

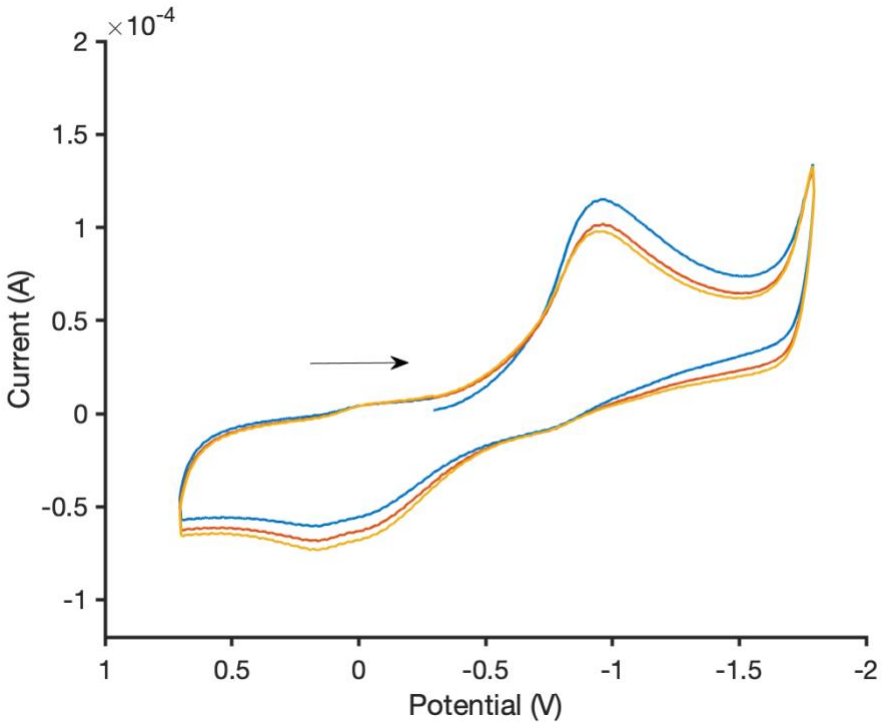

Figure 4.40 Cyclic voltammograms of $^{3/Ph}[Cu_2OH]^{3+}$ at 2000 mV/s scan rate.

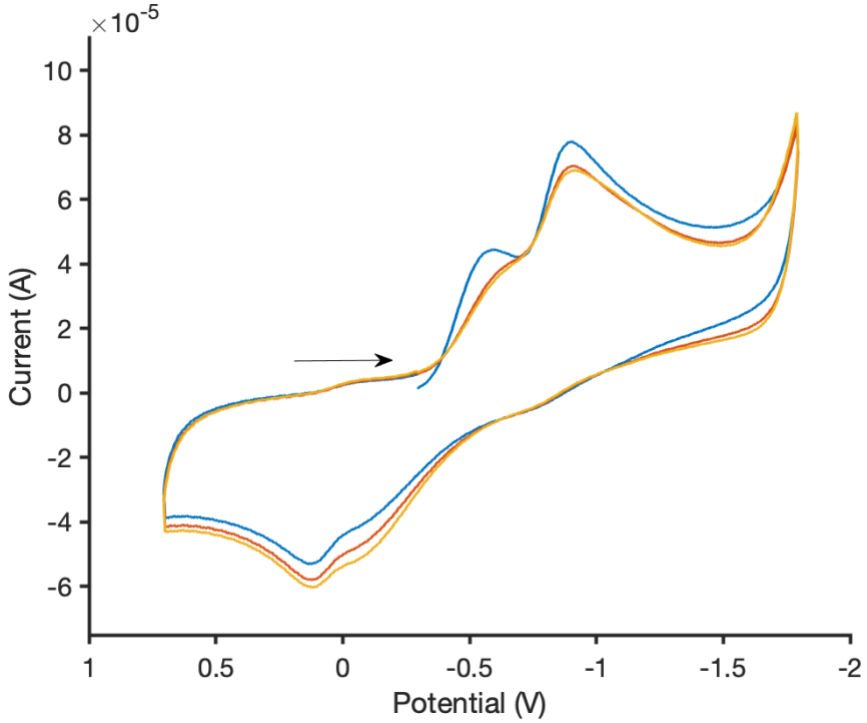

Figure 4.41 Reappearance of the irreversible reduction features of $^{3/Ph}[Cu_2OH]^{3+}$ after washing of the glass carbon electrode (scan rate = 1000 mV/s).

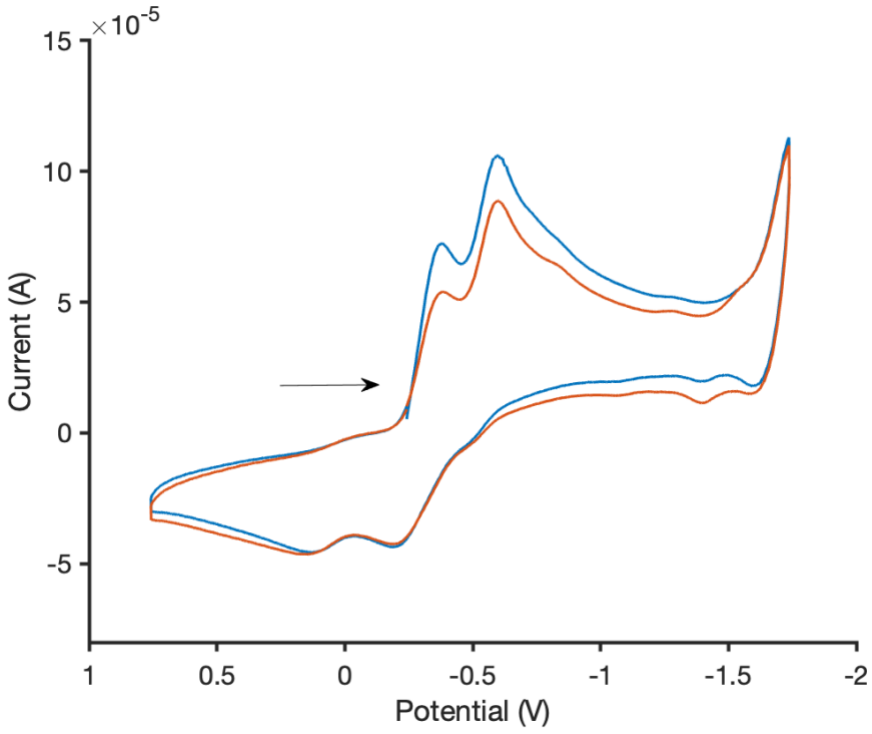

Figure 4.42 Cyclic voltammograms of $^{2/Ph}[Cu_2OH]^{3+}$ at 1000 mV/s scan rate.

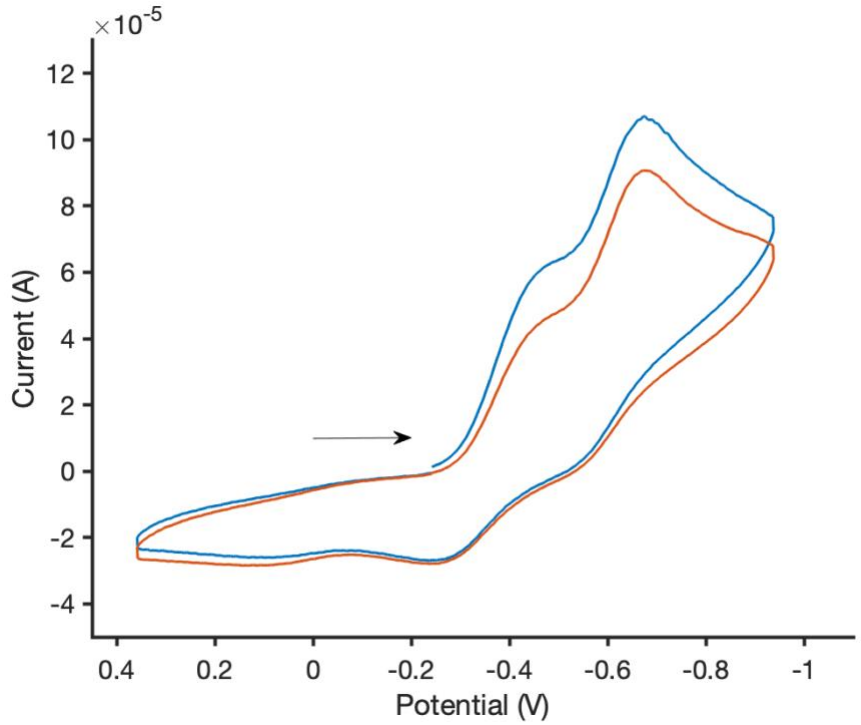

Figure 4.43 Coalescence of irreversible reduction features of $^{2/Ph}[Cu_2OH]^{2+}$ over a shorter potential window.

4.8.6 Chemical Reduction of $^{n/Ph}[Cu_2OH]^{3+}$ (n = 2,3) Complexes

Reduction of $^{3/Ph}[Cu_2OH]^{3+}$ *with Decamethylferrocene*

In the glovebox, a cuvette was charged with 2.4 mL of 0.1 mM $^{3/Ph}[Cu_2OH]^{3+}$ in IBN and sealed with a screw cap equipped with a septum. The cuvette was removed from the glovebox and placed in the pre-cooled cryostat (-65 °C). After 5 minutes, an initial "blank" spectrum was acquired of the complex. Following this measurement, 48 μL of 5.0 mM Cp^*_2Fe in IBN was injected into the cuvette using a 100 μL Hamilton gas tight syringe. Spectra were recorded every 60 seconds for an hour. After 10 minutes, the traces remained nearly identical. (Note: The same procedure was carried out at -30 °C. After 10 minutes, the intensity at 445 nm slowly began to decrease, indicating instability of the reduced species.)

Titration of $^{3/Ph}[Cu_2OH]^{3+}$ *with Decamethylferrocene*

In the glovebox, a cuvette was charged with 2.4 mL of 0.1 mM $^{3/Ph}[Cu_2OH]^{3+}$ in IBN and sealed with a screw cap equipped with a septum. The cuvette was removed from the glovebox and placed in the pre-cooled cryostat (-65 °C). After 5 minutes, an initial "blank" spectrum was acquired of the complex. Following this measurement, 10 μL of 5.0 mM Cp^*_2Fe in IBN was injected into the cuvette using a 100 μL Hamilton gas tight syringe. A spectrum of the reaction mixture was taken after 5 minutes. The procedure was repeated until a total of 12 measurements were made. See Figure 4.18 for absorbance vs. equiv. Cp^*_2Fe plot.

Reduction of $^{3/Ph}[Cu_2OH]^{3+}$ *with Cobaltocene*

1e$^-$ Reduction: In the glovebox, a cuvette was charged with 2.5 mL of 0.1 mM $^{3/Ph}[Cu_2OH]^{3+}$ in IBN and sealed with a screw cap equipped with a septum. The cuvette was removed from the glovebox and placed in the pre-cooled cryostat (-40 °C). After 5 minutes, an initial "blank" spectrum was acquired of the complex. Following this measurement, 43 μL of 5.8 mM Cp_2Co in IBN was injected into the cuvette using a 100 μL Hamilton gas tight syringe. A spectrum of the reaction mixture was taken after 5 minutes. The spectrum of the product is shown in Figure 4.47.

2e$^-$ Reduction: In the glovebox, a cuvette was charged with 2.4 mL of 0.1 mM $^{3/Ph}[Cu_2OH]^{3+}$ in IBN and sealed with a screw cap equipped with a septum. The cuvette was removed from the glovebox and placed in the pre-cooled cryostat (-65 °C). After 5 minutes, an initial "blank" spectrum was acquired of the complex. Following this measurement, 50 μL of 9.7 mM Cp_2Co in IBN was injected into the cuvette using a 100 μL Hamilton gas tight syringe. Spectra were recorded every 60 seconds for 25 minutes. (Note: Icing became an issue at -65 °C. After 5 minutes, the mixture was heated to -30 °C and the issue was resolved. A sample spectrum of the product is shown in Figure 4.47)

Titration of $^{2/Ph}[Cu_2OH]^{3+}$ *with Decamethylferrocene*

In the glovebox, a cuvette was charged with 2.5 mL of 0.1 mM $^{2/Ph}[Cu_2OH]^{3+}$ in IBN and sealed with a screw cap equipped with a septum. The cuvette was removed from the glovebox and placed in the pre-cooled cryostat (-30 °C). After 5 minutes, an initial "blank" spectrum was acquired of the complex. Following this measurement, 10 μL of 5.0 mM Cp^*_2Fe in IBN was injected into the cuvette using a 100 μL Hamilton gas tight syringe. A spectrum of the reaction mixture was taken after 3 minutes. The procedure was repeated until a total of 12 measurements were made.

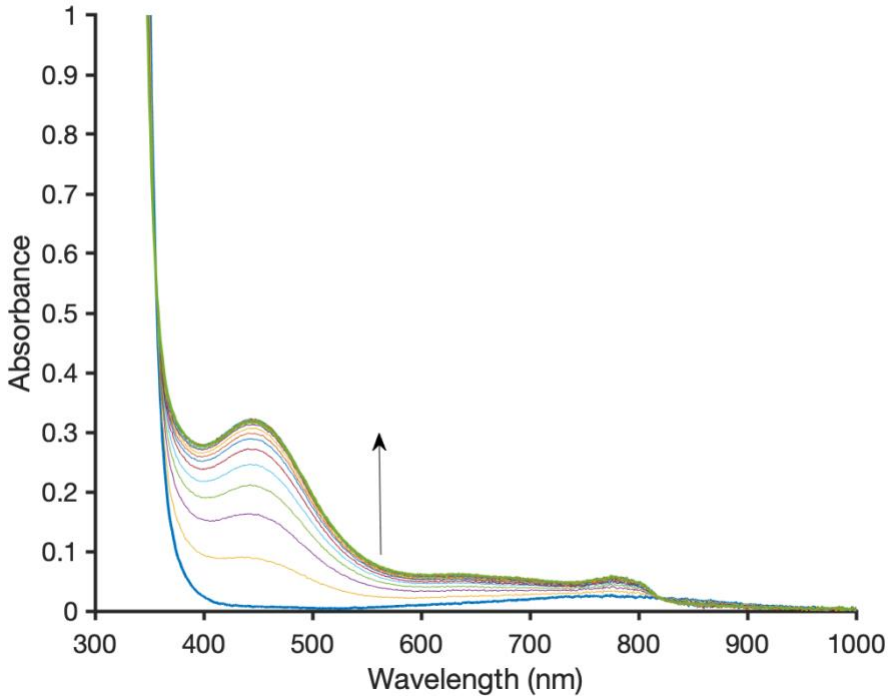

Figure 4.44 Time course of $^{3/Ph}$**[Cu$_2$OH]$^{3+}$** + Cp*$_2$Fe at -65 °C (60 x 1 min. scan; bolded traces represent start and finish).

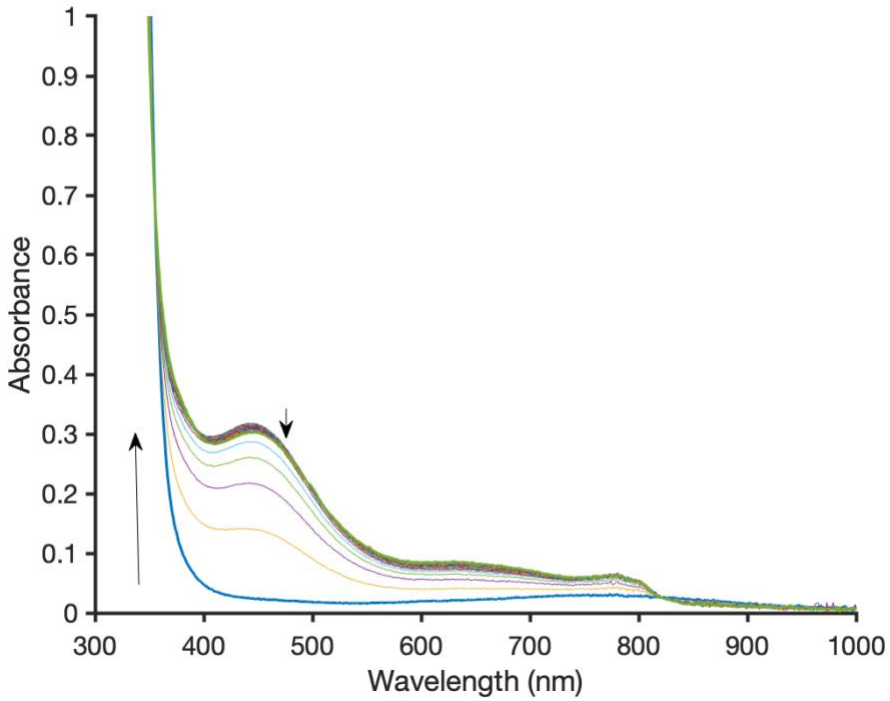

Figure 4.45 Time course of $^{3/Ph}$**[Cu$_2$OH]$^{3+}$** + Cp*$_2$Fe at -30 °C (60 x 1 min. scan; bolded traces represent start and finish).

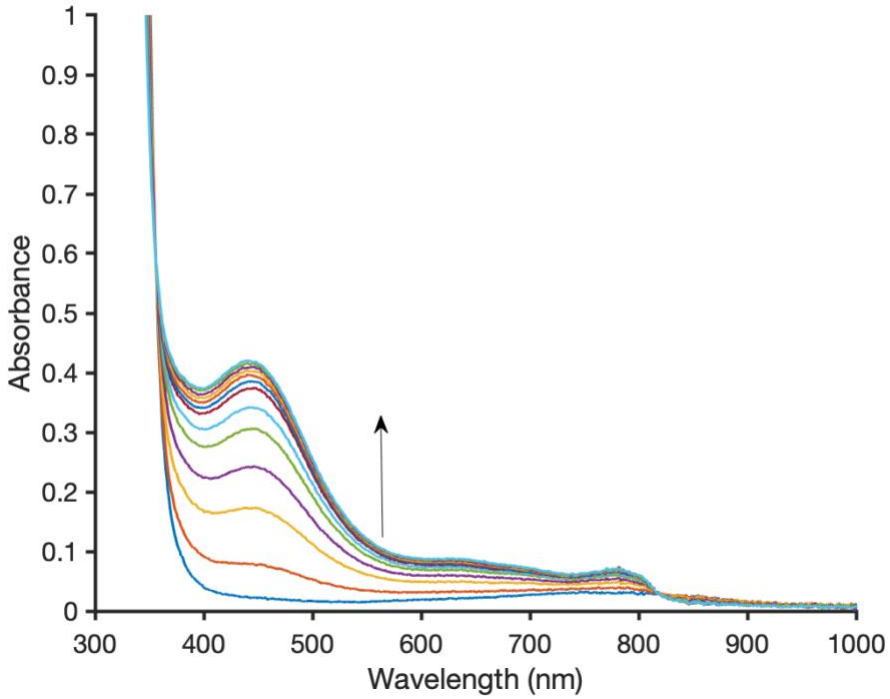

Figure 4.46 Titration of $^{3/Ph}$**[Cu$_2$OH]$^{3+}$** with Cp*$_2$Fe at -65 °C in 0.21 equiv. increments.

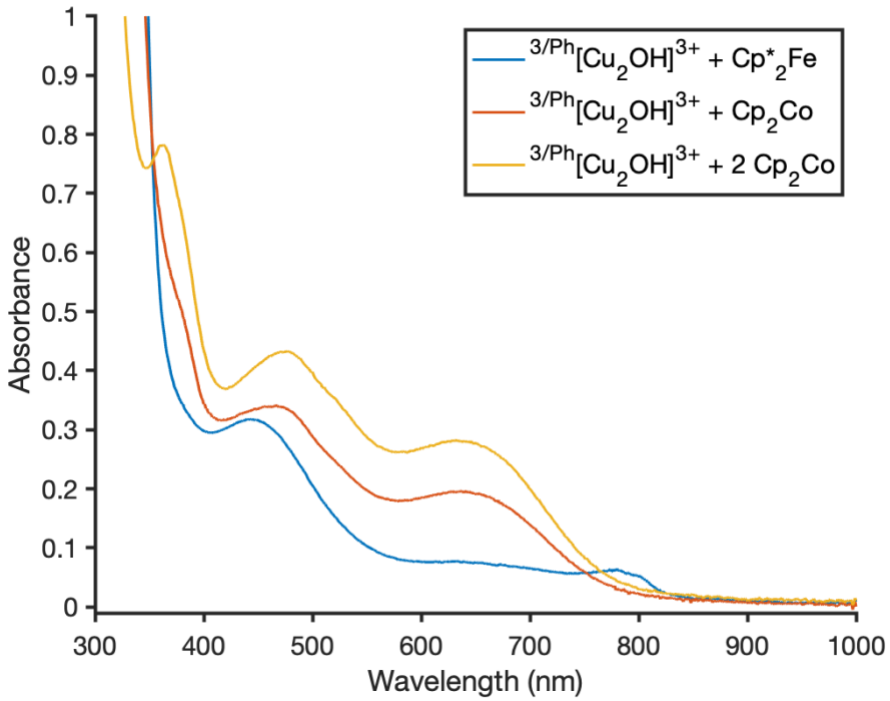

Figure 4.47 Comparison of one- vs. two-electron reduction of $^{3/Ph}$**[Cu$_2$OH]$^{3+}$** with Cp*$_2$Fe or Cp$_2$Co reductants (blue trace – 445 nm maximum; red trace – 460 nm maximum; yellow trace – 475 nm maximum)

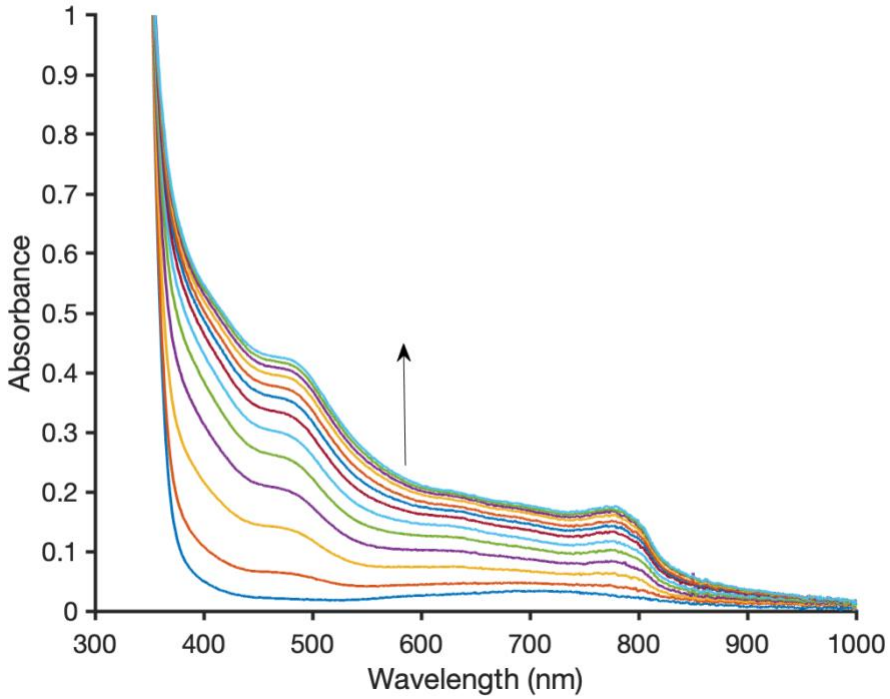

Figure 4.48 Titration of $^{2/Ph}[Cu_2OH]^{3+}$ with Cp^*_2Fe at -30 °C in 0.21 equiv. increments

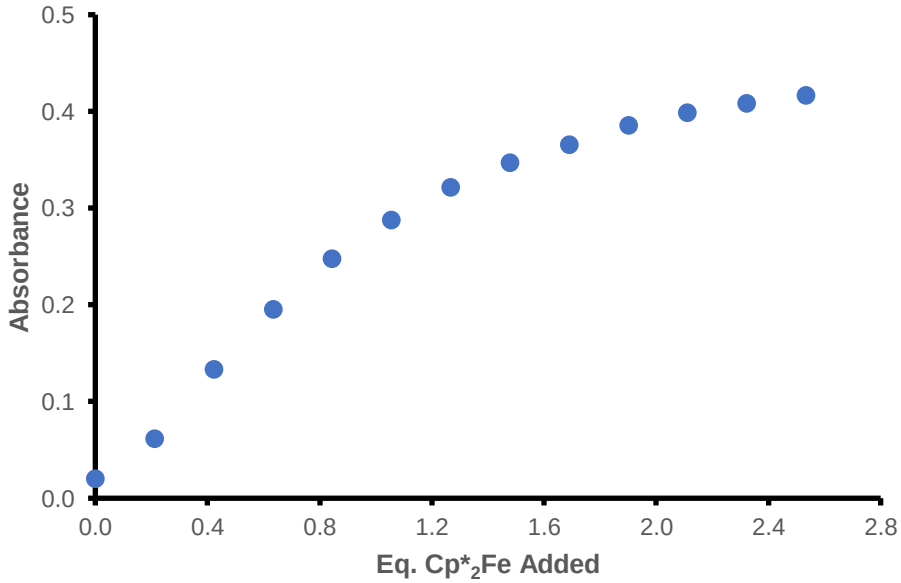

Figure 4.49 Titration of $^{2/Ph}[Cu_2OH]^{3+}$ with increasing quantities of Cp^*_2Fe at -30 °C.

4.8.7 Deprotonation of $^{n/Ph}[Cu_2OH]^{3+}$ (n = 2,3) Complexes

Deprotonation of $^{3/Ph}[Cu_2OH]^{\#+}$ *with DBU*

To a thin-wall J. young NMR tube, $^{3/Ph}[Cu_2OH]^{3+}$ (14.9 mg, 0.0107 mmol, 1.00 equiv.) and CD_3CN (*ca*. 0.6 mL) were added in the glovebox. The green solution was then treated with DBU (1.75 μL, 0.0117 mmol, 1.10 equiv.) using a 10 μL Hamilton gas tight syringe. ^1H NMR spectra were taken at the following time points – 20 minutes, 170 minutes (~3 hours) and 1560 minutes (26 hours). Over the course of the reaction, the NMR solution darkened until red in color. Full protonation of DBU was observed in the final spectrum (Figure 4.50). The time course is depicted in Figure (4.52). Comparison of the final product spectrum to the spectra of DBU and $^{3/Ph}[Cu_2OH]^{3+}$ is shown in Figure 4.54).

Deprotonation of $^{3/Ph}[Cu_2OH]^{3+}$ *with DBU and Protonation of* $^{3/Ph}[Cu_2O]^{2+}$ *with 2,6-lutidinium triflate*

In the glovebox a screw-cap NMR was charged with $^{3/Ph}[Cu_2OH]^{3+}$ (11.3 mg, 0.00810 mmol, 1.00 equiv.) and CD_3CN (*ca*. 0.6 mL), and sealed with a screw cap equipped with a septum. The NMR tube was removed from the glovebox and cooled to -25 °C in a Bruker DMX 500 spectrometer. After 10 minutes, 9 μL of 0.99 MM DBU in CD_3CN was injected into the NMR tube using a 100 μL Hamilton gas tight syringe. After 10 minutes, the ^1H spectrum of the deprotonated product was recorded. Then, 29 μL of 0.28 M 2,6-lutidinium triflate in CD_3CN was injected into the NMR tube using a 100 μL Hamilton gas tight syringe. After 10 minutes, the ^1H spectrum of the re-protonated starting material was recorded. A comparison of the corresponding spectra are presented in Figure 4.56.

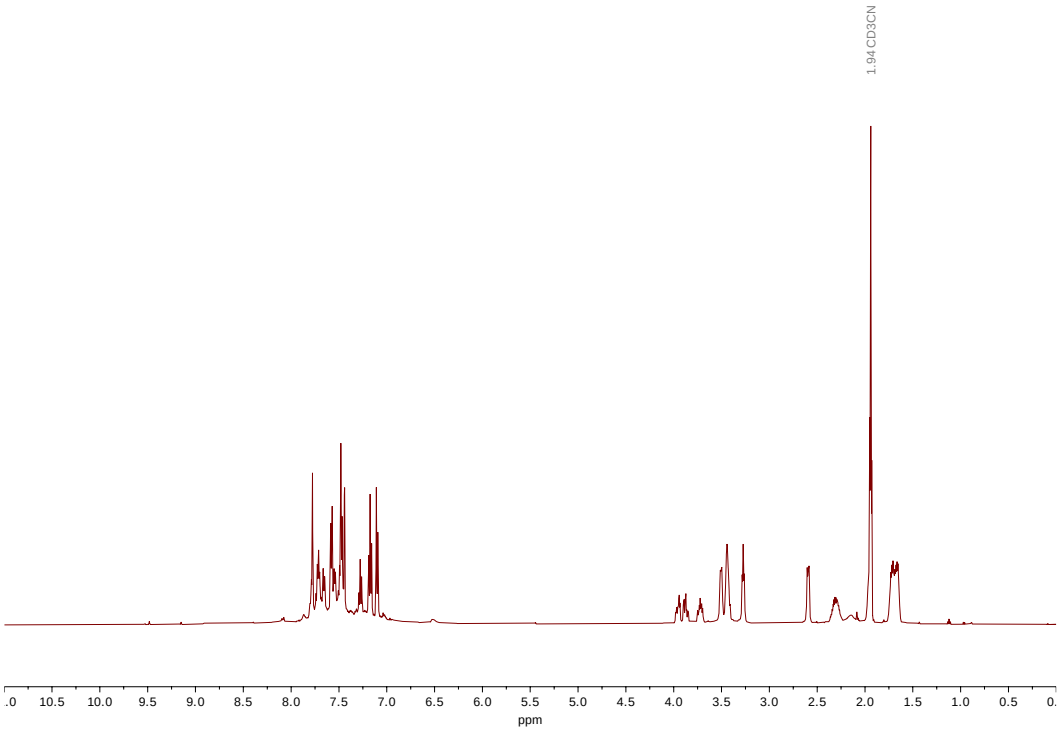

Figure 4.50 ^{1}H NMR spectrum of $^{3/Ph}[Cu_2OH]^{3+}$ + DBU in CD_3CN (26 hours)

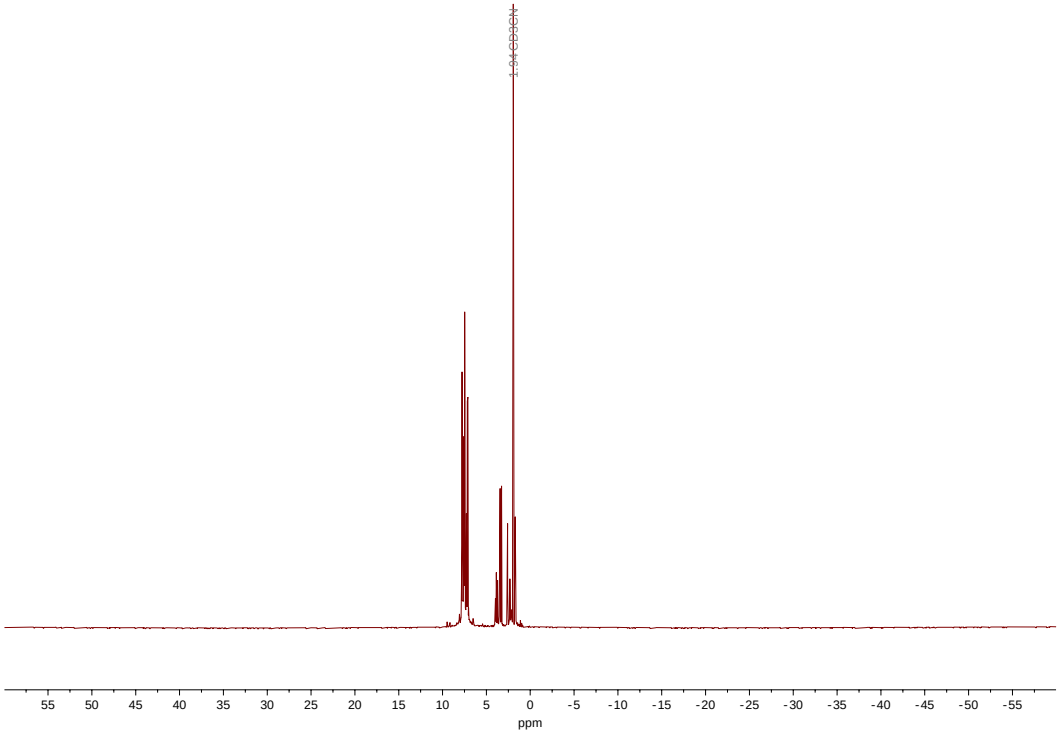

Figure 4.51 Wider window ^{1}H NMR spectrum of $^{3/Ph}[Cu_2OH]^{3+}$ + DBU in CD_3CN (26 hours)

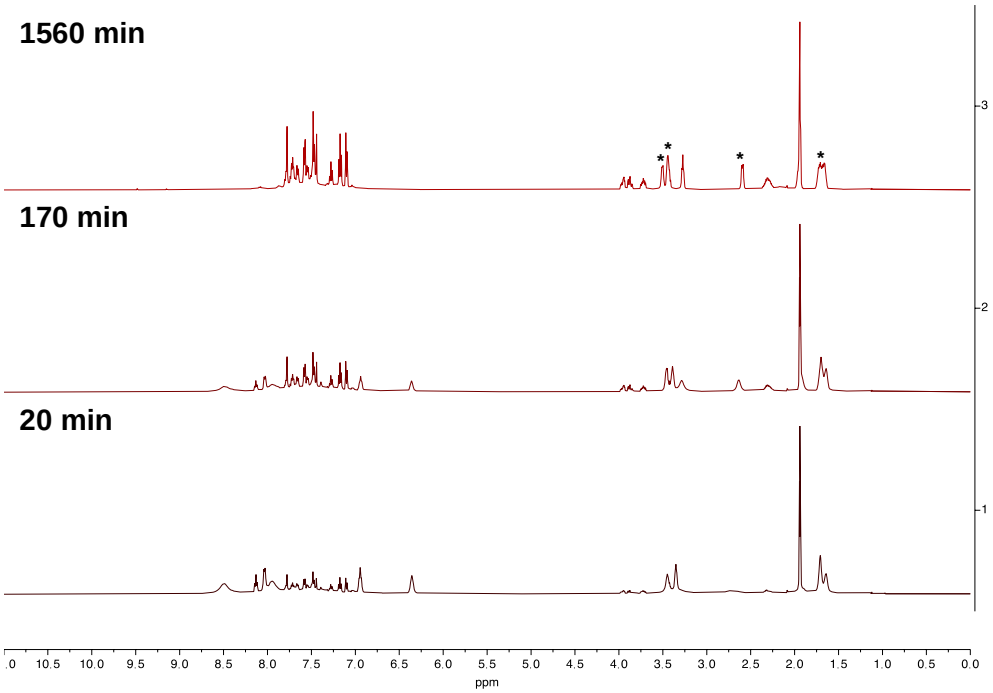

Figure 4.52 Time course of $^{3/Ph}$**[Cu$_2$OH]$^{3+}$** + DBU in CD_3CN (* = [HDBU][OTf]).

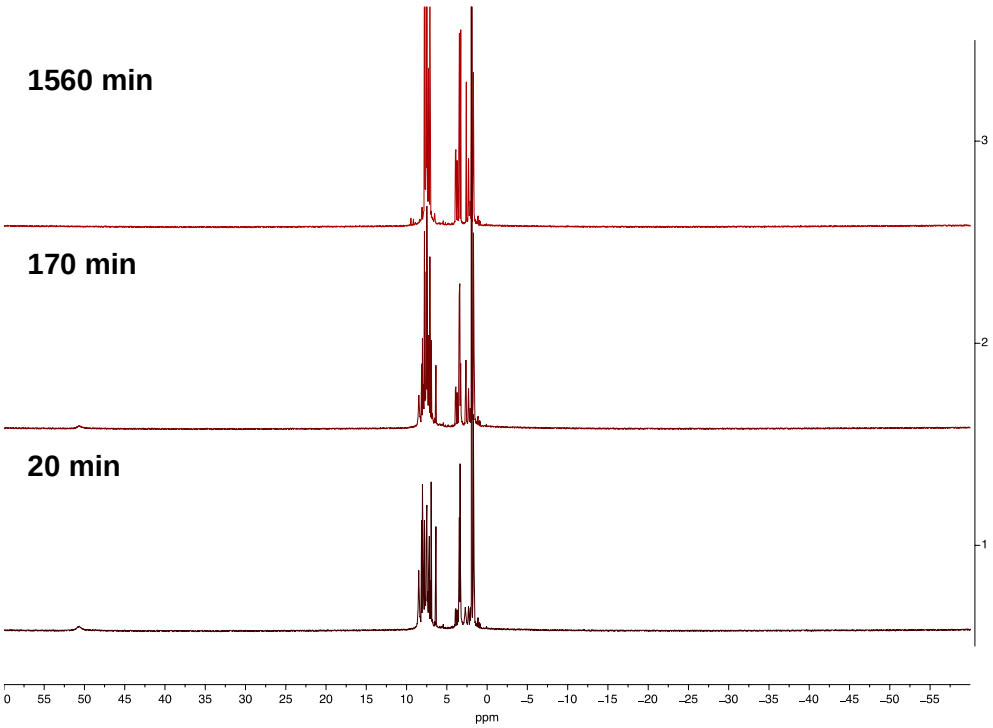

Figure 4.53 Wider window of time course of $^{3/Ph}$**[Cu$_2$OH]$^{3+}$** + DBU in CD_3CN.

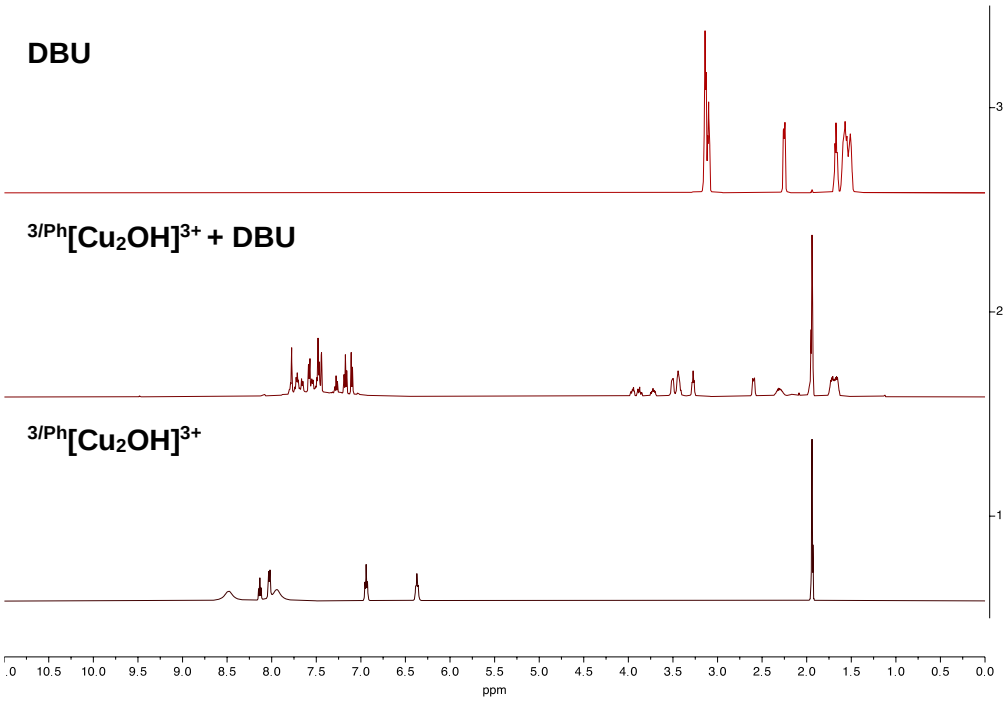

Figure 4.54 ^{1}H NMR Spectroscopic support for DBU protonation at -25 °C.

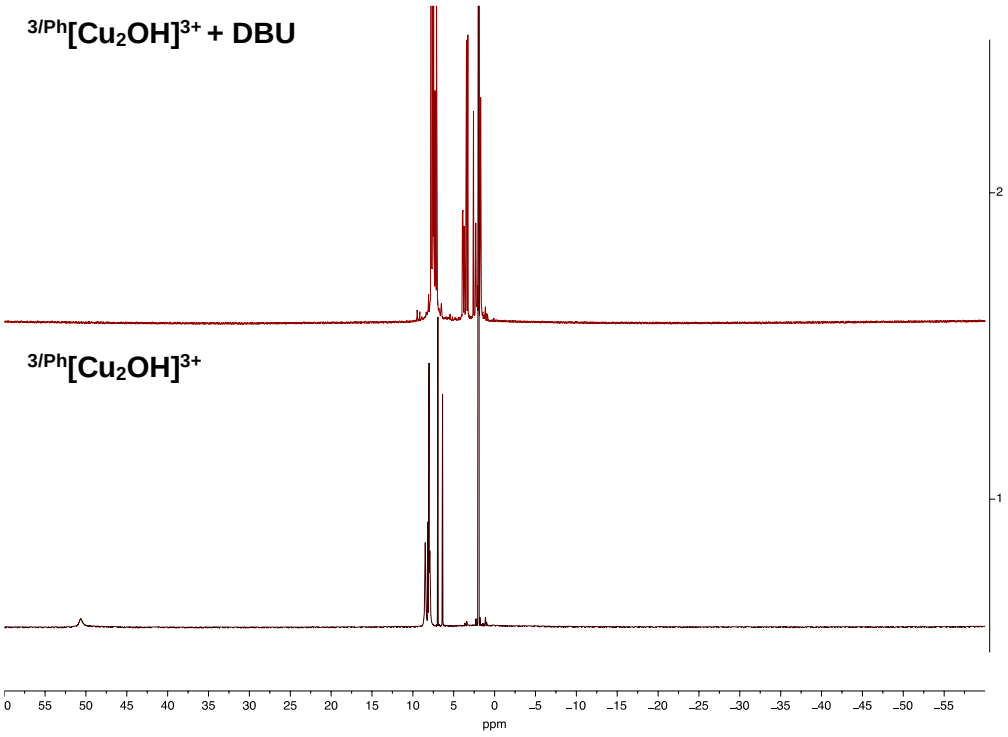

Figure 4.55 Wider window of Figure 4.54.

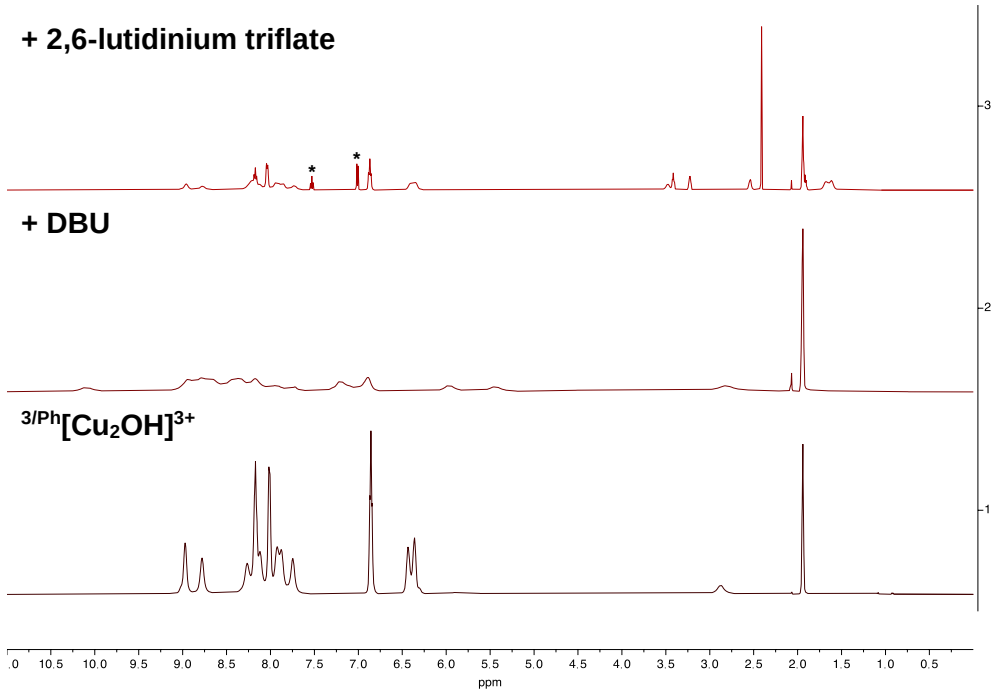

Figure 4.56 Low-temperature (-25 °C) ^{1}H NMR spectroscopic analysis of the deprotonation of $^{3/Ph}[Cu_2OH]^{3+}$ with DBU followed by the protonation of $^{3/Ph}[Cu_2O]^{2+}$ with 2,6-lutidinium triflate (* = 2,6-lutidine).

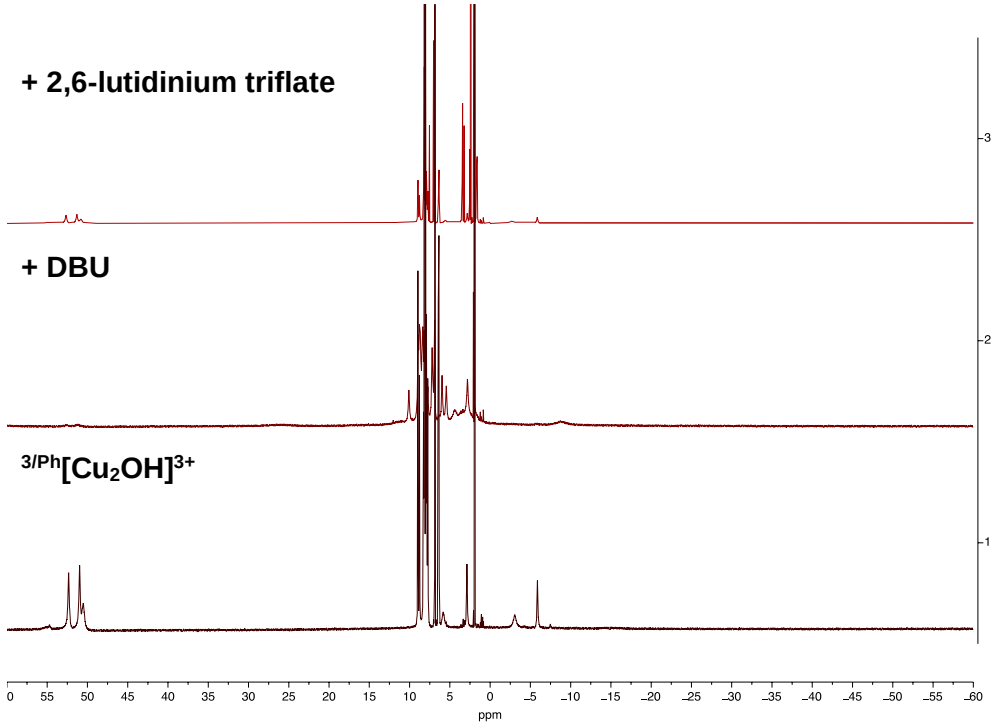

Figure 4.57 Wider window of the spectroscopic analysis in Figure 4.51.

Deprotonation of $^{3/Ph}[Cu_2OH]^{3+}$ *with Verkade*^{iPr}

In the glovebox, a cuvette was charged with 2.4 mL of 0.1 mM $^{3/Ph}[Cu_2OH]^{3+}$ in IBN and sealed with a screw cap equipped with a septum. The cuvette was removed from the glovebox and placed in the pre-cooled cryostat (-65 °C). After 5 minutes, an initial "blank" spectrum was acquired of the complex. Following this measurement, 32 μL of 7.5 mM Verkade^{iPr} in IBN was injected into the cuvette using a 100 μL Hamilton gas tight syringe. Spectra were recorded every 60 seconds for an hour. After 10 minutes, the traces remained nearly identical. (Note: The same procedure was carried out at -30 °C. After 10 minutes, the traces remained nearly identical.)

Thermal Decomposition of $^{3/Ph}[Cu_2O]^{3+}$

In the glovebox, a cuvette was charged with 2.4 mL of 0.1 mM $^{3/Ph}[Cu_2OH]^{3+}$ in IBN and sealed with a screw cap equipped with a septum. The cuvette was removed from the glovebox and placed in the pre-cooled cryostat (-65 °C). After 5 minutes, an initial "blank" spectrum was acquired of the complex. Following this measurement, 32 μL of 7.5 mM Verkade^{iPr} in IBN was injected into the cuvette using a 100 μL Hamilton gas tight syringe. Spectra were recorded every 60 seconds for an hour (Figure 4.**X**). Over the course of the first 40 minutes, the temperature was ramped to 25 °C. A slow decomposition occurred during this timespan. Over the final 20 minutes, the temperature was ramped to 95 °C, showing an increase in the rate of decomposition to $^{3/Ph}[Cu]^{+}$.

Deprotonation of $^{2/Ph}[Cu_2OH]^{3+}$ *with Verkade*^{iPr} *– Method A*

In the glovebox, a cuvette was charged with 2.5 mL of 0.1 mM $^{3/Ph}[Cu_2OH]^{3+}$ in IBN and sealed with a screw cap equipped with a septum. The cuvette was removed from the glovebox and placed in the pre-cooled cryostat (-30 °C). After 5 minutes, an initial "blank"

spectrum was acquired of the complex. Following this measurement, 26 μL of 9.6 mM Verkade^{iPr} in THF was injected into the cuvette using a 100 μL Hamilton gas tight syringe. Spectra were recorded every 15 minutes for 90 minutes.

Deprotonation of **$^{2/Ph}$[Cu$_2$OH]$^{3+}$** *with Verkade^{iPr} – Method B*

In the glovebox, a cuvette was charged with 2.4 mL of 0.1 mM **$^{3/Ph}$[Cu$_2$OH]$^{3+}$** in IBN and sealed with a screw cap equipped with a septum. The cuvette was removed from the glovebox and placed in the pre-cooled cryostat (-65 °C). After 5 minutes, an initial "blank" spectrum was acquired of the complex. Following this measurement, 39 μL of 6.2 mM Verkade^{iPr} in IBN was injected into the cuvette using a 100 μL Hamilton gas tight syringe. Spectra were recorded every 60 seconds for 30 minutes. After 10 minutes, the traces remained nearly identical.

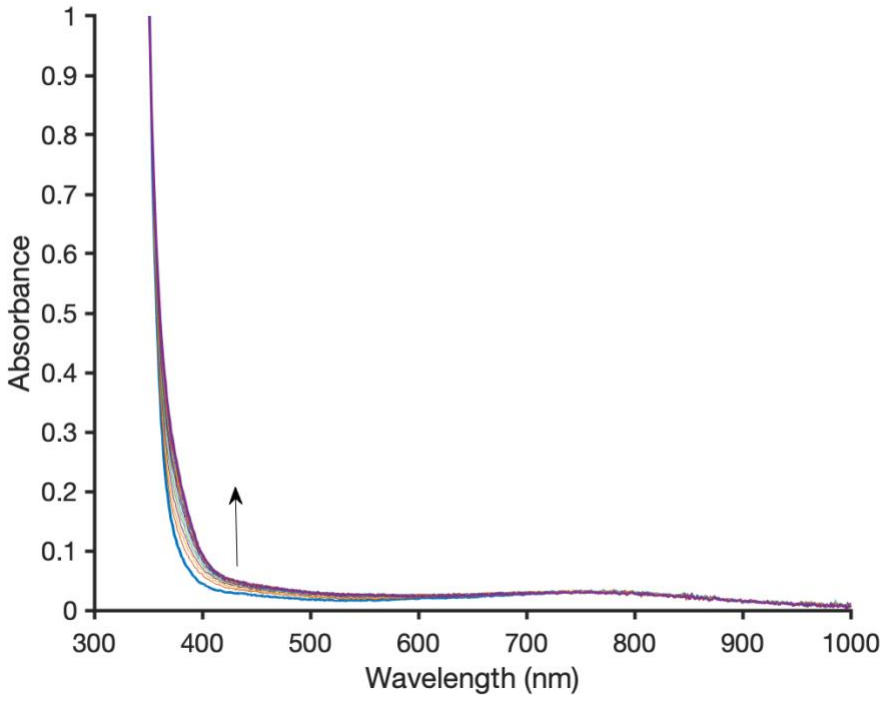

Figure 4.58 Time course of **$^{3/Ph}$[Cu$_2$OH]$^{3+}$** + Verkade^{iPr} at -65 °C (60 x 1 min. scans; bolded traces represent start and finish).

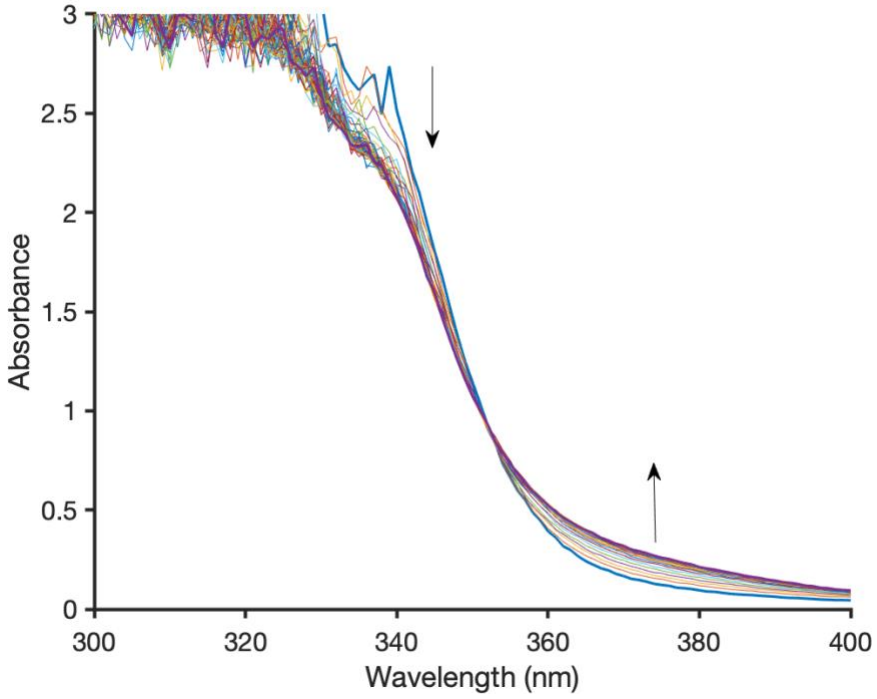

Figure 4.59 Zoomed in view of isosbestic point at 352 nm in reaction of $^{3/Ph}[Cu_2OH]^{3+}$ + Verkade^{iPr} at -65 °C (bolded traces represent start and finish).

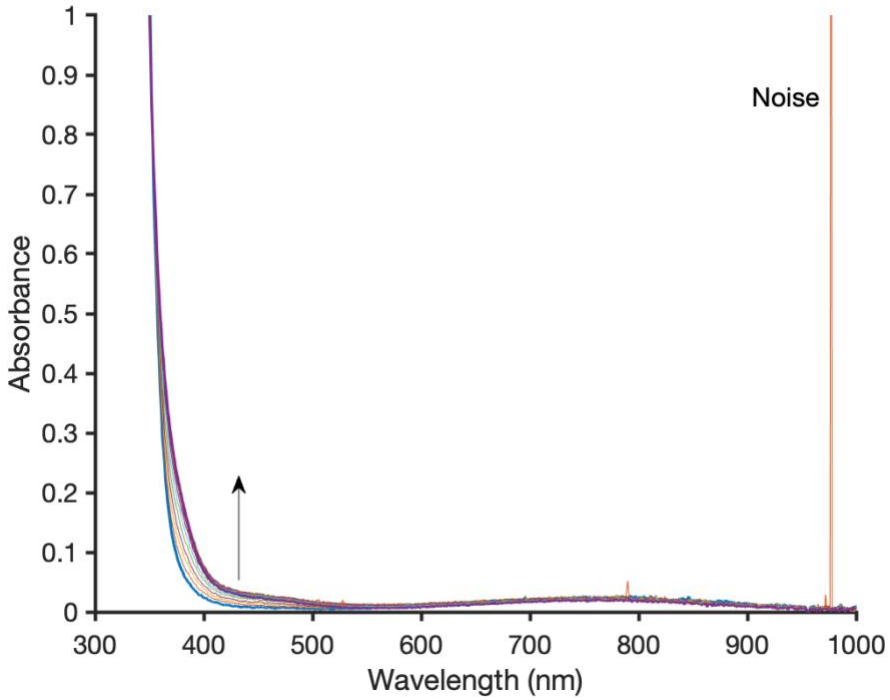

Figure 4.60 Time course of $^{3/Ph}[Cu_2OH]^{3+}$ + Verkade^{iPr} at -30 °C (60 x 1 min. scans; bolded traces represent start and finish).

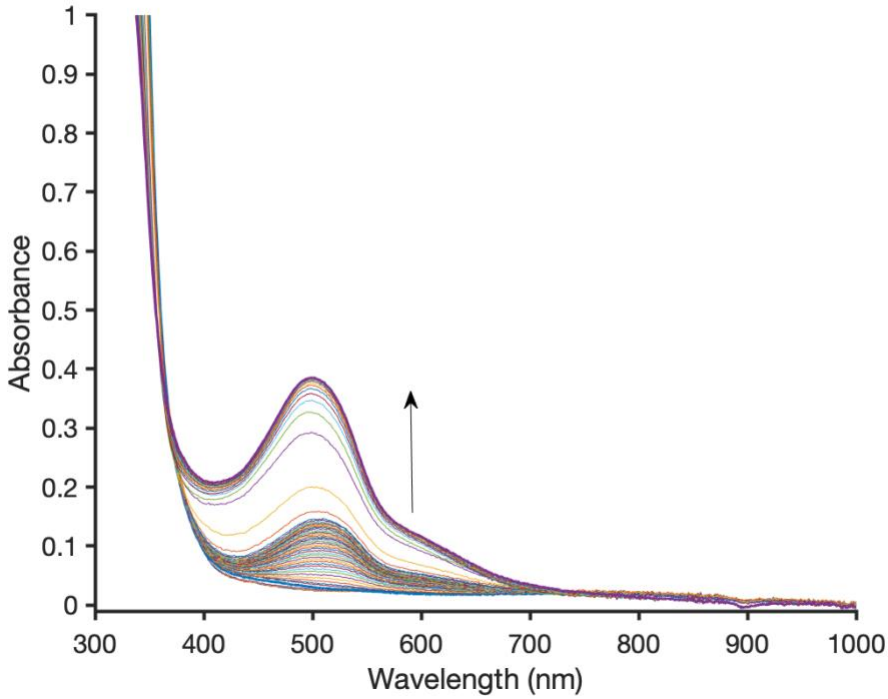

Figure 4.61 Time course of the thermal decomposition of $^{3/Ph}[Cu_2OH]^{3+}$ + Verkade^{iPr} (60 x 1 min. scans; first 40 minutes = ramp from -65 °C to 25 °C; final 20 minutes = ramp from 25 °C to 95 °C; bolded traces represent start and finish).

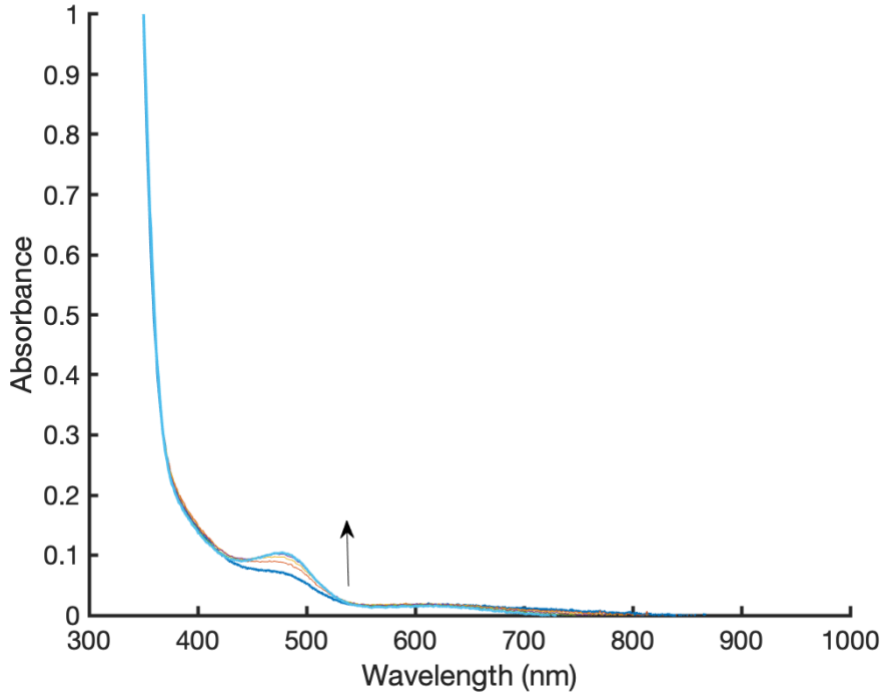

Figure 4.62 Time course of the decomposition of $^{2/Ph}[Cu_2OH]^{3+}$ + Verkade^{iPr} at -30 °C (6 x 15 min. scans; bolded traces represent start and finish).

pKa Determination of $^{3/Ph}$**[Cu$_2$OH]$^{3+}$** *with 1,8-bis(tetramethylguanidino)naphthalene*

In the glovebox, a screw-cap NMR tube was charged with 0.4 mL of 30.8 mM $^{3/Ph}$**[Cu$_2$OH]$^{3+}$** and 12 μL of 511 mM 1,3,5-trimethoxybenzene, both in CD_3CN, and sealed with a screw cap equipped with a septum. The NMR tube was removed from the glovebox and cooled to -30 °C in a Bruker DRX 500 spectrometer. After 15 minutes, an initial "blank" spectrum was acquired of the complex. Following this measurement, 25 μL of 109 mM 1,8-*bis*(tetramethylguanidino)naphthalene in CD_3CN was injected into the NMR tube using a 100 μL Hamilton gas tight syringe. The sample was allowed to equilibrate for 15 minutes before data acquisition. The procedure was repeated until 8 titrations points were collected.

Equilibrium concentrations were calculated using the 1,8-*bis*(tetramethylguanidino)naphthalene (TMG-PS) peak integrations noted in Table 4.1 (see footnote). From the concentrations, K_{eq} was calculated followed by pK_{eq}. The value of pK_{eq} corresponds to the difference between the pK_a of $^{3/Ph}$**[Cu$_2$OH]$^{3+}$** and the known pK_{aH} of 1,8-*bis*(tetramethylguanidino)naphthalene (24.92). Subtraction of pK_{eq} from 24.92 yielded the pK_a of $^{3/Ph}$**[Cu$_2$OH]$^{3+}$**. Values in each set (1-3) were averaged to afford three unique pK_a values, which were subsequently averaged to afford the final pK_a of 24.4 ± 0.4. We believe this value to be an overestimate of the tr*ue* pK_a of $^{3/Ph}$**[Cu$_2$OH]$^{3+}$**. For data sets 1 and 2, uncertainty may arise from possible overlap of the associated 1,8-*bis*(tetramethylguanidino)naphthalene proton resonances with the proton resonances of $^{3/Ph}$**[Cu$_2$O]$^{2+}$**. For data set 3, a doublet associated with the conjugate acid of 1,8-*bis*(tetramethylguanidino)naphthalene (6.44 ppm) overlaps with a broad resonance of $^{3/Ph}$**[Cu$_2$OH]$^{3+}$** (6.38 ppm) introducing a large source of uncertainty into the measurement.

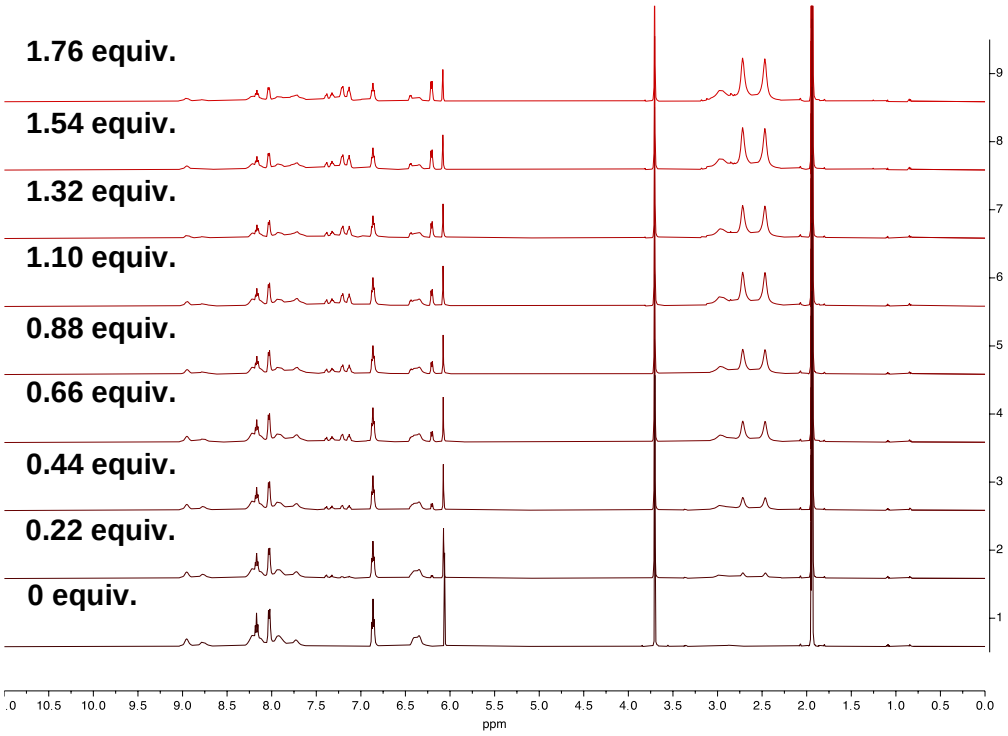

Figure 4.63 ^{1}H NMR spectroscopic titration of $^{3/Ph}[Cu_2OH]^{3+}$ with 1,8-*bis*(tetramethylguanidino)naphthalene at -30 °C in CD_3CN.

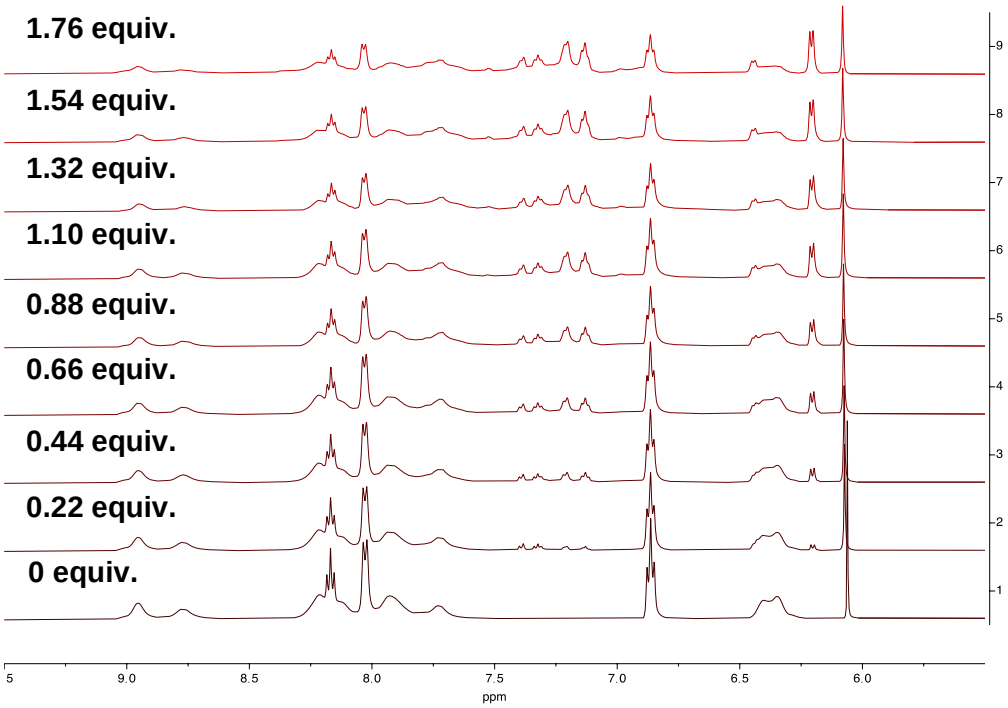

Figure 4.64 Aromatic region of $^{3/Ph}[Cu_2OH]^{3+}$ ^{1}H NMR spectroscopic titration.

Table 4.1 $^{3/Ph}[Cu_2OH]^{3+}$ equilibrium mixtures determined from titration points.[a]

	TMG-PS	$[TMG\text{-}PS]^{H+}$	$^{3/Ph}[Cu_2OH]^{3+}$	$^{3/Ph}[Cu_2O]^{2+}$	K_{eq}	pK_{eq}	pK_a
	-	-	30.8	-	-	-	-
	3.68	4.65	23.5	4.65	0.249	0.603	24.3
	8.12	6.03	20.6	6.03	0.217	0.663	24.3
	12.2	7.34	18.0	7.34	0.246	0.608	24.3
	15.3	8.10	16.2	8.10	0.265	0.577	24.3
1[b]	18.8	9.34	14.0	9.34	0.331	0.480	24.4
	20.7	9.41	13.1	9.41	0.327	0.486	24.4
	25.8	12.6	9.12	12.6	0.671	0.171	24.7
	30.2	15.7	5.32	15.7	1.53	-0.184	25.1
			Average				**24.5**
			Standard Deviation				**0.3**
	3.96	5.41	22.8	5.41	0.325	0.488	24.4
	8.24	7.55	19.1	7.55	0.362	0.442	24.5
	12.1	9.42	15.9	9.42	0.461	0.336	24.6
	15.3	10.7	13.6	10.7	0.544	0.265	24.7
2[c]	18.6	12.3	11.0	12.3	0.741	0.130	24.8
	20.9	12.8	9.77	12.8	0.797	0.098	24.8
	24.5	16.2	5.50	16.2	1.95	-0.291	25.2
	27.2	19.3	1.67	19.3	8.18	-0.913	25.8
			Average				**24.9**
			Standard Deviation				**0.5**
	4.78	3.12	25.1	3.12	0.0813	1.09	23.8
	8.98	3.15	23.5	3.15	0.0469	1.33	23.6
	12.6	3.36	21.9	3.36	0.408	1.39	23.5
	15.6	2.69	21.6	2.69	0.0214	1.67	23.3
3[d]	18.5	4.14	19.2	4.14	0.0482	1.32	23.6
	20.4	3.99	18.5	3.99	0.0421	1.38	23.5
	23.9	7.11	14.6	7.11	0.145	0.840	24.1
	27.1	9.06	11.9	9.06	0.254	0.596	24.3
			Average				**23.7**
			Standard Deviation				**0.3**

a – All concentrations are reported in units of mM.
b – Concentrations determined using integrations of signals at 7.20 and 7.39 ppm.
c – Concentrations determined using integrations of signals at 7.12 and 7.32 ppm.
d – Concentrations determined using integrations of signals at 6.20 and 6.44 ppm.

pKa Determination of $^{2/Ph}$**[Cu$_2$OH]$^{3+}$** *with 1,8-bis(tetramethylguanidino)naphthalene*

In the glovebox, a screw-cap NMR tube was charged with 0.4 mL of 29.0 mM $^{3/Ph}$**[Cu$_2$OH]$^{3+}$** and 25 μL of 511 mM 1,3,5-trimethoxybenzene, both in CD_3CN, and sealed with a screw cap equipped with a septum. The NMR tube was removed from the glovebox and cooled to -30 °C in a Bruker DRX 500 spectrometer. After 15 minutes, an initial "blank" spectrum was acquired of the complex. Following this measurement, 20 μL of 129 mM 1,8-*bis*(tetramethylguanidino)naphthalene in CD_3CN was injected into the NMR tube using a 100 μL Hamilton gas tight syringe. The sample was allowed to equilibrate for 15 minutes before data acquisition. The procedure was repeated until 8 titrations points were collected.

Equilibrium concentrations (Table 4.2) were calculated using the 1,8-*bis*(tetramethylguanidino)naphthalene (TMG-PS) peak integrations at 6.44 and 6.20 ppm. From the concentrations, K_{eq} was calculated followed by pK_{eq}. The value of pK_{eq} corresponds to the difference between the pK_a of $^{2/Ph}$**[Cu$_2$OH]$^{3+}$** and the known pK_{aH} of 1,8-*bis*(tetramethylguanidino)naphthalene (24.92). Subtraction of pK_{eq} from 24.92 yielded the pK_a of $^{2/Ph}$**[Cu$_2$OH]$^{3+}$**. Values were averaged to afford the pK_a of 25.6 ± 0.5. We believe this value to be an overestimate of the tr*ue* pK_a of $^{2/Ph}$**[Cu$_2$OH]$^{3+}$**. At later titration points, the signal at 6.20 ppm began to broaden. Along with this change, a shoulder grew in on the 1,3,5-trimethoxybenzene signal at 6.08 ppm, suggesting a new species was forming. Slow background decomposition may also be occurring on the NMR timescale, as observed in the UV-vis-NIR experiment.

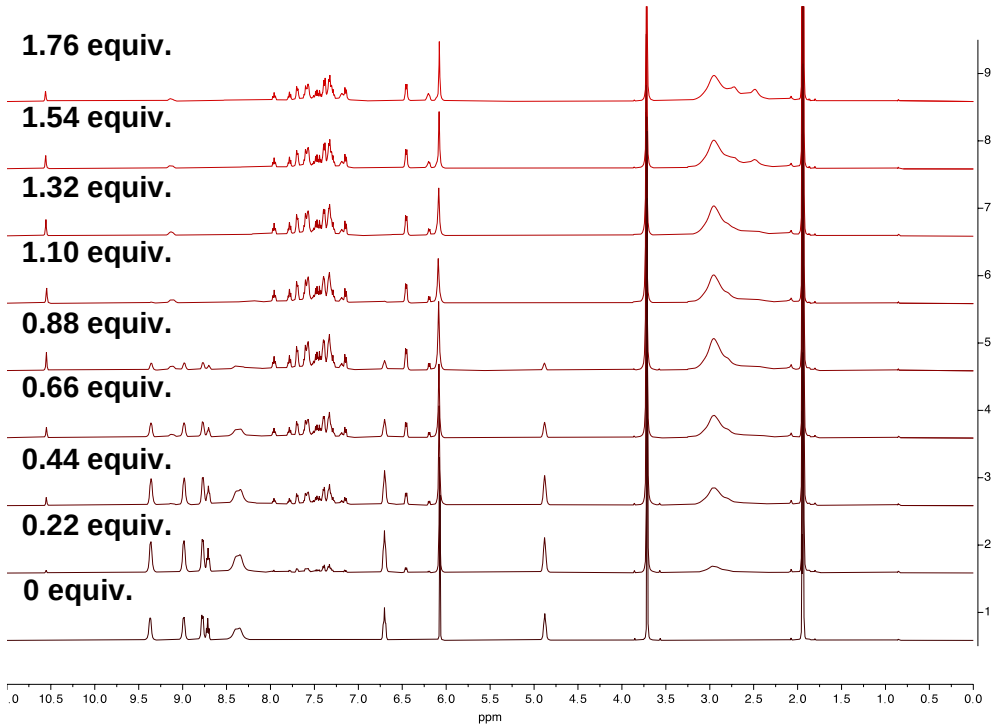

Figure 4.65 ^{1}H NMR spectroscopic titration of $^{2/Ph}[Cu_2OH]^{3+}$ with 1,8-*bis*(tetramethylguanidino)naphthalene at -30 °C in CD_3CN.

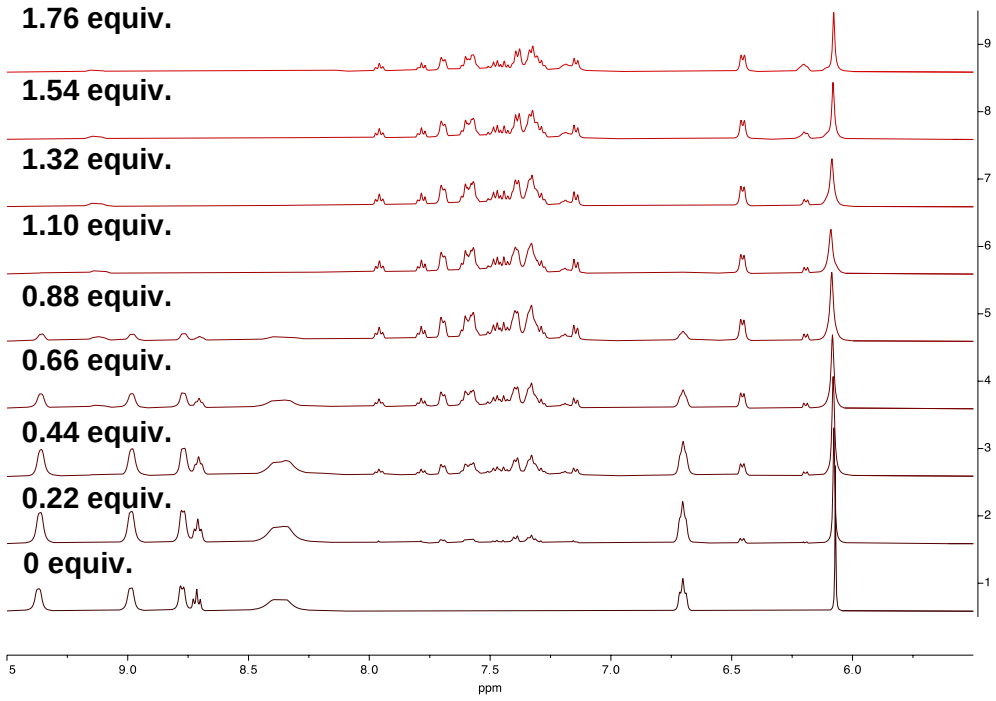

Figure 4.66 Aromatic region of $^{3/Ph}[Cu_2OH]^{3+}$ ^{1}H NMR spectroscopic titration.

Table 4.2 $^{2/Ph}[Cu_2OH]^{3+}$ equilibrium mixtures determined from titration points.[a]

TMG-PS	$[TMG\text{-}PS]^{H+}$	$^{3/Ph}[Cu_2OH]^{3+}$	$^{3/Ph}[Cu_2O]^{2+}$	K_{eq}	pK_{eq}	pK_a
1.71	4.69	21.4	4.69	0.604	0.219	24.7
2.86	8.83	16.1	8.83	1.69	-0.229	25.1
4.30	12.0	11.9	12.0	2.81	-0.449	25.4
4.76	14.8	8.21	14.8	5.58	-0.746	25.7
5.80	16.9	5.22	16.9	9.41	-0.974	25.9
6.63	17.2	4.10	17.2	10.9	-1.04	26.0
7.94	16.9	3.60	16.9	10.0	-1.00	25.9
9.50	16.5	3.29	16.5	8.76	-0.943	25.9
			Average			**25.6**
			Standard Deviation			**0.5**

a – All concentrations are reported in units of mM.

4.8.8 Hydrogen Atom Transfer Reactivity of $^{n/Ph}[Cu_2OH]^{3+}$ (n = 2,3) Complexes

General Procedure for HAT Reactions with $^{3/Ph}[Cu_2O]^{2+}$

In the glovebox, a cuvette was charged with 2.4 mL of 0.1 mM $^{3/Ph}[Cu_2OH]^{3+}$ in IBN and sealed with a screw cap equipped with a septum. The cuvette was removed from the glovebox and placed in the pre-cooled cryostat (-65 °C). After 5 minutes, an initial "blank" spectrum was acquired of the complex. Following this measurement, 32 μL of 7.5 mM Verkade^{iPr} in IBN was injected into the cuvette using a 100 μL Hamilton gas tight syringe. A spectrum of the deprotonated product was taken after 10 minutes. To the cooled cuvette, the HAT reagent was added using a 100 μL Hamilton gas tight syringe. Spectra were recorded every 60 seconds for 15 minutes.

General Procedure for HAT Reactions with $^{2/Ph}[Cu_2O]^{2+}$

In the glovebox, a cuvette was charged with 0.1 mM $^{2/Ph}[Cu_2OH]^{3+}$ in IBN and sealed with a screw cap equipped with a septum. The cuvette was removed from the glovebox and placed in the pre-cooled cryostat (-30 °C). After 5 minutes, an initial "blank" spectrum was acquired of the complex. Following this measurement, Verkade^{iPr} in IBN was injected into the cuvette using a 100 μL Hamilton gas tight syringe. A spectrum of the deprotonated product was taken after 10 minutes. To the cooled cuvette, the HAT reagent was added using a 100 μL Hamilton gas tight syringe. Spectra were recorded every 60 seconds for 15 minutes.

The general procedure for $^{3/Ph}[Cu_2O]^{2+}$ was followed for the addition of 9-cyanoxanthene. In this case, 32 μL of 7.5 mM 9-cyaonoxanthene in IBN was added to the cuvette containing $^{3/Ph}[Cu_2O]^{2+}$. A reaction occurred based on the changes in the UV-vis-NIR profile.

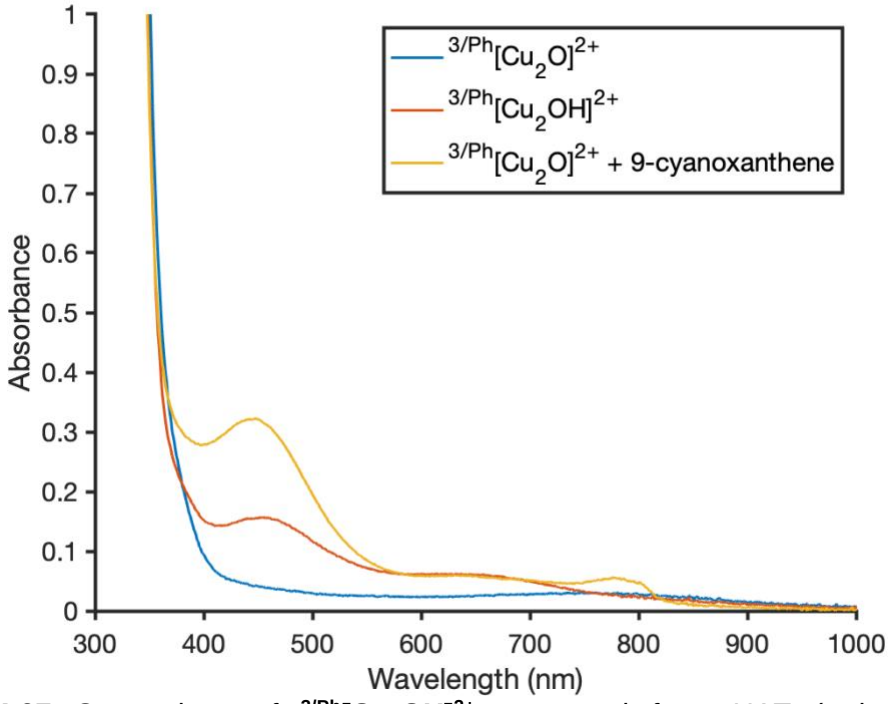

Figure 4.67 Comparison of $^{3/Ph}[Cu_2OH]^{2+}$ generated from HAT (red trace) and $^{3/Ph}[Cu_2OH]^{2+}$ generated from the reduction (yellow trace) at 65°C.

The general procedure for $^{3/Ph}[Cu_2O]^{2+}$ was followed for the addition of phenylhydrazine. In this case, 25 μL of 9.8 mM phenylhydrazine in IBN was added to the cuvette containing $^{3/Ph}[Cu_2O]^{2+}$. A reaction occurred based on the changes in the UV-vis-NIR profile.

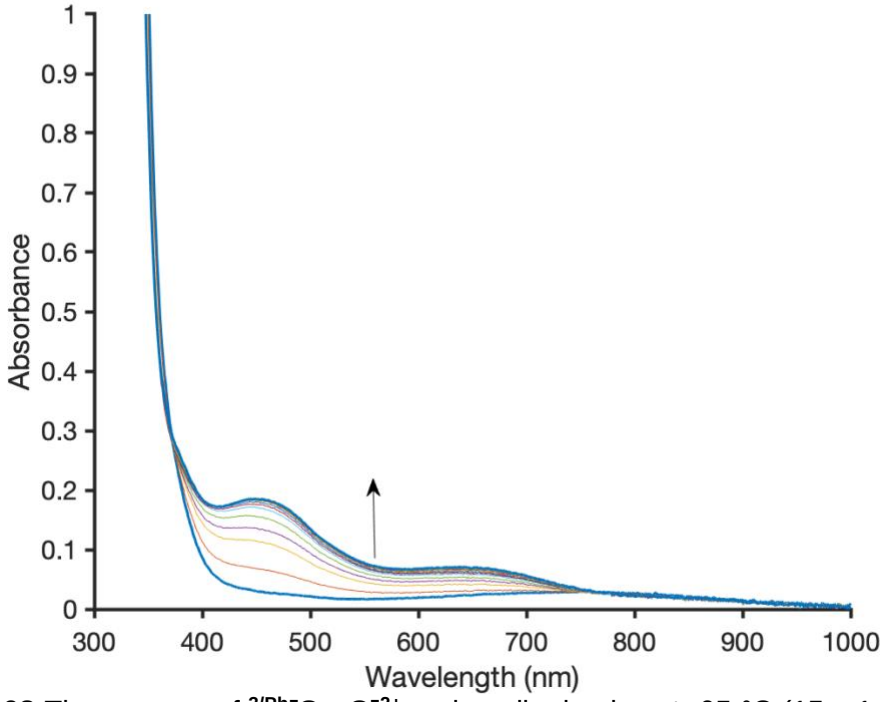

Figure 4.68 Time course of $^{3/Ph}[Cu_2O]^{2+}$ + phenylhydrazine at -65 °C (15 x 1 min. scans; bolded traces represent start and finish).

The general procedure for $^{3/Ph}[Cu_2O]^{2+}$ was followed for the addition of xanthene with modification. In this case, 25 μL of 9.8 mM phenylhydrazine in IBN was added to the cuvette containing $^{3/Ph}[Cu_2O]^{2+}$ at -30 °C. No reaction occurred upon the addition of the HAT reagent. (Note: No change to the spectrum was observed with longer reaction times).

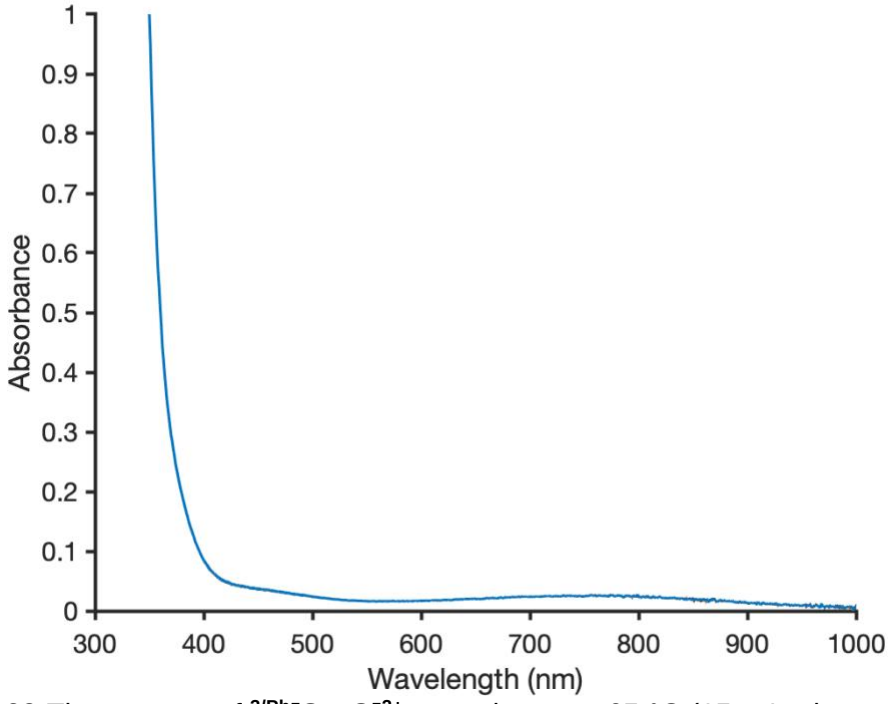

Figure 4.69 Time course of $^{3/Ph}[Cu_2O]^{2+}$ + xanthene at -65 °C (15 x 1 min. scans; bolded traces represent start and finish).

The general procedure for $^{3/Ph}[Cu_2O]^{2+}$ was followed for the addition of 1,4-CHD. In this case, 44 μL of 541 mM 1,4-CHD in IBN was added to the cuvette containing $^{3/Ph}[Cu_2O]^{2+}$. No reaction occurred upon the addition of the HAT reagent. (Note: No change to the spectrum was observed with longer reaction times).

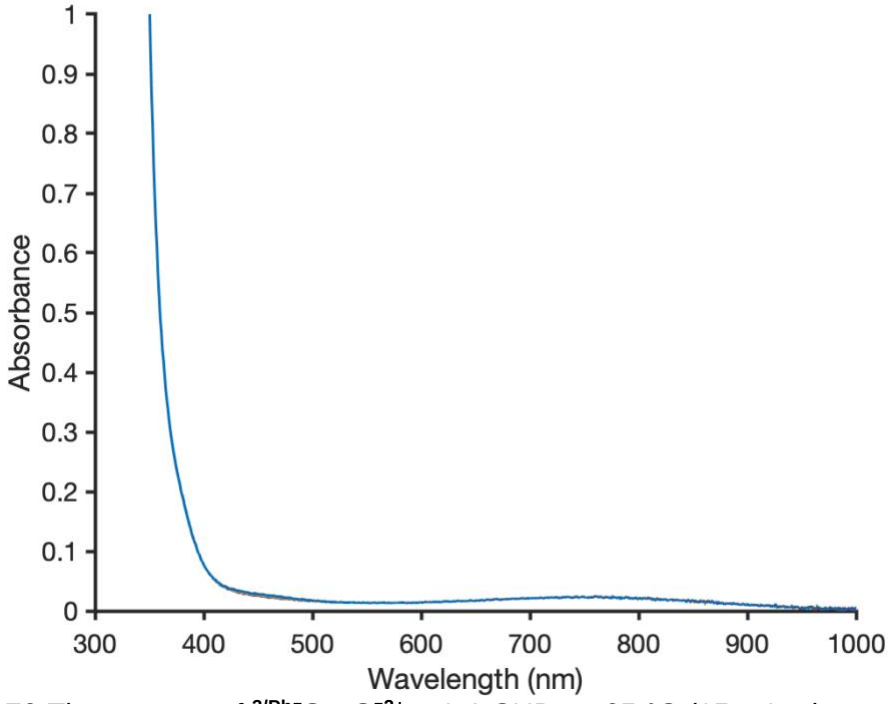

Figure 4.70 Time course of $^{3/Ph}[Cu_2O]^{2+}$ + 1,4-CHD at -65 °C (15 x 1 min. scans; bolded traces represent start and finish).

The general procedure for $^{3/Ph}[Cu_2O]^{2+}$ was followed for the addition of DHA. In this case, 42 μL of 576 mM DHA in IBN was added to the cuvette containing $^{3/Ph}[Cu_2O]^{2+}$. While there was no appearance of the 455 nm feature associated with $^{3/Ph}[Cu_2OH]^{2+}$, the growth of the sharp feature at 377 nm signified HAT from DHA (Tolman and coworkers observed the same signals in HAT experiments with $^{PDA}[Cu_2OH]^{0}$.) The origin of this HAT event is unknown and appears unrelated to $^{3/Ph}[Cu_2O]^{2+}$.

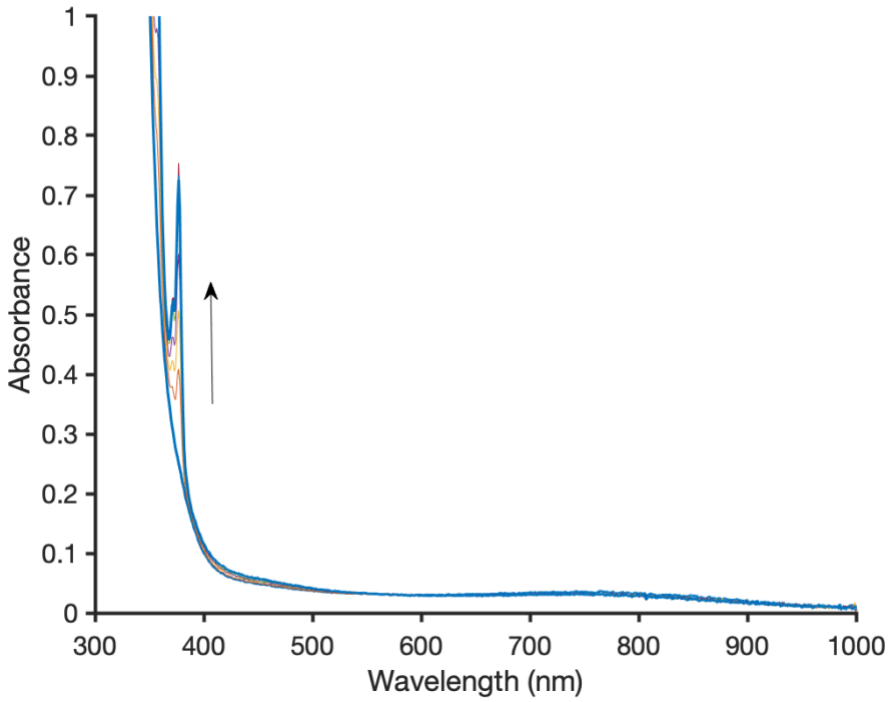

Figure 4.71 Time course of $^{3/Ph}[Cu_2O]^{2+}$ + DHA at -65 °C (15 x 1 min. scans; bolded traces represent start and finish).

The general procedure for $^{2/Ph}[Cu_2O]^{2+}$ was followed for the addition of 9-cyanoxanthene. In this case, 2.4 mL of 0.1 mM $^{2/Ph}[Cu_2OH]^{3+}$ was used. To the chilled cuvette, 39 μL of 6.2 mM Verkade^{iPr} in IBN was added to the cuvette containing $^{2/Ph}[Cu_2OH]^{3+}$. Following, 32 μL of 7.5 mM 9-cyaonoxanthene in IBN was added to the cuvette containing $^{3/Ph}[Cu_2O]^{2+}$. A reaction occurred based on the changes in the UV-vis-NIR profile (see Figure 4.27).

The general procedure for $^{2/Ph}[Cu_2O]^{2+}$ was followed for the addition of xanthene. In this case, 2.0 mL of 0.1 mM $^{2/Ph}[Cu_2OH]^{3+}$ was used. To the chilled cuvette, 21 μL of 9.6 mM Verkade^{iPr} in THF was added to the cuvette containing $^{2/Ph}[Cu_2OH]^{3+}$. Following, 19 μL of 10.5 mM xanthene in IBN was added to the cuvette containing $^{3/Ph}[Cu_2O]^{2+}$. A slow reaction occurred based on the changes in the UV-vis-NIR profile.

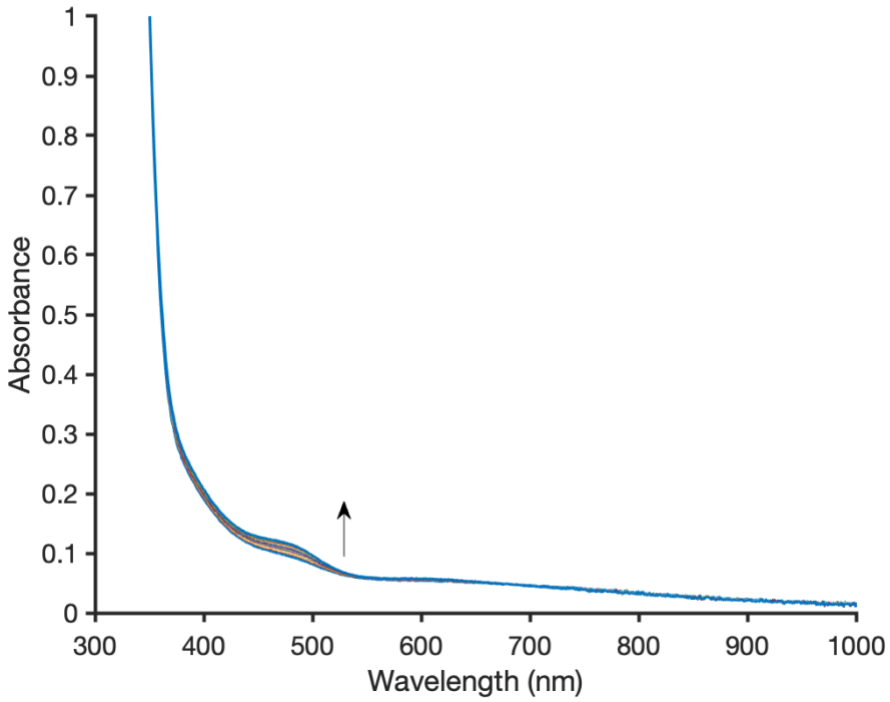

Figure 4.72 Time course of $^{2/Ph}[Cu_2O]^{2+}$ + xanthene at -30 °C (15 x 1 min. scans; bolded traces represent start and finish).

The general procedure for $^{2/Ph}[Cu_2O]^{2+}$ was followed for the addition of DHA with slight modification. In this case, 2.4 mL of 0.1 mM $^{2/Ph}[Cu_2OH]^{3+}$ was used at -65 °C. To the chilled cuvette, 32 μL of 7.5 mM Verkade^{iPr} in IBN was added to the cuvette containing $^{2/Ph}[Cu_2OH]^{3+}$. Following, 42 μL of 576 mM DHA in IBN was added to the cuvette containing $^{3/Ph}[Cu_2O]^{2+}$. While there was no appearance of the 455 nm feature associated with $^{3/Ph}[Cu_2OH]^{2+}$, the growth of the sharp feature at 377 nm signified HAT from DHA (Tolman and coworkers observed the same signals in HAT experiments with $^{PDA}[Cu_2OH]^{0}$.) The origin of this HAT is unknown and appears unrelated to $^{2/Ph}[Cu_2O]^{2+}$.

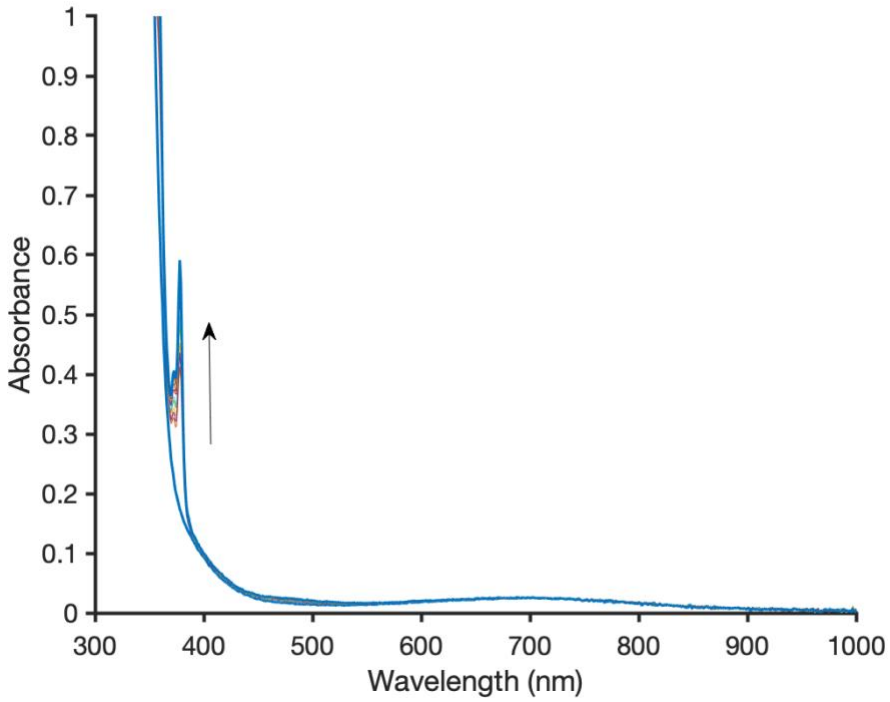

Figure 4.73 Time course of $^{2/Ph}[Cu_2O]^{2+}$ + DHA at -65 °C (15 x 1 min. scans; bolded traces represent start and finish).

4.8.9 X-ray Crystallography

Table 4.3 Summary of structure determination of $^{3/Ph}[Cu_2Cl_2]^{2+}$.

Empirical formula	$C_{58}H_{46}Cl_2Cu_2F_6N_6O_6S_2$
Formula weight	1299.11
Diffractometer	Rigaku XtaLAB Synergy-S (HyPix-6000HE)
Temperature/K	100
Crystal system	monoclinic
Space group	$P2_1/c$
a	18.64740(10)Å
b	17.25520(10)Å
c	17.07510(10)Å
β	96.2690(10)°
Volume	5461.31(5)Å^3
Z	4
d_{calc}	1.580 g/cm^3
μ	3.256 mm^{-1}
F(000)	2648.0
Crystal size, mm	0.13 × 0.08 × 0.07
2θ range for data collection	7 - 149.004°
Index ranges	-23 ≤ h ≤ 23, -18 ≤ k ≤ 21, -21 ≤ l ≤ 21
Reflections collected	90126
Independent reflections	11157[R(int) = 0.0574]
Data/restraints/parameters	11157/810/943
Goodness-of-fit on F^2	1.061
Final R indexes [I>=2σ (I)]	R_1 = 0.0540, wR_2 = 0.1376
Final R indexes [all data]	R_1 = 0.0585, wR_2 = 0.1404
Largest diff. peak/hole	0.82/-0.60 eÅ^{-3}

Table 4.4 Summary of structure determination of $^{3/Ph}[Cu_2Cl]^{3+}$.

Empirical formula	$C_{63}H_{52}ClCu_2F_9N_8O_9S_3$
Formula weight	1494.83
Diffractometer	Rigaku XtaLAB Synergy-S
Temperature/K	100
Crystal system	monoclinic
Space group	$P2_1/m$
a	10.05130(10)Å
b	25.0638(2)Å
c	12.90280(10)Å
β	101.8810(10)°
Volume	3180.89(5)Å^3
Z	2
d_{calc}	1.561 g/cm^3
μ	2.917 mm^{-1}
F(000)	1524.0
Crystal size, mm	0.1 × 0.06 × 0.04
2θ range for data collection	7 - 148.942°
Index ranges	-12 ≤ h ≤ 12, -31 ≤ k ≤ 31, -14 ≤ l ≤ 16
Reflections collected	52956
Independent reflections	6649[R(int) = 0.0482]
Data/restraints/parameters	6649/204/562
Goodness-of-fit on F^2	1.055
Final R indexes [I>=2σ (I)]	R_1 = 0.0411, wR_2 = 0.1093
Final R indexes [all data]	R_1 = 0.0447, wR_2 = 0.1119
Largest diff. peak/hole	0.74/-0.85 eÅ^{-3}

Table 4.5 Summary of structure determination of $^{3/Ph}$**[Cu$_2$OH]$^{3+}$**.

Empirical formula	$C_{61}H_{51}Cl_4Cu_2F_9N_6O_{10}S_3$
Formula weight	1564.13
Diffractometer	Rigaku XtaLAB Synergy-S (Dectris Pilatus3 R 200K)
Temperature/K	100
Crystal system	monoclinic
Space group	$P2_1/c$
a	10.0481(2)Å
b	25.2110(4)Å
c	25.7624(4)Å
β	101.061(2)°
Volume	6405.0(2)Å^3
Z	4
d_{calc}	1.622 g/cm^3
μ	1.018 mm^{-1}
F(000)	3176.0
Crystal size, mm	0.36 × 0.32 × 0.17
2θ range for data collection	4.564 - 56.564°
Index ranges	-13 ≤ h ≤ 13, -33 ≤ k ≤ 33, -34 ≤ l ≤ 34
Reflections collected	122275
Independent reflections	15834[R(int) = 0.0436]
Data/restraints/parameters	15834/111/896
Goodness-of-fit on F^2	1.060
Final R indexes [I>=2σ (I)]	R_1 = 0.0409, wR_2 = 0.1093
Final R indexes [all data]	R_1 = 0.0520, wR_2 = 0.1146
Largest diff. peak/hole	1.02/-0.96 eÅ^{-3}

Table 4.6 Summary of structure determination of $^{3/Ph}$**[Cu]$^{+}$**.

Empirical formula	$C_{57}H_{46}CuF_3N_6O_3S$
Formula weight	1015.60
Diffractometer	Rigaku XtaLAB Synergy-S
Temperature/K	100
Crystal system	monoclinic
Space group	C2/c
a	20.2610(6)Å
b	14.5387(4)Å
c	15.9567(4)Å
β	90.972(3)°
Volume	4699.7(2)Å^3
Z	4
d_{calc}	1.435 g/cm^3
μ	0.576 mm^{-1}
F(000)	2104.0
Crystal size, mm	0.16 × 0.13 × 0.06
2θ range for data collection	5.106 - 56.562°
Index ranges	-26 ≤ h ≤ 26, -19 ≤ k ≤ 19, -21 ≤ l ≤ 21
Reflections collected	47569
Independent reflections	5834[R(int) = 0.0450]
Data/restraints/parameters	5834/95/339
Goodness-of-fit on F^2	1.022
Final R indexes [I>=2σ (I)]	R_1 = 0.0463, wR_2 = 0.1176
Final R indexes [all data]	R_1 = 0.0548, wR_2 = 0.1225
Largest diff. peak/hole	0.77/-0.46 eÅ^{-3}

Table 4.7 Summary of structure determination of $^{3/Ph}[Cu_2Cl_2]^{2+}$.

Empirical formula	$C_{83}H_{77}Cl_2Cu_2F_3N_6O_5PS$
Formula weight	1556.51
Diffractometer	Rigaku XtaLAB Synergy-S (HyPix-6000HE)
Temperature/K	100
Crystal system	triclinic
Space group	$P\bar{1}$
a	11.74710(10)Å
b	16.8904(2)Å
c	20.0531(3)Å
α	70.1480(10)°
β	84.1010(10)°
γ	86.8810(10)°
Volume	3721.73(8)Å^3
Z	2
d_{calc}	1.389 g/cm^3
μ	2.356 mm^{-1}
F(000)	1614.0
Crystal size, mm	0.18 × 0.12 × 0.01
2θ range for data collection	5.564 - 149.002°
Index ranges	-14 ≤ h ≤ 14, -21 ≤ k ≤ 21, -19 ≤ l ≤ 23
Reflections collected	91476
Independent reflections	15053[R(int) = 0.0492]
Data/restraints/parameters	15053/702/1054
Goodness-of-fit on F^2	1.052
Final R indexes [I>=2σ (I)]	R_1 = 0.0574, wR_2 = 0.1582
Final R indexes [all data]	R_1 = 0.0623, wR_2 = 0.1626
Largest diff. peak/hole	0.87/-1.11 eÅ^{-3}

Table 4.8 Summary of structure determination of $^{2/Ph}[Cu_2OH]^{3+}$.

Empirical formula	$C_{59}H_{47}Cl_4Cu_2F_9N_6O_{10}S_3$
Formula weight	1536.08
Diffractometer	Rigaku XtaLAB Synergy-S (HyPix-6000HE)
Temperature/K	100
Crystal system	monoclinic
Space group	$P2_1$
a	10.1659(3)Å
b	23.7638(6)Å
c	12.8259(4)Å
β	99.377(3)°
Volume	3057.08(15)Å^3
Z	2
d_{calc}	1.669 g/cm^3
μ	1.065 mm^{-1}
F(000)	1556.0
Crystal size, mm	0.28 × 0.23 × 0.11
2θ range for data collection	3.646 - 56.558°
Index ranges	-13 ≤ h ≤ 13, -31 ≤ k ≤ 31, -15 ≤ l ≤ 17
Reflections collected	61481
Independent reflections	15121[R(int) = 0.0349]
Data/restraints/parameters	15121/1/839
Goodness-of-fit on F^2	1.041
Final R indexes [I>=2σ (I)]	R_1 = 0.0327, wR_2 = 0.0882
Final R indexes [all data]	R_1 = 0.0349, wR_2 = 0.0893
Largest diff. peak/hole	0.54/-0.93 eÅ^{-3}
Flack parameter	0.495(8)

BIBLIOGRAPHY

(1) Administration, U. S. E. I. *Annual Energy Outlook 2022 (AEO2022)*. 2022. (accessed 2022 April 29, 2022).

(2) Caballero, A.; Pérez, P. J. Methane as raw material in synthetic chemistry: the final frontier. *Chem. Soc. Rev.* **2013**, *42*, 8809.

(3) Sun, L.; Wang, Y.; Guan, N.; Li, L. Methane Activation and Utilization: Current Status and Future Challenges. *Energy Technol.* **2020**, *8*, 1.

(4) Olah, G. A. Beyond Oil and Gas: The Methanol Economy. *Angew. Chem. Int. Ed.* **2005**, *44*, 2636.

(5) da Silva, M. J. Synthesis of methanol from methane: Challenges and advances on the multi-step (syngas) and one-step routes (DMTM). *Fuel Process. Technol.* **2016**, *145*, 42.

(6) Park, M. B.; Park, E. D.; Ahn, W.-S. Recent Progress in Direct Conversion of Methane to Methanol Over Copper-Exchanged Zeolites. *Front. Chem.* **2019**, *7*, 1.

(7) Tomkins, P.; Ranocchiari, M.; van Bokhoven, J. A. Direct Conversion of Methane to Methanol under Mild Conditions over Cu-Zeolites and beyond. *Acc. Chem. Res.* **2017**, *50*, 418.

(8) Snyder, B. E. R.; Bols, M. L.; Schoonheydt, R. A.; Sels, B. F.; Solomon, E. I. Iron and Copper Active Sites in Zeolites and Their Correlation to Metalloenzymes. *Chem. Rev.* **2018**, *118*, 2718.

(9) Newton, M. A.; Knorpp, A. J.; Sushkevich, V. L.; Palagin, D.; van Bokhoven, J. A. Active sites and mechanisms in the direct conversion of methane to methanol using Cu in zeolitic hosts: a critical examination. *Chem. Soc. Rev.* **2020**, *49*, 1449.

(10) Díaz, I.; Kokkoli, E.; Terasaki, O.; Tsapatsis, M. Surface Structure of Zeolite (MFI) Crystals. *Chem. Mater.* **2004**, *16*, 5226.

(11) Kokotailo, G. T.; Lawton, S. L.; Olson, D. H.; Meier, W. M. Structure of synthetic zeolite ZSM-5. *Nature* **1978**, *272*, 437.

(12) Woertink Julia, S.; Smeets Pieter, J.; Groothaert Marijke, H.; Vance Michael, A.; Sels Bert, F.; Schoonheydt Robert, A.; Solomon Edward, I. A [Cu2O]2+ core in Cu-ZSM-5, the active site in the oxidation of methane to methanol. *Proc. Natl. Acad. Sci. U.S.A.* **2009**, *106*, 18908.

(13) Mentzen, B. F.; Bergeret, G. Crystallographic Determination of the Positions of the Copper Cations in Zeolite MFI. *J. Phys. Chem. C.* **2007**, *111*, 12512.

(14) Groothaert, M. H.; Smeets, P. J.; Sels, B. F.; Jacobs, P. A.; Schoonheydt, R. A. Selective Oxidation of Methane by the Bis(μ-oxo)dicopper Core Stabilized on ZSM-5 and Mordenite Zeolites. *J. Am. Chem. Soc.* **2005**, *127*, 1394.

(15) Groothaert, M. H.; van Bokhoven, J. A.; Battiston, A. A.; Weckhuysen, B. M.; Schoonheydt, R. A. Bis(μ-oxo)dicopper in Cu-ZSM-5 and Its Role in the Decomposition of NO: A Combined in Situ XAFS, UV−Vis−Near-IR, and Kinetic Study. *J. Am. Chem. Soc.* **2003**, *125*, 7629.

(16) Smeets, P. J.; Hadt, R. G.; Woertink, J. S.; Vanelderen, P.; Schoonheydt, R. A.; Sels, B. F.; Solomon, E. I. Oxygen Precursor to the Reactive Intermediate in Methanol Synthesis by Cu-ZSM-5. *J. Am. Chem. Soc.* **2010**, *132*, 14736.

(17) Wu, J.-F.; Gao, X.-D.; Wu, L.-M.; Wang, W. D.; Yu, S.-M.; Bai, S. Mechanistic Insights on the Direct Conversion of Methane into Methanol over Cu/Na–ZSM-5 Zeolite: Evidence from EPR and Solid-State NMR. *ACS Catal.* **2019**, *9*, 8677.

(18) Narsimhan, K.; Iyoki, K.; Dinh, K.; Román-Leshkov, Y. Catalytic Oxidation of Methane into Methanol over Copper-Exchanged Zeolites with Oxygen at Low Temperature. *ACS Cent. Sci.* **2016**, *2*, 424.

(19) Haack, P.; Limberg, C. Molecular CuII-O-CuII Complexes: Still Waters Run Deep. *Angew. Chem. Int. Ed.* **2014**, *53*, 4282.

(20) Karlin, K. D.; Gultneh, Y.; Hayes, J. C.; Zubieta, J. Copper(I)-dioxygen reactivity. 2. Reaction of a three-coordinate copper(I) complex with dioxygen, with evidence for a binuclear oxo-copper(II) species: structural characterization of a parallel-planar dihydroxo-bridged dimer. *Inorg. Chem.* **1984**, *23*, 519.

(21) Sanyal, I.; Mahroof-Tahir, M.; Nasir, M. S.; Ghosh, P.; Cohen, B. I.; Gultneh, Y.; Cruse, R. W.; Farooq, A.; Karlin, K. D. Reactions of dioxygen (O2) with mononuclear copper(I) complexes: temperature-dependent formation of peroxo- or oxo- (and dihydroxo-) bridged dicopper(II) complexes. *Inorg. Chem.* **1992**, *31*, 4322.

(22) Obias, H. V.; Lin, Y.; Murthy, N. N.; Pidcock, E.; Solomon, E. I.; Ralle, M.; Blackburn, N. J.; Neuhold, Y.-M.; Zuberbühler, A. D.; Karlin, K. D. Peroxo-, Oxo-, and Hydroxo-Bridged Dicopper Complexes: Observation of Exogenous Hydrocarbon Substrate Oxidation. *J. Am. Chem. Soc.* **1998**, *120*, 12960.

(23) Kitajima, N.; Koda, T.; Hashimoto, S.; Kitagawa, T.; Morooka, Y. Synthesis and characterization of the dinuclear copper(II) complexes [Cu(HB(3,5-Me2pz)3)]2X (X = O2-, (OH)22-, CO22-, O22-). *J. Am. Chem. Soc.* **1991**, *113*, 5664.

(24) Kitajima, N.; Koda, T.; Iwata, Y.; Morooka, Y. Reaction aspects of a .mu.-peroxo binuclear copper(II) complex. *J. Am. Chem. Soc.* **1990**, *112*, 8833.

(25) Nobumasa, K.; Takayuki, K.; Yoshihiko, M.-o. Synthesis of a Novel μ-Oxo Binuclear Copper(II) Complex Ligated by Hydrotris(3,5-dimethyl-1-pyrazolyl)borate. *Chem. Lett.* **1988**, *17*, 347.

(26) Ali, G.; VanNatta, P. E.; Ramirez, D. A.; Light, K. M.; Kieber-Emmons, M. T. Thermodynamics of a μ-oxo Dicopper(II) Complex for Hydrogen Atom Abstraction. *J. Am. Chem. Soc.* **2017**, *139*, 18448.

(27) Réglier, M.; Jorand, C.; Waegell, B. Binuclear copper complex model of tyrosinase. *J. Chem. Soc., Chem. Commun.* **1990**, 1752.

(28) Haack, P.; Kärgel, A.; Greco, C.; Dokic, J.; Braun, B.; Pfaff, F. F.; Mebs, S.; Ray, K.; Limberg, C. Access to a CuII–O–CuII Motif: Spectroscopic Properties, Solution Structure, and Reactivity. *J. Am. Chem. Soc.* **2013**, *135*, 16148.

(29) Jurgeleit, R.; Grimm-Lebsanft, B.; Flöser, B. M.; Teubner, M.; Buchenau, S.; Senft, L.; Hoffmann, J.; Naumova, M.; Näther, C.; Ivanović-Burmazović, I.; et al. Catalytic Oxygenation of Hydrocarbons by Mono-μ-oxo Dicopper(II) Species Resulting from O−O Cleavage of Tetranuclear CuI/CuII Peroxo Complexes. *Angew. Chem. Int. Ed.* **2021**, *60*, 14154.

(30) Solomon, E. I.; Heppner, D. E.; Johnston, E. M.; Ginsbach, J. W.; Cirera, J.; Qayyum, M.; Kieber-Emmons, M. T.; Kjaergaard, C. H.; Hadt, R. G.; Tian, L. Copper Active Sites in Biology. *Chem. Rev.* **2014**, *114*, 3659.

(31) Mendy, J. S.; Saeed, M. A.; Fronczek, F. R.; Powell, D. R.; Hossain, M. A. Anion Recognition and Sensing by a New Macrocyclic Dinuclear Copper(II) Complex: A Selective Receptor for Iodide. *Inorg. Chem.* **2010**, *49*, 7223.

(32) Rhaman, M. M.; Alamgir, A.; Wong, B. M.; Powell, D. R.; Hossain, M. A. A highly efficient dinuclear Cu(ii) chemosensor for colorimetric and fluorescent detection of cyanide in water. *RSC Adv.* **2014**, *4*, 54263.

(33) Mateus, P.; Lima, L. M. P.; Delgado, R. Di- and trinuclear copper(II) complexes of polyaza macrocycles and cryptands as anion receptors. *Polyhedron* **2013**, *52*, 25.

(34) Carsch, K. M.; Lukens, J. T.; DiMucci, I. M.; Iovan, D. A.; Zheng, S.-L.; Lancaster, K. M.; Betley, T. A. Electronic Structures and Reactivity Profiles of Aryl Nitrenoid-Bridged Dicopper Complexes. *J. Am. Chem. Soc.* **2020**, *142*, 2264.

(35) Ziegler, M. S.; Lakshmi, K. V.; Tilley, T. D. Dicopper Cu(I)Cu(I) and Cu(I)Cu(II) Complexes in Copper-Catalyzed Azide–Alkyne Cycloaddition. *J. Am. Chem. Soc.* **2017**, *139*, 5378.

(36) Ziegler, M. S.; Levine, D. S.; Lakshmi, K. V.; Tilley, T. D. Aryl Group Transfer from Tetraarylborato Anions to an Electrophilic Dicopper(I) Center and Mixed-Valence μ-Aryl Dicopper(I,II) Complexes. *J. Am. Chem. Soc.* **2016**, *138*, 6484.

(37) Drew, M. G. B.; McCann, M.; Nelson, S. M. Bi-copper(I) and bi-copper(II) complexes of a 30-membered macrocyclic ligand: the inclusion of substrate molecules and the crystal and molecular structures of a μ-hydroxo- and a μ-imidazolato-complex. *J. Chem. Soc., Dalton Trans.* **1981**, 1868.

(38) Drew, M. G. B.; McCann, M.; Nelson, S. M. Binuclear macrocyclic copper(II) complexes as receptors for small bridging ligands: X-ray crystal and molecular structure of a μ-azido complex. *J. Chem. Soc., Chem. Commun.* **1979**, 481.

(39) Drew, M. G. B.; Nelson, J.; Esho, F.; McKee, V.; Nelson, S. M. Dicopper(II) complexes of a macrocyclic ligand containing single hydroxo-, methoxo-, or 1,1-azido-bridges: synthesis, magnetic properties, electron spin resonance spectra, and the crystal and molecular structure of a μ-hydroxo-derivative. *J. Chem. Soc., Dalton Trans.* **1982**, 1837.

(40) Nelson, S. M.; Esho, F. S.; Drew, M. G. B. Metal-ion controlled reactions of 2,6-diacetylpyridine with 1,2-di-aminoethane and 2,6-diformylpyridine with o-phenylenediamine and the crystal and molecular structure of a pentagonal pyramidal cadmium(II) complex containing unidentate o-phenylenediamine. *J. Chem. Soc., Dalton Trans.* **1982**, 407.

(41) Groom, C. R.; Bruno, I. J.; Lightfoot, M. P.; Ward, S. C. The Cambridge Structural Database. *Acta Crystallogr., Sect. B.* **2016**, *72*, 171.

(42) Römelt, C.; Weyhermüller, T.; Wieghardt, K. Structural characteristics of redox-active pyridine-1,6-diimine complexes: Electronic structures and ligand oxidation levels. *Coord. Chem. Rev.* **2019**, *380*, 287.

(43) Davis, R. N.; Tanski, J. M.; Adrian, J. C.; Tyler, L. A. Variations in the coordination environment of Co2+, Cu2+ and Zn2+ complexes prepared from a tridentate (imino)pyridine ligand and their structural comparisons. *Inorganica Chim. Acta.* **2007**, *360*, 3061.

(44) Trivedi, M.; Pandey, D. S.; Xu, Q. Nickel and copper complexes based on tridentate nitrogen donor ligand 2,6-bis-(1-phenyliminoethyl) pyridine: Synthesis, spectral and structural characterization. *Inorganica Chim. Acta.* **2007**, *360*, 2492.

(45) Fan, R.-Q.; Wang, P.; Yang, Y.-L.; Zhang, Y.-J.; Yin, Y.-B.; Hasi, W. Syntheses, structures, and luminescent properties of copper(II) complexes based on 2,6-bis(imino)pyridyl ligands. *Polyhedron* **2010**, *29*, 2862.

(46) Su, B.; Feng, G. Influence of the metal centers of 2,6-bis(imino)pyridyl transition metal complexes on ethylene polymerization/ oligomerization catalytic activities. *Polym. Int.* **2010**, *59*, 1058.

(47) Le Gall, B. t.; Conan, F.; Cosquer, N.; Kerbaol, J.-M.; Kubicki, M. M.; Vigier, E.; Le Mest, Y.; Sala Pala, J. Unexpected behaviour of copper(I) towards a tridentate Schiff base: synthesis, structure and properties of new Cu(I)□Cu(II) and Cu(II) complexes. *Inorganica Chim. Acta.* **2001**, *324*, 300.

(48) Jurca, T.; Ouanounou, S.; Shih, W.-C.; Ong, T.-G.; Yap, G. P. A.; Korobkov, I.; Gorelsky, S.; Richeson, D. Structural and electronic trends for five coordinate 1st row transition metal complexes: Mn(ii) to Zn(ii) captured in a bis(iminopyridine) framework. *Dalton Trans.* **2016**, *45*, 14327.

(49) Restivo, R. J.; Ferguson, G. Structural characterization of metal complexes of 2,6-diacetylpyridine-bis(imines). Crystal and molecular structure of dinitrato{2,6-bis[1-(phenylimino)ethyl]pyridine}copper(II). *J. Chem. Soc., Dalton Trans.* **1976**, 518.

(50) Alyea, E. C.; Ferguson, G.; Restivo, R. J. Preparation and characterization of metal complexes of 2,6-diacetylpyridine bis(imines). Crystallographic study of dinitrato[2,6-diacetylpyridine bis(anil)]nickel(II). *Inorg. Chem.* **1975**, *14*, 2491.

(51) Cheung, P. M.; Berger, R. F.; Zakharov, L. N.; Gilbertson, J. D. Square planar Cu(i) stabilized by a pyridinediimine ligand. *Chem. Comm.* **2016**, *52*, 4156.

(52) Cui, P.; Wang, Q.; McCollom, S. P.; Manor, B. C.; Carroll, P. J.; Tomson, N. C. Ring-Size-Modulated Reactivity of Putative Dicobalt-Bridging Nitrides: C−H Activation versus Phosphinimide Formation. *Angew. Chem. Int. Ed.* **2017**, *56*, 15979.

(53) Liu, T.; Gau, M. R.; Tomson, N. C. Mimicking the Constrained Geometry of a Nitrogen-Fixation Intermediate. *J. Am. Chem. Soc.* **2020**, *142*, 8142.

(54) Spentzos, A. Z.; Gau, M. R.; Carroll, P. J.; Tomson, N. C. Unusual cyanide and methyl binding modes at a dicobalt macrocycle following acetonitrile C–C bond activation. *Chem. Comm.* **2020**, *56*, 9675.

(55) Thierer, L. M.; Brooks, S. H.; Weberg, A. B.; Cui, P.; Zhang, S.; Gau, M. R.; Manor, B. C.; Carroll, P. J.; Tomson, N. C. Macrocycle-Induced Modulation of Internuclear Interactions in Homobimetallic Complexes. *Inorg. Chem.* **2022**, *61*, 6263.

(56) Wang, Q.; Zhang, S.; Cui, P.; Weberg, A. B.; Thierer, L. M.; Manor, B. C.; Gau, M. R.; Carroll, P. J.; Tomson, N. C. Interdependent Metal–Metal Bonding and Ligand Redox-Activity in a Series of Dinuclear Macrocyclic Complexes of Iron, Cobalt, and Nickel. *Inorg. Chem.* **2020**, *59*, 4200.

(57) Zhang, S.; Cui, P.; Liu, T.; Wang, Q.; Longo, T. J.; Thierer, L. M.; Manor, B. C.; Gau, M. R.; Carroll, P. J.; Papaefthymiou, G. C.; et al. N−H Bond Formation at a Diiron Bridging Nitride. *Angew. Chem. Int. Ed.* **2020**, *59*, 15215.

(58) Zhang, S.; Wang, Q.; Thierer, L. M.; Weberg, A. B.; Gau, M. R.; Carroll, P. J.; Tomson, N. C. Tuning Metal–Metal Interactions through Reversible Ligand Folding in a Series of Dinuclear Iron Complexes. *Inorg. Chem.* **2019**, *58*, 12234.

(59) Wang, Q.; Brooks, S. H.; Liu, T.; Tomson, N. C. Tuning metal–metal interactions for cooperative small molecule activation. *Chem. Comm.* **2021**, *57*, 2839.

(60) Addison, A. W.; Rao, T. N.; Reedijk, J.; van Rijn, J.; Verschoor, G. C. Synthesis, structure, and spectroscopic properties of copper(II) compounds containing nitrogen–sulphur donor ligands; the crystal and molecular structure of aqua[1,7-bis(N-methylbenzimidazol-2′-yl)-2,6-dithiaheptane]copper(II) perchlorate. *J. Chem. Soc., Dalton Trans.* **1984**, 1349.

(61) McKee, V.; Smith, J. Synthesis and X-ray structure of a bicopper(II) Schiff base macrocyclic complex having a single endogenous alkoxy bridge. *J. Chem. Soc., Chem. Commun.* **1983**, 1465.

(62) Bower, J. K.; Cypcar, A. D.; Henriquez, B.; Stieber, S. C. E.; Zhang, S. C(sp3)–H Fluorination with a Copper(II)/(III) Redox Couple. *J. Am. Chem. Soc.* **2020**, *142*, 8514.

(63) Bower, J. K.; Cypcar, A. D.; Henriquez, B.; Stieber, S. C. E.; Zhang, S. Correction to "C(sp3)–H Fluorination with a Copper(II)/(III) Redox Couple". *J. Am. Chem. Soc.* **2022**, *144*, 6118.

(64) Chattopadhyay, S.; Ray, M. S.; Drew, M. G. B.; Figuerola, A.; Diaz, C.; Ghosh, A. Facile synthesis of Cu(II) complexes of monocondensed N,N,N donor Schiff base ligands: Crystal structure, spectroscopic and magnetic properties. *Polyhedron* **2006**, *25*, 2241.

(65) Adhikary, C.; Mal, D.; Sen, R.; Bhattacharjee, A.; Gütlich, P.; Chaudhuri, S.; Koner, S. Synthesis, X-ray crystal structure and magnetic study of a novel μ2-1,1-azido bridged dimeric copper(II) complex. *Polyhedron* **2007**, *26*, 1658.

(66) Rahaman, S. H.; Bose, D.; Ghosh, R.; Mostafa, G.; Fun, H.-K.; Ghosh, B. K. Synthesis, crystal and molecular structures of 1D and 2D supramers of copper(II) with N,N′-{bis(pyridin-2-yl) benzylidene}butane-1,4-diamine. *Struct. Chem.* **2007**, *18*, 237.

(67) Nandy, M.; Shit, S.; Garribba, E.; Gómez-García, C. J.; Mitra, S. Double azido/cyanato bridged copper(II) dimers incorporating tridentate nitrogen donors Schiff base: Structure, EPR and magnetic studies. *Polyhedron* **2015**, *102*, 137.

(68) Camus, A.; Marsich*, N.; Manotti Lanfredi*, A. M.; Ugozzoli, F.; Massera, C. Copper(II)nitrito complexes with 2,2′-dipyridylamine. Crystal structures of the [(acetato)(2,2′-dipyridylamine)(nitrito-O,O′)copper(II)] and [(2,2′-dipyridylamine) (nitrito-O,O′)(μ-nitrito-O)copper(II)]2·2(acetonitrile). *Inorganica Chim. Acta.* **2000**, *309*, 1.

(69) Arnold, P. J.; Davies, S. C.; Durrant, M. C.; Griffiths, D. V.; Hughes, D. L.; Sharpe, P. C. Copper(II) nitrite complexes of tripodal ligands derived from 1,1,1-tris(2-pyridyl)methylamine. *Inorganica Chim. Acta.* **2003**, *348*, 143.

(70) Zhu, R.-Q. Di-[mu]-nitrito-[kappa]4O:O-bis[bis(1-ethyl-1H-imidazole-[kappa]N3)(nitrito-[kappa]O)copper(II)]. *Acta Crystallogr., Sect. E.* **2011**, *67*, m869.

(71) Zhu, R.-Q. Bis([mu]-nitrito-[kappa]2O:O)bis[bis(1-methyl-1H-imidazole-[kappa]N3)(nitrito-[kappa]O)copper(II)]. *Acta Crystallogr., Sect. E.* **2012**, *68*, m398.

(72) McGeary, M. J.; Wedlich, R. C.; Coan, P. S.; Folting, K.; Caulton, K. G. Synthesis and thermal decomposition of copper(I) silyloxide complexes. X-ray crystal structures of [Cu(OSiPh3)]4 and [Cu(OSiPh3)(PMe2Ph)]2. *Polyhedron* **1992**, *11*, 2459.

(73) Dai, X.; Warren, T. H. Dioxygen activation by a neutral β-diketiminato copper(i) ethylene complex. *Chem. Comm.* **2001**, 1998.

(74) Chaudhuri, P.; Ventur, D. C.; Wieghardt, K.; Peters, E. M.; Peters, K. Preparation, Magnetism, and Crystal Structures of the Tautomers [LCu(μ2-OH)2CuL](ClO4)2 (Blue) and [LCu(μ2-OH2)(μ2-O)CuL](ClOμ4)μ2 (Green): μ-Aqua-μ-oxo vs. Di-μ-hydroxo Linkage. *Angew. Chem. Int. Ed.* **1985**, *24*, 57.

(75) Thierer, L. M.; Wang, Q.; Brooks, S. H.; Cui, P.; Qi, J.; Gau, M. R.; Manor, B. C.; Carroll, P. J.; Tomson, N. C. Pyridyldiimine macrocyclic ligands: Influences of template ion, linker length and imine substitution on ligand synthesis, structure and redox properties. *Polyhedron* **2021**, *198*, 115044.

(76) Gibson, V. C.; Redshaw, C.; Solan, G. A. Bis(imino)pyridines: Surprisingly Reactive Ligands and a Gateway to New Families of Catalysts. *Chem. Rev.* **2007**, *107*, 1745
(77) Flisak, Z.; Sun, W.-H. Progression of Diiminopyridines: From Single Application to Catalytic Versatility. *ACS Catal.* **2015**, *5*, 4713.

(78) Small, B. L.; Brookhart, M. Iron-Based Catalysts with Exceptionally High Activities and Selectivities for Oligomerization of Ethylene to Linear α-Olefins. *J. Am. Chem. Soc.* **1998**, *120*, 7143.

(79) Small, B. L.; Brookhart, M.; Bennett, A. M. A. Highly Active Iron and Cobalt Catalysts for the Polymerization of Ethylene. *J. Am. Chem. Soc.* **1998**, *120*, 4049.

(80) van der Vlugt, J. I. Redox-Active Pincer Ligands. In *Metal-Ligand Co-operativity: Catalysis and the Pincer-Metal Platform*, van Koten, G., Kirchner, K., Moret, M.-E. Eds.; Springer International Publishing, 2021; pp 135.

(81) Lions, F.; Martin, K. V. Tridentate Chelate Compounds. I. *J. Am. Chem. Soc.* **1957**, *79*, 2733.

(82) Figgins, P. E.; Busch, D. H. Complexes of Iron(II), Cobalt(II) and Nickel(II) with Biacetyl-bis-methylimine, 2-Pyridinal-methylimine and 2,6-Pyridindial-bis-methylimine. *J. Am. Chem. Soc.* **1960**, *82*, 820.

(83) Alyea, E. C.; Merrell, P. H. Terdentate NNN Donor Ligands Derived from 2,6-Diacetylpyridine. *Synthesis and Reactivity in Inorganic and Metal-Organic Chemistry* **1974**, *4*, 535.

(84) Nückel, S.; Burger, P. Transition Metal Complexes with Sterically Demanding Ligands, 3.1 Synthetic Access to Square-Planar Terdentate Pyridine−Diimine Rhodium(I) and Iridium(I) Methyl Complexes: Successful Detour via Reactive Triflate and Methoxide Complexes. *Organometallics* **2001**, *20*, 4345.

(85) Cámpora, J.; Pérez, C. M.; Rodríguez-Delgado, A.; Naz, A. M.; Palma, P.; Álvarez, E. Selective Alkylation of 2,6-Diiminopyridine Ligands by Dialkylmanganese Reagents: A “One-Pot” Synthetic Methodology. *Organometallics* **2007**, *26*, 1104.

(86) Juan, C.; Naz, A. M.; Pilar, P.; Antonio, R.-D.; Eleuterio, Á.; Incoronata, T.; Laura, B. Iron and Cobalt Complexes of 4-Alkyl-2,6-diiminopyridine Ligands: Synthesis and Ethylene Polymerization Catalysis. Wiley-VCH: 2008.

(87) Bhattacharya, S.; Snehalatha, K.; George, S. K. Synthesis of Some Copper(II)-Chelating (Dialkylamino)pyridine Amphiphiles and Evaluation of Their Esterolytic Capacities in Cationic Micellar Media. *J. Org. Chem.* **1998**, *63*, 27.

(88) Chessa, G.; Canovese, L.; Visentin, F.; Santo, C.; Seraglia, R. Synthesis of poly(pyridylthioether) dendrimers incorporating a Fe2(CO)6 cluster core. *Tetrahedron* **2005**, *61*, 1755.

(89) De Bo, G.; De Winter, J.; Gerbaux, P.; Fustin, C.-A. Rotaxane-Based Mechanically Linked Block Copolymers. *Angew. Chem. Int. Ed.* **2011**, *50*, 9093.

(90) Darmon, J. M.; Turner, Z. R.; Lobkovsky, E.; Chirik, P. J. Electronic Effects in 4-Substituted Bis(imino)pyridines and the Corresponding Reduced Iron Compounds. *Organometallics* **2012**, *31*, 2275.

(91) Ivchenko, P. V.; Nifant'ev, I. E.; Buslov, I. V. A convenient approach for the synthesis of 2,6-diformyl- and 2,6-diacetylpyridines. *Tetrahedron Lett.* **2013**, *54*, 217.

(92) Takalo, H.; Kankare, J.; Lund, H.; Makmur, L.; Norrestam, R. Synthesis of Dimethyl and Diethyl 4-(Phenylethynyl)-2,6-pyridinedicarboxylate. *Acta Chemica Scandinavica - ACTA CHEM SCAND* **1987**, *41*, 219.

(93) Zohuri, G. H.; Seyedi, S. M.; Sandaroos, R.; Damavandi, S.; Mohammadi, A. Novel Late Transition Metal Catalysts Based on Iron: Synthesis, Structures and Ethylene Polymerization. *Catal. Lett.* **2010**, *140*, 160.

(94) Dammann, W.; Buban, T.; Schiller, C.; Burger, P. Dinuclear tethered pyridine, diimine complexes. *Dalton Trans.* **2018**, *47*, 12105.

(95) Matsui, J. K.; Primer, D. N.; Molander, G. A. Metal-free C–H alkylation of heteroarenes with alkyltrifluoroborates: a general protocol for 1°, 2° and 3° alkylation. *Chem. Sci.* **2017**, *8*, 3512.

(96) Zhang, L.; Tang, Y.; Han, Z.; Ding, K. Lutidine-Based Chiral Pincer Manganese Catalysts for Enantioselective Hydrogenation of Ketones. *Angew. Chem. Int. Ed.* **2019**, *58*, 4973.

(97) Gygi, D.; Hwang, S. J.; Nocera, D. G. Scalable Syntheses of 4-Substituted Pyridine–Diimines. *J. Org. Chem.* **2017**, *82*, 12933.

(98) Esteruelas, M. A.; López, A. M.; Méndez, L.; Oliván, M.; Oñate, E. Preparation, Structure, and Ethylene Polymerization Behavior of Bis(imino)pyridyl Chromium(III) Complexes. *Organometallics* **2003**, *22*, 395.

(99) Steves, J. E.; Kennedy, M. D.; Chiang, K. P.; Kassel, W. S.; Dougherty, W. G.; Dudley, T. J.; Zubris, D. L. Synthesis of a bulky bis(imino)pyridine compound: a methodology for systematic variation of steric bulk and energetic implications for metalation. *Dalton Trans.* **2009**, 1214.

(100) Smit, T. M.; Tomov, A. K.; Britovsek, G. J. P.; Gibson, V. C.; White, A. J. P.; Williams, D. J. The effect of imine-carbon substituents in bis(imino)pyridine-based ethylene polymerisation catalysts across the transition series. *Catalysis Science & Technology* **2012**, *2*, 643.

(101) Kleigrewe, N.; Steffen, W.; Blömker, T.; Kehr, G.; Fröhlich, R.; Wibbeling, B.; Erker, G.; Wasilke, J.-C.; Wu, G.; Bazan, G. C. Chelate Bis(imino)pyridine Cobalt Complexes: Synthesis, Reduction, and Evidence for the Generation of Ethene Polymerization Catalysts by Li+ Cation Activation. *J. Am. Chem. Soc.* **2005**, *127*, 13955.

(102) Ye, S.-h.; Li, L.; Zhang, M.; Zhou, Z.; Quan, M.-h.; Guo, L.-F.; Wang, Y.; Yang, M.; Lai, W.-y.; Huang, W. Pyridine linked fluorene hybrid bipolar host for blue, green, and orange phosphorescent organic light-emitting diodes toward solution processing. *J. Mater. Chem. C.* **2017**, *5*, 11937.

(103) Kumar, S.; Paul, D.; Hundal, G.; Hundal, M. S.; Singh, H. Heterocalixarenes Part 3: Bis-oxo-bridged calix[1]cyclicurea[3]arene and calix[1]cyclicurea[1]pyridine[2]arenes. Synthesis, X-ray crystal structure and conformational analysis1. *J. Chem. Soc., Perkin Trans. 1* **2000**, 1037.

(104) Anbarasan, P.; Neumann, H.; Beller, M. A Convenient Synthesis of Benzonitriles via Electrophilic Cyanation with N-Cyanobenzimidazole. *Chemistry – A European Journal* **2010**, *16*, 4725.

(105) Warren, J. J.; Tronic, T. A.; Mayer, J. M. Thermochemistry of Proton-Coupled Electron Transfer Reagents and its Implications. *Chem. Rev.* **2010**, *110*, 6961.

(106) Agarwal, R. G.; Coste, S. C.; Groff, B. D.; Heuer, A. M.; Noh, H.; Parada, G. A.; Wise, C. F.; Nichols, E. M.; Warren, J. J.; Mayer, J. M. Free Energies of Proton-Coupled Electron Transfer Reagents and Their Applications. *Chem. Rev.* **2022**, *122*, 1.

(107) Donoghue, P. J.; Tehranchi, J.; Cramer, C. J.; Sarangi, R.; Solomon, E. I.; Tolman, W. B. Rapid C–H Bond Activation by a Monocopper(III)–Hydroxide Complex. *J. Am. Chem. Soc.* **2011**, *133*, 17602.

(108) Dhar, D.; Tolman, W. B. Hydrogen Atom Abstraction from Hydrocarbons by a Copper(III)-Hydroxide Complex. *J. Am. Chem. Soc.* **2015**, *137*, 1322.

(109) Dhar, D.; Yee, G. M.; Markle, T. F.; Mayer, J. M.; Tolman, W. B. Reactivity of the copper(iii)-hydroxide unit with phenols. *Chem. Sci.* **2017**, *8*, 1075.

(110) Dhar, D.; Yee, G. M.; Spaeth, A. D.; Boyce, D. W.; Zhang, H.; Dereli, B.; Cramer, C. J.; Tolman, W. B. Perturbing the Copper(III)–Hydroxide Unit through Ligand Structural Variation. *J. Am. Chem. Soc.* **2016**, *138*, 356.

(111) Dhar, D.; Yee, G. M.; Tolman, W. B. Effects of Charged Ligand Substituents on the Properties of the Formally Copper(III)-Hydroxide ([CuOH]2+) Unit. *Inorg. Chem.* **2018**, *57*, 9794.

(112) Kindermann, N.; Dechert, S.; Demeshko, S.; Meyer, F. Proton-Induced, Reversible Interconversion of a μ-1,2-Peroxo and a μ-1,1-Hydroperoxo Dicopper(II) Complex. *J. Am. Chem. Soc.* **2015**, *137*, 8002.

(113) Kindermann, N.; Günes, C.-J.; Dechert, S.; Meyer, F. Hydrogen Atom Abstraction Thermodynamics of a μ-1,2-Superoxo Dicopper(II) Complex. *J. Am. Chem. Soc.* **2017**, *139*, 9831.

(114) Quist, D. A.; Ehudin, M. A.; Schaefer, A. W.; Schneider, G. L.; Solomon, E. I.; Karlin, K. D. Ligand Identity-Induced Generation of Enhanced Oxidative Hydrogen Atom Transfer Reactivity for a CuII2(O2•–) Complex Driven by Formation of a CuII2(−OOH) Compound with a Strong O–H Bond. *J. Am. Chem. Soc.* **2019**, *141*, 12682.

(115) VanNatta, P. E.; Ramirez, D. A.; Velarde, A. R.; Ali, G.; Kieber-Emmons, M. T. Exceptionally High O–H Bond Dissociation Free Energy of a Dicopper(II) μ-Hydroxo Complex and Insights into the Geometric and Electronic Structure Origins Thereof. *J. Am. Chem. Soc.* **2020**, *142*, 16292.

(116) Bordwell, F. G.; Cheng, J. P.; Harrelson, J. A. Homolytic bond dissociation energies in solution from equilibrium acidity and electrochemical data. *J. Am. Chem. Soc.* **1988**, *110*, 1229.

(117) Yang, L.; Powell, D. R.; Houser, R. P. Structural variation in copper(i) complexes with pyridylmethylamide ligands: structural analysis with a new four-coordinate geometry index, τ4. *Dalton Trans.* **2007**, 955.

(118) Connelly, N. G.; Geiger, W. E. Chemical Redox Agents for Organometallic Chemistry. *Chem. Rev.* **1996**, *96*, 877.

(119) Tshepelevitsh, S.; Kütt, A.; Lõkov, M.; Kaljurand, I.; Saame, J.; Heering, A.; Plieger, P. G.; Vianello, R.; Leito, I. On the Basicity of Organic Bases in Different Media. *Eur. J. Org. Chem.* **2019**, *2019*, 6735.

(120) Kisanga, P. B.; Verkade, J. G.; Schwesinger, R. pKa Measurements of P(RNCH2CH3)3N. *J. Org. Chem.* **2000**, *65*, 5431.

(121) Zhang, X.; Bordwell, F. G. Acidities and homolytic bond dissociation energies of the acidic carbon-hydrogen bonds in radical cations. *J. Org. Chem.* **1992**, *57*, 4163.